Doctoral thesis

Tomographic reconstruction of gradient indices with rotational symmetry. Application to crystalline lenses.

Daniel Vázquez Martínez

Departamento de Física Aplicada
Facultade de Física

Santiago de Compostela, March, 27th 2007

Eva Acosta Plaza, associate professor of the Universidade de Santiago de Compostela,

STATES:

that this work, entitled *"Tomographic reconstruction of gradient indices with rotational symmetry. Application to crystalline lenses"*, has been carried out under her supervision by the Ph.D. student **Daniel Vázquez Martínez** in the Area of Optics of the Department of Applied Physics of the Universidade de Santiago de Compostela and it constitutes the doctoral thesis he presents to obtain the Degree of Doctor in this university.

Thesis supervisor, Ph.D. student,

Eva Acosta Plaza Daniel Vázquez Martínez

"When you express an idea, you give it an order it does not possess originally. Somehow, you must give it a coherent, synthetic and understandable form for everyone else. As long as you just think of it, it can carry on being the wonderful mess it is. However, once you make up your mind to express it, you start to rule out some things, to assume some other, to illustrate this and to cut out that, to order the whole by giving it some logic: you work on it a while and eventually you have something the people can understand. A clear and defined idea. In the beginning your intention is to do everything as it should be: you try not to get rid of too many things, you would like to save the infinity of the idea you had in your head. You try it"

Alessandro Baricco, *City*

Acknowledgments

"And finally Achilles wins by a (infinitesimal) head to the turtle!" A happy ending, isn't it? Who knows if Zeno was not actually a Ph.D. student of Parmenides and its paradox a hint or just the product of the despair because of a never-ending thesis ("The Being, is it or is it not? Does it matter?"). Well, let us put aside the speculations and go straight to one of the main sections of any thesis, the Acknowledgments, that rear window that allows us to check that inside every scientist there is also a heart that beats and makes poum, poum. Sobriety and style, Dani.

Let us start by the beginning: the Family. Thank you for your constant and unconditional support, for giving me such strong foundations to build on any personal adventure, for a love that does not finish ¡Un bico moi grande!

¡Friends!, both those of my office and surroundings and those I have spread around the outer space: you also deserve here your piece of the cake. Without your company, without your support, without our discussions, without you, in short, I would not have faced this huge work with the same will and spirit. Since I know many of you would have preferred a more explicit mention, I offer to you a solution: to print this sheet and to fill in the dots.

Just thinking of you, ¡Thanks a lot,.....!

I would like to make a special mention to several persons that have helped me throughout this work: the professor George Smith, good friend and researcher who supervised my work in Australia; the professor Leon Garner, who did the same in New Zealand; José Albino Vázquez Aldrey, to whose generosity I owe most of "my crystalline lenses"; and to professor Jer R. Kuszak, who has been so kind as to allow me to use some of his pictures and graphs in my thesis.

I owe another special, very special, mention to my thesis supervisor, Eva. If I have ever stopped being just a graduate to become a scientist is thanks to her, endless source of friendship, knowledge, stress, laughter and many other things, all compacted in no much more than one meter and a half (She will not forgive me!)

Finally, I would like to thank the regional government (Xunta de Galicia) for its economic support throughout my years of doctorate by means of different grants. Likewise, I would like to point out this work has been carried out within the research project financed by the Ministerio de Educación y Ciencia (Ref. AYA2004-07773-C02-02).

Contents

Introduction **1**

1 The crystalline lens **5**
1.1 Embryology 6
1.2 Histology 9
1.2.1 Capsule 9
1.2.2 Anterior epithelium 10
1.2.3 Fibers 10
1.3 Form and layout of the secondary fibers 12
1.3.1 The sutures and their patterns 13
1.4 Metabolism 19
1.5 The crystalline lens as an optical element 20
1.6 Rotational symmetry of the gradient index of the crystalline lens 22

2 Methods of measurement of the gradient index in crystalline lenses **25**
2.1 Destructive methods 25
2.2 Non destructive methods 29
2.2.1 Ray deflectometry 29
2.2.2 Interferometry 32
2.2.3 Fitting of ocular and visual parameters 33
2.3 Hybrid methods 34
Need of a new method of reconstruction of the gradient index in crystalline lenses 35

3 Theoretical bases of a tomographic algorithm **37**
3.1 Light propagation under the approximation of geometrical optics 37
3.1.1 Propagation of rays of light in media with rotationally symmetrical gradient index 39
3.2 Tomography basics 40
3.3 Formulation of a tomographic algorithm on the basis of the geometrical optics and tomography 42

4 Tomographic algorithm of reconstruction of the gradient index 47
4.1 Ray deflectometry applied to tomography . . . 47
4.2 Gradient index model . . . 51
4.3 Tomographic inversion . . . 52
4.3.1 The piston K and its influence on the retrieval of the gradient coefficients . . . 58
4.4 Logical sequence of the tomographic algorithm . . . 61
4.4.1 Monopolynomial reconstruction . . . 61
4.4.2 Bipolynomial reconstruction . . . 63

5 Numerical simulations of the tomographic algorithm 65
5.1 Accuracy of the tomographic algorithm . . . 65
5.1.1 Qualitative estimation of the error in the tomographic retrieval . . 67
5.2 Numerical simulations of reconstruction of gradients with spherical symmetry . . . 68
5.3 Numerical simulations in gradient indices with non spherical rotational symmetry . . . 77

6 Collection, processing and analysis of experimental data 89
6.1 Assembly and operation of an experimental setup of ray deflectometry . . 90
6.1.1 Experimental protocol for the collection of experimental data . . . 95
6.2 Image processing and collection of the input data of the tomographic algorithm . . . 97
6.2.1 Processing of laser beam images . . . 97
6.2.1.1 Sources of error in the processing of laser beams . . . 101
6.2.2 Processing of the images of the surface of the crystalline lens . . . 104
6.2.2.1 Sources of error in the characterization of the surfaces of the lens . . . 107
6.2.3 Collection of the input data of the tomographic algorithm . . . 111
6.3 Calibration of the experimental setup . . . 111
6.3.1 Checking and refinement of the correction of the distortion in MC 111
6.3.2 Search of the best threshold for the detection of the rays . . . 112
6.3.3 Detection and minimization of misalignments . . . 113

7 Experimental results 119
7.1 Teleost fish lenses (spherical symmetry) . . . 119
7.1.1 Analysis of the spherical symmetry in teleost fish lenses . . . 124

7.1.1.1 Profile of the sagittal plane . . . 124
7.1.1.2 Distribution of the sines of deflection at the exit of the lens 125
7.1.1.3 Study of the phase at the exit of the lens by means of the interferometry . . . 126
7.2 Pig lenses (rotational symmetry) . . . 128
7.2.1 Reconstruction of the gradient index . . . 130
7.2.1.1 Analysis of the retrieved gradient indices . . . 134
7.2.2 Optical behaviour of the retrieved gradient indices . . . 137
7.2.3 Analysis of the rotational symmetry in pig lenses . . . 139
7.2.3.1 Symmetry of the surfaces of the lens . . . 140
7.2.3.2 Profile of the eye lens in two different meridional planes . 140
7.2.3.3 Distribution of the sines at the exit of two different meridional planes . . . 141
7.2.3.4 Deflection of the rays in the meridional plane . . . 142
7.2.3.5 Optical characterization of the crystalline lenses by interferometry . . . 143
7.3 Discussion of the results. Comparison with other methods. . . . 145

Conclusions **149**

A Worst tomographic reconstruction (fish) **151**

B Better tomographic reconstruction (fish) **157**

C Worst tomographic reconstruction (pig) **163**
C.1 First projection . . . 167
C.2 Second projection . . . 171
C.3 Third projection . . . 175

D Best tomographic reconstruction (pig) **179**
D.1 First projection . . . 183
D.2 Second projection . . . 187
D.3 Third projection . . . 191

E On axis optics of the average pig lens **195**

F Optics of a crystalline lens with a homogeneous refractive index **199**
F.1 First projection . . . 201

F.2 Second projection 204
F.3 Third projection 207

Bibliography **211**

Papers published during this research **219**

Tomographic reconstruction of gradient indices with rotational symmetry. Application to crystalline lenses.

Introduction

Gradient index media, or GRIN media, have been one of the more outstanding objects of study throughout the history of Optics. Such media are characterized by a refractive index that changes from one point to the other. As a result, the trajectory of the rays inside these media is generally curved. Throughout the last decades the importance of these media has increased with the development of technologies that have allowed the implementation of such gradients in different optical elements [Iga84]. However, it is not necessary to think of elements of artificial origin to find examples of GRIN media. Very well known optical phenomena, like mirages, are due to the existence of gradient indices of natural origin. Another example, discovered in the 19th century and that might have inspired Maxwell for the first theoretical model of a GRIN lens [Fer90], is that of the crystalline lens.

The crystalline lens is one of the two lenses that compose the ocular system of any vertebrate, where the other one is the cornea. Due to a variable concentration of a special type of proteins, the crystalline lens is not a homogeneous optical medium, but a GRIN one. This feature has important consequences on its optical behaviour. It allows to decrease its optical aberrations in relation with those the lens would present if the index were constant [Chr91, p. 96] and also to obtain higher effective paraxial indices than the maximum value the refractive index might reach in a crystalline lens [Gar01], thus increasing its paraxial power.

A first reason to tackle the reconstruction and study of such gradient is to determine with accuracy the contribution of that gradient index in the optical properties of the eye lens. With that information the theoretical modeling of a schematic eye could be completed. This would be useful to predict with some accuracy the outcomes of all kind of ocular surgery. The importance of this goal is better understood if it is taken into account the crystalline lens is the ocular component that undergoes the biggest changes throughout life and accommodation, the reflex action whereby the eye is able to focus objects at different distances. On the other hand, assuming a previous knowledge of the dependence of the refractive index with the histological and biochemical properties of the lens, the characterization of the gradient index may be very useful for a non invasive study

of those properties. Likewise, it might be of big help for a better design of intraocular lenses aimed at replacing the eye lens. Ophthalmological instrumentation is another field that would also benefit from a method for the reconstruction of the gradient index of the crystalline lens. An example would be the correction of ophthalmoscopic images and another that of the correct measurement of the ocular dimensions in techniques like the optical coherence tomography [Tom05] or Scheimpflug photography [Dub05], with results that depend on the assumed refractive index of the eye lens.

The main topics of this work will be the formulation and experimental implementation of a new method for the reconstruction of the gradient index of the crystalline lens. As the title states, in the formulation of this method we will assume the refractive index follows a tridimensional distribution with a rotational symmetry such

$$n = n\left(\rho, z\right),$$

where z is the coordinate along the optical axis of the eye lens (also the axis of symmetry) and ρ the radial coordinate in the orthogonal plane. The reasons of this approximation, as well as that of the rotational symmetry of the geometry of the lens, will be explained and analyzed in several sections of this work. We will start with the histological reasons in chapter 1, where we will also provide an overview of the eye lens as a biological structure. Hence, its embryology, metabolism and main structural features will explain its most outstanding optical properties. In chapter 2 we will make a brief review of the methods that have been developed for the measurement of the gradient index of the lens, distinguishing between those that imply an alteration of its original structure and those that do not, among which the method we propose is included. The theoretical basis of the new method, light propagation in the approximation of geometrical optics and tomography, and how the fundamentals of this method are obtained from the relationship of both fields will constitute chapter 3. In the following chapter these fundamentals give way to a more detailed formulation, paying special attention to the tomographic algorithm that constitutes the mathematical core of the proposed method. Its precision and sensitivity to experimental error are analyzed in chapter 5, with numerical simulations that consider both gradient indices with rotational symmetry and the particular case of gradient index of spherical symmetry, of special interest for the characterization of teleost fish lenses. Chapter 6 is completely focused on the experimental implementation of the method of reconstruction, describing both the experimental setup and the obtaining and processing of the experimental data. Special attention is paid to the main sources of error, how they are minimized and the final magnitude of these errors. Finally, the experimental results

obtained for two different types of crystalline lenses, those of teleost fish and those of pigs, are presented and analyzed in the last chapter, along with their precision. In both cases the goodness of the assumed symmetries, spherical and rotational respectively, is studied with different techniques, as well as how it would affect the lack of symmetry to the retrieved gradient indices.

1 The crystalline lens

The main goal of this chapter [1], besides offering an overview of the eye lens as a biological structure, is to provide the basis of the assumption of the rotational symmetry in the crystalline lens. Assumed this symmetry, this chapter is not essential for the understanding of this work and it is possible to go on the following chapter. Nevertheless, we have deemed necessary its inclusion in this thesis to better understand the biological mechanisms that explain the optical properties of the eye lens, among which the gradient index stands out.

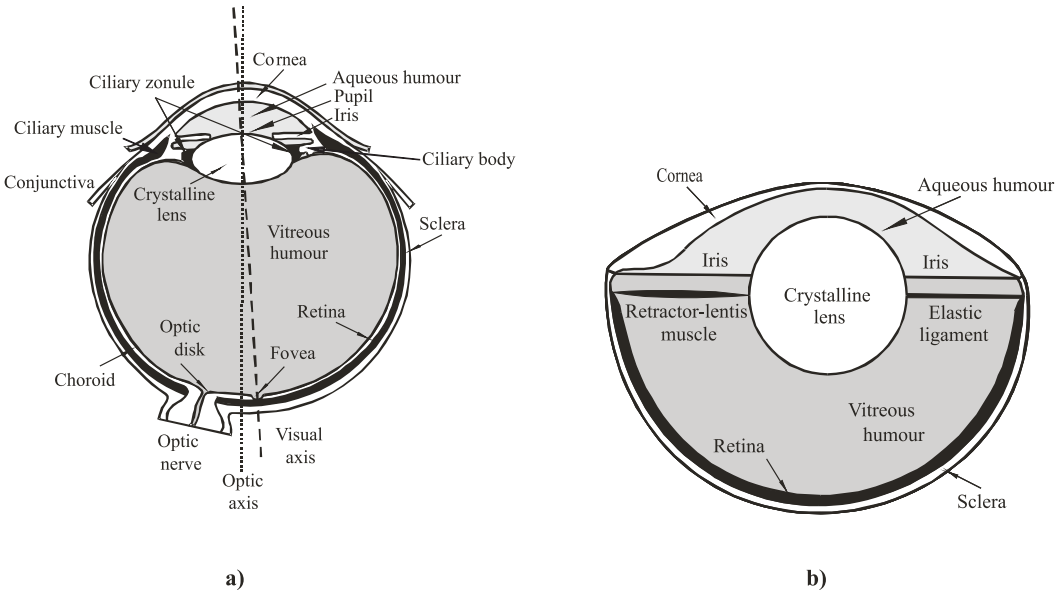

Figure 1.1: Sections of a) A human eye and b) A fish eye.

The crystalline lens, a biconvex lens suspended between the cornea and the retina (see Fig. 1.1), is an optical element common to all vertebrate eyes. Such lens is held within the eyeball by means of the accommodation muscular system, the mechanism whereby

[1] This chapter is, with the exception of the punctual references throughout the text, a compilation and summary of references [Chr91, Rob04, Kus04a, Bas04, Pat94, Kau94]

the ocular system can focus objects at different distances. Its anterior surface is immersed in the aqueous humour of the anterior and posterior chambers of the eye, whereas the posterior surface is immersed in the vitreous humour. The shape of the eye lens can be approximated by that of a spheroid asymmetrical about its equatorial plane and with a degree of asymmetry that varies depending on the species, the age of the individual and, in many cases, of the state of accommodation.

From the optical point of view, the crystalline lens has two relevant functions: as the dioptric element that complements the focusing action of the cornea and that of providing the eye with the possibility of imaging objects at different distances by means of the mechanism of accommodation. In both cases, the quality of the resulting image is due to the geometry and two optical properties of the lens: its transparency within the range of the visible spectrum and the existence of a gradient of the refractive index within the volume of the lens. The first property stems from the special histological features of the crystalline lens, made up by multiple cell layers arranged with a very precise order, and the second property from the variable concentration of a specific type of crystalline lens proteins, the crystallins, that can achieve high concentrations without aggregating and causing light scattering. Any alteration of these features involves an immediate degradation of the eye lens as an optical element. That is why the study of its optical properties would be incomplete without referring to the structural ones. Hence, throughout this chapter a brief review of the embryology and histology of the crystalline lens will be done. It will be also studied the arrangement of the lens cells and its possible variations, considering the consequences that these variations may have on the optical and physiological properties of the lens. Besides, after reviewing the most relevant aspects of the crystalline metabolism, each one of the functions of the eye lens as an optical element of the ocular system will be explained. Finally, based on the former points we will argue the assumption of rotational symmetry of the gradient index of the lens about its optical axis.

1.1 Embryology

The vertebrate crystalline lens has its origin in the embryo surface ectoderm, like the corneal epithelium and the skin. For this reason, like these tissues, the crystalline lens generates new cells throughout life, although with an important difference: since it can not get rid of the older cells, these cells are kept inside the lens, making it larger and forcing it to develop the necessary metabolic strategies in order to prevent this fact from compromising the optical quality of the lens.

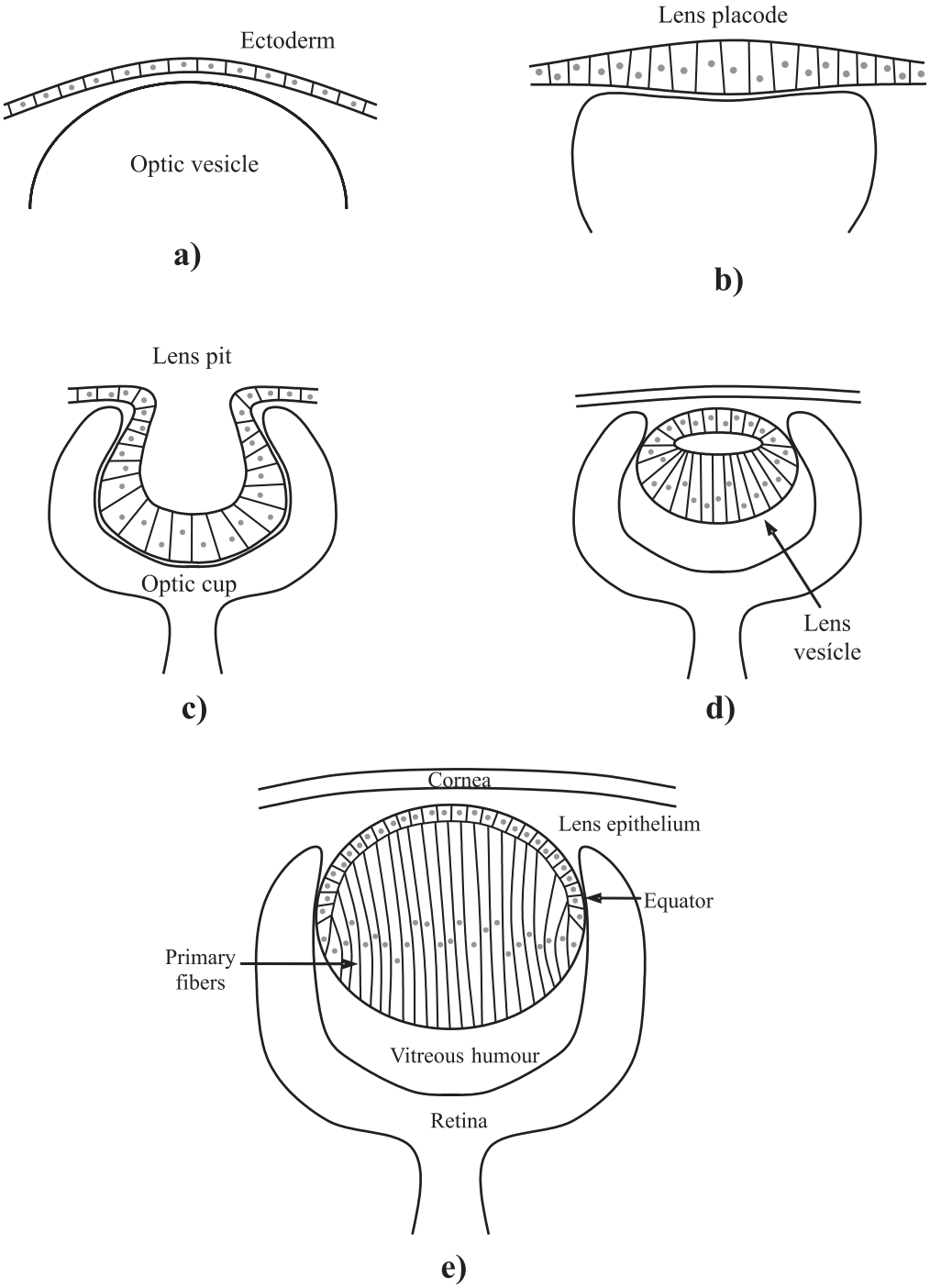

Figure 1.2: Different stages in the embryonic development of the crystalline lens.

The development of the crystalline lens in the embryo starts with the interaction of two bilateral areas of its head surface ectoderm with two internal structures named optic vesicles, embryonic origin of the future retina (see Fig. 1.2.a). As a result of the interaction, those areas differentiate themselves into lens placodes (Fig. 1.2.b), a single layer of columnar cells that invaginates gradually, forming the lens pit (Fig. 1.2.c) and invaginating also the vesicle, what forms the optic cup upon which the embryonic lens is settled. The process of invagination follows until the lens pit separates itself from the ectoderm and is closed off, forming the lens vesicle, where the basal portions of the cells face outward (Fig. 1.2.d). As a product of the secretion of these basal portions, components of the basal lamina are synthesized and deposited externally throughout life, encasing the lens with a membranous envelope that will eventually form the capsule. At the same time, a vascular net, the tunica vasculosa lentis, is formed around the embryonic lens. The aim of this net is to provide nutrients to the lens until the anterior chamber and the aqueous humour are operational. Once they are, that vascular net disappears, leaving the lens without blood supply for the rest of life.

Once the lens vesicle splits off from the surface ectoderm, which later on will form the corneal epithelium, its posterior cells start to elongate until they fill in all the empty space of the vesicle and contact the apical portions of the anterior cells. These elongated cells are named primary fibers (Fig. 1.2.e). Regarding the anterior cells, they increase in number and differentiate into a single layer of cubic cells named lens epithelium. This differentiation between anterior epithelium and fibers, as well as their spatial location, will be maintained throughout life. Gradually, primary fibers lose their intracellular organelles and nuclei, whereas epithelial cells maintain all their organelles. However, the mitotic activity of epithelial cells ends up largely restricted to the preequatorial epithelium, which make up the germinative zone of the lens. This name is due to the fact the new cells generated in this zone are displaced toward the lens equator, giving rise to parallel rows of cells in the meridian of the lens that elongate toward the poles and move away from the equator, forming the secondary fibers. With the continual addition of new fibers, the primary fibers become separated from the epithelium anteriorly and from the capsule posteriorly, forming eventually the embryonic nucleus of the lens. Regarding the secondary fibers, they will keep on adding on former layers of fibers as they are generated in the germinative zone of the epithelium, making up the cortex of the lens. In this process of addition, their nuclei migrate forward until they eventually disappear along with most of the intracellular organelles.

1.2 Histology

The basic cellular structure that can be found in any vertebrate crystalline lens is made up of a densely and neatly arranged bulk of crystalline fibers and an anterior epithelium, both enveloped by an acellular and elastic membrane, the capsule (see Fig. 1.3). Next, we will explain the features of each one of these tissues and how they are interrelated.

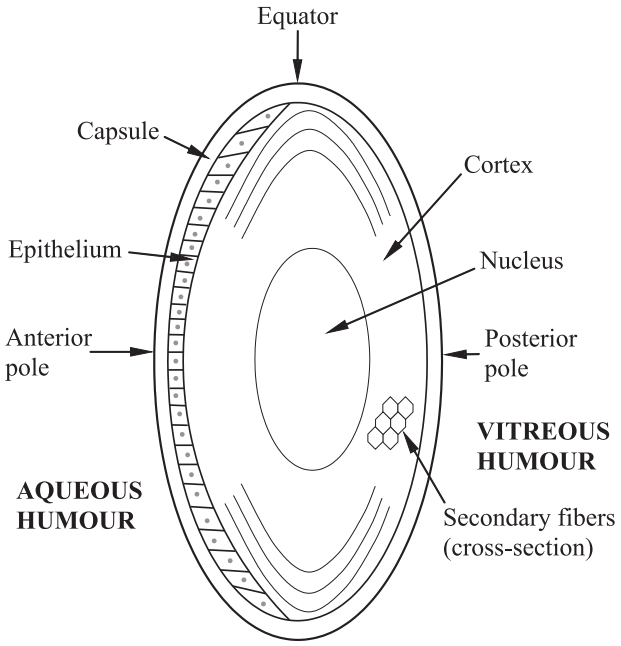

Figure 1.3: Diagram of the histological structure of the crystalline lens.

1.2.1 Capsule

The capsule is a basal membrane like that of other epithelia that envelops completely the crystalline lens. Due to its elasticity it contributes to shape the lens and in some species to convey the tensions exerted upon it by the musculature in charge of the accommodation. The main capsule components are the collagen and a 10% of glycosaminoglycans. Their synthesis takes place mainly in the anterior surface of the crystalline lens, in the basal tips of the anterior epithelium cells, and to a lesser extent in the posterior surface, through the basal tips of the crystalline fibers that migrate along such surface. This asymmetry in the capsular growth is the cause of a variation of the thickness of the capsule along the surface of the lens, being thicker in the anterior pole (from 11 to 15 μm in the case of the human being) than in the posterior one (3.5 μm of average in the human being).

Although permeable to low molecular weight components, the capsule limits the move-

ment of colloidal materials of larger size.

1.2.2 Anterior epithelium

As it has been mentioned in the Embryology section, the growth and development of the lens throughout life is equivalent to that of any stratified epithelium, where the anterior epithelium of the lens would constitute the basal layer. However, unlike a normal stratified epithelium, the mitotic activity of the anterior epithelium is restricted to a reduced number of cells located in its preequatorial portion, which constitutes the germinative zone of the crystalline lens. These cells divide actively throughout life, differentiating a part of them into secondary crystalline fibers. Regarding the remaining epithelium, which normally has not mitotic activity, plays two important roles for the whole of the lens: to synthesize capsular material and to mediate in the transport of different solutes between the crystalline lens and the aqueous humour.

Since it is made up by one single layer of cells, the thickness of the anterior epithelium is determined by their height, from 5.5 to 8 μm.

1.2.3 Fibers

As it has been previously mentioned, there are primary and secondary fibers. Primary fibers are those produced from the posterior epithelial cells of the lens vesicle and they constitute the embryonic nucleus. Essentially parallel oriented to the anteroposterior axis of the lens, their thickness varies largely from one fiber to another. In the adult lens, their metabolism is reduced to a minimum.

Secondary fibers are those which are produced throughout life from epithelial cells of the germinative zone, close to the equator, and that constitute the cortex of the lens. The differentiation of the epithelial cells into secondary fibers gives rise to multiple structural and molecular changes which allow us to distinguish four different stages in such a process of differentiation:

- Fiber cell precursors: those produced by mitosis in the germinative zone and that at the equator of the lens start to change their columnar shape and to elongate, in such a way the apical tips move forward and the basal backward, without losing contact with the capsule.

- Elongating fiber cells: in this stage fibers still concentrate most of their cell junctions in their apical and basal tips, whereas the remaining cell membrane is relatively

smooth and regular. The fiber cell basal membrane is firmly attached to the posterior capsule in order to resist possible tensions due to the accommodation. Through the basal membrane is also secreted the capsule substrate upon which the fiber migrates until, when contacting with the basal tip of another fiber, it separates from the capsule and joins to that other tip. Regarding the apical tip, the fiber keeps a direct contact with the anterior epithelium, upon which it migrates at a slower rate than upon the capsule. Once it reaches the apical tip of other fiber, it joins to it after losing contact with the epithelium. The geometric locations formed by these unions between secondary fiber tips are called sutures and both their patterns and their optical and physiological relevance will be discussed later. Regarding the cause of the fiber elongation in this stage, it is thought to be due to the accumulation of crystallin and non crystallin polypeptides that start to be synthesized from the beginning of the differentiation process of the fibers.

- Maturing fiber cells: this stage starts at the moment the fiber has completely elongated once each one of its tips reaches a suture. Like other common epithelial tissues, the separation of the fibers from its basal lamina (the capsule) is the starting sign for a whole series of biochemical and cellular changes. One of them is the increase of the interdigitations among the cellular membranes, as well as an important increase of different types of cell junctions in such membranes. For instance, in some regions of the crystalline lens, gap junctions comprise between 30% and 60% of the membrane surface, when in most of tissues is not higher than a 4%. This higher complexity in the intercellular communications responds to a higher isolation of the fibers in relation with the nutrients that can reach them by passive diffusion, what forces the tissue to develop new strategies to increase the communication among the bulk of cells inside the lens and the relatively small number of metabolically active cells in its surface. On the other hand, a higher number of interdigitations is useful to stabilize the crystalline cells in those accommodation processes that involve changes in the lens shape. Another relevant change that takes place at the fiber in this maturing stage is the sudden loss of most of their organelles at a constant distance from the lens surface. Although more slowly, the fibers nuclei end up disappearing too. Such a cellular degradation is a feature that other stratified epithelia share, like the skin. In the case of the crystalline lens, this fact allows to increase the transparency by decreasing the possible sources of light scattering. For instance, certain pathologies where the transparency of the lens is low are due to the persistence of those organelles in the mature crystalline fibers, like in the case of the human congenital cataract. Another factor in the decrease of

the lens transparency, the intercellular space, is also minimized by partially fusing the cellular membranes, leaving spaces of just 20 nm. Once the fiber has lost its organelles, it starts a process of compaction of the fiber that in the case of primates produces a decrease in the fiber section to one third of its original size. This compaction is due to a dehydration of the cells and the modification and interaction of the crystallins, the proteins that cause the gradient index in the lens.

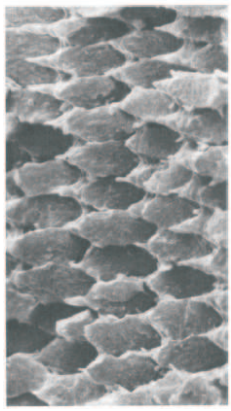

Figure 1.4: Cross-sectioned secondary fibers of the crystalline lens [Kus96] (Courtesy of J.R. Kuszak).

- Mature fiber cell: it is the fiber that results from all processes formerly explained and that ends up being part of the growing lens nucleus, more hardened than the surrounding cortex.

1.3 Form and layout of the secondary fibers

The secondary fibers of the crystalline lens are generally hexagonal in their cross-section (see Fig. 1.4), with two wide faces parallel to the lens surface and four narrow faces. The distance between the wide faces is named fiber thickness and that between the angles formed by the narrow faces is named fiber width. In spite of the large variations of size in crystalline lenses, the thickness and the width of secondary fibers is relatively constant. Therefore the difference in the size of the lens is mainly due to the its number of fibers. In the equator, the fiber width is roughly 10-12 μm and its thickness 1.0-1.5 μm, being a bit thicker in the posterior segment of the crystalline lens, what would explain the larger proportion of this segment in most of species [Kus96].

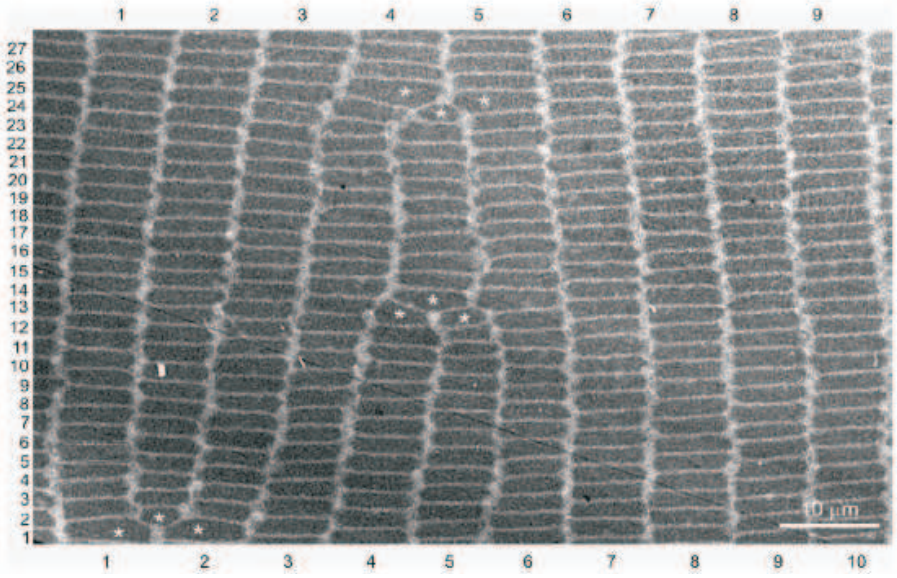

Figure 1.5: Equatorial cross section of the crystalline lens, where it can be seen how the secondary fibers are arranged in radial cell columns. Note the presence of pentagonal fibers in those points where one of those columns splits into two [Kus04b] (Courtesy of J.R. Kuszak).

In a equatorial cross section of the lens (see Fig. 1.5) it can be seen how, at a certain distance from the surface, the fibers are arranged in radial cell columns, perfectly packed. This very high degree of packing and order might be the main reason for the hexagonal shape of the fibers, the most optimum configuration to minimize the extracellular space and the surface of the membranes, both very important aspects in the transparency of the resulting tissue. The only exception to this pattern are some fibers with a pentagonal shape (see Fig. 1.5), that occur when a radial cell column splits into two as a result of the continuous growth of the dimensions of the eye lens.

1.3.1 The sutures and their patterns

As it was mentioned in a former section, crystalline fibers start their maturing stage when they stop elongating and that happens when their tips contact those of another fiber or fibers. These unions are not randomly distributed inside the crystalline lens. Instead, they describe lines or surfaces perfectly defined named sutures and with a pattern that is limited to four possibilities:

- Umbilical suture lenses (see Fig. 1.6): it is simples type of lens, that we can find in fish, birds and some reptiles, mainly snakes and turtles. Their secondary fibers

elongate along the meridians of the lens, becoming narrower as they converge on the anterior and posterior poles. The continuous superposition of new layers of fibers produces two umbilical sutures, anterior and posterior, extending like two lines from the surface of the embryonic nucleus, which has not sutures, to the respective poles of the crystalline lens.

- Line suture lens (see Fig. 1.7): in this case it can be distinguished two types of secondary fibers depending on the orientation of their tips in relation with the poles of the lens. Firstly, there are straight fibers that, like in the umbilical suture lens, elongate along one of the meridians, although in this case just one of their tips reach a pole, whereas the other stops halfway (Fig. 1.7.c). The second type of fiber, the S-shaped fiber, is the most common and its two tips are curved in opposite directions, without reaching their respective poles and giving to the fiber a S-shape when it is observed from the equator of the lens (Fig. 1.7.a). Therefore, it is a fiber that does not extend along a plane that also contains the anteroposterior axis of the lens (Fig. 1.7.h). Next, the arrangement of these two types of fiber is described. In each layer of fibers there are two pairs of straight fibers. Each pair of fibers is joined at one of the poles, one fiber at 180^o of the other, and ends halfway of the opposite hemisphere. These pairs are rotated 90^o between them, forming a cross. In each hemisphere the tips of the straight fibers that do not reach the poles define a straight line, at 90^o the line of one hemisphere in relation with the line of the other hemisphere. The opposite tips of the S-shaped fibers are arranged along each one of these defined straight lines (see Fig. 1.7.d-f). Thus, each layer of fibers shows two sutures, one orthogonal to the other, that give rise to two isosceles triangles, orthogonal one to the other and that extend from the surface of the embryonic nucleus to the surface of the lens. This type of suture pattern is found in amphibians and some small mammal, like the rabbit.

- Y suture lens (see Fig. 1.8): the type of lens found in most of mammals (mice, rats, hamsters, guinea pigs, dogs, cats, sheep, cows, pigs, etc). In this lens there are also straight and S-shaped fibers (Fig. 1.8.a). However, in this case each layer of the crystalline lens contains six straight fibers, three in each hemisphere joined at the corresponding pole and angularly equidistant (120^o) (Fig. 1.8.c). The two trios of fibers are rotated 60^o between them. As a result, the tips of the straight fibers that do not reach the poles define in each hemisphere a Y-shaped suture, rotated 60^o between them. (Fig. 1.8.b,d,e-h).

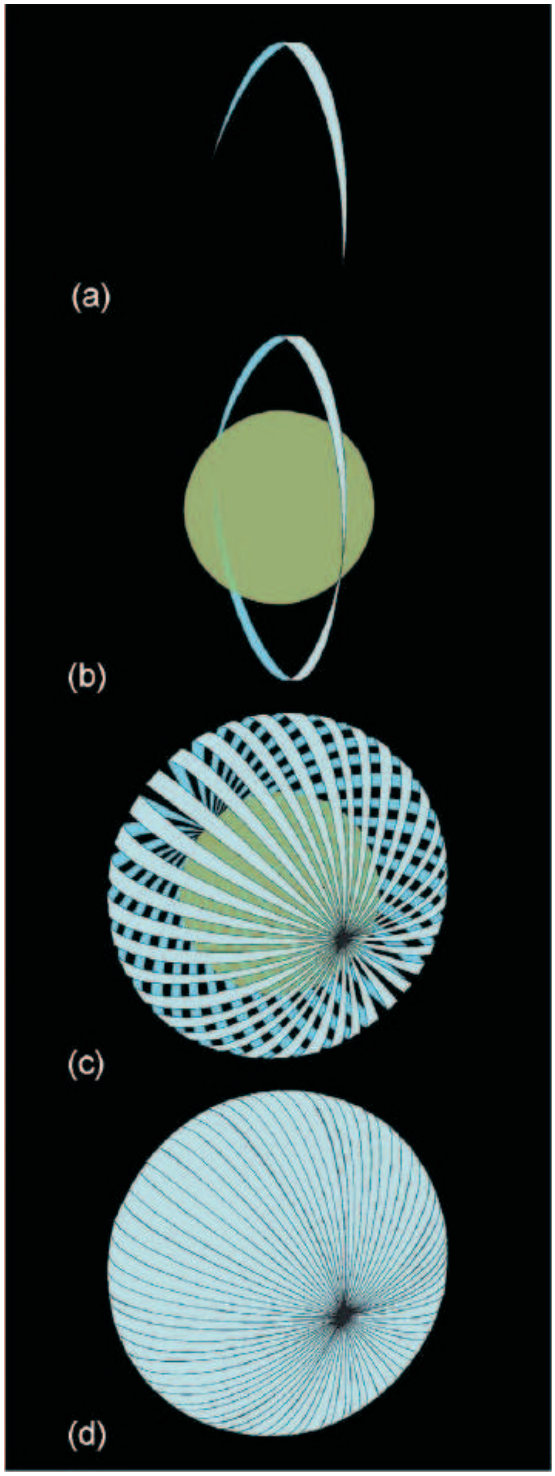

Figure 1.6: Layout of the secondary fibers in an umbilical suture lens, disposed along the meridians (a) over the embryonic nucleus (b) and giving rise to layers of fibers that converge on the anterior and posterior poles of the crystalline lens (c-d) [Kus04b] (Courtesy of J.R. Kuszak).

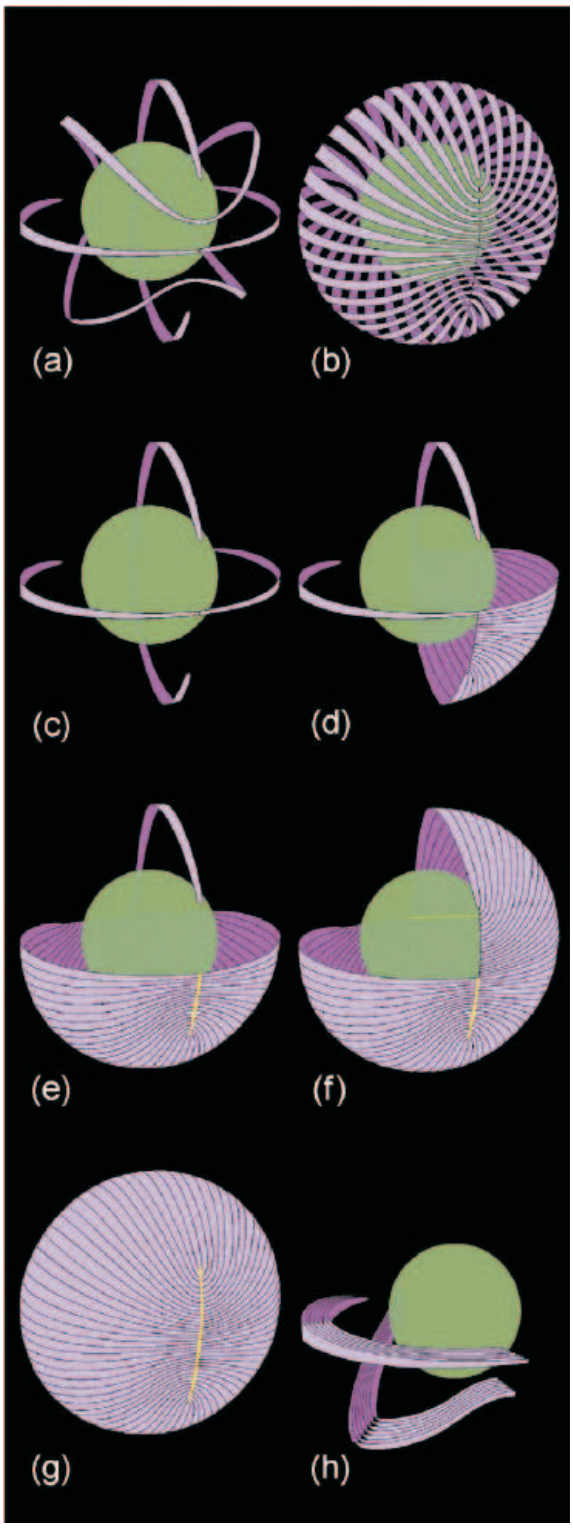

Figure 1.7: Layout of secondary fibers in the line suture lens [Kus04b] (Courtesy of J.R. Kuszak).

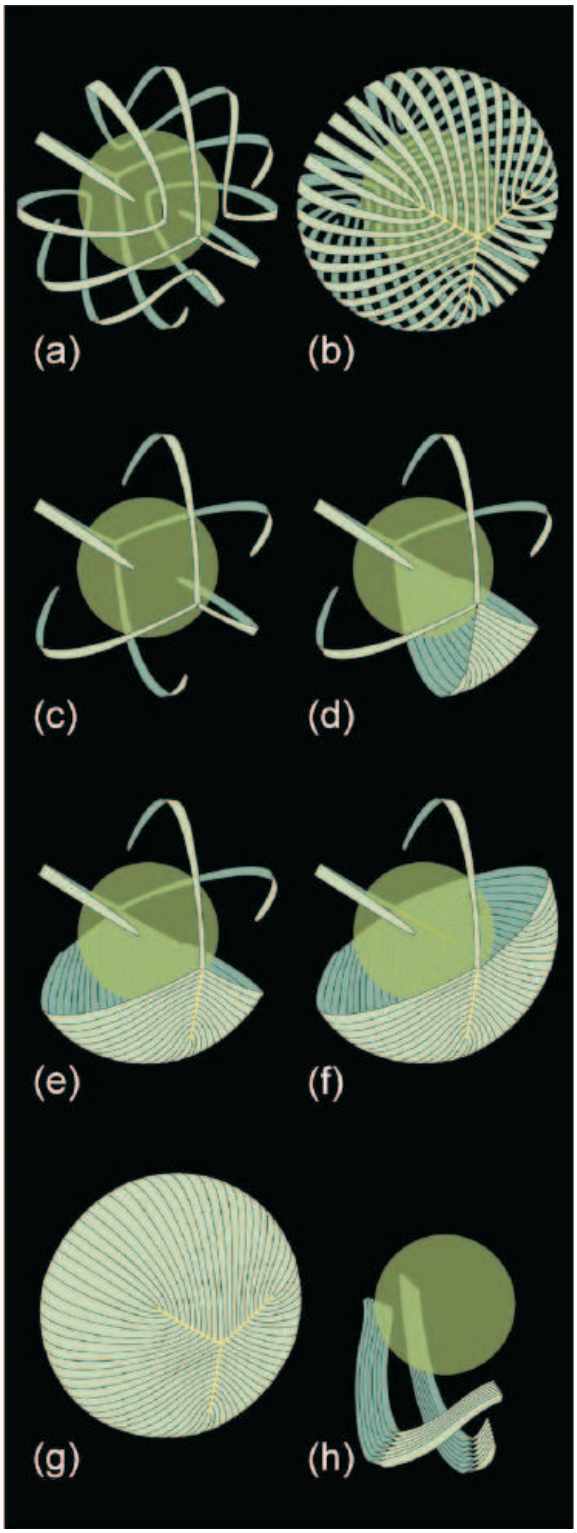

Figure 1.8: Layout of secondary fibers in the Y suture lens [Kus04b] (Courtesy of J.R. Kuszak).

- Star suture lens (see Fig. 1.9): it is the most complex pattern and it is exclusive to the primates. Throughout its fetal period of development, the crystalline lens shows a Y suture lens pattern. However, after birth three star suture patterns, each one more complex than the former, are gradually formed through childhood, adolescence and adulthood, respectively. This process starts when, in a new layer of secondary fibers, one pair of straight fibers overlay S-shaped fibers of the layer underneath. Since, as it has been shown, the tips of straight fibers delimit sutures, new groups of S-shaped fibers are defined at both sides of the new straight fibers, producing two little sutures that converge on one the original sutures and forming a Y at its periphery. As new longer straight fiber superpose, two new sutures that reach the pole end up forming. This process occurs in the whole of the lens, producing at the end of childhood a star suture pattern with six branches in each hemisphere, rotated 30^{o} between them. This pattern becomes more complex during adolescence, with nine branches stars, and eventually in the adulthood the last star configuration is formed, with twelve branches in each hemisphere. As a result of all this process, the adult lens shows discontinuous suture planes from the embryonic nucleus to the periphery of the lens. Such discontinuities explain those observed in the primate crystalline lens with the slit lamp.

As we have seen before, the dense packing of crystalline fibers, as well as the loss of their intracellular organelles, turns the lens into a structure of minimum diffraction and scattering (the light scattered by the lens is about 5% of the incoming light). However, the fact the fiber tips are not uniform, neither in their shape nor in their size, makes the lens not so optically good at the suture planes. This effect becomes more important with age, as the lack of uniformity of the fibers in such planes increases. It is though that this would be the reason that would justify the discontinuity of the suture planes in primates, by reducing and distributing their optical effect and improving the optics of the whole.

In the last years there have been speculations on the role of sutures in the transport of metabolites and nutrients in the crystalline lens. If the tips of secondary fibers, like those of other epithelial cells, show an important number of cell junctions, the sutures, composed by these tips, should allow the diffusion and transport of metabolites and nutrients. Hence, the more complex the suture pattern, like in primates, the more efficient that transport system.

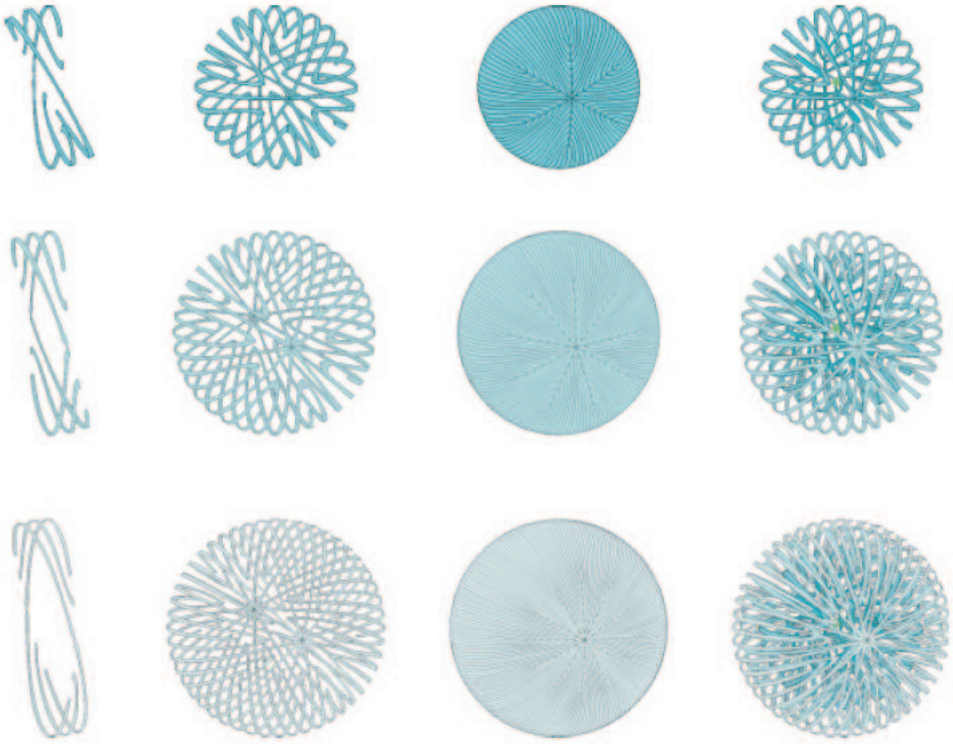

Figure 1.9: Layout of secondary fibers in the star suture lens of a child (first row), of an adolescent (second row) and of an adult (third row) [Kus04c] (Courtesy of J.R. Kuszak).

1.4 Metabolism

The lens metabolism is essential for the maintenance of a proper transparency. Any alteration can cause the aggregation of proteins, hydration changes, separation of phases of cellular components and/or cytoskeletal changes, all factors that can lead to cataract. That is why so important the role played by the system of cell junctions to guarantee all of them have access to nutrients that arrive from the aqueous and vitreous humour. Passive diffusion by itself would not be enough to supply nutrients to the whole of the lens, just to the periphery. For this reason, it has been proposed the existence of an active transport system that would make use of that network of cell junctions and that would generate a circulating flux of ions and water that would carry metabolites and nutrients from the poles to the equator.

Regarding the energy production in the crystalline lens, it depends almost completely on glucose, obtaining 70% of the energy from anaerobic glycolysis. Although it is less

efficient than the aerobic one, that takes place essentially in the epithelium, it is a good solution to the lack of oxygen inside the lens.

Another important contribution of the lens metabolism to the tissue transparency is that of the regulation of the electrolytic equilibrium to maintain a proper hydration degree, which in the case of an adult human is about a 65%, much less than what is normal in other tissues. An important amount of this water does not diffuse freely in the crystalline lens but it is associated to different molecular structures, mainly proteins, which make up 35% of the wet weight of the eye lens.

The protein synthesis of secondary fibers has a big relevance when explaining two important optical features of the crystalline lens: its gradient index and the existence of refractive indices as high as 1.56 [Gar01]. This is achieved by means of a special type of proteins, the crystallins, where it can be distinguished alpha, beta, gamma and delta crystallins (this last type just present in reptiles and birds). These proteins are characterized for being able to reach high concentrations without aggregating and scattering light and due to variations in their synthesis along the differentiation of secondary fibers the crystalline lens shows a gradient index.

1.5 The crystalline lens as an optical element

The refractive power of the lens depends on the power of the other lens of the ocular system, the cornea, and this power itself on the refractive index of the surrounding medium. For instance, in aquatic vertebrates, like fish, the refractive power of the cornea is negligible because of the little difference between its refractive index (1.376) and that of the water (1.333), as well as its low curvature. Therefore, fish have very powerful crystalline lenses, with almost spherical geometries and values of the refractive index higher than those of any terrestrial animal. This configuration, which also occurs in the larval stage of amphibians, changed with the adaptation of vertebrates to life on the emerged land. A larger difference between the air refractive index and that of the cornea made the cornea the main lens of the ocular system, what would explain the decrease in the anteroposterior axis of the eye lens. As a result, in the case of the human eye, for instance, for far vision, the lens contributes with about one third of the refractive power of the eye, with about twenty diopters.

The gradient index plays an important role in the quality of the image produced by the lens. For instance, in the case of the almost spherical fish lens, if its refractive index were homogeneous the spherical aberration would be so high that it would not allow to resolve properly any detail. However, when the optical quality of these lenses is

tested, it is observed a very good correction of the spherical aberration that can only be attributed to the gradient index. Likewise, this gradient is also partially responsible for the refractive power of the lens, along with its geometry. Another property of the gradient index, according to some researchers [Kro99], is to generate multifocal lenses in some species that would compensate the chromatic aberration by means of the monochromatic spherical aberration, in such a way each concentric third of the lens would form a correct image in the retina for each one of the main wavelengths to which their cones are sensitive.

The eye lens is also essential in the accommodation, the mechanism through which the ocular system can form in the retina a good image for objects placed at different distances. The accommodation amplitude, or range of the object space that can be properly focused, and the mechanism in charge of providing it changes depending on the species and the need that this species may have of modifying the refractive power of its ocular system.

The most simple fashion of accommodation is moving the lens, as it occurs in the most primitive vertebrates. The most representative case is that of the fish, with a rigid lens that it would be very difficult to deform. In the teleost fish, the most common ones, the lens is moved both along the visual axis and orthogonally to it by means of a retractor muscle (see Fig. 1.1), reaching accommodation amplitudes up to 20 D. It must be pointed out that in those cases where the movement is confined to the pupil plane, objects places at different distances are imaged at different parts of the retina. Other type of vertebrates that also move their lenses to accommodate are the amphibians and the snakes. The latter have some muscular fibers in the base of the the iris that exert pressure on the vitreous humour when contracted, pushing the lens forward.

The most common mechanism of accommodation in mammals, birds and most of reptiles is that of the modification of the shape of the lens. In these last two cases, that modification is due to the direct pressure exerted on the lens by the ciliary body and the iris, what increases the curvature of the anterior surface of the lens generating a iridogenic lenticone. A good contact of the ciliary processes with the crystalline lens is ensured with a pad produced by the anterior epithelium in the region of the equator, as well as a correct distribution of the exerted forces. In cases like those of the aquatic birds the amplitude of accommodation can reach values up to 50 D (cormorants) or more, since once in the water they compensate the loss of refractive power of the cornea by increasing that of the lens. In primates, the crystalline lens modifies its shape by means of the tensions exerted by some fibers inserted in its equatorial capsule (zonular fibers) and which are connected themselves to the ciliary muscle. According to the Helmholtz theory of accommodation, when the ciliary muscle is relaxed, the zonular fibers are tensioned and the lens increases

its diameter and flattens, decreasing its refractive power. However, if the zonular fibers are relaxed and the lens becomes rounder and gets closer to the cornea, its refractive power is increased. Among mammals, primates show one of the largest amplitudes of accommodation, which in the case of human beings is about 14 D in the childhood.

The eye lens also works in the ocular system as a ultraviolet filter, preventing this damaging radiation from reaching the retina. Almost all light with a wavelength within the range of 300 and 400 nm is transmitted through the cornea up to the lens, where is mostly absorbed. This absorption is due to the reactivity of the aminoacid residuals of its proteins, as well as to the presence of pigments and fluorophores. As a result, the lens becomes yellowish with age, although other more dangerous effects include the cellular DNA damage, which may end up giving rise to cataractogenic processes.

1.6 Rotational symmetry of the gradient index of the crystalline lens

As it can be ascertained from what has been explained in the former sections, the refractive index in a given point of the lens depends on the concentration of crystallins in the cellular cytoplasm [Mof02a]. Since this concentration depends itself on the protein synthesis that occurs in the differentiation process of crystalline fibers from their stage of fiber cell precursors in the epithelium until their stage of mature fibers, the symmetry of the gradient index, as well as the shape of the lens, will be a reflection of the layout of the different layers of crystalline fibers. Therefore, according to what has been explained in section 1.3, there are just two factors that might produce deviations in relation with the assumption of rotational symmetry of the gradient index and geometry of the lens about its optical axis:

- the perturbations generated by the sutures in the distribution of the refractive index.
- the deviations of the actual lenses regarding the ideal models described in section 1.3.

Thus, as a first approximation, rotational symmetry seems to be the most adequate one to describe both the geometry and the gradient index of the crystalline lens. Besides, as it will be shown later, this feature simplifies the mathematical formulation of the reconstruction of the gradient index. For both reasons, in the formulation of the new method of reconstruction that it is presented in this work we will consider the gradient index and

the geometry of the crystalline lens rotationally symmetrical about its optical axis. Later on, in the last chapter, we will discuss the degree of goodness of this approximation on the basis of the experimental data obtained by different techniques.

2 Methods of measurement of the gradient index in crystalline lenses

There have been several methods applied or developed for the measurement of the distribution of the refractive index in the crystalline lens since Thomas Young proposed the existence of such variable index in 1801 [You01][1]. The aim of this chapter is to do a review of all these methods, explaining their main features and limitations. These methods of measurement can be classified depending on the need of altering or not the structural integrity of the eye lens to perform the measurement of the gradient. A first group would comprise the destructive methods, the first ones to be used and that in all cases carry out a zonal reconstruction (point by point) of the distribution of the refractive index. A second group would be that of the non destructive methods, a group that includes the new method proposed in this work and of special interest for not implying the destruction of the lens. As it will be shown, in these methods the reconstruction of the gradient index may be both zonal and modal (calculation of the coefficients of a functional series expansion). Finally, in a third group would be the hybrid methods, zonal methods that require a previous calibration that implies the destruction of one or several crystalline lenses. Nevertheless, once properly done, the results of the calibration can be used for later measurements of the gradient index without causing any structural alteration of the studied lens.

2.1 Destructive methods

Abbe refractometer

The first scientist in measuring the variation of the refractive index inside the lens was Ludwig Matthiessen [Mat82]. In order to do so, he took samples of the lens in different zones and measured their refractive index with an Abbe refractometer. Until the

[1] Throughout this work we will call *algorithm* the mathematical protocol through which some experimental data are processed with the aim of reconstructing the refractive index and *method* the whole of the experimental technique used to obtain the data and the algorithm.

sixties of the former century this was the only method used for the characterization of the crystalline gradient index [Hug48, Wea63]. Although easy to implement, it has two important drawbacks. The first of them is the fact of measuring a refractive index in a sample with a non constant value. The stronger the gradient, the less representative the measurement. On the other hand, and this is a drawback of the other destructive methods, the fact of sectioning or extracting samples of the lens implies a very aggressive modification of the conditions of osmotic and metabolic equilibrium that guarantee locally the existence of given concentration of crystallins, as well as their proportion and solubility (see section 1.4).

Schlieren interferometry

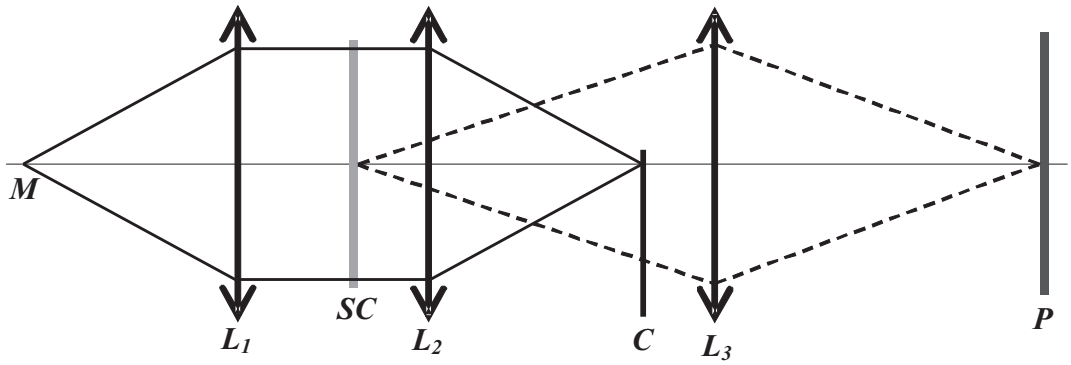

Figure 2.1: Diagram of the *schlieren* interferometer for the measurement of the gradient index in the lens, where M represents for the monochromatic source of light, L_1 y L_2 two condenser lenses, SC a frozen section of the lens, C a blade y L_3 the lens that projects the interferogram on the screen P.

The first alternative to the Abbe refractometer was the use of the *schlieren* interferometry [Bru65] with plane-parallel sections of formerly frozen crystalline lenses [Nak68, Nak69]. This type of interferometry is based on the interposition of an optical inhomogeneity (the lens section) in the trajectory of a plane wavefront to be focused. Depending on the gradient index in a given zone of the section, light that traverses that zone will be deviated more or less from its ideal focus in case no inhomogeneity were placed (see Fig. 2.1). By measuring such deviations at the focal plane a map of the gradient index corresponding to that lens section can be reconstructed. In the case of references [Nak68] and [Nak69], that measurement was carried out with a technique similar to the Foucault knife edge and afterwards the distribution of the index in that studied section was obtained by numerical integration of the map of gradients. To perform such an integration

the refractive index at the center of the section was used as an initial value, obtaining that index with an Abbe refractometer. This method, more elaborate than the former one, in addition to involve the freezing and cut of the lens has the disadvantage of being very sensitive to any misalignment or lack of plane-parallelism of the sections of the lens.

Protein densitometry

A third destructive method makes use of the the protein densitometry to relate the concentration of proteins in a zone of the lens with a refractive index. The theoretical base of this method is relatively simple. The index n of a solution and the concentration C of its solute can be related for many solutes [Bar57] by linear expressions like

$$n = n_0 + \alpha C \tag{2.1}$$

where n_0 is the solvent medium index, α is a constant that depends on the nature of the solute named specific refractive increment and C is expressed in mass of solute by unit of volume of the solution. In the specific case of the protein solutions, their refractive index is determined by an expression like that of the equation 2.1 (in references [Bar57, Pie87] we can find values of the constant α for different types of proteins). Hence, by measuring in a zone of the lens the protein concentration it is possible to obtain a first approximation of its refractive index. By using the microradiography on frozen sections of eye lenses, several works [Phi68, Fag81] show protein concentration maps of those sections. Afterwards, and by means of the equation 2.1, the corresponding index distributions are calculated. Besides the mentioned error due to the freezing and cut of the lens, this method does not distinguish the optical contribution of different types of biological compounds like the lipoproteins, polypeptides or minerals and in the mentioned works all dry mass detected by microradiography is considered as soluble protein. Likewise, it is not determined how the proportion of concentrations of the different types of crystallins affect the gradient index [Pie95].

Pulfrich refractometry

Pulfrich refractometry is based on the phenomenon of total reflection to determine the refractive index of a given substance. This substance is placed in contact with one of the catethi of a rectangular prism, of which the index is known and it is higher than that of the substance (see Fig. 2.2). By illuminating tangentially this side of the prism, some light enters the prism with the critic angle that corresponds to the relationship of the indices of the prism and the substance to be measured. When light ends up emerging

through the opposite side of the prism, the measurement of the exit angle along with the knowledge of the dimensions and the index of the prism allows to calculate the refractive index of the substance. This method was applied by W.S. Jagger [Jag90] to sections of lenses frozen for the cutting and unfrozen to be measured, with the aim of obtaining maps of their isoindicial lines. Some of its main drawbacks, besides the alterations that may take place in the lens, are the indetermination of the borders of such isoindicial lines because of the finite size of the aperture of the registering camera and the refraction that may occur to the incoming light in the lens gradient index before entering the prism, producing as a result wrong measurements.

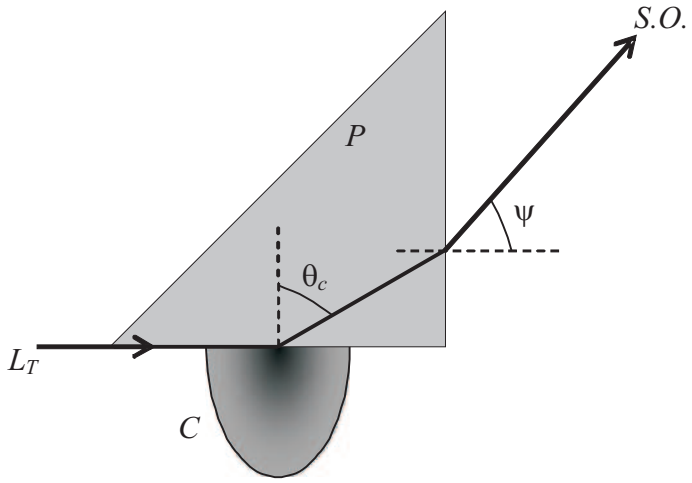

Figure 2.2: Diagram of a Pulfrich refractometer, where L_T represents the beam of light that enters tangentially the prism P, in contact with the half of the crystalline lens, and that enters the prism with the critic angle θ_c which corresponds to the relationship between the indices of the prism and that of the lens at the point of refraction. Light exits the prism forming an angle ψ, which is registered by an optical system $S.O.$

Reflectometry

The newest of the destructive methods applied on the measurement of the gradient index of crystalline lenses is based on reflectometry. It makes use of a monomode optical fiber as a sensor to measure the reflectance that occurs at different points of the lens for the light guided for such a fiber [Pie93, Pie97]. Although not as invasive as the former methods, the fact that the sensor, with a flat head, is gradually introduced inside the lens makes highly possible that the fibers accumulate on its tip, affecting the measurements. It can also be told that the algorithm that retrieves the index of the examined point assumes

normal incidence of light. This might be a source of error in those zones of stronger gradient of the index.

2.2 Non destructive methods

An alternative for the retrieval of the distribution of the refractive index is the measurement of certain quantitative parameters of the optical behaviour of the lens and its posterior processing with an algorithm that takes into account the existing relationship between such optical behaviour and the refractive index. Depending on which are those optical parameters three groups of non destructive methods can be distinguished: those that use data from ray deflectometry, from interferometry and from the fitting of ocular parameters.

2.2.1 Ray deflectometry

Ray deflectometry (usually named laser scanning or laser ray-trace method) is based on the characterization of the deflection produced at the exit of a lens for a collection of incoming laser beams. This characterization is based on the obtaining of the parameters of the trajectories of the incoming and outgoing beams, their correlation and the calculation of their intersection with the surface of the lens.

Abel integral inversion

The first method that used ray deflectometry for the measurement of the gradient index in crystalline lenses implemented an algorithm designed originally for optical fiber preforms [Chu77]. Such an algorithm stems from the mathematical relationship between the incidence height of the ray, x, and its deflection angle at the exit of the preform, φ. For a gradient index with a radial dependence $n(\rho)$ in a circular section orthogonal to its axis, from the ray equation [Mar78, cap. 2] it is deduced the following relationship between the height x at which a ray parallel to the optical axis enters the preforms and the angle φ that it forms with such an axis at its exit

$$\varphi(x) = 2\arccos\left(\frac{x}{b}\right) - 2xn(b)\int_{\rho_0}^{b} \frac{\mathrm{d}\rho}{\rho\sqrt{n^2(\rho)\,\rho^2 - n^2(b)\,x^2}} \quad \text{if } n_{ext} = n(b)\,, \tag{2.2}$$

where b is the section radius, n_{ext} the index of the external medium and ρ_0 a function of x (see Fig. 2.3). Inverting equation 2.2 by means of an Abel integral inversion, $n(\rho)$ can be expressed as a function of, $\varphi(x)$, a measurable variable [Cam84]. Therefore,

matched n_{ext} and $n(b)$ and known the deflection function $\varphi(x)$ for $x \in [0, b]$, the radially symmetrical function $n(\rho)$ can be reconstructed point by point from the border of the optical element.

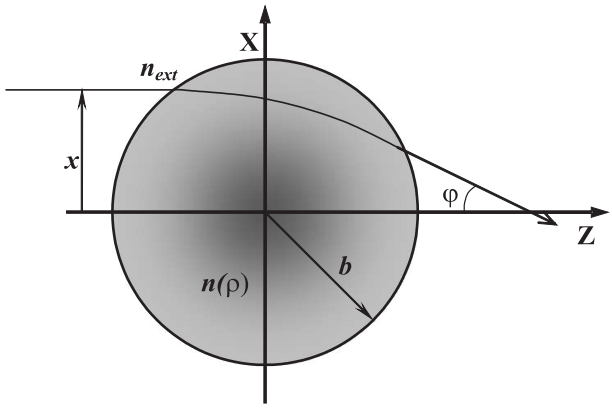

Figure 2.3: Ray deflected by a cross section of a preform with surface and external indices matched.

With this formulation this method has been used for the determination of the gradient index of teleost fish lenses [Kro94, Kro01, Kro96]. Since, such lenses can be assumed to be spherical, the method is applicable to any meridional plane of the lens and the result can be generalized to three dimensions. However, in most of the vertebrates the geometry of the crystalline lenses is not spherical and for these cases two strategies have been considered to apply this deflectometric method:

- To assume the existence of a plane of the lens with a radially symmetrical geometry and gradient index where the method can be applied (in those works which have done so, such a plane is the equatorial plane of the lens, orthogonal to the optical axis [Cha88, Pie89]). Afterwards, the result is projected to the rest of the lens by assuming that the retrieved isoindicial surfaces are sections in the equatorial plane of ellipsoids concentric with the surface of the lens.

- To generalize the method for slightly elliptical sections and index profiles [Brl78]. According to this generalization, gradient indices of meridional planes of slightly elliptical lenses could be retrieved [Cam84].

Another constrain of this method is the matching of n_{ext} and $n(b)$, what means an accurate knowledge of $n(b)$. This limitation was studied in the work [Cha88], where assuming a little difference between both indices, maintaining the radial symmetry and knowing n_{ext} a series of approximations were proposed to estimate $n(b)$.

In spite of these modifications regarding the geometry and index matching, this deflectometric method show important shortcomings for its generalized application to all kind of crystalline lenses. On the one hand, the assumed gradient index model is too constrained, with isoindicial surfaces that have to be concentric with the surface of the lens and circular or almost circular at the measurement plane. On the other hand, external indices must be matched or almost matched to the surface index, what makes more difficult the experimental implementation of the measuring process and involves a previous knowledge of such a surface index.

Optimization algorithms

A second deflectometric method is based on the use of optimization algorithms for the reconstruction of the distribution of the refractive index. By assuming rotational symmetry, it is considered a description of the gradient as a linear combination of a base of functions $f_i(\rho, z)$ that satisfies

$$n(\rho, z) = \sum_{i=1}^{N} a_i f_i(\rho, z) \tag{2.3}$$

where a_i are the coefficients that the optimization algorithms have to calculate. It is, thus, a modal reconstruction of the gradient index, unlike the zonal reconstruction of the former method.

The first work that it could be included within this group is that of the reference [Axe88], which made use of very simple models of the index distribution. From the fitting of certain experimental data to some paraxial equations some initial coefficients a_i were proposed. By using a numerical ray tracing, incoming rays were traced with the same parameters as the experimental ones and depending on the difference of the parameters of the theoretical and experimental exit rays those coefficients a_i were changed by trial and error until the the parameters of the propagated exit rays converged with those of the experimental ones. This procedure was refined later with the implementation of real optimization algorithms [Gar01, Bro04], like that of conjugate directions, that automatized the process of variation of the coefficients a_i and allowed to work with more complex gradient models.

A first drawback of this method is the need of implementing a numerical ray tracing, a demanding computational process if a good accuracy is expected. The second drawback can be extended to all optimization algorithms used so far in this field of research: the lack of unicity of the solution. If the initial coefficients a_i are too far from the real ones,

if the algorithm does not vary them properly in each iteration and/or if the topological space defined by the merit function is too complex (what increases with the number of coefficients), the likelihood of falling in a local minimum of the merit function increases, as well as the time of convergence. All these factors have made no possible to apply this method to crystalline lenses with more complex symmetries than the spherical one.

Characterization of the internal ray trajectories

A particular case based on ray deflectometry is that published by Beliakov and Chan in 1998 [Bel98]. Instead of considering the trajectory of the rays outside the lens they use, as initial data, the images of the internal ray trajectories in a meridional plane of the lens with rotational symmetry. Since these trajectories are seen through a semilens of variable index, the registered trajectories are not the real ones but their images as formed by the lens. Thus, the method has to take into account this fact when, by inverting the ray equation, retrieves the gradient index from the ray trajectories. With some mathematical complexity, the main drawback of this method is the high computational cost of its implementation. Regardless of the numerical simulations performed in the mentioned reference, this method has never been put into practice.

2.2.2 Interferometry

Instead of optically characterizing an element from the gradient of the phase at its exit (rays), it is possible to directly measure that phase by using interferometry. This experimental technique has been the basis of different methods used for the reconstruction of the gradient index at cross sections of optical fibers [Iga78, Chu79]. In the case of eye lenses its use has been rare and limited to one group of researchers [Nil83, Nil05] focused on the study of gradient indices of invertebrate lenses. From the interferogram formed by an interference microscope, the positions of maxima and minima of the phase map corresponding to a cross section of the lens are obtained, with the axis of symmetry orthogonal to the optical axis of the microscope. Such a cross section is supposed to be radially symmetrical and made up by a series of concentric rings within which the refractive index varies linearly, being the distribution continuous but not necessarily differentiable between rings. The radial position of each ring, as well as their extreme indices, is calculated by using an iterative algorithm that involves the refinement of a ray tracing, initially assumed straight. Such a iterative refinement is function of the difference between the distribution of the phase for that ray tracing and that of the experimental case. This method is specially sensitive to the error in the calculation of the

gradient in the most peripheral rings, since the calculation of such a gradient in each one of the rings depends on that calculated in those more external. In fact, in the published works the error in the calculation of the index increases towards the center of the lens, reaching values up to the second decimal digit of the index over a total variation of the first decimal digit of the index between the periphery and the center of the lens.

2.2.3 Fitting of ocular and visual parameters

One way of obtaining quantitative parameters of the optical properties of the lens is to characterize previously the whole of the ocular system and to leave out the effect of all what is not crystalline lens, that is, cornea, intraocular distances and refractive indices of the vitreous and aqueous humour, which are supposed to be perfectly parametrized by means of *in vivo* or *in vitro* measurements. In 1984 it was published a first work that made use of this method to characterize the gradient index of the human lens [Pom84]. It was modeled as a rotationally symmetrical lens about the optical axis and asymmetrical about its equatorial plane, made up by multiple aspheric layers with an increasing refractive index towards the nucleus. As a result, the lens was defined by 33 variables that had to be calculated, through a minimization algorithm, from the above mentioned ocular parameters and the average axial spherical aberration measured in 100 emmetropic eyes, as well as some initial data of the lens, as its central index, curvature radii in the poles and thickness. Besides using a not very elaborate minimization algorithm, this method is too ambitious in its modeling of the lens taking into account the limitations in its input optical data: the approximated position of the circle of least confusion and the axial spherical aberration. With 33 variables and those input data it can not be guaranteed the unicity of the solution and that it is the closest to the real gradient, mainly out of axis.

This method was reformulated some years later with a more simple lens model [Hem95]. In this case, assuming as known the central index, it was proposed a polynomial gradient index depending on one single parameter β. Besides, the aim was just to characterize the gradient on axis. To do so, the mathematical relationships among the different parameters which were available to calculate β were linearized and such a parameter was obtained by fitting. Without discussing the validity of these linearizations, this method was limited by the paraxial nature of its reconstruction.

2.3 Hybrid methods

As it has been defined in the introduction of this chapter, a hybrid method includes a calibration procedure which is destructive but other measurement procedure which is not and is based on the data obtained in the calibration. Nowadays, the only hybrid method that has been developed for the retrieval of the lens gradient index is based on the technique of magnetic resonance imaging, MRI [Mof02a, Jon05]. This method makes use of the linear relationship that exists for a wide range of protein solutions between the transverse relaxation time T (or its inverse $R = 1/T$) of the hydrogen protons and the protein concentration [Hil89]. As it was shown in section 2.1, there is also a similar linear relationship for the refractive index of a protein solution (see Eq. 2.1). Therefore, by assuming that R in the lens cells is mainly influenced by the proton exchange between the intracellular water and proteins, once known the empirical relationship between the refractive index n and R, from the measurement of the latter for a section of the lens the gradient index of such a section can be obtained. The obtaining of this empirical relationship between n and R constitutes the calibration stage of the method. In this stage a certain number of crystalline lenses are decapsulated and its internal tissue homogenized with a spatula. Afterwards, the resulting tissue is gradually dehydrated. The outcome of this process is essentially a concentrate of crystalline proteins. Thus, by diluting samples of this concentrate in artificial aqueous humour it can be obtained the whole possible range of protein concentrations within the crystalline fibers. Once prepared the samples, the value of n and R are measured. Since the experimental devices used in the measurement of R in the samples and later in the lens are different, in the calibration stage is also necessary to measure R in each one of the samples with both devices and check that the result is the same, as well as the margin of error.

Once there are reliable calibration data, these data can be used in a measurement stage to calculate the refractive index distributions that correspond to the R maps obtained for sections of 1 mm thickness of intact lenses immersed in biocompatible solutions.

This method, the newest of the above mentioned, has the following shortcomings:

- The first is to assume that with a physical procedure like that of the spatula the cell walls can be broken up and a homogeneous protein solution be generated in order to use it in the calibration stage.
- From the study of the empirical relationship between n and R and the calibration of the two experimental devices used in the measurement of R it can be deduced that for indices higher than 1.40 the measurement error is in the second decimal digit [Jon05].

- The maps of R obtained in the crystalline lens correspond to average values within a section of 1 mm of thickness, that is, about a 10% of the equatorial diameter of the lens.

- In the the images of R shown in some of the works [Jon05] there is a noise in the biocompatible solution that makes R to reach values like those of the periphery of the lens. Inside the lens, this might generate errors of about the second decimal digit in the retrieval of the gradient index.

- In the comparison of the numerical ray tracing of the retrieved gradient indices with the data obtained by ray deflectometry there is not a good correlation [Jon05].

- Finally, even without considering the calibration stage, the experimental setup needed to implement this method is very expensive.

Need of a new method of reconstruction of the gradient index in crystalline lenses

Once all methods applied for the reconstruction of the gradient index of crystallines lenses have been put forward, the question of the need of the development of a new one raises. To answer this question, the features that should have an ideal retrieval method will be listed next, as well as in which degree the methods already developed satisfy them:

1. Minimal alteration of the lens tissue and, therefore, of its gradient in the measurement process: as it has been shown, the main drawback of the destructive methods is that they do not fulfill this condition.

2. Minimal constrains in the modeling of the gradient index and that, in case there are some, they limit as less as possible the application of the method to the lens: this is not the case of the deflectometric method based on the Abel integral inversion, the non destructive interferometric and that of axial reconstruction of the gradient index from ocular and visual parameters.

3. Unicity of the solution obtained from the experimental data: it has already mentioned that the lack of unicity is a problem that affects all methods that have used optimization algorithms, because of the type of the algorithms that have been implemented.

4. Average precision in the third decimal digit of the index in the retrieval of the gradient: from the results obtained with all the former methods it is clear that the variation of the refractive index in any lens is within the order of the first decimal digit (fish) or the second decimal digit (mammals). Hence, it is reasonable to ask for an average error in the retrieval no higher, at least, than the third decimal digit. So far, none of the applied methods has been able to guarantee the fulfillment of this condition.

5. Reproducibility of the optical behaviour of the lens by the reconstructed gradient index, both on axis and out of axis: the optical reproducibility out of axis has not been studied by any method and when it has been studied on axis [Jon05, Kro94] the results are not good either.

6. Simple experimental implementation: the need of matching external and surface indices in some of the deflectometric methods or the high cost of the MRI devices makes difficult their experimental implementation.

7. Low computational cost: the implementation of a precise numerical ray tracing (internal ray deflectometry, optimization algorithms) slows down the mathematical process of the retrieval of the gradient index.

Since none of the methods applied so far is able to fulfill these seven conditions, the possibility of developing one that does fulfill them would imply a clear improvement in relation with the current situation. This is the aim of this work.

3 Theoretical bases of a tomographic algorithm of reconstruction of rotationally symmetrical gradient indices

Throughout this chapter we will show the theoretical bases upon which a new tomographic algorithm of reconstruction of the gradient index will be formulated. These bases include concepts both from geometrical optics and tomography. Hence, firstly it will be necessary to do a brief introduction in both fields and how these are interrelated. The first section of the chapter will be a review of the most important concepts of the light propagation under the approximation of geometrical optics in a dielectric, inhomogeneous and isotropic medium. Amid those concepts two will stand out: ray of light and optical path. Later, a brief introduction to tomography will be done, since it is a mathematical tool that will constitute the core of the new algorithm. Finally, in a third section, from the relationship of the formerly mentioned concepts of geometrical optics and tomography, the basic idea for the theoretical formulation of the algorithm will be explained.

3.1 Light propagation under the approximation of geometrical optics

Let us assume a monochromatic wave $V(\vec{r},t) = A(\vec{r})\exp\{-ig(\vec{r})\}\exp\{i\omega t\}$ which propagates in a dielectric and isotropic medium. If for a generic point of that medium with a position vector $\vec{r_0}$ it is verified that for a region of the order of magnitude of its wavelength the medium can be considered homogeneous and that

$$\begin{aligned} A(\vec{r}) &\approx A(\vec{r_0}) \\ g(\vec{r}) &\approx g(\vec{r_0}) + (\vec{r}-\vec{r_0}) \bullet \nabla g(\vec{r_0}) \end{aligned} \tag{3.1}$$

then the wave can be locally expressed in that region [Mej99] as

$$V(\vec{r},t) = A(\vec{r}_0)\, exp\left\{-ik_0\vec{r}\nabla\hat{L}(\vec{r}_0)\right\} exp\{i\omega t\} \tag{3.2}$$

where $A(\vec{r}_0)$ is the wavelength amplitude, k_0 the angular wave number and $\hat{L}(\vec{r})$ a function named eikonal and that verifies the following equation of the same name

$$\left[\nabla\hat{L}(\vec{r})\right]^2 = n^2(\vec{r}) \tag{3.3}$$

being $n(\vec{r})$ the refractive index of that medium [Bor59].

As it will be seen next, under this approximation it is possible to move from a wave description of light to a geometrical one, where it is considered that the light propagates following lines named rays and that the laws that rule their behaviour are geometrical. Nevertheless, it is important to note, as it can be deduced from the conditions 3.1, that such an approximation has no validity in those cases where there are sudden changes of the intensity or the phase is not continuous, differentiable and univaluated en regions of the order of magnitude of λ, for instance, diffractive and interferential phenomena or caustics.

From the study of the equation 3.2 it can be seen that the wave has locally the same functional structure as a plane wave, where the direction of the vector $\nabla\hat{L}$ would be direction of propagation of the planes of constant phase and luminous energy. Therefore, if it is defined as ray of light the curve with tangents at each of its points with the same direction of propagation than the luminous energy in these points, there is a first link between the geometrical and wave descriptions of light. The tangent direction at each point of the ray would fit in, for locally plane waves, with that of $\nabla\hat{L}$. Hence, the unitary vector $\hat{s}$ tangent at each one of its points can be written as

$$\hat{s} = \frac{\nabla\hat{L}}{\left|\nabla\hat{L}\right|} = \frac{\nabla\hat{L}}{n} \tag{3.4}$$

On the other hand, given the position vector $\vec{r}(s)$ of a point P of the curve that represents the ray of light, where s is the arc length measured along the ray (see Fig. 3.1), $\hat{s}$ can also be written as

$$\hat{s} = \frac{\mathrm{d}\vec{r}}{\mathrm{d}s} \tag{3.5}$$

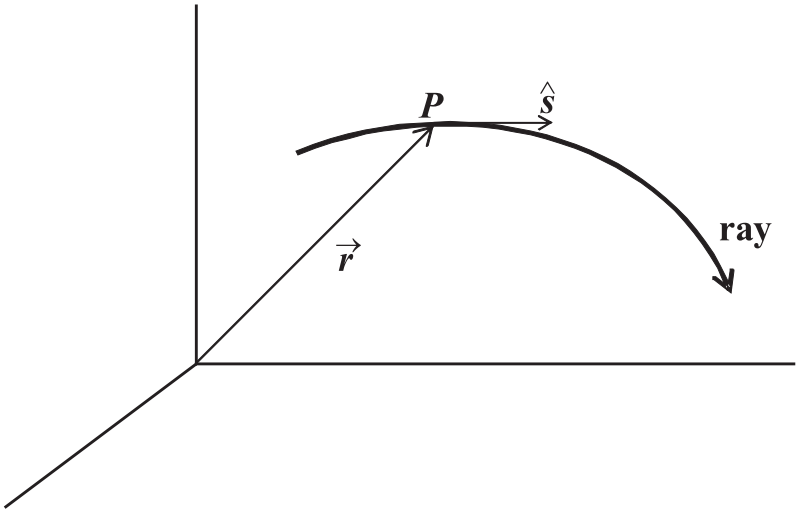

Figure 3.1: Representation of a ray of light.

From these last two expressions we obtain the following relation

$$n\frac{\mathrm{d}\vec{r}}{\mathrm{d}s} = \nabla\hat{L} \tag{3.6}$$

This relation is known as the ray equation since it determines their trajectories, orthogonal to the surfaces that verify that

$$\hat{L}\left(\vec{r}\right) = \text{constant}, \tag{3.7}$$

named geometrical wavefronts.

Another important concept in the framework of geometrical optics is that of the optical path. The optical path between two points A and B of a curve described by a ray of light in a medium with a refractive index $n\left(\vec{r}\right)$ is defined as the integration

$$S\left(AB\right) = \int_{A}^{B} n\left(\vec{r}\right)\mathrm{d}s \tag{3.8}$$

Since, as it can be deduced from the equation 3.6, $\mathrm{d}\hat{L} = n\left(\vec{r}\right)\mathrm{d}s$, the optical path covered by a ray of light gives the variation of the eikonal function along its trajectory.

3.1.1 Propagation of rays of light in media with rotationally symmetrical gradient index

As it was mentioned in section 1.6, in this work crystalline lenses are going to be supposed media of rotationally symmetrical gradient. Thus, it is interesting to know how this

symmetry affects the propagation of rays and to do so it is necessary to study such an effect in the ray equation. This equation can be expressed as a function of the refractive index n [Bor59] in the following way

$$\frac{\mathrm{d}}{\mathrm{d}s}\left(n\frac{\mathrm{d}\vec{r}}{\mathrm{d}s}\right) = \nabla n \tag{3.9}$$

From the study of this equation for the particular case of the gradient index with rotational symmetry, $n(\rho, z) = n\left(\sqrt{x^2+y^2}, z\right)$, the following invariant condition in the propagation of rays is obtained [Mar78, cap. 9]

$$c = xq - yp = x_0q_0 - y_0p_0, \tag{3.10}$$

where x, y, p and q are the position coordinates and the optical director cosines in x and in y of a ray at any point of its trajectory, respectively (with the subscripts 0 we note the values of these magnitudes in the initial point of the trajectory of the ray). For any ray that enters the gradient in such a way the value of the invariant c (or skewness invariant) is zero, its trajectory will be contained within a single plane of the gradient [Mar78, cap. 9], which contains the initial point of the ray (x_0, y_0) and the axis z. This plane, as all those that contain the axis of symmetry of the distribution, is named meridional plane of the gradient.

3.2 Tomography basics

It is named tomography the reconstruction of the distribution of a given physical magnitude, $f(x, z)$, by means of measurements that are line integrations of such a magnitude.

The basic tool of tomography is an operator named Radon transform, $\Re$, that represents the integration of the function $f(x, z)$ along a line characterized by its distance to the origin of the coordinate system, p, and its angular position regarding that system, θ. Assumed a surface $\sum$, like that of figure 3.2, within which a certain magnitude $f(x, z)$ of compact support is distributed, the Radon transform of $f(x, z)$ at the point (p, θ) (transformed space) is defined [Her80] as

$$[\Re f](p, \theta) = \int_{-\infty}^{\infty}\int_{-\infty}^{\infty} f(x, z)\,\delta(p - z\cos\theta - x\mathrm{sin}\theta)\,\mathrm{d}x\,\mathrm{d}z \tag{3.11}$$

where $\delta(p - z\cos\theta - x\mathrm{sin}\theta)$ is the Dirac delta function in the line defined by (p, θ) [Pap81].

An important concept in tomography is that of projection. Given an angle θ, a projection is defined as the set of values of the Radon transform for $p \in [p_1, p_2]$, where p_1 and p_2 are the extreme values of p that verify a line traverses the surface $\sum$ (see Fig. 3.2). Once known the values of the projections for all angles $\theta \in [0, \pi)$ it can be shown that the distribution $f(x, z)$ can be tomographically retrieved [Her80]. In practice the available information for the reconstruction is discrete, regarding both the number and distribution of projections and the measurements that correspond to each one of those projections. Depending on the degree of discretization of these input data the type of algorithm to be used for the tomographic reconstruction is different.

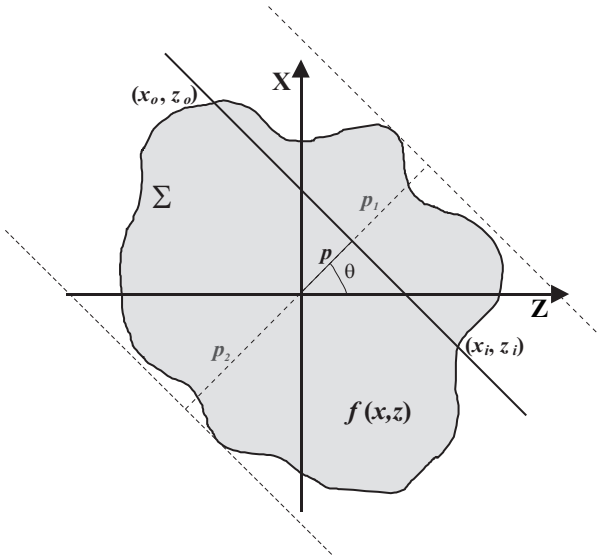

Figure 3.2: Surface $\sum$ where a Radon transform is calculated along the line defined by coordinates (p, θ).

A first type are the transform algorithms. These are zonal reconstruction algorithms that numerically implement the Radon inverse transform for the calculation of $f(x, z)$ at each point of the surface $\sum$. The existence of the inverse transform [1], $\Re^{-1}$, is shown for all square integrable function $f(x, z)$ with compact support:

$$\left[\Re^{-1}\Re f\right](x, z) = f(x, z) \tag{3.12}$$

The implementation of these transform algorithms requires a very complete set of input

[1] The operator $\Re^{-1}$ is made up by a sequence of more simple operators $\left(\Re^{-1} = -\frac{1}{2\pi}\mathcal{B}\mathcal{H}_p\mathcal{D}_p\right)$, where $\mathcal{D}_p$ is the partial differentiate with respect of the first variable, $\mathcal{H}_p$ the Hilbert transform with to its first variable and $\mathcal{B}$ the backprojection operator [Her80].

data, close to the theoretical ideal of having projections and transforms for all θ and p.

In case of having a much more discretized and incomplete input information the alternative are the series expansion algorithms. These are modal reconstruction algorithms that, to compensate the lack of information, assume that the distribution $f(x,z)$ can be approximated by a linear combination of a series of base or modal functions $b_i(x,z)$:

$$f(x,z) = \sum_{i=1}^{N} a_i b_i(x,z) \tag{3.13}$$

being the aim of these algorithms to calculate the values of the modal coefficients a_i.

The reconstruction of the function $f(x,z)$ as a series expansion is based on the properties of linearity and continuity of the Radon transform, since it can be stated that

$$\Re f = \sum_{i=1}^{N} a_i \Re b_i \tag{3.14}$$

The calculation of the coefficients a_i from the input data provided by the different projections of the distribution $f(x,z)$ can be performed by using different minimization algorithms, like Bayesian estimation, least variance fitting or least squares fitting .

3.3 Formulation of a tomographic algorithm on the basis of the geometrical optics and tomography

Let us consider a surface $\sum$ like that of figure 3.3 that shows a distribution of the refractive index $n(x,z)$ that is intended to be measured. According to the expression 3.11, the Radon transform of the gradient index $n(x,z)$ at the point (p,θ) is defined as

$$[\Re n](p,\theta) = \int_{x_i}^{x_o}\int_{z_i}^{z_o} n(x,z)\,\delta(p - z\cos\theta - x\sin\theta)\,\mathrm{d}x\,\mathrm{d}z = \int_{P_i(p,\theta)}^{P_o(p,\theta)} n(x,z)\,\mathrm{d}l \tag{3.15}$$

By comparing the expression 3.15 with that of 3.8, it is noticed that the Radon transform of $n(x,z)$ for a given direction is equivalent to the optical path covered by a hypothetical ray of light that propagates along that direction

$$S(P_iP_0) = [\Re n](p,\theta) = \int_{P_i(p,\theta)}^{P_o(p,\theta)} n(x,z)\,\mathrm{d}l \tag{3.16}$$

However, that direction of propagation may not agree with the trajectory a ray would really follow in such a medium.

If now the Radon transform is redefined along curves (generalized transforms [Ram96, p. 63]) and, specifically, curves that agree with the real trajectory of the rays inside the bidimensional gradient $n(x,z)$ (see Fig. 3.4), the optical path covered by a ray and the (generalized) Radon transform along its trajectory become equivalent concepts.

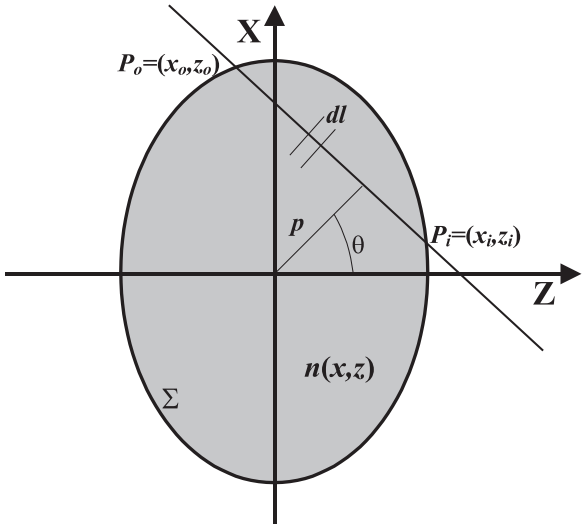

Figure 3.3: Surface $\sum$ with a gradient index $n(x,z)$ where a Radon transform defined by the coordinates (p,θ) is calculated.

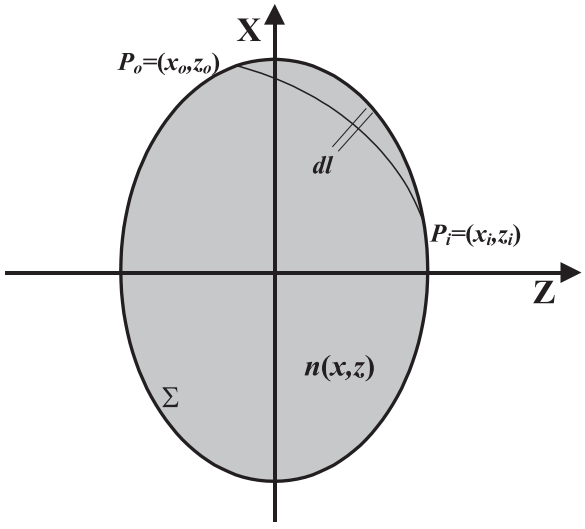

Figure 3.4: Trajectory of a ray within the gradient index $n(x,z)$ of the surface $\sum$.

Thus, given a set of parallel rays that, having entered the surface $\sum$ with an entry

angle θ, traverses all its points, the registration of the optical path covered for each one of the rays inside the lens provides the measurements corresponding to a tomographic projection of $n(x,z)$ at an angle θ. Hence, a projection is defined as a function of the incidence angle of the incoming rays. Finally, gathered all data corresponding to all possible projections and having guaranteed that every point of the surface $\sum$ has been traversed by rays in all directions, it is theoretically possible a point by point tomographic reconstruction of $n(x,z)$. In our case the tomographic reconstruction will have several limitations. Firstly, and regarding the experimental input data, there will be just a relatively small number of projections, with a angular distribution limited in their maximum values. In addition, such data will shown experimental noise. Besides, the trajectory of the rays inside the gradient will not be known *a priori*. We will tackle the first of the problems, the discretization of the tomographic information, by using series expansion algorithms, which also have the advantage of its more immediate application to generalized transforms than the transform algorithms. However, the remaining problems will need other type of strategies that will be explained in the next chapter.

A rotationally symmetrical distribution results from the rotation about its axis of symmetry of the distribution of each one of its meridional planes. In section 3.1.1 it was explained that in the case of lenses with rotationally symmetrical gradients every incident ray contained within one of its meridional planes will not leave such a plane along its trajectory, both inside and outside the lens. We deduce, hence, that the tridimensional tomographic reconstruction of the gradient index in rotationally symmetrical lenses can be limited to a bidimensional reconstruction of the distribution $n(\rho,z)$ shown by each one of its meridional planes, where ρ is the radial coordinate and z the coordinate of the axis of symmetry. In the following chapters we will show that in order to calculate $n(\rho,z)$ it will be enough with illuminating one of those planes with sets of meridional rays arranged in a limited number of incidence angles, obtaining at their exit the optical path covered by each one of them inside the lens and adapting the a tomographic algorithm designed for the inversion of those data. Since ρ is defined like $\rho^2 = x^2 + y^2$, hereinafter all calculations and reasonings can be done for $Y = 0$ without loss of generality, using $n(x,z)$ instead of the equivalent $n(\rho,z)$.

Finally, given the equivalence of optical path and phase, it is important to point out that any experimental technique that measures the phase accumulated by the rays directly (interferometry) or indirectly (curvature, Hartmann-Shack, ray deflectometry) would be potentially useful for its use along the tomographic algorithm. Nevertheless, as it will be explained in the following chapter, the technique that shows more advantages in the case of rotationally symmetrical lenses is ray deflectometry, also known as laser

scanning. Because of this, this work will deal with the development and implementation of the tomographic algorithm from the experimental data provided by ray deflectometry, naming the whole tomographic method of reconstruction of gradient indices.

4 Tomographic algorithm of reconstruction of the gradient index

In the former chapter we have presented the initial idea of the formulation of a new tomographic algorithm for the reconstruction of rotationally symmetrical gradient indices. Such an algorithm would use as input data the measurements of optical path accumulated inside the lens by sets of rays projected at different entry angles. At first sight, this idea does not seem very different to that which underlies tomographic algorithms used in other fields, like medicine [Ram96, p. 6]. However, its application to the particular case of the measurement of a gradient of the refractive index show some specific features and difficulties that will be explained and tacked throughout this chapter. Firstly we will deduce the theoretical relationships that link the measurements provided by ray deflectometry with the optical path covered by the rays. Afterwards, we will deal with the issue of the functional model of the gradient index proposed for its modal tomographic reconstruction. From there we will move on the tomographic inversion, that from the calculated optical paths and through an iterative process will retrieve the index $n(x, z)$. In this section we will study and solve a series of difficulties of this retrieval, like the *a priori* ignorance of the trajectory of the rays inside the lens.

4.1 Ray deflectometry applied to tomography

As it has been explained in section 2.2.1, ray deflectometry is based on the characterization, at the exit of a lens, of the deflection undergone by a set of incoming laser beams. An advantage of this technique compared with others that measure phase is its experimental simplicity: *a priori* just a laser, a holder for the lens and a system of acquisition and processing of images are required. Once characterized the ray deflections, we will see that it is possible to calculate the optical paths covered by each one of them inside the lens from the theoretical relationships that we explain next.

Let us consider the case of rotationally symmetrical lens with a thickness t, immersed in a homogeneous medium of refractive index n_{ext}, with a gradient index $n(x, z)$ at any of its sagittal or meridional planes and illuminated with a set of parallel rays inclined an

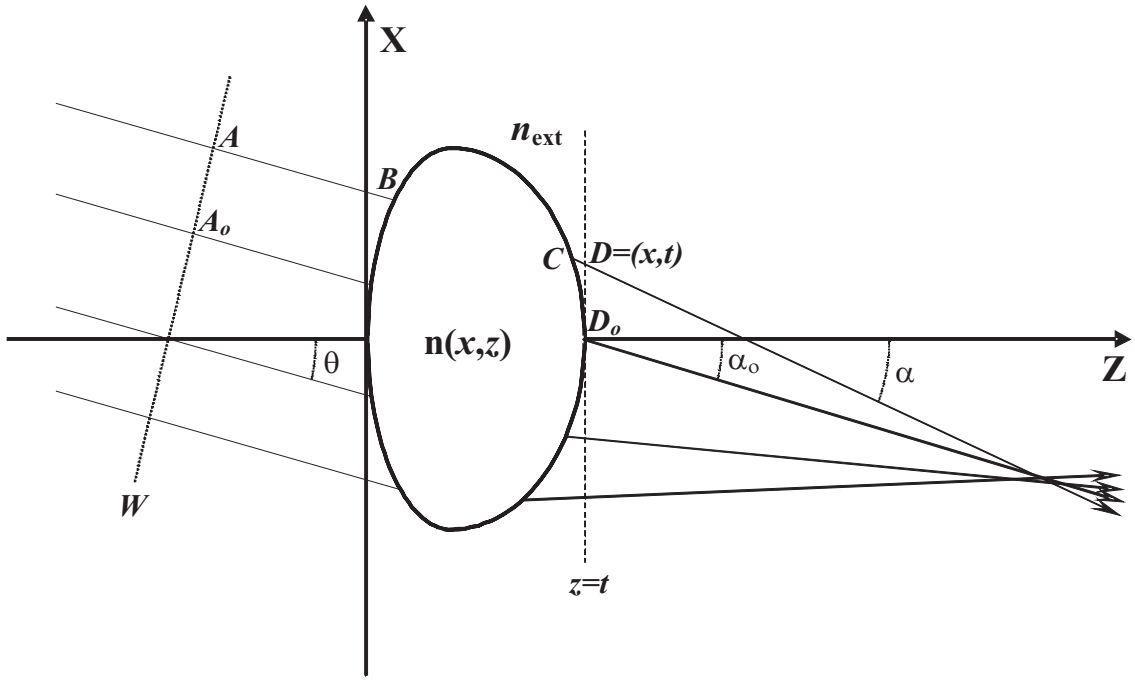

Figure 4.1: Sagittal plane of a lens with refractive index $n(x,z)$ illuminated by a set of parallel rays inclined an angle θ with respect to the axis of symmetry Z.

angle θ (see Fig. 4.1). By using the deflectometry technique the entry and exit rays are registered in order to obtain the positions of the points of intersections B and C with the anterior and posterior surfaces, respectively, the entry angle θ and the angles of deflection α at the exit. From these data the distribution of the sines of the angles of deflection, $\sin\alpha(x,z)$, can be calculated at any plane, for instance, $z=t$. On the other hand, this set of parallel rays at the entry of the lens can be seen, under the wave description of light, as its corresponding plane wavefront W, orthogonal to all of them, entering the lens with an angle θ. As a result of the propagation of this wavefront inside the lens, the eikonal shows at the plane $z=t$ a distribution that we will denote as $\hat{L}(x,t)$. This distribution and that of the sines of the angles of deflection of the rays, $\sin\alpha(x,z)$, can be related, through the ray equation (see Eq. 3.6), by means of the following expression

$$n_{ext}\sin\alpha(x,t) = \frac{\partial \hat{L}(x,t)}{\partial x} \tag{4.1}$$

Integrating this equation we have that

$$\hat{L}(x,t) = n_{ext}\int_0^x \sin\alpha(x,t)\,\mathrm{d}x + \hat{L}(0,t) \tag{4.2}$$

Since the optical path $S(P_1, P_2)$ between two points P_1 and P_2 has been defined as the difference of the value of the eikonal between those two points (see section 3.1), then

$$\begin{aligned} S(AD) &= \hat{L}(D) - \hat{L}(A) \\ S(A_oD_o) &= \hat{L}(D_o) - \hat{L}(A_o) \end{aligned} \tag{4.3}$$

and, since A and A_o are points of the same wavefront W, we have that

$$\hat{L}(A) = \hat{L}(A_o) \tag{4.4}$$

Thus, the equation 4.2 can be rewritten as

$$S(AD) = \tilde{S}(AD) + K \tag{4.5}$$

where $\tilde{S}(AD) \equiv \int_0^x \sin\alpha(x,t)\,\mathrm{d}x$ and $K = S(A_oD_o)$. Therefore, from the experimental measurement of the deflection angles is possible to calculate $\tilde{S}(AD)$, that represents the optical path covered by each ray from an initial position of the wavefront W up to the exit plane $z = t$[1] but an additive constant K, usually named piston.

The following step is to calculate $S(BC)$ from $\tilde{S}(AD)$. As it can be seen in figure 4.1, the optical path accumulated by a ray that goes from a point A to another point D is given by

$$S(AD) = n_{ext}\overline{AB} + S(BC) + n_{ext}\overline{CD} \tag{4.6}$$

To obtain $S(BC)$ is necessary to calculate first the length of the segments $\overline{AB}$ and $\overline{BC}$. At this point it stands out the main advantage of the ray deflectometry when compared with other techniques of phase measurement for the tomographic retrieval of rotationally symmetrical gradient indices. In deflectometry, because of characterizing both entry rays and their corresponding exit rays, the calculation of B and C for each ray is trivial once the lens surfaces are known. This is not the case of other techniques of phase measurement, where, usually, it is not possible to assign to each exit ray its corresponding entry ray, with its point of intersection B with the anterior surface of the lens.

As it has been shown in section 3.1, the optical path $S(BC)$ is defined as

$$S(BC) = \int_B^C n(x,z)\,\mathrm{d}s \tag{4.7}$$

where $\mathrm{d}s$ is the differential arc length differential along the ray. Applying equations 4.5

[1] It is important to point out that this exit plane can be any plane and not necessarily $z = t$.

and 4.7 to the equation 4.6 we get

$$S(BC) = \int_B^C n(x,z)\,\mathrm{d}s = \tilde{S}(AD) + K - n_{ext}\left(\overline{AB} + \overline{CD}\right), \tag{4.8}$$

which allows to define a new magnitude $\tilde{S}(BC)$, which represents the optical path covered by each ray inside the lens but a piston K and that can be calculated from the experimental data obtained by ray deflectometry:

$$\tilde{S}(BC) \equiv \int_B^C n(x,z)\,\mathrm{d}s - K = \int_0^x \mathrm{sin}\alpha(x,t)\,\mathrm{d}x - n_{ext}\left(\overline{AB} + \overline{CD}\right) \tag{4.9}$$

Therefore, from the deflectometry data what we will obtain is $\tilde{S}(BC)$ and not directly $S(BC)$, as it was intended in the initial formulation of the tomographic algorithm (see section 3.3). This will imply that in the tomographic reconstruction of $n(x,z)$ it will be necessary to take also into account the existence of an additive unknown constant K that will be the same for all rays of a given projection. Thus, for the projection p at an angle θ we will have a number N of measured values of $\tilde{S}(B_rC_r)$ (one value for each ray $(r = 1,\ldots,N)$) and an unknown piston K_p, that according to equation 4.9 are related as

$$\tilde{S}(B_rC_r) = \tilde{S}(A_rD_r) - n_{ext}\left(\overline{A_rB_r} + \overline{C_rD_r}\right) = \int_{B_r}^{C_r} n(x,z)\,\mathrm{d}s_r - K_p \tag{4.10}$$

These values $\tilde{S}(B_rC_r)$ measured for each ray of each projection are the input data from which the tomographic algorithm will retrieve the distribution of the refractive index $n(x,z)$, as well as the values of the constants K_p corresponding to each projection. As we had explained in section 3.3, having those values $\tilde{S}(B_rC_r)$ for all possible rays and projections, a point by point tomographic reconstruction of $n(x,z)$ can be carried out. However, in the case of a tomographic characterization of a crystalline lens this type of reconstruction is not feasible because of the following three reasons:

- The projections are limited both in their number and in their angular distribution. As we will explain in section 4.2, this limitation can be compensated with the implementation of series expansion algorithms, that is to say, with a modal reconstruction of the gradient index.
- *A priori* ignorance of the ray trajectories inside the lens. In section 4.3 it will be explained the procedure through which we will try to get the best possible approximations to those trajectories.

- Lack of knowledge of pistons K_p and of their influence in the reconstruction of the gradient index. This issue will be tackled in section 4.3.

4.2 Gradient index model

We already saw previously that the available number of data for the tomographic reconstruction will be limited. The main effect of this limitation is the lack of enough information to carry out the tomographic reconstruction. By using a series expansion algorithm we can compensate that lack of information with the proposal of a functional model of the gradient index approximated to that we wish to retrieve. Thus, a general model for a rotationally symmetrical distribution of the refractive index about the optical axis Z is the following Taylor series expansion of an even function in ρ [Moo71, Bla80, Smi91]:

$$n(\rho, z) = n_0(z) + n_1(z)\rho^2 + n_2(z)\rho^4 + \ldots = \sum_{i=0}^{M} n_i(z)\rho^{2i}, \tag{4.11}$$

where

$$n_i(z) = \sum_{j=0}^{2(M-i)} n_{ij} z^j$$

and[2]

$$\rho^2 = x^2 + y^2$$

We will make use of this series expansion throughout this work. A slight variation of this model that we will also explore is that of considering two different segments of the lens, anterior and posterior, each one with its own refractive index distribution described by the the equation 4.11, $n^{ant}(x, z)$ y $n^{pos}(x, z)$, respectively [3]. The union of both segments would take place at a plane $z = z_H$, where continuity and differentiability conditions of $n^{ant}(x, z)$ y $n^{pos}(x, z)$ are determined by the arrangement of the crystalline fibers (see section 1.2.3): formed at the equator of the lens and generators of its gradient due to its process of cellular differentiation, these fibers extend both to the anterior and posterior poles of the lens without sudden variations on their shape [Kus96]. As a result, both the anterior and the posterior segments share the same fibers, without having been noticed on them any discontinuity that implies that their cellular features are different in every segment, just their arrangement. Therefore, since the gradient index is the result

[2] As it was previously mentioned (see section 3.3), all calculations will be carried out at the plane $Y = 0$ without loss of generality.

[3] Hereinafter we will call this model bipolynomial and the former monopolynomial.

of such features, specifically of their protein concentrations, and of its layout within the lens, it seems very plausible and not restrictive to assume the following two conditions of continuity and differentiability [Jag90]:

$$n^{ant}(x, z_H) = n^{pos}(x, z_H)$$
$$\frac{\partial n^{ant}(x, z_H)}{\partial z} = \frac{\partial n^{pos}(x, z_H)}{\partial z} \tag{4.12}$$

In this case, the tomographic algorithm will have to retrieve not only the coefficients n_{ij}^{ant} y n_{ij}^{pos}, but also z_H. It must be noted that the position of this plane of continuity has not necessarily to agree neither with the equatorial plane of the crystalline lens nor the plane where the derivative of the index has a given value. The surface $z = z_H$ has just a mathematical sense and not a physiological one, that of providing a geometrical degree of freedom that allows the best possible calculation of the gradient index in two different sections by satisfying always the conditions of continuity 4.12. To do so, we place z_H in the position of the optical axis where the distribution of the refractive index reaches a a global maximum.

Besides the gradient index model described by the expression 4.11 for the eye lens, other two functional forms have been proposed in literature: an elliptical or bielliptical model [Jag90, Cha88, Smi91], which is a particular case of 4.11 (or its bipolynomial expression) and an exponential model, with a variation of the index characterized by a single parameter [Alh95, Pop98], what makes it a bit limited.

4.3 Tomographic inversion

From all what has been previously mentioned it is inferred that the ultimate goal of the tomographic algorithm will be to retrieve the values of the coefficients n_{ij} in the case of the model of monopolynomial gradient or n_{ij}^{ant}, n_{ij}^{pos} and z_H in the case of the bipolynomial one, in addition to the pistons K_p for each projection. Since there is not a previous statistic that can be implemented in a more complex minimization process, we have considered that a good option to obtain those values is a least squares fitting. Thus, according to the equation 4.10, for the monopolynomial case it would be necessary to minimize the following difference:

$$\sum_{p=1}^{P}\sum_{r=1}^{N_p}\left[\left(\sum_{i=0}^{M}\sum_{j=0}^{2(M-i)}\int_{B_{pr}}^{C_{pr}} n_{ij}x^{2i}z^{j}\mathrm{d}s_{pr} - K_p\right) - \tilde{S}\left(B_{pr}C_{pr}\right)\right]^2, \qquad (4.13)$$

where P represents the total number of projections, N_p the number of rays per projection and $\mathrm{d}s_{pr}$ the differential arc length along the ray r of the projection p. At this point we find an important difficulty: we do not know the trajectories of the rays along which take place the integrations of the equation 4.13. Therefore, to continue with the formulation of the tomographic algorithm is necessary to find an approximation, as accurate as possible, to this trajectories that allow to uncouple the index $n\left(x,z\right)$ and the trajectories of the rays and to guarantee the accuracy of the reconstruction of the gradient.

A first approximation, appropriate for very weak gradients, is to consider straight lines joining points B_{pr} and C_{pr}. However, although the lenses do not show large variations in the refractive index [Nak68, Cam84, Gar01, Aco05, Jon05], this approximation considerably limits the range of possible gradients for which the algorithm would provide an accurate result. The result obtained with straight lines, $n^{rct}\left(x,z\right)$, can be a very good first estimation of $n\left(x,z\right)$, but if we wish to ensure the versatility of the algorithm for its application to the widest possible range of gradients it is necessary to consider other more complex approximations for the ray trajectories that allow to refine that result. The possibilities are two:

- To consider more complex functional forms than straight lines, like parabolas, sines, etc. In a certain type of eye lenses this alternative offers good results, as we have shown by using parabolas in spherical symmetrical gradients [Aco05], also useful in optical fiber preforms [Aco02]. However, its application to more general gradients requires more complex functional forms than those we can work with according to the available experimental data..

- To approximate the ray trajectories as a finite series of straight line segments. This second option has as main advantages its flexibility to approximate the ray trajectories with very different geometries and the fact of working with functions as simple as the straight lines. That is why we have chosen this second alternative to improve the result obtained with the approximation of rays as straight lines.

The implementation of this second method implies an approximate knowledge of some intermediate points of the trajectory of the rays inside the lens. Since we can have a first estimation of $n\left(x,z\right)$, $n^{rct}\left(x,z\right)$, by means of a numerical ray tracing algorithm a

first estimation of such intermediate points can be also obtained and, by joining them with straight lines, to approximate the actual trajectory of the rays and to obtain a new estimation of the index. This is the basis of an iterative procedure where we will assume that the approximation to the actual trajectory of the rays is more accurate at each iteration, yielding a more accurate retrieved gradient too. This assumption depends mainly in how accurate is the first estimation of the gradient with the approximation of the rays as straight lines. Since we have not found strong variations of the eye lens refractive index in the related literature, it is reasonable to expect this first estimation to be good.

For the interpolation of the intermediate points of the ray trajectories, any of the existing numerical ray tracing algorithms can be used. Because of its good ratio of computational cost versus result precision, we have chosen the algorithm designed by Sharma *et al.* [Sha82]. This algorithm solves the differential ray equation (see Eq. 3.9) by using the Runge-Kutta method [Pre99, p. 710] with a proper change of variable that allows to achieve very accurate outcomes with relatively large steps.

An important issue to notice in the iterative procedure is the number of intermediate points interpolated for each ray. The higher this number, the longer the time of computation, since it involves using smaller steps of the numerical ray tracing. According to what has been explained, the less deviated the ray trajectories from a straight line, the lower the number of interpolated points needed to approximate those trajectories. Therefore, rays curvature and number of interpolated points are going to be strongly related. Thus, for those gradients where the rays are very curved, that we will call strong gradients, the necessary number of points will be larger than in those gradients where the rays are hardly curved, that we will call weak gradients. Assuming that anyway the crystalline gradients will never be very strong, from the point of view of the computational time the most reasonable strategy is to increase gradually the number of interpolated points at each iteration (or, equivalently, to gradually use smaller steps in the numerical ray tracing algorithm). Thus, if the gradient that is intended to be retrieved is not too strong, just a few iterations and a limited use of the numerical ray tracing will be needed. It is important to note that this difference between strong and weak gradient can be justified according to the functional form of $n(x,z)$, since from the differential ray equation we deduce that the ray curvature depends on the following two factors: the variation of $n(x,z)$ between its extreme values and the maximum values reached by the gradient of this distribution, $\nabla n(x,z)$.

With the aim of fixing the positions of entry and exit of each ray (B_{pr} and C_{pr}, respectively) it is necessary that the intermediate points are calculated from both positions, so

that the number of point will always be even. Let us consider, for instance, the following iteration to the approximation of the rays as straight lines ($Q = 0$), that we will label as iteration $Q = 1$ and where two intermediate points are interpolated for the trajectory of each one of the rays (see Fig. 4.2). Once calculated $n^0(x, z) \equiv n^{rct}(x, z)$, a first point is interpolated from the entry angle and point of the ray in the lens, θ_p and B_{pr} respectively, and the second from its exit angle and point, α_{pr} and C_{pr}. Regarding the position of these interpolated points, it is necessary to take into account that the Sharma *et al.* algorithm does not work with spatial coordinates. By considering, for instance, an approximate average index of $\bar{n} = 1.4$ for the case of the human lens [Pie89, Jon05] and taking the length $\overline{B_{pr}C_{pr}}$ from B_{pr} to C_{pr}, the step of the numerical ray tracing [Sha82] for $Q = 1$, where each straight line segment should comprise approximately one third of the whole trajectory of the ray, can be written as

$$\Delta\tau = \frac{\overline{B_{pr}C_{pr}}/3}{\bar{n}} = \frac{\overline{B_{pr}C_{pr}}}{4.2} \tag{4.14}$$

At following iterations the number of interpolated points will increase in two by two, so that for iteration Q the used step in that tracing will be

$$\Delta\tau = \frac{\overline{B_{pr}C_{pr}}/(2Q+1)}{\bar{n}}, \tag{4.15}$$

paying special attention to prevent the propagated rays from B_{pr} and C_{pr} to cross, since, as it was mentioned, the Sharma *et al.*'s algorithm does not work with spatial coordinates.

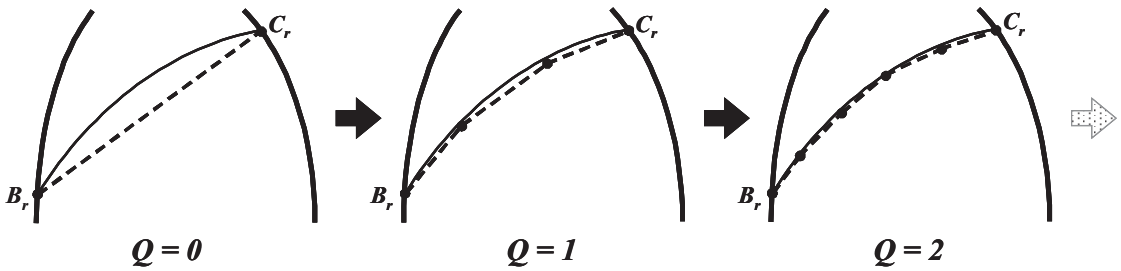

Figure 4.2: Increase of the number of interpolated point at each one of the iterations of the tomographic algorithm for a ray that propagates inside the lens, where the solid line represents the actual trajectory of the ray and the dashed line the approximation done at each iteration.

To calculate at each iteration Q the coefficients n_{ij}^Q and the pistons K_p^Q of each projection, it is necessary to minimize the equation 4.13, that we can now write in a fashion

we can work with:

$$\sum_{p=1}^{P}\sum_{r=1}^{N_p}\left[\left(\sum_{i=0}^{M}\sum_{j=0}^{2(M-i)} n_{ij} f_{ijpr}^{Q} - K_p\right) - \tilde{S}\left(B_{pr}C_{pr}\right)\right]^2, \tag{4.16}$$

where

$$f_{ijpr}^{Q} = \begin{cases} \int_{B_{pr}^{Q}}^{C_{pr}^{Q}} x^{2i} z^{j} \mathrm{d}l_Q & \text{if } Q = 0 \\ \sum_{q=0}^{Q-1} \int_{B_{pr}^{q}}^{B_{pr}^{q+1}} x^{2i} z^{j} \mathrm{d}l_q + \int_{B_{pr}^{Q}}^{C_{pr}^{Q}} x^{2i} z^{j} \mathrm{d}l_Q + \sum_{q'=0}^{Q-1} \int_{C_{pr}^{q'}}^{C_{pr}^{q'+1}} x^{2i} z^{j} \mathrm{d}l_{q'} & \text{if } Q > 0 \end{cases} \tag{4.17}$$

f_{ijpr}^{Q} represents the line integrations along the $2Q+1$ interpolated segments used to approximate the trajectory of the rays. In the equation 4.17 B_{pr}^{q} denotes the qth interpolated point from B_{pr} $\left(B_{pr}^{0} \equiv B_{pr}\right)$, $C_{pr}^{q'}$ the q'th interpolated point from C_{pr} $\left(C_{pr}^{0} \equiv C_{pr}\right)$ and $\mathrm{d}l_q$, $\mathrm{d}l_Q$ y $\mathrm{d}l_{q'}$ the line elements for the segments joining B_{pr}^{q} and B_{pr}^{q+1}, B_{pr}^{Q} and C_{pr}^{Q} and $C_{pr}^{q'}$ and $C_{pr}^{q'+1}$, respectively (see Fig. 4.3). It is important to point out the linearization of the problem of tomographic inversion that can be noticed in equations 4.16 and 4.17, consequence of the performed approximation to the ray trajectories and through which we can minimize the expression 4.13.

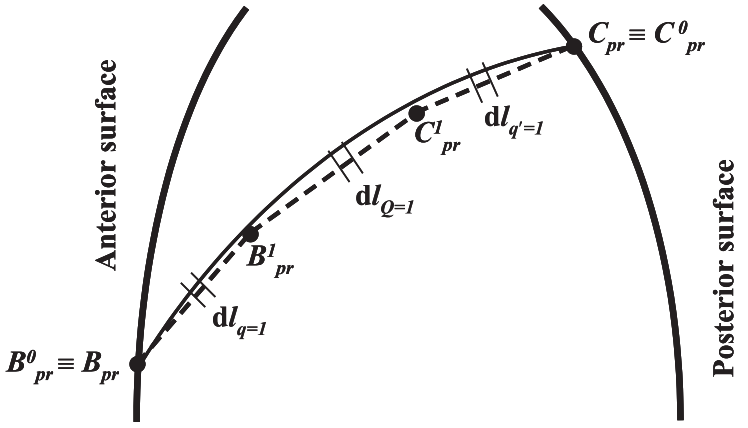

Figure 4.3: Interpolation of two points, B_{pr}^{1} and C_{pr}^{1}, in the iterative procedure to obtain an approximated trajectory (dashed line) to that of the actual ray (solid line) from B_{pr} and C_{pr}.

As new estimations of the gradient are calculated at each one of the iterations of the algorithm, we use the root mean square, *rms* , of the difference of the obtained gradients

at two consecutive iterations to evaluate the convergence of the iterative procedure. Thus, we say the algorithm converges when such a difference

- reaches a minimum,
- tends to a given value,
- or reaches a value (convergence tolerance) that is considered indicative of a good result, for instance, a value one order of magnitude lower than the accuracy we expect in the gradient retrieval.

Once the iterative procedure converges and retrieves a monopolynomial gradient index $n(x,z)$, this distribution must be used to assess the quality of the result in optical terms. This is due to the fact that in the description we have given so far of the tomographic algorithm there is not strictly speaking a merit function that provides an estimation of the difference between experimental measurements and the results obtained in a given iteration, what would be the case if we minimize directly the expression 4.13. In our case, we work with an approximation of that expression (see Eq. 4.16) and what we do is to compare the results obtained at two consecutive iterations. Therefore, from the numerical ray tracing and by using the experimental θ_p and B_{pr}, it is necessary to propagate the rays through the retrieved gradient $n(x,z)$ to obtain the corresponding distributions of the optical path $\hat{S}_p(x,t)$ at the plane $z=t$. Once added the retrieved piston K_p to the experimentally obtained distributions $\tilde{S}_p(x,t)$, we calculate the differences $\Delta S_p(x,t)$, that we define as

$$\Delta S_p(x,t) = \left[\tilde{S}_p(x,t) + K_p\right] - \hat{S}_p(x,t) \tag{4.18}$$

These differences show with which precision $n(x,z)$ reproduces the optical behaviour of the eye lens. Thus, if those differences are lower than the measurement error of $\tilde{S}_p(x,t)$, the tomographic algorithm can be halted at this point. Nevertheless, if those differences are larger or within the same order of magnitude than the error in $\tilde{S}_p(x,t)$, the result of the monopolynomial retrieval can be used to start a second stage in which a bipolynomial gradient index is considered.

From $n(x,z)$ an initial estimation of the plane $z=z_H$ can be obtained by calculating the position $z \in (0,t)$ where $n(0,z)$ reaches a global maximum (this is why a previous monopolynomial retrieval is needed before performing a bipolynomial one). Otherwise, the same iterative procedure previously described is applied again at this stage of the bipolynomial reconstruction. The only changes will be those that need to be carried out in equations 4.16 and 4.17 to take into account the existence of two refractive index distributions at both sides of z_H with their own coefficients n_{ij}^{ant} and n_{ij}^{pos} and the continuity

conditions set in 4.12. Besides, the length of the steps $\Delta\tau$ must be adjusted to ensure half of the interpolated points lie within each one of the segments of the lens delimited by z_H.

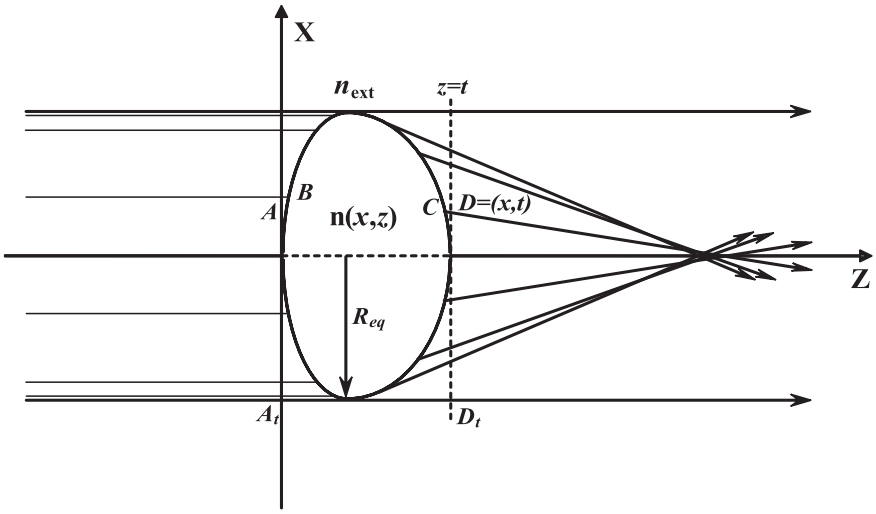

Figure 4.4: Sagittal plane of a lens illuminated by a set of rays on axis when the indices of the external medium and that of the lens surface are matched..

4.3.1 The piston K and its influence on the retrieval of the gradient coefficients

As we will see in this section, the lack of knowledge of the additive constant or piston K (see Eq. 4.5) force us to reconsider some relevant aspects of the application of classical tomographic techniques to the particular case of the reconstruction of the gradient index in crystalline lenses. To better understand this, firstly it is necessary to study the condition of matching between indices n_{ext} and $n\,(x,z)$ in the surface of the lens. Let us assume the ideal case of having matched both indices for a lens illuminated with a set of parallel rays on axis, $\theta = 0^{o}$ (see Fig. 4.4). At its exit there would be other continuous set of refracted rays from $x = R_{eq}$ up to $x = -R_{eq}$, where R_{eq} is the equatorial radius of the lens. The equation 4.5 could be then reformulated as

$$S\,(AD) = \int_{-R_{eq}}^{x} \sin\alpha\,(x,t)\,\mathrm{d}x + K, \tag{4.19}$$

where K would be in this case the optical path covered by the ray tangent to the inferior border of the lens that goes from $A_t = (-R_{eq}, 0)$ up to $D_t = (-R_{eq}, t)$, i.e. $K = tn_{ext}$. K would be so a known variable for each one of the projections and, from equation 4.8,

the optical paths $S(B_{pr}C_{pr})$ could be directly calculated. Unfortunately, this matching condition is extremely unlikely, not just because of the experimental difficulty to ensure it, but also because the surface of the lens may not have a constant index. This would give rise to two important problems regarding a classical tomographic reconstruction:

- For reasons of biocompatibility, the external indices we will work with are lower than the superficial index of the lens. As a result, when entering the lens the rays are refracted in a way the periphery of the lens is never illuminated (see Fig. 4.5). The area of this peripheral zone will depend on the magnitude of difference between the external and superficial indices. Since the classical mathematical formulation of tomography tackles the reconstruction from the possibility of sampling completely the distribution to retrieve [Her80, Ram96], the existence of this non sampled zone makes more difficult from the onset the reconstruction of the gradient. This fact, added to the discretization and limitation in the number of experimental measurements, makes more necessary to work with tomographic algorithm of modal reconstruction like the one proposed, which compensates the lack of tomographic information with a good model of the gradient index. It is important to point out that these "peripheral gaps of information" also affect to zonal reconstruction algorithms, like those used in ray deflectometry (see 2.2.1), where the index is reconstructed from the surface towards the center.

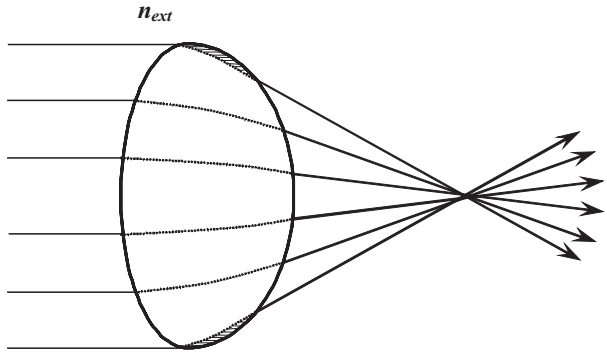

Figure 4.5: Sagittal plane of a crystalline lens illuminated by a set of rays on axis with an external index n_{ext} lower than the index of the lens surface. As a result of this difference, the periphery of the lens can not be scanned by any ray of light (striped zones).

- Studying the equation 4.5 it is noticed that the value of K for a given projection varies depending on the point of the plane $z = t$ that we choose as origin to

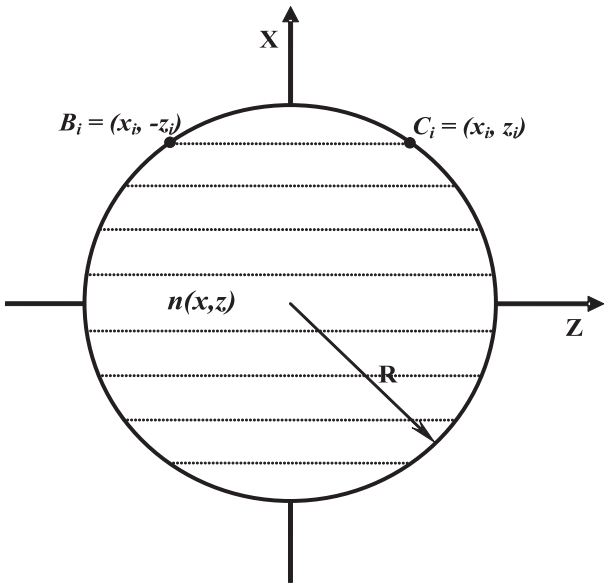

Figure 4.6: Surface of radius R with a refractive index distribution $n(x,z)$ where rays are propagated (solid lines).

integrate the sines of the angles of deflection. This raises the question of whether this can affect and how to the unicity of the set of coefficients that we retrieve tomographically. In order to illustrate this issue we will consider the particular case of a circular surface with a distribution $n(x,z)$, where we approximate the trajectory of the rays as straight lines (see Fig. 4.6). For each one of those rays the optical path, but the piston, that they accumulate from the entry point $B_i = (x_i, -z_i)$ up to the exit one $C_i = (x_i, z_i)$ can be written as

$$\tilde{S}(B_iC_i) = \int_{-\sqrt{R^2-x_i^2}}^{\sqrt{R^2-x_i^2}} n(x,z)\,\mathrm{d}z - K = \int_{-\sqrt{R^2-x_i^2}}^{\sqrt{R^2-x_i^2}} [n(x,z) - g(x,z)]\,\mathrm{d}z, \quad (4.20)$$

where R is the radius of the surface and $g(x,z)$ a function that satisfies

$$\int_{-\sqrt{R^2-x^2}}^{\sqrt{R^2-x^2}} g(x,z)\,\mathrm{d}z = K \qquad \forall x \in [0,R] \quad (4.21)$$

Taking into account the properties of the line integrations in circular domains [Cor64], it can be shown that for this case $g(x,z)$ has the following form

$$g(x,z) = \frac{K}{\sqrt{R^2 - x^2 - z^2}}, \quad (4.22)$$

that is no longer analytical in the circular domain in $x^2 + z^2 = R^2$. For the most general case of rotationally symmetrical geometries and realistic ray tracings is obvious that $g(x, z)$ will have other functional form, much more complex and that in the case of applying tomographic transform algorithms would be necessary to know. However, it is also obvious that, whatever the form, it will maintain its non analytical nature, since it is the only way of satisfying a condition like that of the equation 4.21, i.e. that regardless of how small is the path over which $g(x, z)$ is integrated, the result has to be constant. This very fact, the non analyticity of $g(x, z)$, makes possible to include directly K in the least squares fitting and calculate it along with the modal coefficients of $n(x, z)$ without affecting its unicity, since there is no linear combination of powers in x and z that can contribute to the value of the piston, avoiding so the singularity of the fitting inversion matrix too. In other words, the non existence of a refractive index with a functional dependence like that of equation 4.22 makes possible that the retrieval of the piston does not affect that of the gradient index.

4.4 Logical sequence of the tomographic algorithm

Next, each one of the steps that make up the tomographic algorithm and its logical sequence are explained in order to provide a clear and concise idea of how to implement the algorithm. To do so, we use flow charts, one for the monopolynomial reconstruction and other for the bipolynomial one.

4.4.1 Monopolynomial reconstruction

Each one of the following points explains one of the steps of the flow chart of figure 4.7:

- INPUT DATA : these are the data provided by the deflectometry ray technique for P projections and N_p rays per projection: θ_p, B_{pr}, C_{pr} and $\sin\alpha_{pr}(x, t)$ ($p = 1, \ldots, P$ and $r = 1, \ldots, N_p$).

- PROCESS 1 (Optical path calculation, but K_p) : by using the data obtained by deflectometry and the equations 4.5 and 4.10, the set of values $\tilde{S}(B_{pr}C_{pr})$ is calculated.

- PROCESS 2 (Monopolynomial GRIN retrieval - commencement of the iterative procedure) : with the calculated values of $\tilde{S}(B_{pr}C_{pr})$, the equation 4.16 is minimized to

obtain the coefficients n_{ij} and the pistons K_p, by assuming $2Q$ interpolated points (see Eq. 4.17).

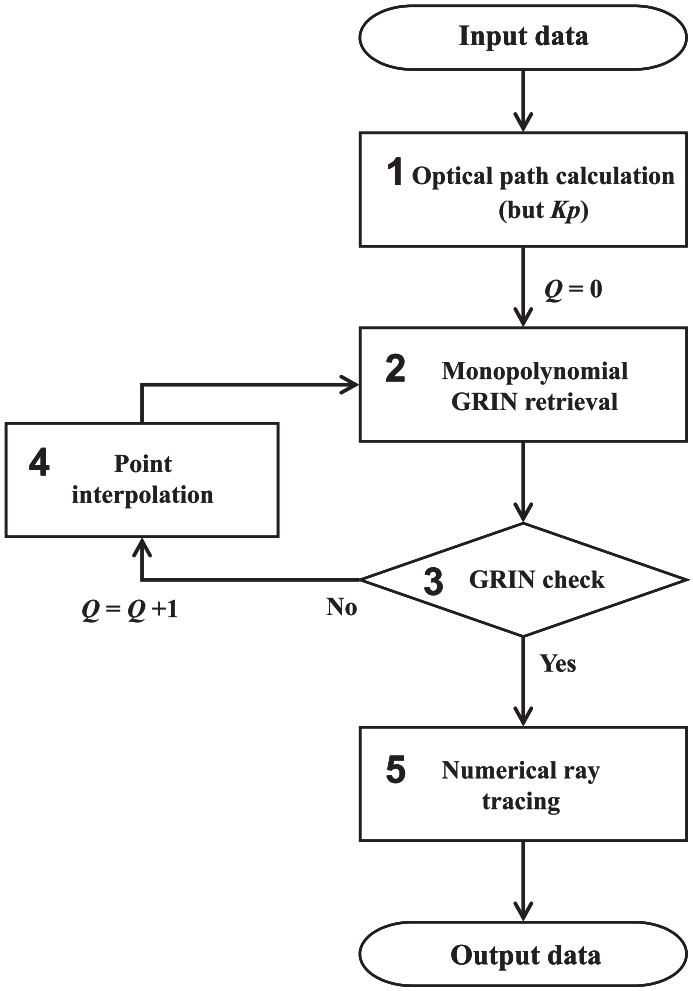

Figure 4.7: Flow chart of the tomographic algorithm for the monopolynomial reconstruction of the gradient index.

- PROCESS 3 (GRIN check) : This calculates the *rms* of the difference between the refractive index distribution retrieved at the current iteration, $n^Q(x,z)$, and the preceding one, $n^{Q-1}(x,z)$ and compares it with the previous values of the *rms*. If the evolution of this magnitude does not meet any of the conditions set in section 4.3, another iteration $Q = Q + 1$ starts by performing PROCESS 4. In this case, the algorithm ends the iterative procedure and goes on to PROCESS 5. For the first two iterations, this check is inactive.

- PROCESS 4 (Point interpolation) : the core of the iterative procedure, making use of the Sharma *et al.*'s ray tracing algorithm to interpolate $2Q$ points for each ray by using the refractive index distribution previously retrieved and incremental steps as expressed in equation 4.15.

- PROCESS 5 (Numerical ray tracing) : to obtain the optical path differences $\Delta S_p(x,t)$ from which we can infer how accurately the retrieved function $n(x,z)$ reproduces the experimental optical data and decide whether to refine the result with a bipolynomial reconstruction. For this reason the incremental step of this ray tracing must be small enough to reproduce the optical behaviour of the lens with an accuracy equal or higher than the experimental errors in the measurement of the optical path distribution at the exit of the lens.

- OUTPUT DATA : consist of the retrieved monopolynomial gradient index $n(x,z)$ and the optical path differences $\Delta S_p(x,t)$.

4.4.2 Bipolynomial reconstruction

In the event that the monopolynomial retrieval does not provide a good result as defined previously, the tomographic algorithm could be improved with a second stage of the retrieval (see Fig. 4.8) in which a bipolynomial model of the gradient index is considered:

- INPUT DATA : the experimental points B_{pr} and C_{pr}, the set of values $\tilde{S}(B_{pr}C_{pr})$ and the $n(x,z)$ retrieved at the monopolynomial stage.

- PROCESS 6 (z_H calculation and point interpolation - commencement of the iterative procedure) : point interpolation is carried out as in PROCESS 4, but taking into account that half of the interpolated points fall into each of the lens segments, $(0, z_H)$ and (z_H, t) respectively. Two points for each ray are interpolated at the first iteration.

- PROCESS 7 (Bipolynomial GRIN retrieval) : the only difference in terms of the minimization performed at PROCESS 2 is that in equation 4.16 both the anterior and posterior proposed refractive index distributions, $n^{ant}(x,z)$ and $n^{pos}(x,z)$, must be included. Likewise, such a division must also be taken into account in the integrations of equation 4.17. As a result of the subsequent least squares fitting, coefficients n_{ij}^{ant} and n_{ij}^{pos} and pistons K_p are retrieved.

- PROCESSES 4 and 5 : they operate as in the monopolynomial retrieval.

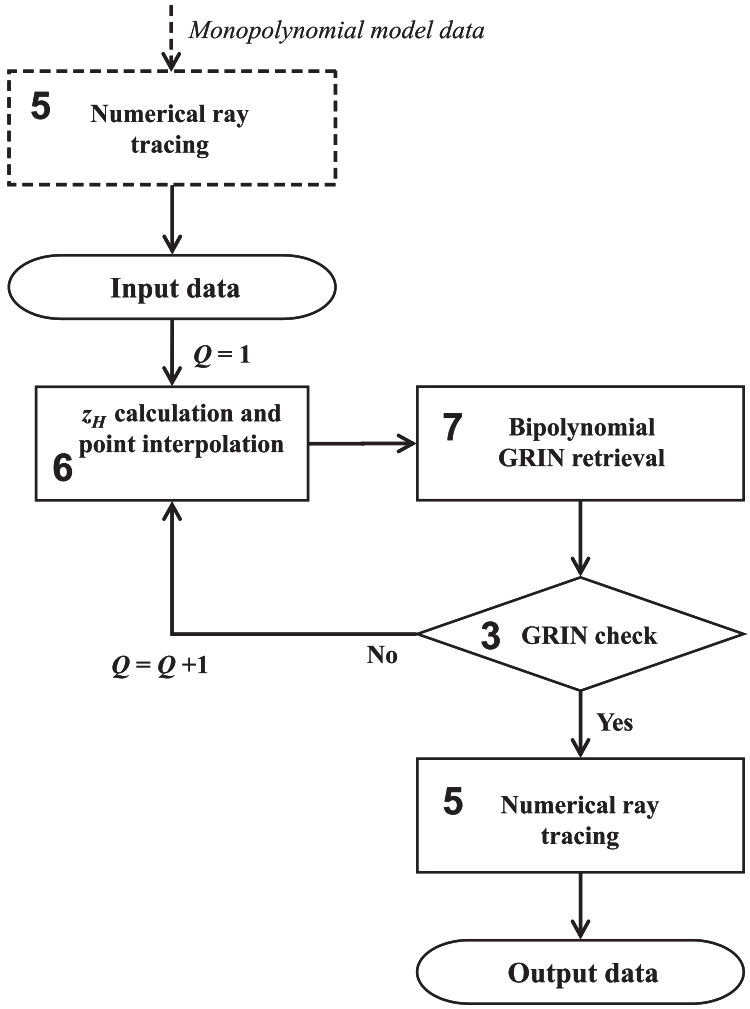

Figure 4.8: Flow chart of the tomographic algorithm for the bipolynomial reconstruction of the gradient index.

- OUTPUT DATA : they consist of the retrieved bipolynomial gradient index described by distributions $n^{ant}(x,z)$ and $n^{pos}(x,z)$ and the optical path differences $\Delta S_p(x,t)$.

Finally, a parameter that has not been discussed so far is order of the polynomial expansion of the refractive index distributions, M in the monopolynomial case and M^{ant} and M^{pos} in the bipolynomial one (see Eq. 4.11). The logical procedure we follow is to start running the tomographic algorithm with low orders and then try to refine the results with increasing order value, checking the significance of the added coefficients by means of an F-test [Bev92, pp. 205-209] of the tomographic inversion.

5 Numerical simulations of the tomographic algorithm

Once formulated the tomographic algorithm of reconstruction of the gradient index, the following step is to study the theoretical accuracy of this algorithm. In order to do so, it is necessary to previously analyze on which factors such an accuracy depends. This analysis and the deduction of a qualitative relationship between the magnitude of the experimental error and that of the retrieval accuracy will constitute the first part of this chapter. Next we will present and study the results of different numerical simulations for representative models of the gradient index in different types of lenses. With these numerical simulations we aim at quantifying the order of magnitude of the dependence of the accuracy of the algorithm regarding the formerly mentioned factors, by paying special attention to the propagation of experimental errors. Due to reasons we will explain later, we will distinguish two cases: the particular case of the reconstruction of spherically symmetrical gradient indices and the more general of gradients with non spherical rotational symmetry.

5.1 Accuracy of the tomographic algorithm

From the tomography basics explained in section 3.2 and the formulation of the tomographic algorithm of reconstruction of the gradient index (see chapter 4) we infer the existence of four factors that influence the accuracy of this algorithm:

1. Modal reconstruction of the gradient index : the approximation of the distribution of the actual refractive index as a given functional form involves a systematic error in the modal tomographic reconstruction of $n(x,z)$ (see section 3.2). This error is the main reason of the likely divergence between accuracy and precision in our tomographic retrieval of the gradient index [Bev92, p. 2]. This is why so important to use a model of the gradient general enough as that proposed in the equation 4.11, with the only constraints of the rotational symmetry and its analyticity in the area for which it is defined.

The chosen functional model can also affect the tomographic inversion described in section 4.3. Depending on the number of modal coefficients and on the order of its modes, the minimization of the expression 4.16 might be ill conditioned (close to singularity), mainly if the experimental tomographic data show a large error. For this reason the propagation of errors is especially sensitive to the order of the polynomial expansion used to model the gradient (see Eq. 4.11).

2. Approximation to the actual ray trajectories : as it was explained in section 4.3, there is not a previous knowledge of the actual ray trajectories inside the lens. Because of this, an iterative procedure has been implemented in the tomographic algorithm to approximate such trajectories as a finite series of straight line segments. Nevertheless, this procedure does not guarantee that we eventually obtain a good approximation of the actual trajectories. It is important that the first of the iterations, that where the trajectories are approximated as straight lines, provides an initial results that allows the approximation to become more exact at the following iterations. An outstanding role is played here by the strength of the gradient, which we had defined as a function of the curvature this gradient causes on the rays that propagate through the gradient (see section 4.3). The curvature of these trajectories is, in turn, function of the maximum variation of $n(x, z)$ within the lens and the maximum values reached by its first derivatives. Thus, the larger these values, the stronger the gradient and the more curved the ray trajectories, so that its approximation as straight lines will be less accurate. As a result, the iterative procedure can end up diverging or yielding an outcome without physical meaning.

3. Number and distribution of the tomographic data : like in any tomographic method, the larger and the more distributed the number of data, the more accurate will be the tomographic reconstruction. This is achieved by increasing:

   a) The number of rays and projections.
   b) The scanned area of the lens, that will depend on the illuminated section of the lens, on the relationship between the indices of the external medium and the surface of the lens and on the distribution of the projections.

4. Error or noise in the experimental tomographic data : the larger this error, the lower the accuracy of the reconstruction. Throughout this chapter we will quantify this effect for different cases by means of numerical simulations, since a linear propagation of errors is not possible due to the fact the trajectory of the rays depends on

the refractive index through coupled differential equations.

5.1.1 Qualitative estimation of the error in the tomographic retrieval

By assuming that the error in the tomographic retrieval of $n(x,z)$, ε_n, is due essentially to the experimental error, it is possible to obtain a qualitative estimation at first order of the error ε_n as a result of the error ε_{sin} in the measurement of the sines of the angles of deflection, $\sin\alpha_{pr}(x,t)$. To deduce this relationship between error in the index and error in the sine, we use as a starting point the equation 4.10. Thus, from this equation and by denoting σ_f the standard deviation of the least squares fitting through which the gradient and the pistons, $\hat{n}(x,z)$ and $\hat{K}_p$ (see Eq. 4.16), are retrieved

$$\left\langle \left[\left(\sum_{i=0}^{M} \sum_{j=0}^{2(M-i)} \hat{n}_{ij} f_{ijpr} - \hat{K}_p \right) - \tilde{S}(B_{pr}C_{pr}) \right]^2 \right\rangle \approx \sigma_f^2, \tag{5.1}$$

it can be stated that in the absence of experimental error

$$\sum_{i=1}^{2Q+1} \int_{B_{pr}}^{C_{pr}} \hat{n}(x,z)\,\mathrm{d}l_i \approx \tilde{S}(B_{pr}C_{pr}) + \hat{K}_p + \sigma_f, \tag{5.2}$$

being Q the final number of iterations needed to obtain $\hat{n}(x,z)$. By considering the experimental errors $\Delta\tilde{S}(B_{pr}C_{pr})$ and the relations $\hat{n}(x,z) = n(x,z) + \Delta n(x,z)$, where $\Delta n(x,z)$ denotes the error in the calculation of the gradient we try to retrieve, $n(x,z)$, the equation 5.2 can be written as

$$\sum_{i=1}^{2Q+1} \left[\int_{B_{pr}}^{C_{pr}} n(x,z)\,\mathrm{d}l_i + \int_{B_{pr}}^{C_{pr}} \Delta n(x,z)\,\mathrm{d}l_i \right] \approx \tilde{S}(B_{pr}C_{pr}) + \Delta\tilde{S}(B_{pr}C_{pr}) + \hat{K}_p + \sigma_f \tag{5.3}$$

By assuming that the approximation of the ray trajectories as a series of straight line segments allows to state that

$$\sum_{i=1}^{2Q+1} \int_{B_{pr}}^{C_{pr}} n(x,z)\,\mathrm{d}l_i \approx \tilde{S}(B_{pr}C_{pr}) + \hat{K}_p, \tag{5.4}$$

then we get

$$\sum_{i=1}^{2Q+1} \int_{B_{pr}}^{C_{pr}} \Delta n(x,z)\,\mathrm{d}l_i \approx \Delta\tilde{S}(B_{pr}C_{pr}) + \sigma_f \tag{5.5}$$

Besides, if it is assumed that $\Delta n\,(x,z)$ and $\Delta\tilde{S}\,(B_{pr}C_{pr})$ do not vary substantially along the integration domain, i.e. $\Delta n\,(x,z) \approx \varepsilon_n$ and $\Delta\tilde{S}\,(B_{pr}C_{pr}) \approx \varepsilon_{\tilde{S}}$, the following estimation of ε_n can be provided:

$$\varepsilon_n \sim \frac{\varepsilon_{\tilde{S}} + \sigma_f}{t}, \tag{5.6}$$

where t is the thickness of the lens.

On the other hand, the error in the measurement of the optical paths, $\varepsilon_{\tilde{S}}$, and the error in the measurement of the sines of the angle of deflection, ε_{sin} , can be related from the equation 4.5, so that it can written that

$$\varepsilon_{\tilde{S}} \sim n_{ext}\varepsilon_{sin}R_{eq}, \tag{5.7}$$

where R_{eq} is the equatorial radius of the lens. By replacing this expression in 5.6 the qualitative relation between ε_n and ε_{sen} is finally obtained:

$$\varepsilon_n \sim \frac{n_{ext}\varepsilon_{sin}R_{eq} + \sigma_f}{t} \tag{5.8}$$

From this equation 5.8 and the numerical simulations that we will show next, we want to do something that we have not usually found in literature: to justify the provided accuracy of the retrieved gradient indices and to relate it with the errors of the experimental data.

5.2 Numerical simulations of reconstruction of gradients with spherical symmetry

The crystalline lenses of teleost fish, the most common one [Wik], are generally approximated as lenses of spherical symmetric gradient [Fer90, Siv90, Jag92]. This means that, under this assumption, any of its meridional planes shows a gradient index with a radial symmetry $n\,(r)$ and a functional form that can be written as a particular case of the equation 4.11:

$$n\,(r) = n_0 + n_1r^2 + n_2r^4 + \ldots = \sum_{i=0}^{M} n_ir^{2i}, \tag{5.9}$$

where $r = \sqrt{x^2+z^2}$ is the radial coordinate. This fact alone should not be enough to justify the performance of some specific numerical simulations. Any result obtained for eye lenses with a gradient with generic rotational symmetry $n\,(x,z)$ could be extrapolated

to the particular case of spherical symmetry. Nevertheless, there is a specific feature in the eye lenses that indeed justifies a particular study for this case: the variation of the refractive index between the nucleus and the surface of the lens. Whereas in the case of the teleost fish this variation, quite constant in all species and sizes, is about 0.16-0.21 [Axe88, Jag92, Kro94, Kro01, Gar01], for the human case the larger of the measured variations has been about 0.07 [Mof02a]. As it was explained in section 1.5 the fish lenses need to be much more powerful that those of the vertebrates, what explains such a large variation of the index as well as its geometry.

For the numerical simulations we have used as models of gradients those obtained in literature for different species and with different methods [Axe88, Kro94, Gar01]. However, in this work we show the results of just one of them, illustrative enough of the others: the gradient index retrieved by using optimization algorithms and ray deflectometry for the *Allocytus Niger* [Gar01]. This gradient is described by the coefficients of table 5.1 (see Eq. 5.9), defined for a radius R of the lens normalized to unity. Given the spherical symmetry, for the reconstruction of this type of gradients just one projection is needed. By using a numerical ray tracing [Sha82] we obtain at the exit of the lens the optical path distribution corresponding to one projection for a variable number of rays, $S(B_rC_r)$. In order to simulate the lack of knowledge of the piston in the experimental data we add to the distribution $S(B_rC_r)$ an arbitrary constant value $K = 6$, obtaining $\tilde{S}(B_rC_r)$ (the use of other values of K, both positive and negative, does not modify the results obtained in the numerical simulations). Regarding the refractive index of the external medium, n_{ext}, we choose that of a 0.9% sodium chloride solution (physiological saline solution) for $\lambda = 633$ nm at 22 °C, $n_{ext} = 1.3332$.

n_0	n_1	n_2	n_3	n_s
1.543	-0.121	-0.033	-0.021	1.368

Table 5.1: Coefficients n_i of the *Allocytus Niger* lens gradient index, as well as its superficial index n_s.

Without adding any noise in the input data $\tilde{S}(B_rC_r)$, we first check the influence of the number of rays in the tomographic retrieval. Thus, we retrieve the gradient index for a variable number of parallel rays equally spaced in an entrance aperture of the 99% of the lens diameter. The accuracy of the retrieval is measured by using the peak-valley difference between the retrieved an the theoretical index, $PV_{\Delta n}$, and the root mean square of such a difference, $rms_{\Delta n}$. These data are given in table 5.2 for 25, 50, 100 and 200 incoming rays. For all cases the results are practically the same. The convergence in

the iterative procedure used to approximate the ray trajectories is essentially identical too. In absence of experimental noise and by assuming that the approximation of the trajectories is reasonably good, no many rays are needed to retrieve with an almost negligible error a gradient index like the one used. Thus, the order of magnitude of the final error is 10^5 times lower than the variation of the index from the nucleus to the surface.

	25 rays	**50 rays**	**100 rays**	**200 rays**
$\mathbf{rms_{\Delta n}}$	6.0×10^{-7}	6.1×10^{-7}	6.3×10^{-7}	6.2×10^{-7}
$\mathbf{PV_{\Delta n}}$	1.5×10^{-6}	1.7×10^{-6}	1.7×10^{-6}	1.7×10^{-6}

Table 5.2: Precision of the retrieval of the *Allocytus Niger* lens gradient index for a different number of rays.

Once set the external index, the tomographed area depends on the aperture used for the incoming set of rays . In figure 5.1 it is shown the result of the retrieval of the gradient index for 50 rays and three different apertures: 99%, 90% and 80% of the lens diameter. As it can be seen, as this aperture decreases, the accuracy decreases too, mainly at the lens periphery. This is related with what has been mentioned in section 4.3.1 about the nature of piston K and the associate non analytical function $g(x, z)$. The smaller the aperture, the lower the accuracy of the retrieval, above all in the higher order terms, and the higher the possibility the piston K that has not been properly calculated affects such a retrieval with a non analytical component that makes the accuracy to diverge at the lens periphery. Even so, it must be noticed that the accuracy of the retrieval is higher than the fourth decimal digit of the index for apertures larger than the 60% of the lens diameter.

As it has been previously mentioned, the gradient of the lens of the *Allocytus Niger* is very similar to that obtained in other species of teleost fish lenses and with other methods. Nevertheless, we want to check that the tomographic algorithm is useful and accurate for a widest possible range of hypothetical fish gradients. In order to produce alternative but physiological plausible models of gradients it must be taken into account that:

- The values retrieved for $n(r)$ at $r = 0$ and $r = R$ are quite constant for different species and reconstruction methods: the valued of $n(0)$ is around 1.54-1.57 and that of $n(R)$ around 1.36-1.38 for $\lambda = 633$ nm [Axe88, Jag92, Kro94, Kro01, Gar01]. Since the protein concentrations and other metabolic conditions of the most

external and internal cells of the lens can be supposed to be constant throughout life, the values of $n(r)$ at $r = 0$ and $r = R$ can also be supposed not to vary over that time.

- As it is inferred from what has been explained in the first chapter, $n(r)$ is a monotonically decreasing function, due to the gradual increase of the protein concentration towards the center of the lens.

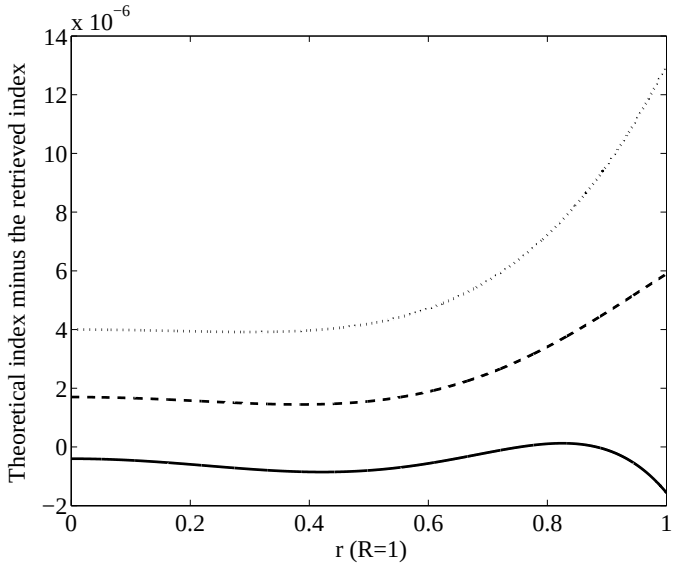

Figure 5.1: Accuracy of the retrieval of the gradient index of the *Allocytus Niger* lens for three different apertures: 99% of the lens diameter (solid line), 90% (dashed line) and 80% (dotted line).

Therefore, the main difference among the possible gradients that could be found in the fish lenses would be the strength of the gradient. According tho this fact, we produce two models of the gradient alternative to that of the *Allocytus Niger*, that we will label $n^{\mathrm{A}}(r)$ and that would represent the gradients retrieved so far. By keeping constant the values of $n^{\mathrm{A}}(r)$ at the extremes, $n^{\mathrm{A}}(0) = 1.543$ and $n^{\mathrm{A}}(R) = 1.368$, we modify the variation of the refractive index in between and generate $n^{\mathrm{B}}(r)$ and $n^{\mathrm{C}}(r)$ (see Fig. 5.2). A first consequence of the increase of the strength of the gradient in the tomographic retrieval is a clear worsening at the first estimation of the gradient, where rays are approximated as straight lines. Indeed, for $n^{\mathrm{C}}(r)$ this estimation is so bad that the iterative procedure ends up diverging. The cause of this divergence is the retrieval of refractive index distributions with superficial values lower than n_{ext}. For this reason, we repeat the retrievals by implementing in the tomographic algorithm the

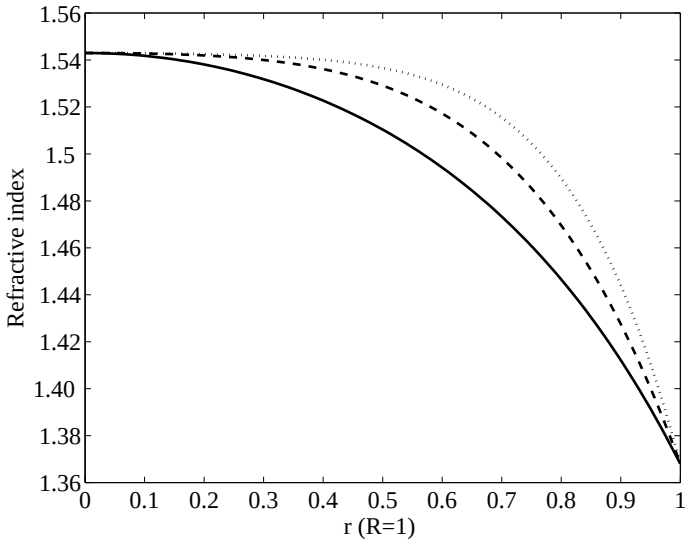

Figure 5.2: Refractive indices $n^{\mathrm{A}}(r)$ (solid line), $n^{\mathrm{B}}(r)$ (dashed line) and $n^{\mathrm{C}}(r)$ (dotted line).

following condition: to assume a superficial index $n(R) = 1.34$, a bit higher than n_{ext}, for the calculation of the rays refraction at the lens surface when at a given iteration a $n(R) < n_{ext}$ is obtained. The result of the retrievals is shown in figures 5.3 and 5.4, where it can be seen how the parameters $rms_{\Delta n}$ and $PV_{\Delta n}$ evolve in 50 iterations of the tomographic retrieval of $n^{\mathrm{A}}(r)$, $n^{\mathrm{B}}(r)$ and $n^{\mathrm{C}}(r)$ for 50 incoming rays with an aperture of the 90% of the lens diameter. In each one of the cases the algorithm converge more or less rapidly and it even starts to oscillate from a given iteration, like in $n^{\mathrm{C}}(r)$, but in all of them the accuracy achieved in the retrieval of the gradient index is above the fourth decimal digit (it has yet to be pointed out that the algorithm never converges to zero error because of the approximations we have assumed in the retrieval). This accuracy shows how versatile is the algorithm for a wide range of possible gradients.

When the optical behaviour of the gradients $n^{\mathrm{A}}(r)$, $n^{\mathrm{B}}(r)$ and $n^{\mathrm{C}}(r)$ is studied, it is noticed that the latter is very unlikely to occur in a fish lens. In figure 5.5 the posterior vertex distance dc_p [1], a representative magnitude of the longitudinal spherical aberration, is shown for rays entering the lens at different heights. According to literature [Fer90, Siv90], the low spherical aberration is a feature of the fish lenses, in addition to have values of dc_p comprised between 1.2 and 1.8 ($R = 1$). Hence, due to the non optical plausibility of $n^{\mathrm{C}}(r)$ or any other stronger gradient, we can *a priori* guarantee

[1] We define the posterior vertex distance as the distance between the point of intersection of each exit ray with the optical axis and the posterior vertex of the lens.

the convergence of the tomographic algorithm for the reconstruction of the gradient index in teleost fish lenses.

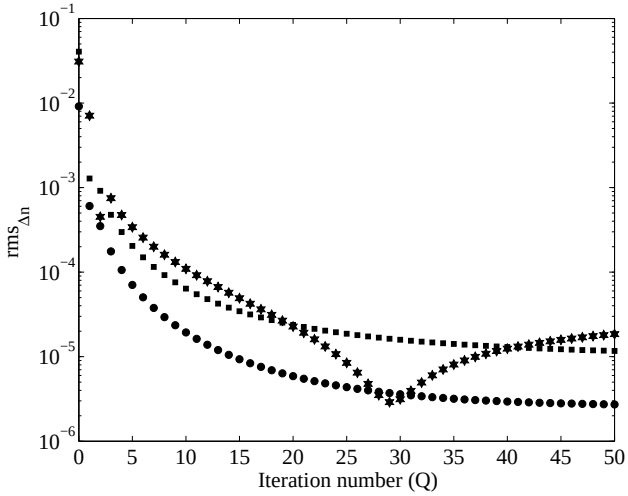

Figure 5.3: Evolution of $rms_{\Delta n}$ for 50 iterations in the tomographic retrieval of the gradients $n^{\mathrm{A}}(r)$(circles), $n^{\mathrm{B}}(r)$ (squares) and $n^{\mathrm{C}}(r)$ (stars).

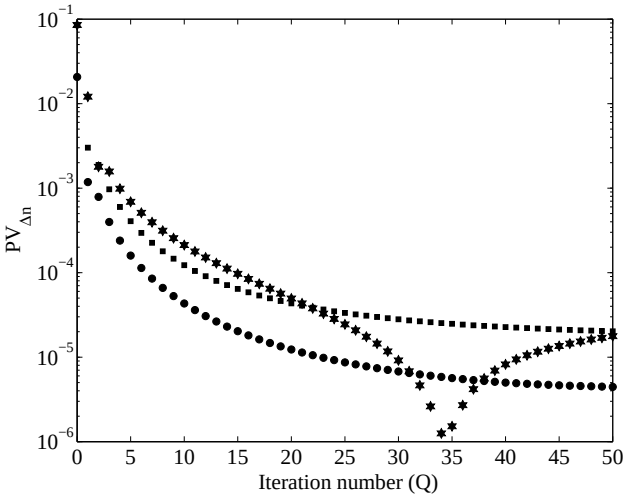

Figure 5.4: Evolution of $PV_{\Delta n}$ for 50 iterations of the tomographic retrieval of the gradients $n^{\mathrm{A}}(r)$(circles), $n^{\mathrm{B}}(r)$ (squares) and $n^{\mathrm{C}}(r)$ (stars).

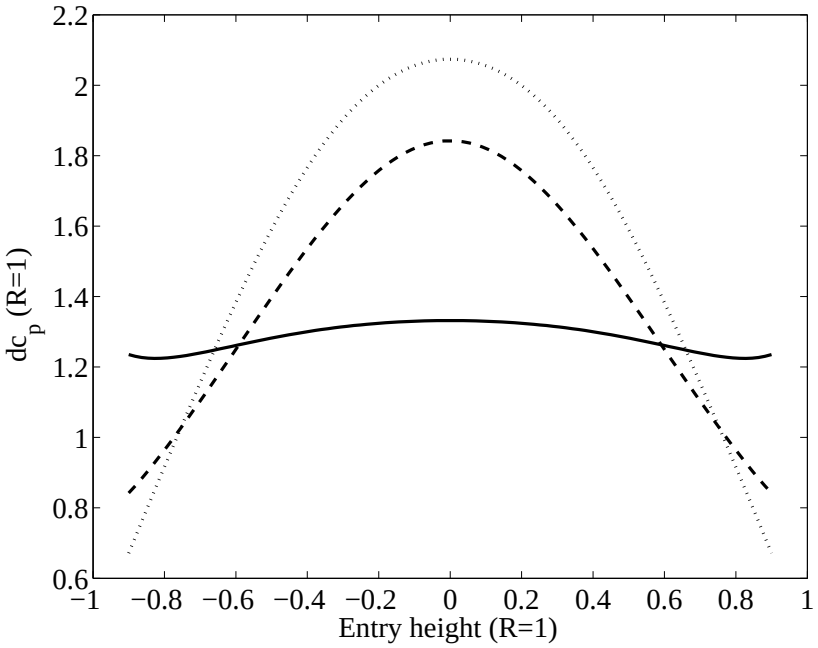

Figure 5.5: Posterior vertex distance dc_p for rays entering the lens at different heights and the following refractive index distributions: $n^{\mathrm{A}}(r)$ (solid line), $n^{\mathrm{B}}(r)$ (dashed line) and $n^{\mathrm{C}}(r)$ (dotted line).

Next, we will analyze the whole effect on the tomographic retrieval of the following three factors:

1. A Gaussian error added to the sines of deflection $\sin\alpha_{pr}(x,t)$ with zero mean and a standard deviation σ_{sin} with values 1×10^{-5}, 1×10^{-4} and 1×10^{-3} to simulate the experimental error ε_{sin} (we propagate this error in the sines of deflection to the points of intersection of the exit rays with the lens, C_{pr}). As we will see in the next chapter, the order of magnitude of the experimental error in the measurement of the sines of deflection will be around 1×10^{-3}. This is why we have chosen this value as maximum value of σ_{sin}, analyzing too which will be the outcome if we were able to reduce this error in one or two orders of magnitude.

2. Different number of rays: 100 and 500 incident rays equally spaced within an aperture of the 90% of the lens diameter.

3. Different strength of the gradient: we consider the distributions $n^{\mathrm{A}}(r)$ and $n^{\mathrm{B}}(r)$.

For each combination of factors the tomographic algorithm has been simulated 2000 times, a number that has been proved enough to ensure the convergence of the statistic

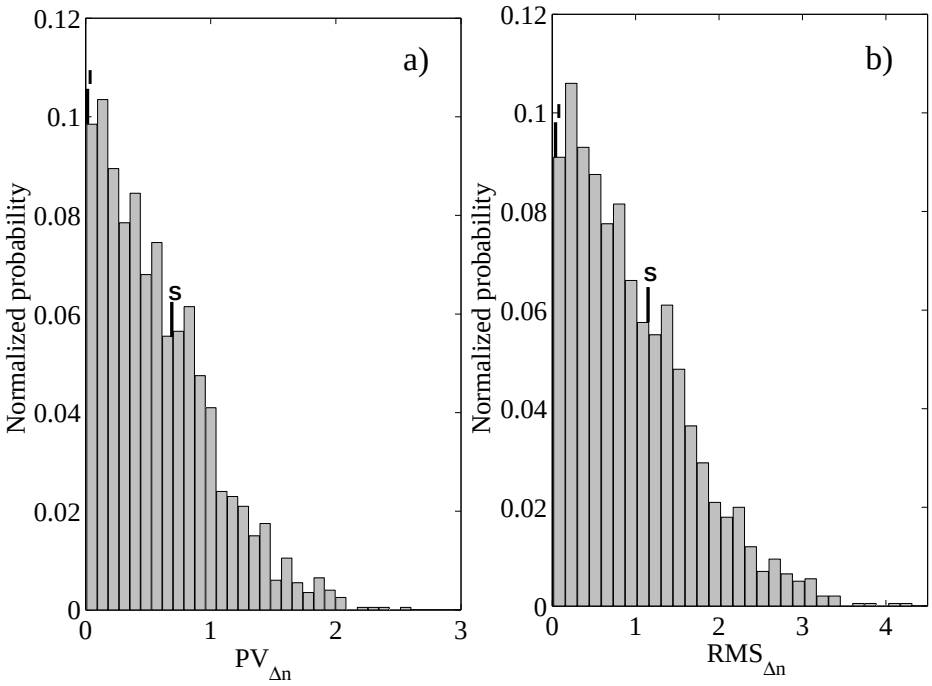

Figure 5.6: Distributions of normalized probability of the peak-valley (a) and *rms* (b) difference between the retrieved and theoretical gradient indices for the particular case of $n^{\mathrm{A}}(r)$ with an error of $\sigma_{sin} = 1 \times 10^{-3}$ and 500 incident rays. Upper (S) and lower (I) bounds define an interval that includes approximately 68% of the cases around the mode.

results. This results consist of the $PV_{\Delta n}$ and $rms_{\Delta n}$ distributions that correspond to each case. Given the asymmetry of these distributions (see Fig. 5.6), instead of their mean and standard deviation we found it to be more representative to provide the mode and the extremes of the interval that include approximately the 68% of the cases about the mode (see Figs. 5.7 and 5.8). From the analysis of the results it can be inferred that:

1. As the error increases, the accuracy of the tomographic algorithm for the distributions $n^{\mathrm{A}}(r)$ and $n^{\mathrm{B}}(r)$ becomes more similar, with an order of magnitude of the third decimal digit in the worst of cases represented. Due to the formerly explained representativeness of $n^{\mathrm{A}}(r)$ and $n^{\mathrm{B}}(r)$, this result can be extended to very wide range of likely gradients of teleost fish lenses.

2. The number of rays has a relatively small influence in the value of the obtained modes, although it contributes to shift the distributions towards lower values of $PV_{\Delta n}$ and $rms_{\Delta n}$.

3. The relationship that can be noticed in figure 5.7 between $rms_{\Delta n}$ and σ_{sin} seems to confirm that deduced for ε_n and ε_{sin} in the expression 5.8. Thus, for an added error of $\sigma_{sin} = 1 \times 10^{-3}$ we have that $\sigma_f \sim 10^{-4}$ both for $n^{\mathrm{A}}(r)$ as for $n^{\mathrm{B}}(r)$, from what an average estimated error in the index of $\varepsilon_n \sim 7 \times 10^{-4}$ is obtained ($R = 1$ and $t = 2$), not very different to the modes achieved for the corresponding cases.

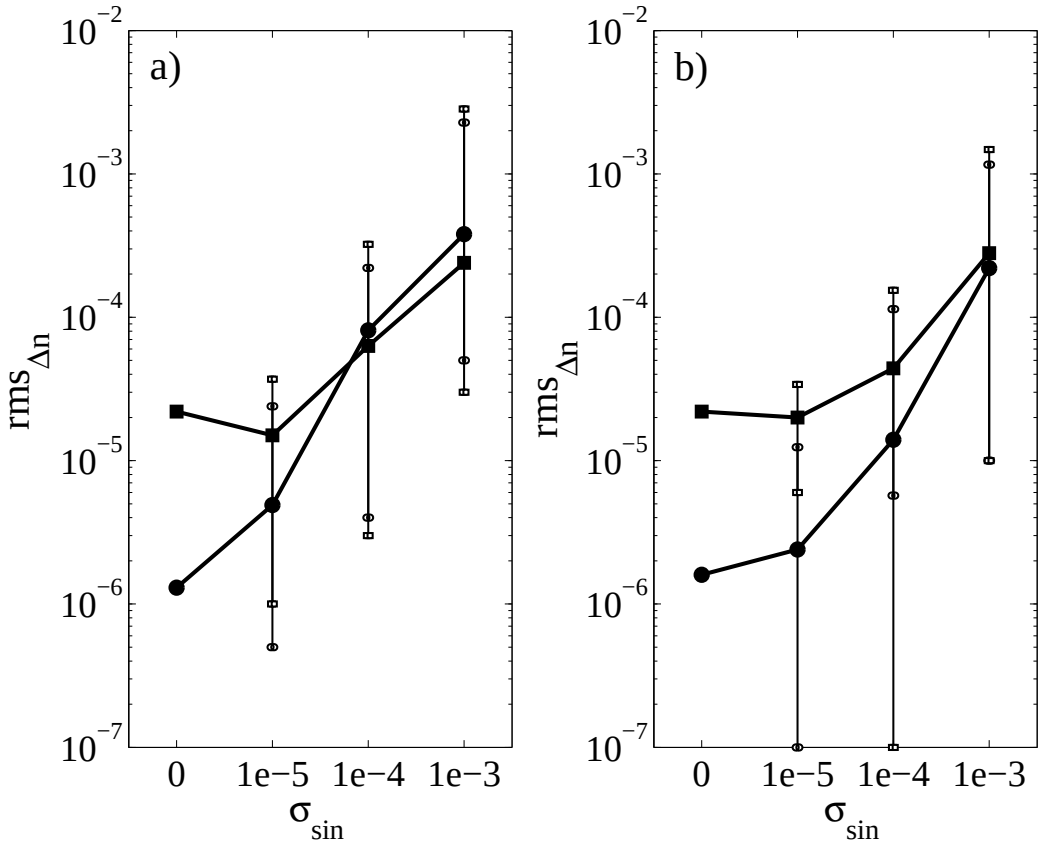

Figure 5.7: Root mean square of the difference between the retrieved and theoretical gradient indices for 100 (a) and 500 (b) incident rays and errors of different magnitude in the sines of deflection. The results are shown for the distributions $n^{\mathrm{A}}(r)$ (circles) and $n^{\mathrm{B}}(r)$ (squares).

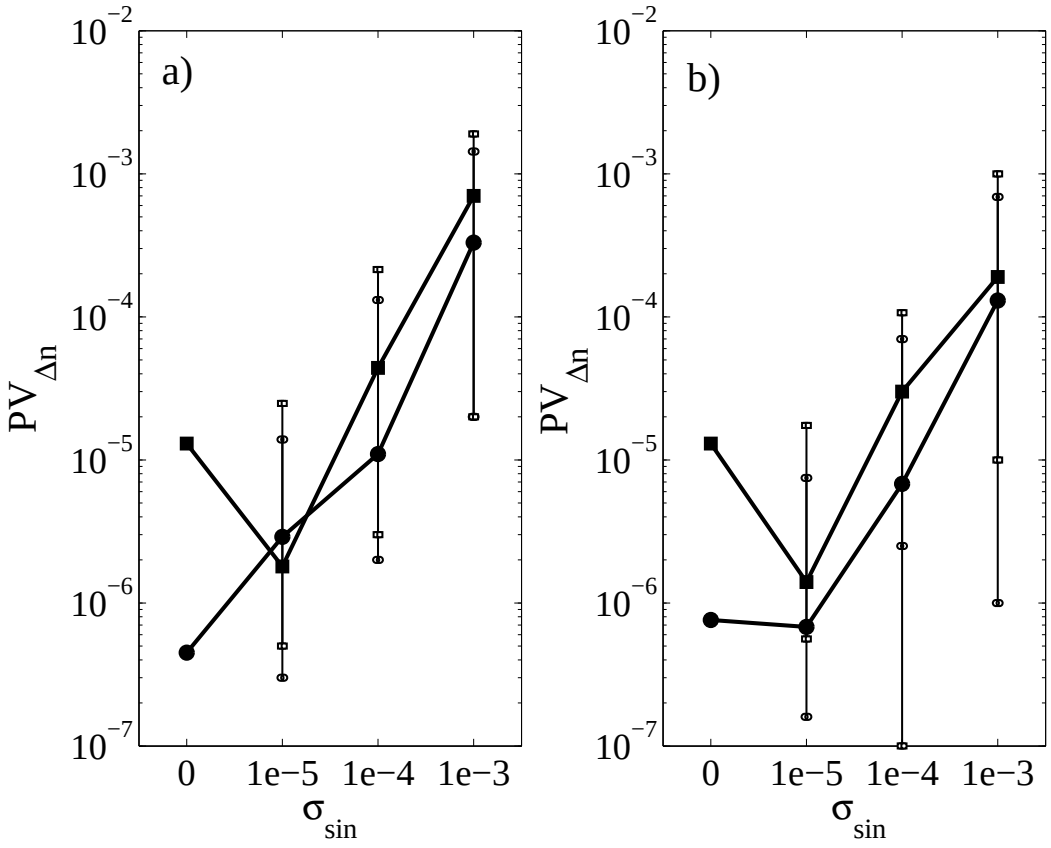

Figure 5.8: Peak-valley difference between the retrieved and theoretical gradient indices for 100 (a) and 500 (b) incident rays and errors of different magnitude in the sines of deflection. The results are shown for the distributions $n^{\mathrm{A}}(r)$ (circles) and $n^{\mathrm{B}}(r)$ (squares).

5.3 Numerical simulations in gradient indices with non spherical rotational symmetry

In this section we will tackle the more general case of lenses with non spherical rotational symmetry. Most of the terrestrial vertebrates have lenses that show a larger or lower deviation regarding the spherical geometry, with an anteroposterior axis shorter than the equatorial diameter of the lens. This geometric modification has an equivalent effect on the refractive index distribution, for reasons already mentioned in the first chapter of this work. A representative lens of this more general symmetry is that of the human being. For this reason and for being the lens with more abundant data in literature, it is the lens we use in the numerical simulations we will show throughout this section.

However, it is important to point out that the obtained results, along with those shown for the fish lenses, can be extrapolated to any other vertebrate lens that has the mentioned symmetries.

In section 5.2 we check that the accuracy of the tomographic algorithm, specially the iterative procedure of approximation to the actual ray trajectories, depends on the analyzed strength of the gradient. From the existing data in literature it is difficult to assign a profile to the derivatives of the index in the human lenses. This difficulty is even more if we take into account that the lens substantially modifies its geometry and hence its gradient in the process of accommodation. In order to ensuring the accuracy and functionality of the algorithm, we have carried out the numerical simulations by considering two models of the gradient index, one weak and other strong, that represented the extremes of the range of plausible refractive index distributions in the human lens.

The weakest gradient index referred to in literature is that proposed by Gullstrand [Gul09] in 1909 for the accommodated lens (see Fig. 5.9). The calculation of this gradient was based on the measurements of the refractive index at the poles, nucleus and equator of the lens, the anterior and posterior vertex radii of curvature ($R_{ant} = -R_{pos} = 5.333$ mm) and the power of the lens. With a thickness of $t = 4$ mm, both the anterior and posterior surfaces are assumed to be spherical, and while this is now known to be inaccurate, it does not affect the aim of these simulations. As for the refractive index distribution proposed by Gullstrand, its corresponding coefficients n_{ij} (see Eq. 4.11) for a coordinate system centered at the anterior vertex of the lens are shown in table 5.3.

Regarding the strong gradient, we produced our own model using data from the two sources:

- Gradient index data were extracted from the magnetic resonance imaging measurements made by Moffat *et al.* [Mof02b] (see section 2.3), as some of their subjects had the strongest gradient index reported in literature. However, for the geometrical data related to the lens shape we needed another reference since that paper showed only paraxial parameters.

- Geometrical data were extracted from the work carried out by Koretz *et al.* [Kor02]. The thickness of the lens and the shapes of the anterior and posterior surfaces up to height of $x = \pm 4$ mm were obtained. Assuming that in moving from the accommodated to the unaccommodated state there is only a renormalization of the refractive index distribution to the new dimensions of the lens, and therefore the unaccommodated lens would have a stronger gradient index, we decided to use the geometrical data referring to the unaccommodated state. For that case, the anterior

and posterior surfaces are described by the following parabolas, respectively:

$$z = 0.027x^2 \tag{5.10}$$

$$z = -0.064x^2 + 3.47 \tag{5.11}$$

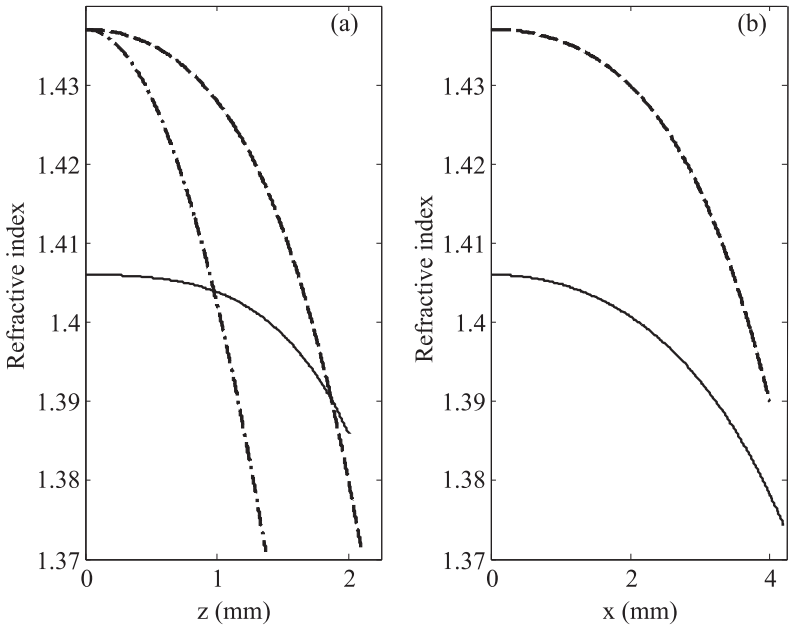

Figure 5.9: (a) Profile at $x = 0$ of the weak (solid line) and strong (dashed-dotted for the anterior segment, dashed for the posterior) gradient indices, where z shows the distance from z_H to the periphery. (b) Profile at z_H of the weak (solid line) and strong (dashed line) gradient indices.

With regard to the proportions of the anterior and posterior segments of the lens, we decided to place such a division in $z_H = 1.37$ mm, approximately a 40% of the lens thickness, $t = 3.47$ mm, and then fit the refractive index values of each segment as described in the reference [Mof02b] into a fourth-order polynomial (see Eq. 4.11 and conditions of continuity 4.12). The coefficients n_{ij} of each segment for a coordinate system centered at the anterior vertex of the lens are shown in table 5.3.

Since we showed previously the effect of the number of rays and the tomographed area on the tomographic retrieval without added experimental noise, it is not necessary to show equivalent simulations for the proposed models of human gradient. We proceed,

Coefficients	Weak Gradient	Strong Gradient Anterior	Strong Gradient Posterior
n_{00}	1.386	1.371	1.4171
n_{01}	3.4994×10^{-2}	9.9541×10^{-2}	3.7893×10^{-2}
n_{02}	-2.3742×10^{-2}	-4.0986×10^{-2}	-2.6831×10^{-2}
n_{03}	7.4969×10^{-3}	3.3996×10^{-3}	9.4904×10^{-3}
n_{04}	-9.3711×10^{-4}	-6.2037×10^{-4}	-1.7318×10^{-3}
n_{10}	-3.2806×10^{-3}	-2.2983×10^{-3}	-2.9183×10^{-3}
n_{11}	2.1085×10^{-3}	1.3492×10^{-3}	2.2543×10^{-3}
n_{12}	-5.2712×10^{-4}	-4.9241×10^{-4}	-8.2272×10^{-4}
n_{13}	-3.4996×10^{-5}	-9.7711×10^{-5}	-9.7711×10^{-5}

Table 5.3: Coefficients n_{ij} of the weak (monopolynomial) and strong (bipolynomial) gradients for fourth-order polynomials.

thus, to analyze the outcome of the application of the tomographic algorithm to the data obtained for three projections (0^o, 20^o y 40^o) on each one of the models, considering an aperture of 90% of the diameter of the lens and 100 incoming rays equally spaced within the aperture diameter. Like in the previous simulations, the input data were the optical paths covered by the rays inside the lens $S\left(B_{pr}C_{pr}\right)$ as calculated with the Sharma *et al.*'s algorithm [Sha82] plus a randomly chosen constant K_p for each projection.

In figure 5.10 the evolution of $rms_{\Delta n}$ for the tomographic retrieval of the weak and strong gradients is shown. In the first case, only the monopolynomial phase of the retrieval was applied. It can be observed that because of its weak gradient the algorithm converges much faster and with greater accuracy than in the case of the strong gradient. Thus, with just six interpolated points its $rms_{\Delta n}$ is lower than 1×10^{-5}. For the strong gradient, both monopolynomial and bipolynomial phases of the tomographic retrieval need to be applied. In the first phase the algorithm converges very fast. However, once reached a solution very close to the best monopolynomial approximation of the bipolynomial distribution the tomographic algorithm can not improve the result. At that point the bipolynomial phase is applied, improving the accuracy of the retrieval at

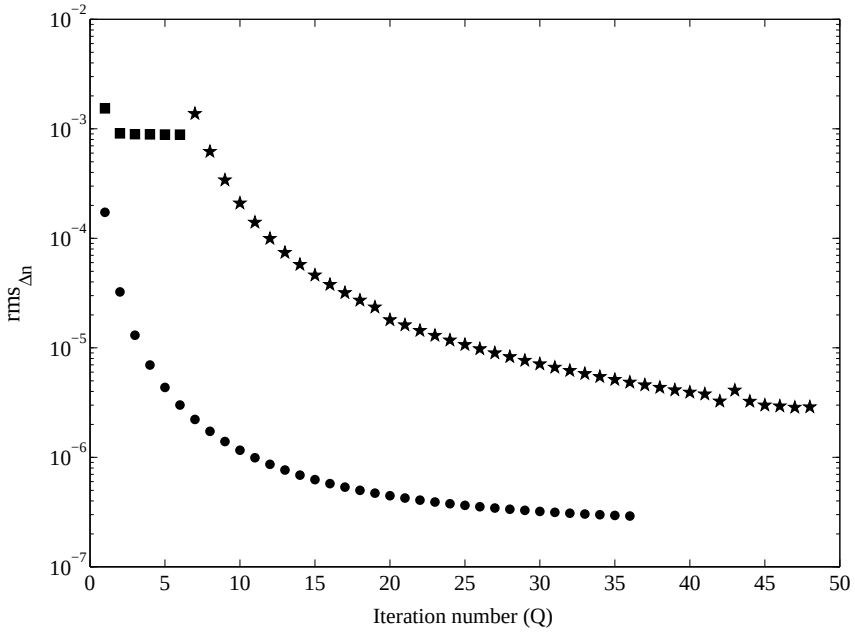

Figure 5.10: Evolution of the tomographic retrieval for the weak (circles) and strong (squares for the monopolynomial retrieval, stars for the bipolynomial) gradient indices.

each iteration and reaching values lower than 1×10^{-5} with 42 interpolated points. Along with the final results of the tomographic retrievals, in table 5.4 we can see the retrieved gradients are able to reproduce the optical behaviour of the theoretical ones for each one of the projections and with which accuracy. This accuracy is shown by the root mean square of the difference between the distributions of the original optical paths and those obtained by numerical ray tracing in the retrieved gradients, $rms_{\Delta S}$.

In the simulations we analyze next we will consider the whole effect of the following three factors on the tomographic retrieval:

1. A Gaussian error added to the sines of deflection $\sin\alpha_{pr}(x,t)$ with zero mean and a standard deviation σ_{sin} with values 1×10^{-5}, 1×10^{-4} and 1×10^{-3} to simulate the experimental error ε_{sin} (we propagate this error in the sines of deflection to the points of intersection of the exit rays with the lens, C_{pr}).

2. Setting the number of projections in 3, the retrievals for each one of the following angular distributions are performed: (0^o, 5^o, 10^o), (0^o, 15^o, 30^o), (0^o, 25^o, 50^o) and (0^o, 35^o, 70^o). We limit to three the number of projections because, as we will explain in the following chapter, this is the number of projections we will work with experimentally.

Gradient models	**Interpolated points**	$\mathbf{rms}_{\boldsymbol{\Delta n}}$	$\mathbf{rms}_{\boldsymbol{\Delta S}(0^o)}$ **(mm)**	$\mathbf{rms}_{\boldsymbol{\Delta S}(20^o)}$ **(mm)**	$\mathbf{rms}_{\boldsymbol{\Delta S}(40^o)}$ **(mm)**
Weak	70	2.9×10^{-7}	1.4×10^{-7}	1.4×10^{-7}	1.9×10^{-7}
Strong	6 (monopolynomial)	8.9×10^{-4}	1.6×10^{-3}	1.6×10^{-3}	1.6×10^{-3}
	74 (bipolynomial)	3.2×10^{-6}	2.9×10^{-6}	2.8×10^{-6}	2.2×10^{-6}

Table 5.4: Results of the tomographic retrieval for the weak and strong gradients when using data from 0^o, 20^o and 40^o projections.

3. Different number of rays per projection: we consider two possible cases, with 100 and 500 rays equally spaced within an aperture of 90% of the diameter of the lens.

For each one of the combinations of factors and each one of both gradients the tomographic algorithm has been simulated 2000 times. As in the simulations of the former section, the resulting distributions of $PV_{\Delta n}$ and $rms_{\Delta n}$ are asymmetrical (see Fig. 5.11). Therefore, also in this case, instead of the mean and the standard deviation, we found it to be more representative the mode and the extremes S and I of the interval that comprises approximately 68% of the cases about the mode. These values are shown in the graphs of figures 5.12-5.15, where we can easily analyze the whole effect of the error in sines, angular distribution of projections and number of rays on the reconstruction of the weak and strong gradients.

The most important conclusions that can be taken from study of the graphs of figures 5.12-5.15 are these:

1. The weaker the gradient, the higher the tolerance to errors and the lower the number of rays and projections needed to obtain an accurate reconstruction. Likewise, the projections need not to be as widely distributed as in the case of a strong gradient.

2. Although a larger number of rays per projection increases the accuracy of the re-

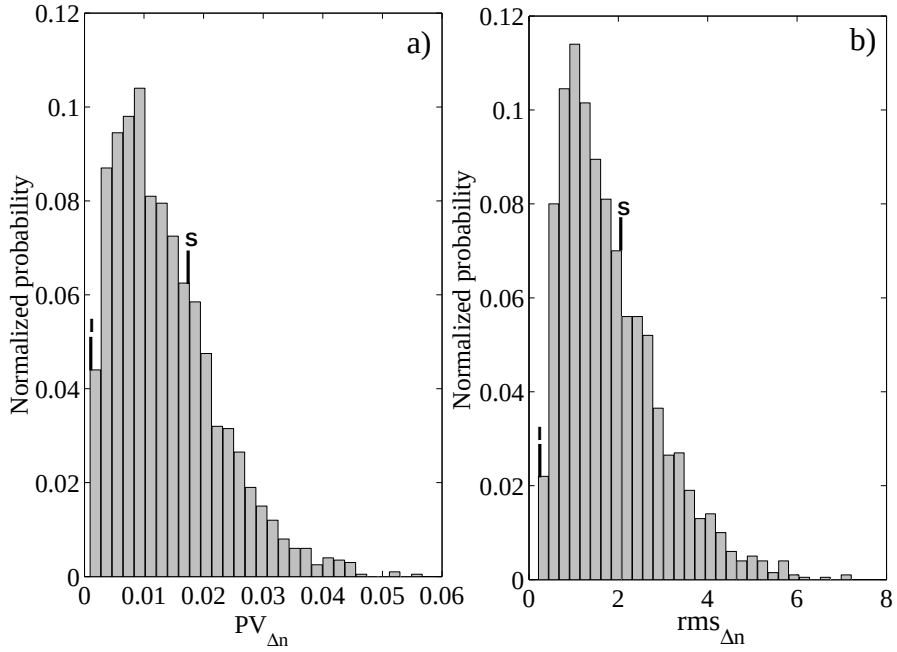

Figure 5.11: Distributions of the normalized probability of the peak-valley (a) and *rms* (b) difference between the retrieved and theoretical gradient indices for the particular case of the weak gradient with an error of $\sigma_{sin} = 1 \times 10^{-3}$, projection at ($0^o$,$25^o$,$50^o$) and 100 incident rays. The upper (S) and lower (I) bounds define an interval that includes approximately 68% of all cases about the mode.

trieval, the influence of a higher and more distributed number of projections is more important, since it provides a better sampling of the refractive index distribution.

3. As error increases, a larger number and distribution of rays and projection is needed to obtain a given degree of accuracy.

In the particular case of the weak gradient, even with an error such as $\sigma_{sin} = 1 \times 10^{-3}$ accuracies of $PV_{\Delta n} \sim 10^{-3}$ and $rms_{\Delta n} \sim 10^{-4}$ can be obtained with projections distributed up to 70^o and 100 incident rays. If we consider the same number of rays but with projections up to 30^o we still get a good accuracy, $rms_{\Delta n} \sim 10^{-3}$. By decreasing the error and increasing the number of rays, this accuracy can reach values as low as $PV_{\Delta n} \sim 10^{-5}$ and $rms_{\Delta n} \sim 10^{-6}$ for $\sigma_{sin} = 1 \times 10^{-5}$, for instance. Nevertheless, the strong gradient is much more demanding, since the maximum acceptable error for an accuracy of $PV_{\Delta n} \sim 10^{-3}$ is $\sigma_{sin} = 1 \times 10^{-4}$ with projections up to 50^o. Even so, an accuracy of $rms_{\Delta n} \sim 10^{-3}$ is feasible for $\sigma_{sin} = 1 \times 10^{-3}$ if projections reach

the 70°. Besides the strength of the gradient, the lower accuracy in the retrieval of the strong gradient is strongly related to its bipolynomial nature. As it was previously mentioned, the results of the monopolynomial phase of the retrieval are limited by how accurately the actual bipolynomial distribution can be fitted with a monopolynomial function. In addition, the bipolynomial retrieval involves the calculation of a higher number of coefficients and, thus, a higher sensitivity to the experimental errors in the tomographic inversion, specially if the previous monopolynomial reconstructions was not very accurate. This is why, as seen in figures 5.14 and 5.15, the angular distribution of projections need to be large enough and the error small enough to make the bipolynomial reconstruction to improve the result of the monopolynomial reconstruction in terms of statistically significance, as checked with the F-test.

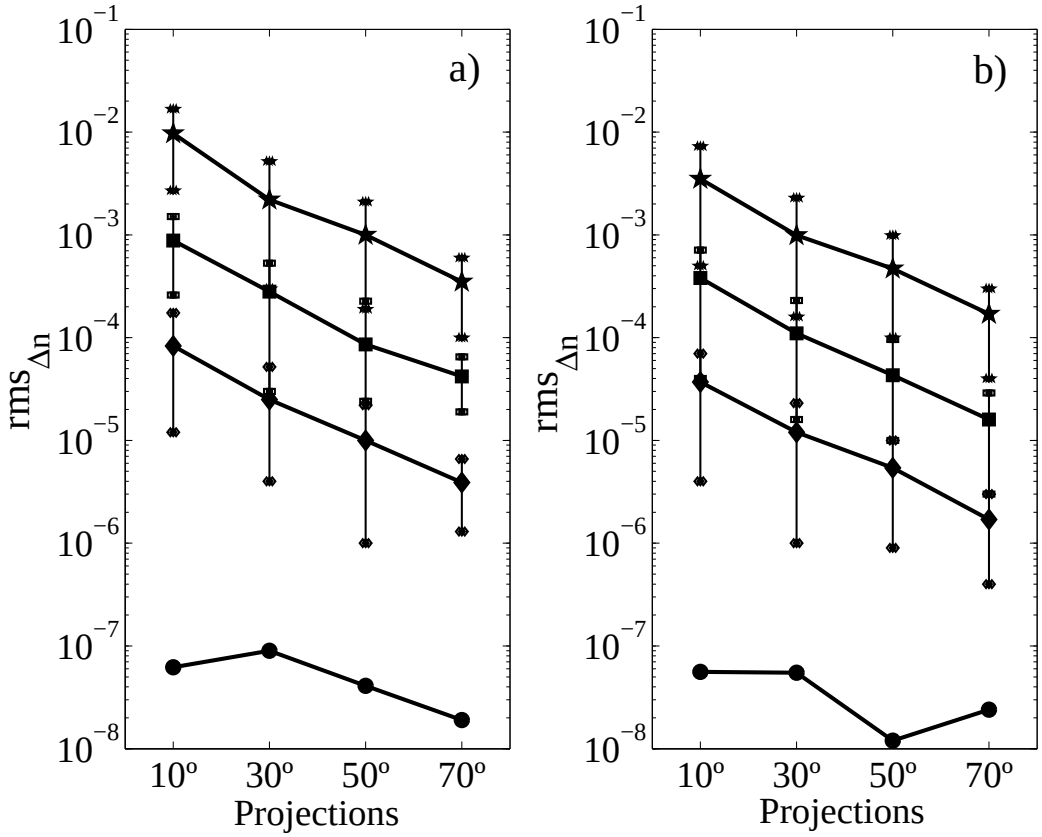

Figure 5.12: Root mean square of the difference between the retrieved and theoretical weak gradient index for $\sigma_{sin} = 0$ (circles), $\sigma_{sin} = 1 \times 10^{-5}$ (diamonds), $\sigma_{sin} = 1 \times 10^{-4}$ (squares) and $\sigma_{sin} = 1 \times 10^{-3}$ (stars). The error bars represent the upper and lower bounds, S and I, respectively. (a) and (b) are the results for 500 and 100 incident rays, respectively.

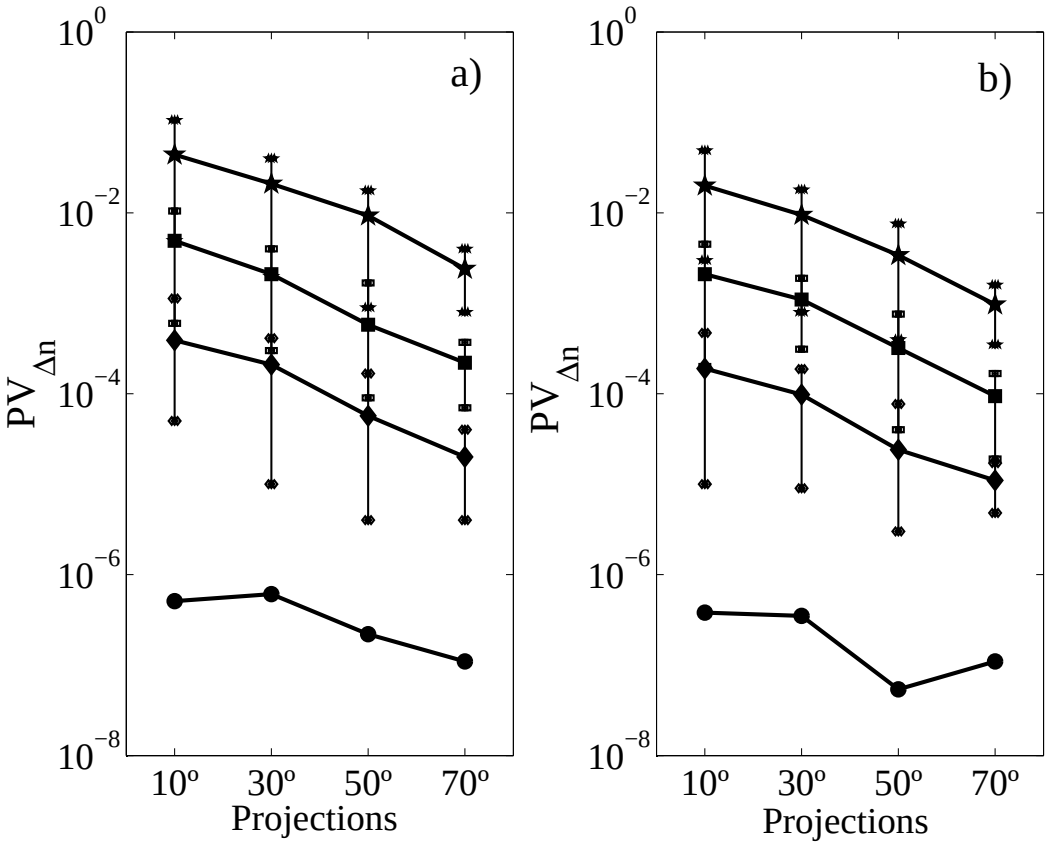

Figure 5.13: Peak-valley difference between the retrieved and theoretical weak gradient index for $\sigma_{sin} = 0$ (circles), $\sigma_{sin} = 1 \times 10^{-5}$ (diamonds), $\sigma_{sin} = 1 \times 10^{-4}$ (squares) and $\sigma_{sin} = 1 \times 10^{-3}$ (stars). The error bars represent the upper and lower bounds, S and I, respectively. (a) and (b) are the results for 500 and 100 incident rays, respectively.

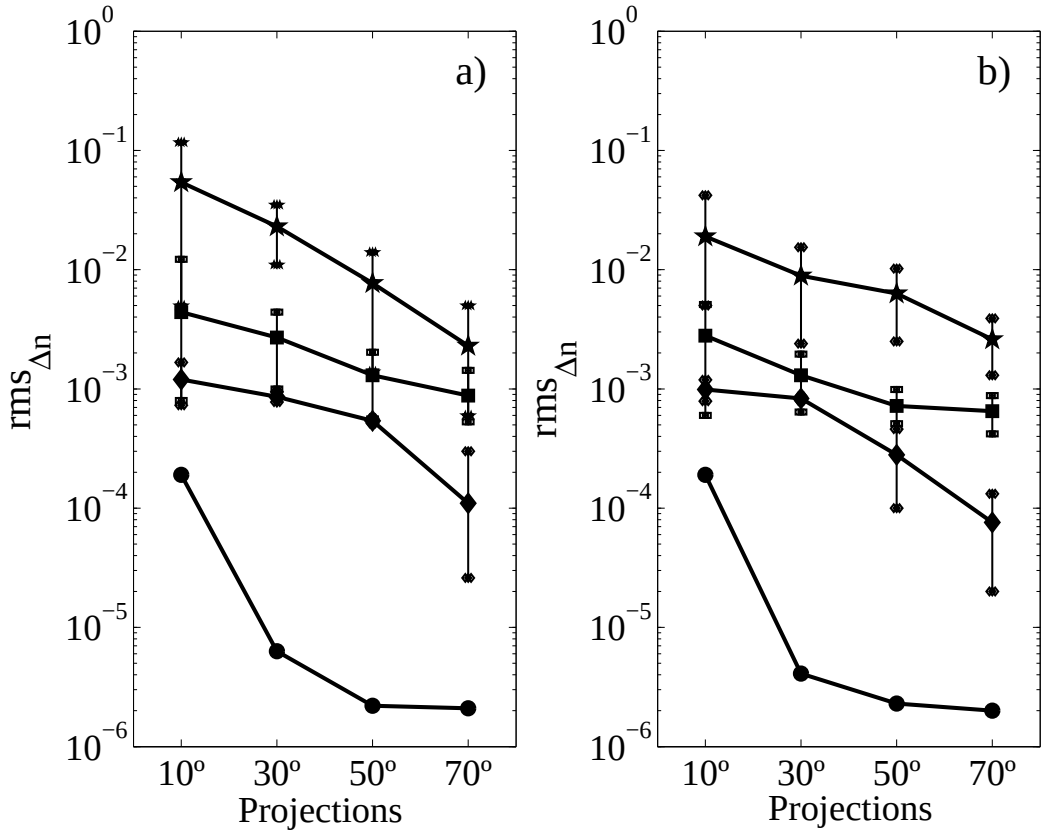

Figure 5.14: Root mean square of the difference between the retrieved and theoretical strong gradient index for $\sigma_{sin} = 0$ (circles), $\sigma_{sin} = 1 \times 10^{-5}$ (diamonds), $\sigma_{sin} = 1 \times 10^{-4}$ (squares) and $\sigma_{sin} = 1 \times 10^{-3}$ (stars). The error bars represent the upper and lower bounds, S and I, respectively. (a) and (b) are the results for 500 and 100 incident rays, respectively.

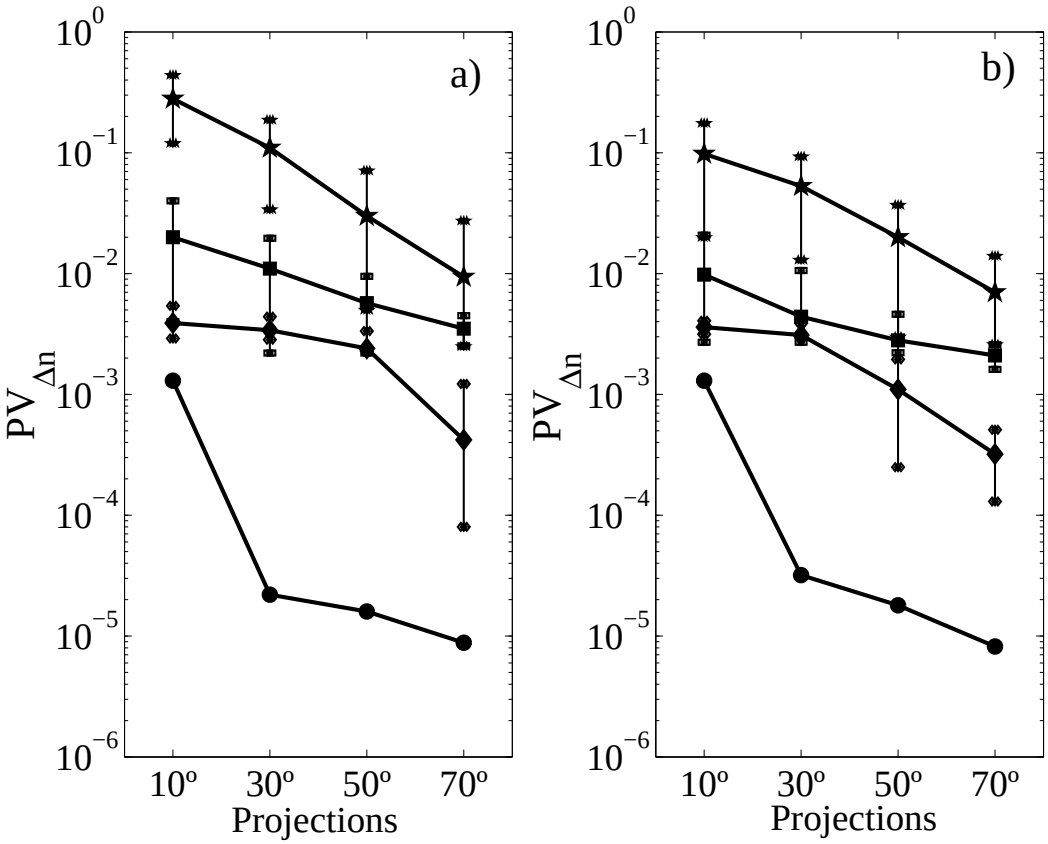

Figure 5.15: Peak-valley difference between the retrieved and theoretical strong gradient index for $\sigma_{sin} = 0$ (circles), $\sigma_{sin} = 1 \times 10^{-5}$ (diamonds), $\sigma_{sin} = 1 \times 10^{-4}$ (squares) and $\sigma_{sin} = 1 \times 10^{-3}$ (stars). The error bars represent the upper and lower bounds, S and I, respectively. (a) and (b) are the results for 500 and 100 incident rays, respectively.

In the last section of chapter 2 we showed a series of ideal features a new method of reconstruction of the gradient index in crystalline lenses should have. Amid them, it was pointed out the aim of reaching average accuracies of $\varepsilon_n \sim 10^{-3}$. Assuming that the actual lens is an intermediate case of the extreme examples we have worked with, with the numerical simulations we have shown that our tomographic algorithm can provide even higher accuracies, depending on the type of gradient, the tomographic data and the errors. Due to the lack of reliable statistics, in the lab we can just evaluate these last two factors, but according to relation 5.8 and the numerical simulations we will be able to obtain quite a good estimation of the maximum accuracy we can aim for. In fact, for this reason we have tried to include in the simulations cases that corresponded to those we will find in the lab, by considering, for instance, an error in sines of 1×10^{-3}, a set of approximately 100 rays per projection or a maximum number of three projections.

A last issue regarding the numerical simulations is the time of computation needed to retrieve a gradient index. This time mainly depends on two factors: the total number of rays used in the tomographic retrieval and the number of computed iterations. As a result, the time of computation includes values from five seconds in the case of the spherical symmetric gradient, where just one projection and no more than 100 rays were needed, up to approximately 90 seconds in the case of working with 3 projections and 500 rays per projection (these values correspond to those obtained with a computer with a Pentium 4 processor at 2.4 Ghz with 1 gigabyte of RAM and the algorithm programmed in Matlab).

6 Collection, processing and analysis of experimental data

Once laid the foundations of the tomographic algorithm it is possible to move on to the last part of this work, focused on its experimental implementation. To do so it will be necessary to explain first the procedure followed for obtaining the input data of the tomographic algorithm. This includes the assembly and operation of an own experimental setup of ray deflectometry, as well as the obtaining of the input data through the processing of the images recorded with such a setup. Likewise, a previous study of the sources of error will be indispensable too, comprising the detection, minimization and estimation of the order of magnitude of the error those sources produce on the experimental data.

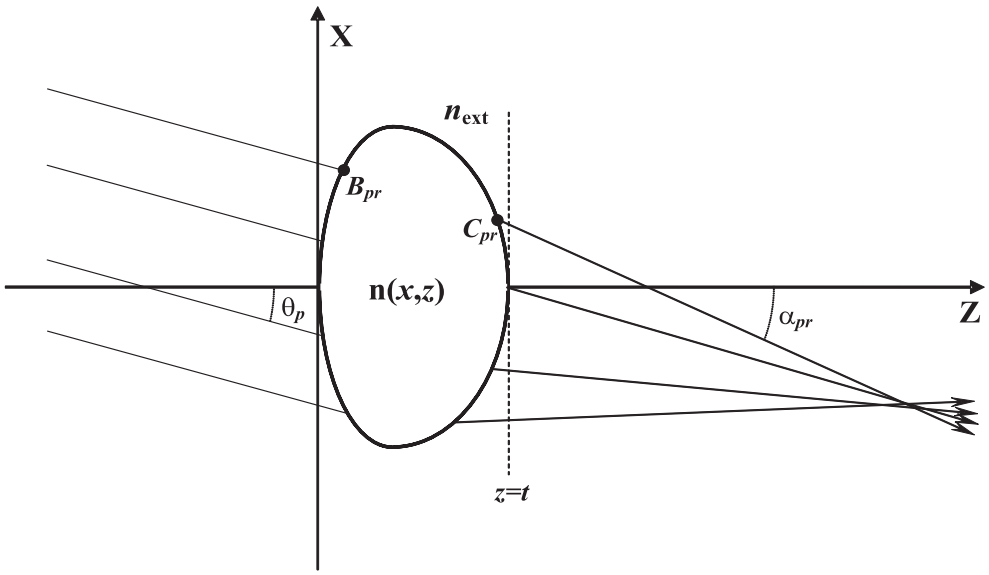

Figure 6.1: Illustration of the input data of the algorithm, θ_p, B_{pr}, C_{pr} and $\sin\alpha_{pr}(x,t)$, for a given projection p in a crystalline lens with a gradient index $n(x,z)$ and thickness t.

6.1 Assembly and operation of an experimental setup of ray deflectometry

As it was explained in section 4.1, the tomographic algorithm is designed to work with a set of parameters of the deflection caused by an eye lens on rays of light entering the lens at different angles and heights. Specifically, and for a given projection p, these input data of the algorithm are:

- The angle of incidence θ_p of these rays (which are supposed to be parallel).
- Their entry points B_{pr} on the surface of the lens (where the subscript r represents each ray).
- The exit points C_{pr}.
- The distribution of the sines of their angles of deflection on a plane $z = t$, $\sin\alpha_{pr}\,(x, t)$, where t is the thickness of the lens (see Fig. 6.1).

To obtain these data, to do it with the highest possible accuracy and for a wide range of values of θ are the main aims of the experimental setup we have designed for the reconstruction of the gradient index in crystalline lenses.

In figure 6.2 a diagram of the experimental setup is shown:

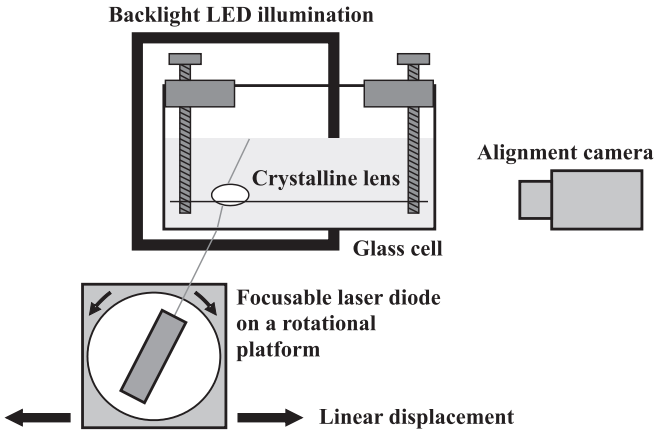

Figure 6.2: Diagram of the experimental setup as seen from the measurement camera.

In the former diagram we distinguish the following parts (see Fig. 6.3):

1. A laser diode (0.9 mW; $\lambda = 633$ nm) fixed to a rotational platform that allows to rotate it 360° with an accuracy of 5 minutes of arc. The diode has a special feature:

it has an adjustable lens that allows to focus the laser beam from 150 mm to the infinite. By varying this distance we can narrow the beam up to 100 μm in the area of analysis of the eye lens.

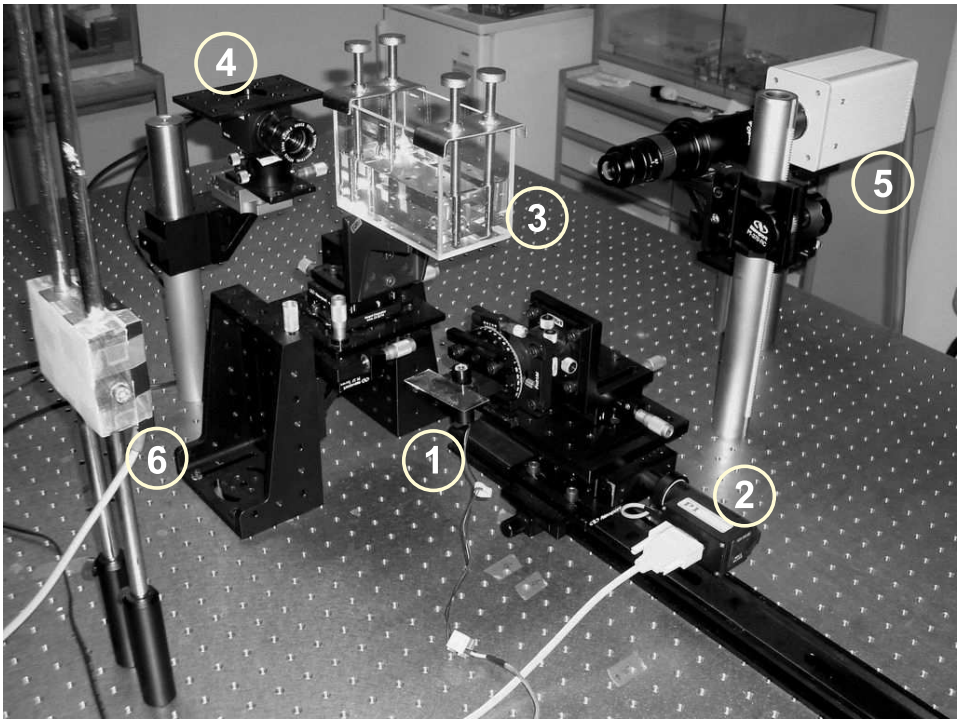

Figure 6.3: Picture of the experimental setup, where we can distinguish the laser diode (1), the motorized travel stage fastened to a rail (2), a glass cell that contains the lens (3), the alignment camera (4), the measurement camera (5) and the white LED diffuse backlight (6).

2. The system laser-rotational platform is mounted on a motorized travel stage with a range of movement of 254 mm. Once fixed the angular position of the laser, we can displace it by moving the stage for each one of the projections in order to sample the whole aperture of the lens. The travel stage is fastened itself to a rail of 750 mm, on which we slide the stage to modify its position from one projection to the other. Since both the position of the lens and the height of the system laser-rotational platform are fixed, each time we rotate the laser it is necessary to horizontally displace such a laser to illuminate once again the lens.

3. A glass of cell of $137 \times 72 \times 92$ mm contains the lens immersed in a biocompatible solution (BSS Plus® of Alcon [Bss]). Some drops of milk are added to the solution

to make visible by scattering the trajectory of the laser beams. With the aim of observing the laser beams before entering the lens and correcting small misalignments of its position we have designed a supporting system of the lens to be coupled to the glass cell (see details in Fig. 6.4).

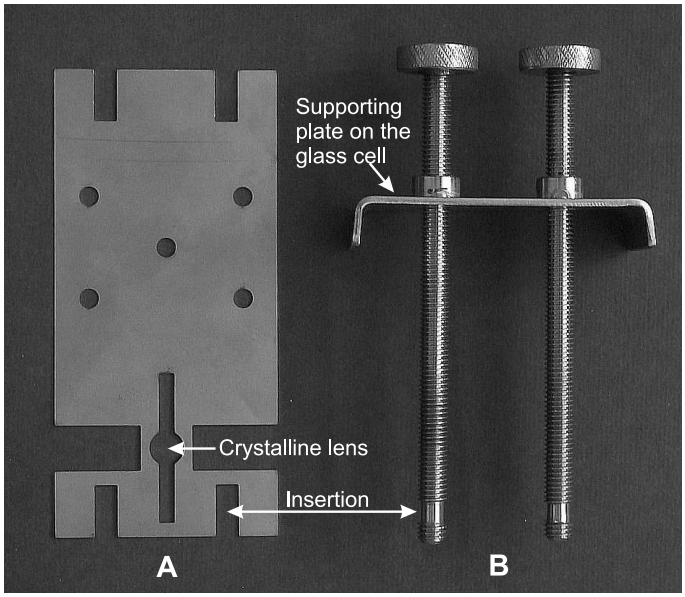

Figure 6.4: Components of the supporting system of the lens. To the left (A) there is a 0.5 mm thick steel plate with five holes to ease its immersion and another hole to support the lens. The diameter of this sixth hole varies from one plate to another, comprising values from 8 up to 11 mm, which are those formerly measured in pig and some fish lenses. In order to see the laser beams at both sides of the lens, this hole is extended with two lateral slots. Besides, to decrease the portion of the lens hidden to the measurement camera because of the plate A, the width of this plate has been reduced in this area. On the other hand, there are other two plates that leans on the superior surface of the glass cell, one of them shown to the right of the image (B). Each one of them has two screws with a polished area at their end. Those areas are inserted in each one of four lateral notches of the plate A, in order to hold it. By means of the screws we can change the height and the inclination of the lens inside the cell.

4. An alignment CCD camera (AC), with a resolution of 768×576 pixels (8 bits/pixel), is used to check the level of the glass cell, the orthogonality of the laser beam with the base of the glass cell and that throughout each one of the projections such a beam is aligned with the meridional plane of the lens to be tomographed (see Fig. 6.5).

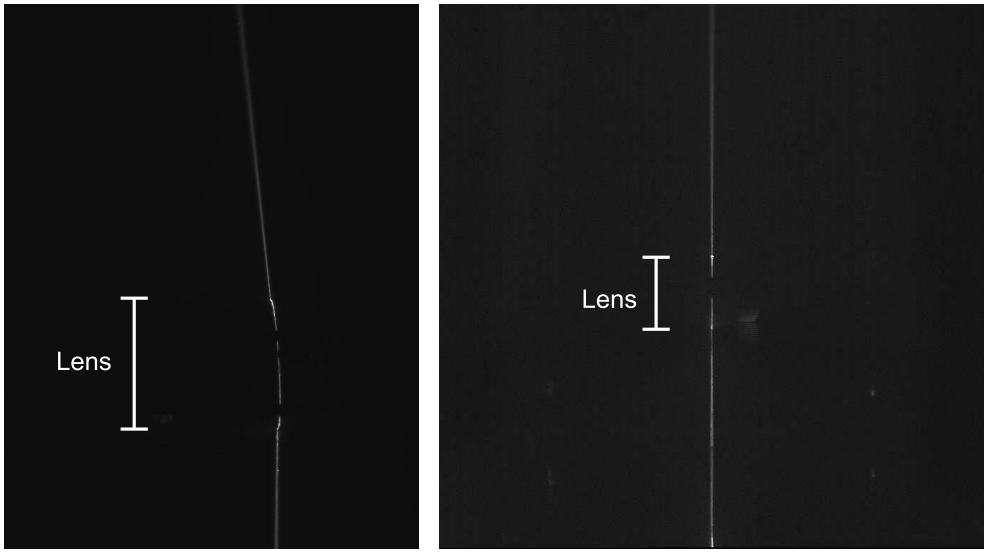

Figure 6.5: Views of the deflection of a laser beam caused by an eye lens as seen from the measurement camera (a) and the alignment camera (b). This second camera is used to check such a deflection is contained within the tomographed meridional plane.

5. A measurement CCD camera (MC), orthogonal to the alignment camera and with a resolution of 1344×1024 pixels (12 bits/pixel), is used to record the images of the beams deflected by the eye lens at each one of the projections (see Fig. 6.6).

6. A diffuse source of illumination, made up by white LED's, is used to backilluminate the lens and obtain by contrast an image of its profile with MC (see Fig. 6.7), which is placed in front of the LED lamp. The specific use of the diffuse illumination allows to avoid the presence of shadows or areas of half-light that might distort the profile of the lens. In fact, this technique is also used in other areas of knowledge that require a very accurate determination of the surface of some objects [Hol02].

We will obtain the input data of the tomographic algorithm from the processing of the image of the lens profile (see Fig. 6.7) and those recorded for each one of the projections by MC (see Fig. 6.6). Except for the system motorized travel stage-rail and the white LED backlight, all the other elements are mounted on platforms that allow to minimize any tip and/or tilt.

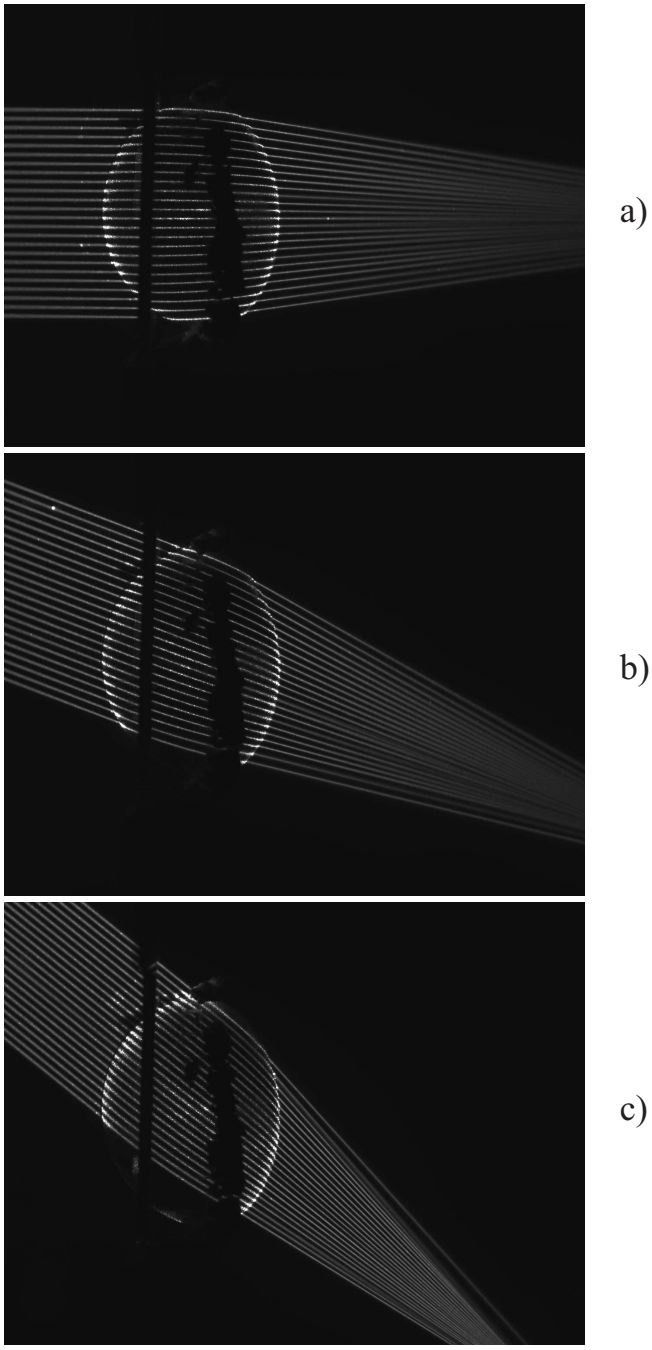

Figure 6.6: Images of the deflections produced at three projections, spaced about 20° among them.

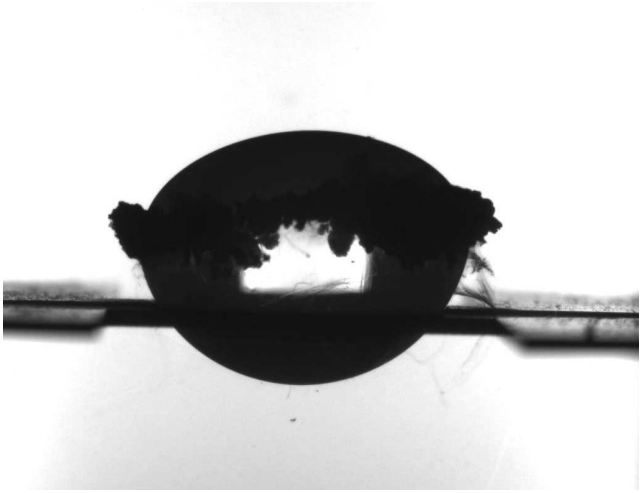

Figure 6.7: Image of a lens profile obtained from the measurement camera with a background diffuse illumination. The anterior surface of the lens, the closest one to the cornea, is oriented upwards and the posterior surface downwards.

6.1.1 Experimental protocol for the collection of experimental data

In order to minimize the errors due to misalignments and guarantee the quality of the data, when taking measurements we have followed some steps that make up the following experimental protocol:

1. We level both cameras and the glass cell by using levels and by analyzing the images of the cell base and the solution level recorded from each one of the cameras (the details of this analysis, as well as of all those performed on the recorded images, will be explained in a subsequent section).

2. Once fixed the laser on a given angular position, its beam is focused to make it as narrow as possible in the area of analysis of the lens. By means of the images obtained from AC we check the orthogonality of the laser beam with the base of the cell and we displace it towards the exact center of the image. By doing so we prevent the parallax errors from distorting the detection of possible lateral movements of the laser beam as we displace it along a projection, since the lens of AC is not telecentric [Edm].

3. A crystalline lens is extracted and, from a previous estimation of its diameter with a rule, we choose a supporting plate with a diameter a bit lower and we place it in the cell. Next, we put the lens on the corresponding hole of the plate, always with the most curved surface downwards to minimize the lack of data due to the portion

of the lens hidden by the plate. Since the ultimate aim is to scan a meridional plane of the lens, it is necessary to align the lens so that the laser beam propagates along such a plane. To do so, by displacing the glass cell and tilting the supporting system, we search for the plane of the lens orthogonal to the object plane of AC that contains both the incoming laser beam and the deflected beam, which is the condition that defines a meridional plane of a rotationally symmetrical optic system. We verify such a condition for three positions of the incoming laser beam equally spaced along the meridional plane. A more thorough check is not done due to the sensitivity of the lens to the modification of the external biological conditions (see section 1.4). This is why it is necessary to reduce as much as possible to total time of data gathering and alignment, although without compromising their accuracy.

4. Once finished the former step, it is necessary to ensure that the meridional plane of the lens and the laser beam are properly imaged by MC.

5. We switch on the LED lamp to obtain a first image of the lens profile. After switching it off, we use MC to record the images that correspond to one projection. By displacing the motorized travel stage at equal intervals, the whole lens and its adjacent regions are scanned. Once the scanning is done, another image of the profile of the lens is taken to detect any possible displacement or modification of its shape.

6. Once finished the image recording of one projection, the laser is rotated and the motorized travel stage slid along the rail up to the position from where the lens can be scanned. Once fastened the stage to the rail, the laser beam is focused again to decrease as much as possible the beam width at the area of analysis of the lens. This set of operations (rotation, displacement, focusing) misaligns the laser beam and it is necessary to realign it so that its position and inclination agree with that of the former projection. Thus, we guarantee the beam is once again in the object plane of MC and aligned with the same meridional plane of the lens that was scanned at the former projection. Hereinafter steps 5 and 6 are repeated as many times as projections are needed. Given the configuration of the experimental setup, the theoretical limit to the entry angle θ, without considering possible inclinations of the lens, is provided by the following function

$$\theta_{max} = \arcsin\left(\frac{1}{n_{ext}}\right) \tag{6.1}$$

where n_{ext} is the index of the biocompatible solution. Any of the solutions used in

literature [Cam84, Kro94, Vil01, Aco05] would allow to achieve up to 49°. However, due to the vignetting produced by the setup itself, we will not exceed the 40° (According to the numerical simulations of section 5.3, three projections distributed from 0° to 40° should guarantee an average accuracy of the order of $10^{-3} - 10^{-2}$ in the reconstruction of the gradient).

7. The last step is the measurement of n_{ext} for the laser wavelength ($\lambda = 633$ nm) with an Abbe refractometer. To the error in the measurement of the refractometer, 0.0002, we have to add that of the possible variation of the temperature of the laboratory during the data collection. With a thermometer we have checked that this variation rarely exceeds two degrees. Therefore the final error in the measurement of n_{ext} is still in the fourth decimal digit [Qua95].

Regarding the time needed for each one of the projections, the average is about 25 minutes, where 10 of them corresponds to the projection strictly speaking and the remaining 15 to the alignment procedure.

Finally, it is important to point out that throughout this research alternative experimental setups have been assembled and from their study and improvement results the one we present in this work. Among these alternative setups stands out that used in reference [Vaz06].

6.2 Image processing and collection of the input data of the tomographic algorithm

The collection of the input data of the tomographic algorithm (θ_p, B_{pr}, C_{pr} and $\sin\alpha_{pr}(x,t)$), as well as those needed to detect and correct all misalignments mentioned in the former section, requires a previous processing of the images recorded by MC and AC, respectively. As we will see next, this processing is different depending on the fact the image is that of a laser beam or that of the lens surface.

6.2.1 Processing of laser beam images

From the application of the Ehrenfest's theorem to optics [Coo75] a very useful property in the characterization of the propagation of light beams is inferred: in a weakly inhomogeneous optical medium the centroid of such a beam propagates like a paraxial ray in an effective refractive index that corresponds to the transverse gradient of the refractive index averaged over the irradiance profile of the beam. In a homogeneous medium,

like that of the biocompatible solution, this means the centroid of a beam follows a straight line, so that in our case we can approximate the trajectory of the laser beam as the ray characterized by the parameters of this straight line, slope and intercept. This makes possible to "come back" to the approximation of geometrical optics under which we have formulated the tomographic algorithm and to relate our experimental measurements with its input data, which are also of geometrical nature. Therefore, the ultimate aim of the processing of laser beam images will be that of calculating their centroids and the parameters of the straight line they fit the best. To do so, we follow the next steps:

1. For obtaining the data of just a beam or those of all entry and exit beams, we define the regions of the images where we will carry out the processing (see Fig. 6.8). This has two objectives: to prevent other illuminated zones of the image, like the lens, from affecting the calculation of the centroids in the following steps and to decrease the time of computation by reducing the areas of the image to be analyzed.

2. For each image of a ray and for each row of its corresponding region of analysis the position of the maximum of intensity (or level of gray, equivalently) is searched and from that point, rightwards and leftwards, the pixels where the intensity falls below a threshold previously defined by us (see Fig. 6.9). With the values of the intensity and the positions of the pixels contained by these threshold pixels the centroids of intensity of the ray for each row is calculated, imposing a condition: the number of pixels in between must be higher than two. This condition is intended to avoid the detection of false centroids due to glares of particles in suspension.

   The choice of a suitable threshold is essential for an accurate and precise calculation of the centroids. With the aim of automatizing the process of calculation of this threshold, in the beginning we used filters of gradient, like those of Sobel [Gon93]. This technique is useful for laser beams with a small divergence in the region of analysis and a very homogeneous profile in its propagation. However, the refraction due to the lens along with the focalization of the laser (see section 6.1) cause an important divergence on the beams that must be taken into account (see Fig. 6.10). Hence, we have decided to set a threshold intensity to distinguish the ray from the image background both in the positions where the waist is very straight and in those where it has widened, with the corresponding drop in the maximum levels of intensity. The choice of the value of this threshold intensity will be explained in the final section of this chapter, focused on the calibration of the experimental setup.

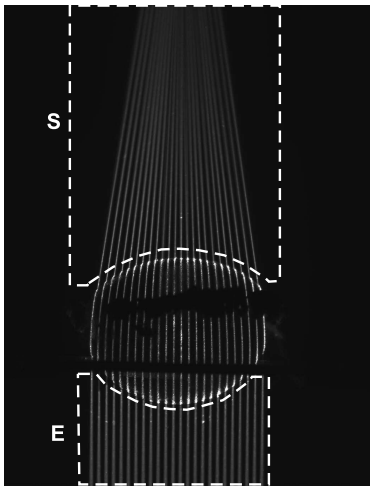

Figure 6.8: Combination of images of several laser beams deflected by the lens where two regions of analysis (dashed line) are defined: one for the entry beams (E) and other for the exit beams (S).

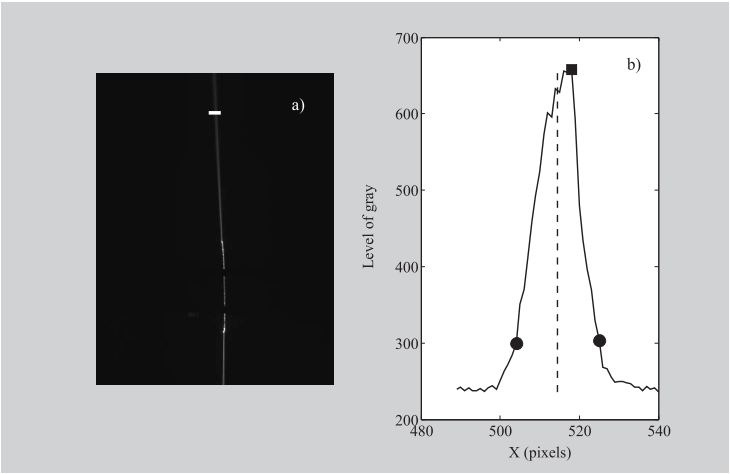

Figure 6.9: Image of a laser beam (a) where the centroid is calculated at the position marked by the white line. In the intensity profile that corresponds to this position (b), it can be seen the positions of its maximum (square), of a threshold level of gray of 310 (circles) and of the centroid calculated for that threshold (vertical dashed line).

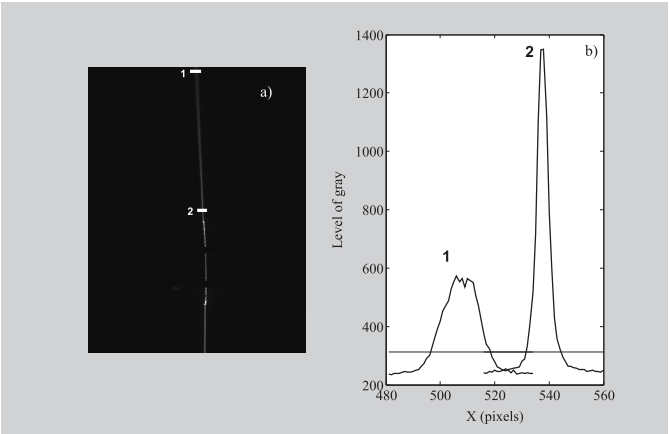

Figure 6.10: Image of a laser beam at the exit of a lens (a) where the profile of the intensity is analyzed for the two points of its trajectory marked with two thick white lines. These profiles are shown in graph (b), where it can be seen how the beam has diverged as well as a possible estimation of a threshold for the calculation of centroids (horizontal solid line).

3. Once calculated the centroids of a beam along its trajectory, they are fitted to a straight line to obtain the parameters of such a line: the slope b and the intercept a (see Fig. 6.11). To decrease the influence of wrong values of those centroids because of accidental glares, this fit is performed by using a robust least squares fitting [Mtl].

   It is important to notice that in the case of the incoming rays the fitting is different. In order to have a widest possible section of the exit beams and of the lens in the image, we have decided to reduce that of the incoming beams. Since, theoretically, the slope of these beams is the same along the projection, what we do is to take several images of non deviated rays at both sides of the lens. Afterwards, with a robust fitting, we obtain their average slope. From this value and the centroids of the incoming beams, we calculate the intercepts of these beams by assuming they all have that same slope.

The processing of the laser beams is applied to both the images taken by MC for the collection of the input data of the tomographic algorithm and to those taken by AC to detect and to correct all misalignments mentioned in section 6.1.1. In table 6.1 it can be seen the results obtained for a study of the precision of the processing of 500 and 100 images of the same laser beam recorded from MC and AC, respectively. These results are representative of those obtained for different angles of the beam, as well as of the

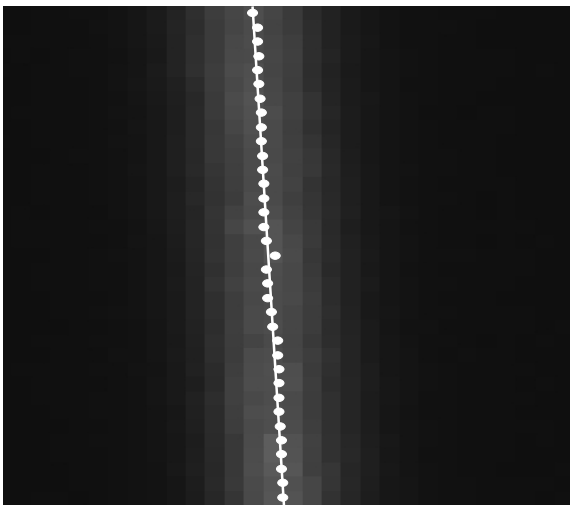

Figure 6.11: Portion of a laser beam where it can be seen its centroids of intensity (points) and the straight line they fit the best (solid line).

statistical distributions of the slope b and the intercept a. These distributions, except for slight asymmetries that may be due to small tilts of the system laser-rotational platform (see section 6.1), can be approximated as Gaussian, like the error added in the numerical simulations of chapter 5. It is important to point out that whereas the intercept of the beams characterized from MC is given in microns, that of AC is given in pixels. This is because the beams recorded from MC always show the same magnification, since they are at the same plane, and those of AC are moved within a range of distances of about 10 mm in relation to the camera. Within this range the magnification includes values between 67 and 80 μm/pixel, what makes more practical to give the value of the intercept a in pixels.

6.2.1.1 Sources of error in the processing of laser beams

Next, we will list the main sources of error in the processing of the laser beams and the fitting of the evolution of their centroids to a straight line:

- Geometrical distortion of the image: for both cameras the distortion is assessed with an array of dots equally spaced 500 μm that occupies all their field of view. In the case of AC the only noticeable distortion is that due to the rectangular shape of their pixels, that requires a correction of 2% in one of the dimensions of the image in relation to the other. Regarding MC, the distortion is exclusively due to its objective. From the image of the array of dots, the detection of their centroids by

Camera	Analyzed segment of the beam	$\mathbf{SD}_b$	$\mathbf{PV}_b$	$\mathbf{SD}_a$	$\mathbf{PV}_a$
MC	Whole image	2×10^{-5}	2.1×10^{-4}	0.5 μm	3.7 μm
	Half image	6×10^{-5}	3.7×10^{-4}	0.7 μm	4.4 μm
AC	Whole image	1×10^{-4}	7.4×10^{-4}	0.04 pixels	0.16 pixels
	Half image	2×10^{-4}	1.3×10^{-3}	0.04 pixels	0.24 pixels

Table 6.1: Precision in the characterization of the laser beams as straight lines. This precision is provided by means of the standard deviation (SD) and the peak-valley (PV) in the calculation of the slope b and the intercept a. The analysis has been done for the beam occupying the whole image along its larger dimension and also for the case it occupies just half of the image.

using an own developed software and the application of a bilinear transformation between the positions of the centroids in the image and in the original array [Hol02] a filter of correction is obtained to correct most of the distortion of the image. In figure 6.12 it is shown the result of the correction of the distortion for the fitting of the centroids of a given beam, thus decreasing the standard deviation of the fitting from SD = 0.46 pixels $\approx$ 8.5 μm to SD = 3 μm and modifying the value of the calculated slope in $\sim 1 \times 10^{-3}$. Since the correction of the distortion is carried out for an object plane of the objective of the camera, any defocus decreases the accuracy of this correction.

- Value of the threshold of the level of gray used in the calculation of centroids: theoretically the variance of a centroid should become lower by decreasing the value of the threshold, since the number of positions of the profile of intensity considered it its calculation would increase. However, when reducing too much the threshold the inclusion of pixels with a low ration signal-noise can increase that variance [Are04]. For this reason, it is necessary to search for the range of values

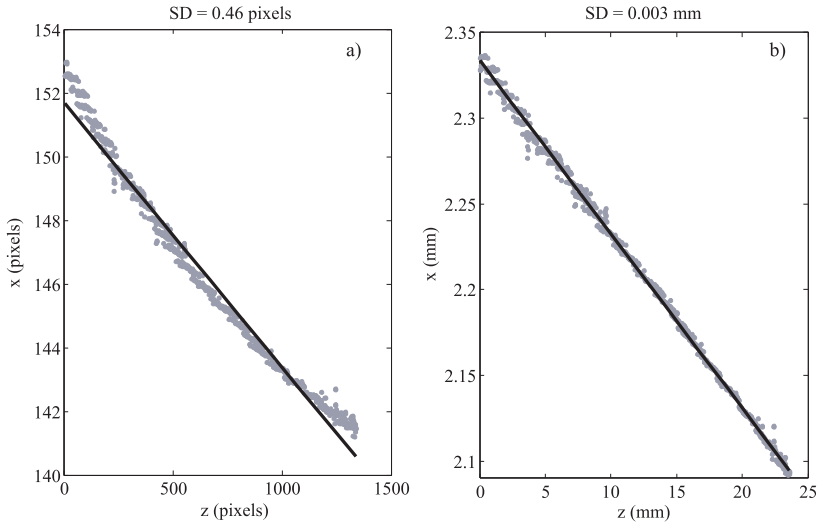

Figure 6.12: In graph (a) it can be seen the fit of the centroids obtained for a distorted image of a laser beam from MC, whereas in (b) it is shown the fit by previously correcting the distortion.

of the threshold that satisfies that the fitting of the beams to straight lines is as precise and accurate as possible As we have mentioned before, we will analyze this issue thoroughly in the last section of this chapter.

- Validity of the calculation of centroids: theoretically, the calculation of centroids should be performed in planes orthogonal to those of the direction of propagation of the beams, whereas we have performed it along the rows of pixels of the images. The less symmetric the distribution of intensity in these orthogonal planes and the higher the inclination of the beams, the larger the error in the calculation of the centroids should be according to the way we have carried it out. However, in our case, due to the resolution in pixels and the remaining non corrected distortion, there is not a significant difference by performing the calculation one way or the other. On the other hand, it is also necessary to consider the effect that might have the projection of a tridimensional distribution of intensity to just two dimensions. Taking into account we will work in theoretically meridional planes, the beams should be symmetric about that plane and its projection on it should not affect the calculation of the position of the centroid.

- Resolution of the image: the higher the resolution in pixels of the image, the more accurate the calculation of centroids. Besides, a higher resolution, as a larger size of the image of the beam for the same resolution, implies a larger number of calculated

centroids, what should mean a better fit.

- Noise in the image: with a dynamic range higher than 60 dB, the noise due to MC is much less important than that produced by the accidental glares caused by milk particles in suspension. With the aim of reducing its effect it was implemented the capture of several images for each beam and a subsequent average [Vaz06]. Nevertheless, after several tests we have checked that the use of a robust least squares fitting rules out the need of that step, thus decreasing the time needed to scan a crystalline lens.

- Maximum values of the profiles of intensity: due to the low power of the laser, the divergence of the beams and the need to work with not very long exposition times, we could not use all the dynamic range of MC. Thus, the profiles of the beams do not exceed in any case the level of gray 1900 out of a maximum of 4095.

- Approximation of a laser beam as a ray of light: the wider the beam and the closer to regions of caustics, the less representative the approximation of a laser beam deflected by a lens as a ray. We have minimized the first of factors by focusing the laser beam in the region of the lens, so that we always work with beam widths between 100 and 300 μm.

- Variation of the slope of the incoming beams along a projection: it has been checked that for the apertures used in the scanning of the eye lens the *rms* variation of that slope is of the order of 1×10^{-3}.

6.2.2 Processing of the images of the surface of the crystalline lens

The characterization of the surface of the lens is carried out through the detection and fitting of the profile of the scanned meridional plane, assuming that the result can be extended to three dimensions given the assumption of rotational symmetry. In the processing of the images of the surface we distinguish the following three stages:

1. Detection of the pixels that correspond to the surface of the lens from the image obtained from MC with diffuse background illumination. Due to the refraction that takes place in the lens, when it is illuminated with a diffuse source of light there is a strong contrast between the portion of the image occupied by the lens and the rest of the image (see Fig. 6.7). Thus, the levels of gray fall sharply at the edge of the lens, so that the surface of the lens can be approximated by the line formed by those points where the module of the gradient of those levels of gray is higher than

a given threshold of detection. The detection of such points is possible by using filters of gradient, among which that of Sobel stands out due to its minimization of noise [Gon93]. However, even modifying the threshold of detection, the use of these filters ends up including many points that do not form part of the surface of the lens, like the edges of the plate and remains of ciliars and vitreous humour which are yet stuck on the lens. For this reason, we just apply the filters on that zone of the image occupied by the lens and later we refine the result by eliminating manually those points that do not belong clearly to its surface (see Fig. 6.13).

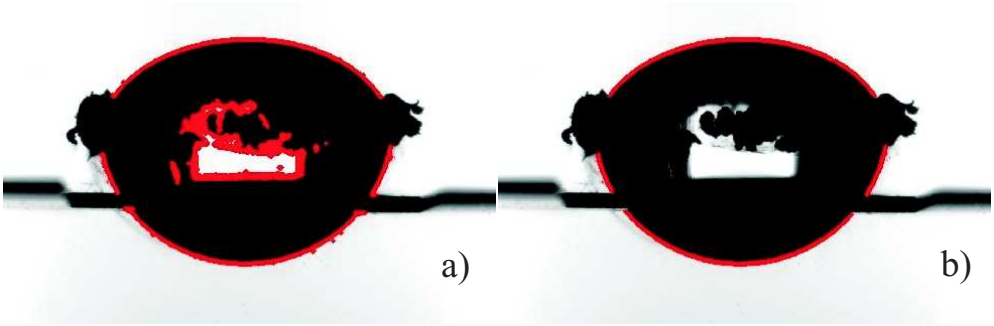

Figure 6.13: Application of the Sobel filters to an image of the profile of a lens (a), where those points that do not belong clearly to its surface are eliminated manually (b).

2. From the previously obtained filters of correction (see section 6.2.1.1) the distortion of the points of the surface of the lens are corrected.

3. Fitting of the points of the surfaces according to the following steps:

   a) Fitting of the anterior surface: in previous works [Aco05, Vaz06] it was shown that surfaces of fish and pig lenses (species we work with) fit to ellipses and circles, respectively. For this reason, to detect and to leave out later the rotation, as well as the centering, in the fitting of the anterior surface we have decided to initially use a least squares fitting algorithm specifically designed for ellipses, whatever their orientation [Hal98].

      Once rotated and translated the coordinate system to the center of the fitted ellipse, by using a Levenberg-Marquardt algorithm [Pre99, p. 683] and according to a F-test [Bev92] and to the standard deviation the best fit to the

following function is calculated:

$$z = \frac{R_a - \sqrt{R_a^2 - (1+Q_a)x^2}}{(1+Q_a)} + \sum_{i=1}^{N} c_i^a x^i \tag{6.2}$$

This is a conic with polynomial terms where, in absence of such terms, R represents the radius of apical curvature and Q the asphericity (z denotes the direction along the optical axis of the lens and x the orthogonal direction contained within the image of the surface).

b) Fitting of the posterior surface, where we consider three possibilities:

i. Assuming that the lens is rotationally symmetric, the rotation of the posterior surface should fit with that of the anterior one, as well as its center in x. Therefore, according to the coordinate system given by the fitting of the anterior surface, we fit the points of the anterior surface to the following function:

$$z = z_o + \frac{R_p + \sqrt{R_p^2 - (1+Q_p)x^2}}{(1+Q_p)} + \sum_{i=1}^{N} c_i^p x^i \tag{6.3}$$

It is obvious that if the lens is rotationally symmetric and the data of the surfaces are well centered and rotated, their fit should not show significant odd polynomial coefficients.

ii. Assuming that the posterior surface has the same rotation as the anterior one we allow a decentering in x, what implies a lack of rotational symmetry:

$$z = z_o + \frac{R_p + \sqrt{R_p^2 - (1+Q_p)\,(x-x_o)^2}}{(1+Q_p)} + \sum_{i=1}^{N} c_i^p x^i \tag{6.4}$$

iii. Finally, by using the original coordinates of the image we apply to the posterior surface an elliptical fitting identical to that of the anterior surface and according to the resulting coordinate system (x', z') we fit to

$$z' = \frac{R_p - \sqrt{R_p^2 - (1+Q_p)x'^2}}{(1+Q_p)} + \sum_{i=1}^{N} c_i^p x'^i, \tag{6.5}$$

As it was mentioned, a rotationally symmetric lens would just admit a fit of the posterior surface as the one expressed by the equation 6.3 without odd polynomial terms and this is the only fit we will consider for the retrieval of the gradient index (see Fig. 6.14). However, according to the F-test and the standard deviation, we will also analyze which is the best of all fittings in order to study possible deviations of the rotational symmetry.

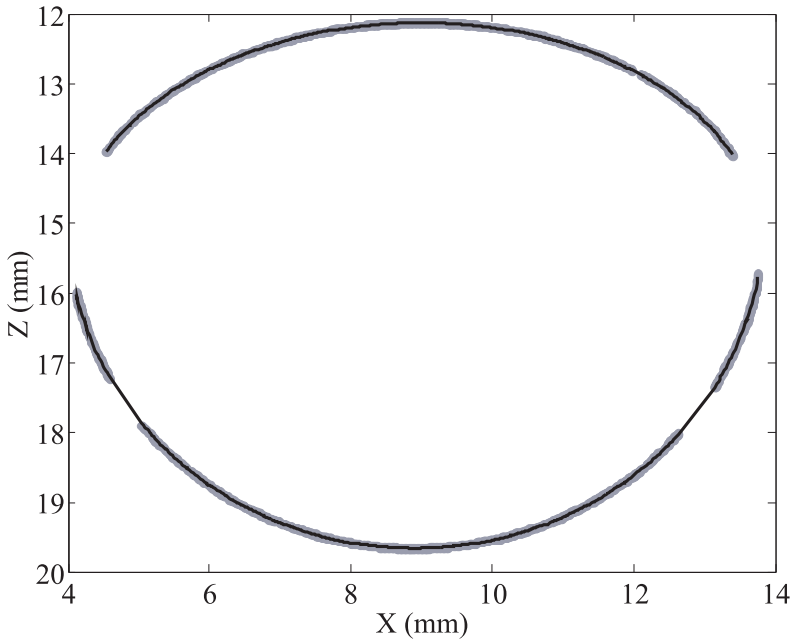

Figure 6.14: Fits of the points of the anterior (up) and posterior (down) surface where the fits are shown as black solid lines and the points as gray dots.

Finally, it is important to point out that the detection of the rotation is initiated in the anterior surface because of its higher asphericity in non spherical lenses, what implies a lower error in such a detection. If the detection is initiated in the posterior surface, the resulting error considerably worsens the fitting of the anterior one assuming equal rotation. On the other hand, when the lens is spherical, as it can be the case in some fish, we fit directly to a circumference with least squares fitting by using polar coordinates [Lop02, Appendix II].

6.2.2.1 Sources of error in the characterization of the surfaces of the lens

The main sources of error in the detection and fitting of the surfaces of the lens:

- Remains of the vitreous humour on the posterior surface of the lens: after extracting

the lens from the eye ball we try to eliminate all vitreous humour stuck on the posterior surface. In this process it is very important not to produce any damage to the capsule, since that would cause a rapid loss of transparency of the lens.

- Non corrected distortion: in section 6.2.1.1 this point was already explained. Depending on the accuracy of the filter of correction and on the possible defocus of the image, there will be a residual non corrected distortion.

- Time of exposition of the image recording and threshold of the Sobel's filters: by ensuring the highest possible contrast between the periphery of the lens and the surrounding image we decrease the error in the detection of the surface due to the use of the Sobel's filters. On one hand, this causes the variation of the levels of gray to occur in few pixels and, on the other hand, the range of possible values of the module of the gradient on the edge is reduced. However, it is important not to saturate the pixels outside the lens, since we might be also saturating pixels of the edge that reflect or refract some light, thus "shrinking" the lens. Therefore, it is important to find a time of exposition that guarantees levels of gray as highest as possible but without coming to their saturation.

- Resolution of the image: the higher the resolution of the image, the higher the accuracy in the characterization of the surface of the lens. However, it is also necessary that in such an image we can record large enough sections of the incoming and outgoing beams as to ensure an accurate fit of such beams. In the experimental results that will be shown in this paper a resolution of ~ 18.5 μm/pixel is used for MC (this is an average resolution, since distortion makes it to change throughout the image).

- Geometrical modification of the lens throughout the image capture: in spite of not having found any related comment in the literature of optical characterization of the lens, we have noticed that the lens swells throughout the whole experimental procedure. According to what was explained in section 1.4, this fact is not really surprising, given the metabolic dependence of the lens regarding its external medium. In fact, this swelling is much more visible in its anterior surface, where the epithelium plays an essential role in the transport of solutes between the aqueous humour and the interior of the lens (see section 1.2.2). Therefore, the choice of a proper biocompatible solution is important to reduce as much as possible the variation of the shape of the lens during the data collection. Throughout our research we have used three different solutions:

- A 0.9% NaCl solution in distilled water [Pri99].
- A phosphate-buffered saline solution (pH = 7.4) (P-4417 [Sgm], Sigma) [Axe88, Gar01, Jon05].
- A solution specially designed for surgery purposes in the anterior chamber of the eye (BSS Plus® [Bss], Alcon), that, besides of the buffer (pH = 7.6), has several essential metabolites among which stand out the glutation (an antioxidant) and the glucose.

To compare the effect of each one of the solutions in the pig lens we have studied the swelling produced by them in an interval of 50 minutes. This is the approximate elapsed time between the images of the lens recorded before the first and the third projection, since this is the maximum number of projections we will work with. As it can be seen in figure 6.15 and in table 6.2[1], the solution that produces a larger swelling is the phosphate-buffered solution, which in many cases also causes lack of transparency. This latter point is not surprising if such a swelling is caused by an important alteration in the exchange of solutes and liquids between the lens and the outside. On the other hand, the solution that produces a lower variation of the shape of the lens is the BSS Plus®, because of being more chemically similar to the humours in which the lens is immersed in the eye ball. Nevertheless, the fact that there is still a noticeable swelling and that the solution BSS Plus® lose some of its features six hours after its preparation force us to reduce as much as possible the procedures of alignment (see section 6.1.1), as well as the number of projections and rays that constitute them. In the retrieval of the gradient index we will use as surfaces of the lens those obtained in the second projection so that the average variation of the shape of the lens does not exceed 20-30 μm.

In the case of the fish lens the noticed swelling is much lower, as well as its demands regarding the solution of immersion. Thus, for the phosphate-buffered solution the swelling noticed in an interval of 50 minutes is of the order of 0.1%, much lower than in the case of the pig lenses. Besides other metabolic reasons, the main reason might be the higher rigidity of the fish lenses, that would not allow modifications of its shape as noticeable as those of the mammals.

[1] Although the results are those obtained for a crystalline lens in each one of the solutions, such results are representative of more cases.

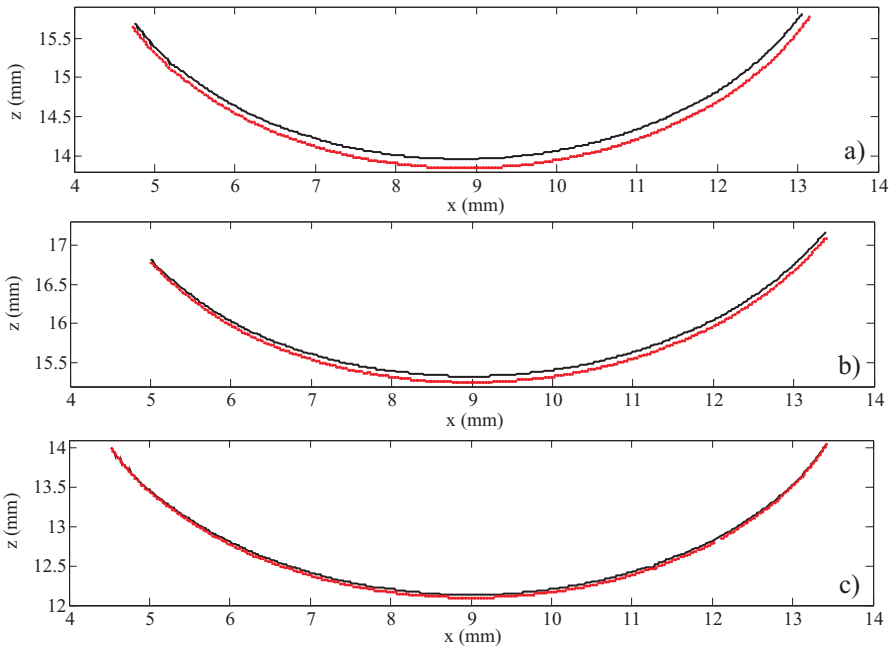

Figure 6.15: Points of the anterior surface detected by Sobel's filters in an interval of 50 minutes (black line in the beginning and red points at the end of the interval). The results are shown for three different solutions: (a) phosphate-buffered saline solution (P-4417, Sigma); (b) saline solution (0.9% NaCl in distilled water); (c) BSS Plus® solution of Alcon.

Solution	**Δant. sur.** (μ**m**)	**Δpos. sur.** (μ**m**)	**Swelling (%)**
Buffered saline solution	108.6	64.5	2.3
Saline solution	68.0	42.5	1.5
BSS Plus®	28.7	10.6	0.5

Table 6.2: *rms* variation of the anterior surface (**Δant. sur.**) and of the posterior surface (**Δpos. sur.**) of the lens in an interval of 50 minutes, as well as the resulting swelling in relation with the thickness of the lens.

6.2.3 Collection of the input data of the tomographic algorithm

Once obtained the slopes and the intercepts of the entry and exit rays and the surfaces of the lens, all data have to be referenced with regard to the same coordinate system. Thus,we can calculate the points of intersection of the beams with those surfaces and obtain θ_p, B_{pr}, C_{pr} and $\sin\alpha_{pr}(x,t)$.

Other data that are obtained from the anterior processings are those of the entry beams as seen from AC, useful to align the setup. Besides, this processings are also useful to characterize the edges of the glass cell and the level of the solution. With this information it is possible to level the cameras and the glass cell.

6.3 Calibration of the experimental setup

Throughout the previous sections we have explained different sources of error that will affect the accuracy of our measurements. It is obvious that if we wish a good tomographic reconstruction of the gradient index we have to quantify and minimize the effect of those sources of error in a previous calibration of the experimental setup. The best way to do it is to use a lens of which we have an accurate knowledge of its optics and geometry and to reproduce with it all the experimental procedure in the same fashion we would do it with an actual lens. All discrepancy between the theoretical and experimental results will be indicative of errors we will have to correct or, at least, take into account. To carry out the calibration, we have worked with a spherical BK7 lens with known diameter and refractive index ($\emptyset = 10000 \pm 5$ μm; $n(\lambda = 633\text{ nm}) = 1.51509$). In this calibration we will consider the following three points:

1. Checking and refinement of the correction of the distortion in MC.
2. Search of the best threshold for the detection of the rays.
3. Detection and minimization of misalignments.

None of the published works where ray deflectometry has been used in crystalline lenses show accurate data of the calibration of the setup. However, to make a realistic estimation of the accuracy and validity of the retrieved gradients a correct previous calibration of the setup is needed.

6.3.1 Checking and refinement of the correction of the distortion in MC

In section 6.2.1.1 we explained that the distortion is corrected by using an array of dots equally spaced 500 μm, with dots of a diameter of 200 μm. This array was created

with a graphic design software and afterwards printed with a laser printer at its higher resolution (1200 points per inch $\simeq$ 21 microns/point). To verify the spacing between dots we firstly used a microscope with an accuracy of 10 μm and we measured the spacing in random positions of the array, obtaining an average value of 500 ± 20 μm. By using this information as an initial value we took several images of the calibration lens and fitted its surface as it is explained in section 6.2.2. As a result of the fitting we obtained an average value of the radius of the lens of $\bar{\emptyset} = 10031.4 \pm 0.6$ μm. According to this value and to the theoretical diameter we could determine better the spacing between the dots of the array of correction of the distortion, with a final value of 493.5 ± 0.4 μm. Besides, we could also check the good performance of the correction of the geometrical distortion, with standard deviations of 7 μm in the fitting of the profile of the lens to a circumference, of the same order than the accuracy of the diameter provided by the manufacturer.

6.3.2 Search of the best threshold for the detection of the rays

We had seen that the calculation of the beam centroids depends on the level of gray chosen as threshold between the background of the image and the laser beam (see section 6.2.1). Depending on the chosen level of gray the approximation of the beam as a straight line will more or less accurate, what reveals its importance. In our case, we have used the spherical lens to find the best threshold. Once known the external index and the radius and index of the lens, we can calculate the parameters of the exit ray that corresponds to any entry ray. According to the difference between the theoretical and experimental exit ray we can quantify the influence both of the threshold used in the fitting of the laser beams and the misalignments of the experimental setup. Therefore, to characterize both effects we carried all the experimental procedure with the spherical lens as it was an actual crystalline lens, analyzing later the difference between the theoretical and the experimental behaviour of the lens for different thresholds.

According to the experimental protocol explained in section 6.1.1 and once immersed the lens in deionized water ($n_{ext}\,(\lambda = 633$ nm; $T = 19^{o}$ C) $= 1.3318 \pm 0.0002$), we took the images corresponding to three projections spaced about 20^{o} ($\theta_1 = 0.56^{o} \pm 0.02^{o}$, $\theta_2 = 21.21^{o} \pm 0.05^{o}$, $\theta_3 = 38.90^{o} \pm 0.04^{o}$), scanning the 90% of the aperture of the lens with laser beams equally spaced 125 μm. In addition, we recorded the images of 15 beams at each side of the lens for the calculation of its entry slope (see section 6.2.1, point 3). Once characterized the surface of the lens, we fitted the entry and exit beams with different thresholds, with values that range from 250 (slightly above the level of gray of the image background) and 625 (slightly above the minimum value that reach the maxima of

intensity of the beams). Later, for each threshold and each projection we calculated the root mean square of the difference between the theoretical and experimental distributions of sines of deflection at the exit of the lens (see Fig. 6.16). From the analysis of that difference we decided to select the threshold value of 437, because of producing a low and stable error in relation with the closer levels of gray. For the camera AC we follow a similar procedure.

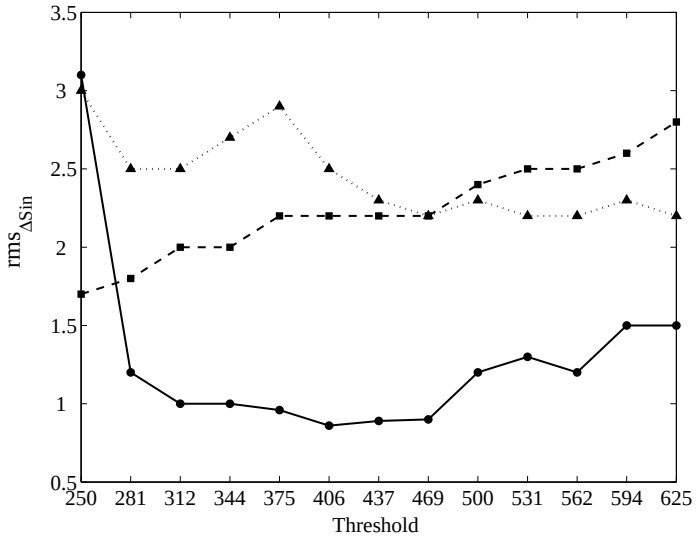

Figure 6.16: Variation with the threshold of the *rms* error in the sines of deflection at the exit of the lens for θ_1 (solid line and circles), θ_2 (dashed line and squares) and θ_3 (dotted line and triangles).

6.3.3 Detection and minimization of misalignments

Once selected a threshold, the data of the previous procedure were used to detect the misalignments of the experimental setup. Among these misalignments we are interested in two:

- The misalignment between the meridional plane of the lens and that containing the laser beams throughout one projection [Lop02, cap. 4].
- The misalignment between those two planes, that theoretically should be the same, and the object planes of the alignment and measurement cameras [Lop02, cap. 4].

In figures 6.17, 6.18 and 6.19 (see pages 116-117) the error in the experimental sines of deflection on the exit surface of the lens is shown. From its study it is inferred that:

1. Whereas for the first projection the error does not seem to follow a defined trend, there is one at the extremes of the distributions of the second and third projection. This trend is different in each of the two cases. Therefore, the most likely reason is a variable misalignment between the meridional plane of the lens and that containing the entry beams. As it was explained in section 6.1.1, we check both planes are aligned in the first projection, by displacing the lens so that its meridional plane fits in with the plane of the laser beams. In the following projections we just place the entry beam within that same plane, of which we know its relative position regarding AC. According to table 6.1, the error in this repositioning of the entry beam can reach the third decimal digit in the slope and 0.2 pixels in the position, what might explain the noticed misalignment. Other factor to take into account is the variation with θ of the accuracy of the fitting of the laser beams. As θ increases, AC images a beam that extends partially along its optical axis so that it does not end up properly focused in all its length. Although no variation is noticed in the precision of the fitting in relation with $\theta \simeq 0^{o}$, the fitted beam show different intensity distributions in each case and that affects the accuracy of the fitting. In fact, throughout each projection, when comparing from AC the variation of the slope and the intercept at the exit of the lens with regard to the non deflected beam, such a variation is larger in the second and third projections, with *rms* values of $\sim 5 \times 10^{4}$ and ~ 0.1 pixels, respectively.

2. The error in the distribution of sines at the exit of the lens rises with θ as a result of the misalignment between the meridional plane and the laser beam (see table 6.3). Even so, its *rms* value is not higher than 2.3×10^{-3} for an aperture of 90% and when this is reduced to 80% the effect of the misalignment is not noticeable, with an *rms* error lower than 1×10^{-3} in the three cases.

3. The experimental data of each one of the projections can be used to retrieve the value of the refractive index of the lens by using the tomographic algorithm. In this case just one projection is needed, due to the spherical symmetry, and one iteration, since the approximation of the trajectories as straight lines is exact. Therefore, the retrieved index provides an idea of the accuracy the algorithm can achieve with all the required tomographic information and once known the trajectories of the rays inside the lens, as well as its ability to calculate the piston and the index separately. In fact, this case is exactly the one proposed in section 4.3.1 (see Fig. 4.6) to explain the influence of the piston K on the calculation of the refractive index, where the rays were supposed to be straight lines. Thus, the equation 4.20

would be written in this case as

$$\tilde{S}\left(B_iC_i\right) = \int_{-\sqrt{R^2-x_i^2}}^{\sqrt{R^2-x_i^2}} n\left(x,z\right)\mathrm{d}z - K = \int_{-\sqrt{R^2-x_i^2}}^{\sqrt{R^2-x_i^2}} \left[cte - \frac{K}{\sqrt{R^2-x^2-z^2}}\right]\mathrm{d}z, \tag{6.6}$$

As it can be seen in table 6.3, for θ_1 the error in the retrieved refractive index in relation with the actual one is that of a commercial Abbe refractometer. For θ_2 and θ_3, this error rises due to the higher error in the experimental data, but it does not become higher than 1×10^{-3}. By applying the Snell's law to each pair (entry ray)-(exit ray) the index of the lens can be also calculated by least squares fitting [Mar78, Lop02, cap. 4], obtaining in this case results up to one order of magnitude worst than the tomographic ones, although the error is not yet higher than the third decimal digit of the index.

	$\mathbf{\Delta}\sin_{\mathbf{90\%}}$	$\mathbf{\Delta}\sin_{\mathbf{80\%}}$	$\mathbf{\Delta n_{Snell}}$	$\mathbf{\Delta n_{tomo}}$
$\theta_\mathbf{1}$	8.9×10^{-4}	8.9×10^{-4}	1×10^{-3}	2×10^{-4}
$\theta_\mathbf{2}$	2.2×10^{-3}	9.3×10^{-4}	9×10^{-4}	4×10^{-4}
$\theta_\mathbf{3}$	2.3×10^{-3}	9.8×10^{-4}	3×10^{-3}	7×10^{-4}

Table 6.3: For each one of the projections the *rms* error of the sines of deflection is shown for a 90%, $\mathbf{\Delta}\sin_{\mathbf{90\%}}$, and a 80%, $\mathbf{\Delta}\sin_{\mathbf{80\%}}$, of the aperture of the lens, as well as the error in the calculation of the homogeneous index by Snell, $\mathbf{\Delta n_{Snell}}$, and the tomographic algorithm,$\mathbf{\Delta n_{tomo}}$, from the experimental data.

4. According to the errors obtained for the sines of deflection and the results of the numerical simulations (see chapter 5) we can make a initial estimation of the order of magnitude of the *rms* error in the retrieval of the gradient index in crystalline lenses. Thus, in fish it is reasonable to expect gradients with a maximum error of the third decimal digit of the index. In lenses like those of human beings or similar, this upper bound of the error could reach up to a very low second decimal digit in

the worst of cases, but accuracies in the third decimal digit are also possible, the more possible the weaker the gradient index.

In order to ensure the experimental errors are within the mentioned orders of magnitude, we have calibrated the experimental setup each time we have used it, although just for one projection. Besides, to avoid wasting the biocompatible solution and to make use of the alignment that results from the calibration, such a calibration has been carried out with deionized water that is removed with a syringe at the end of the calibration. Thus, we have not moved neither the glass cell nor the rest of the setup. With another syringe we have added the biocompatible solution where the lens is eventually immersed.

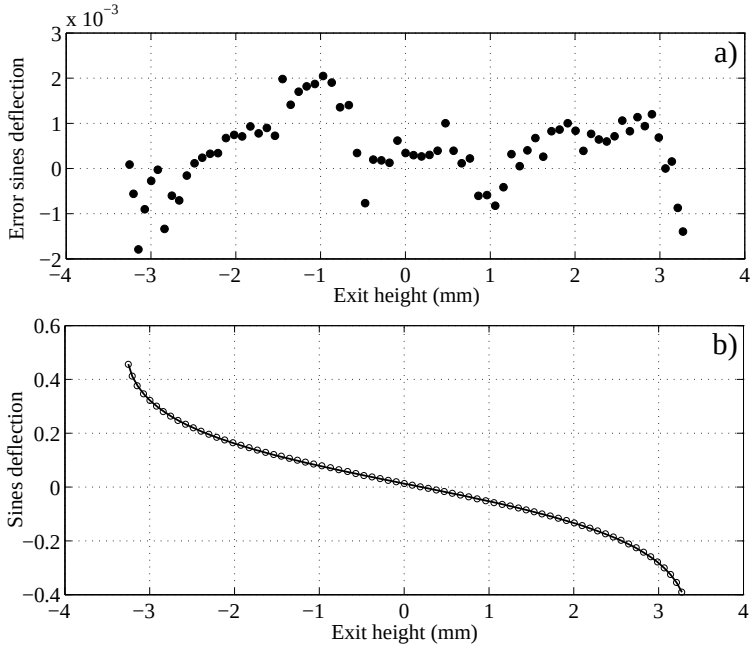

Figure 6.17: Distribution of the theoretical (solid line) and experimental sines of deflection (circles) at the exit of the lens (b), as well as the difference between both (a) for the case of θ_1.

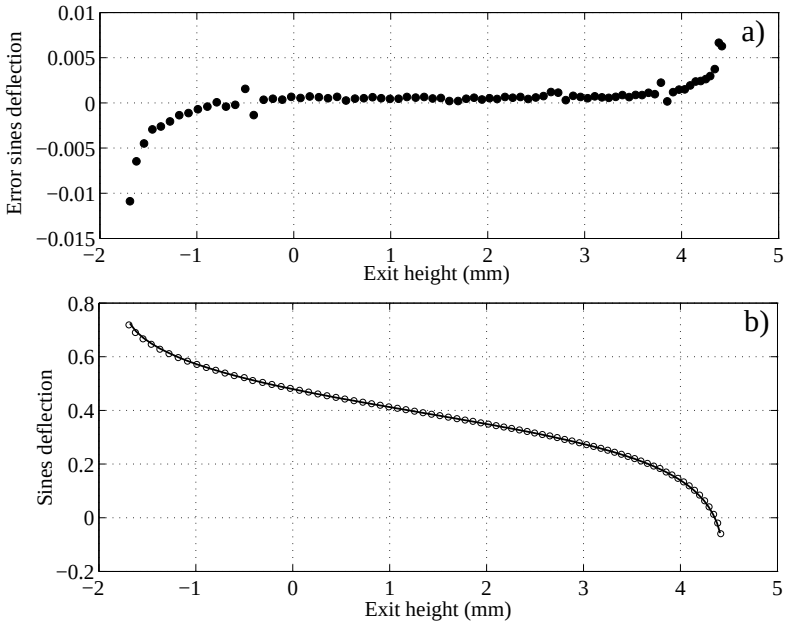

Figure 6.18: Distribution of the theoretical (solid line) and experimental sines of deflection (circles) at the exit of the lens (b), as well as the difference between both (a) for the case of θ_2.

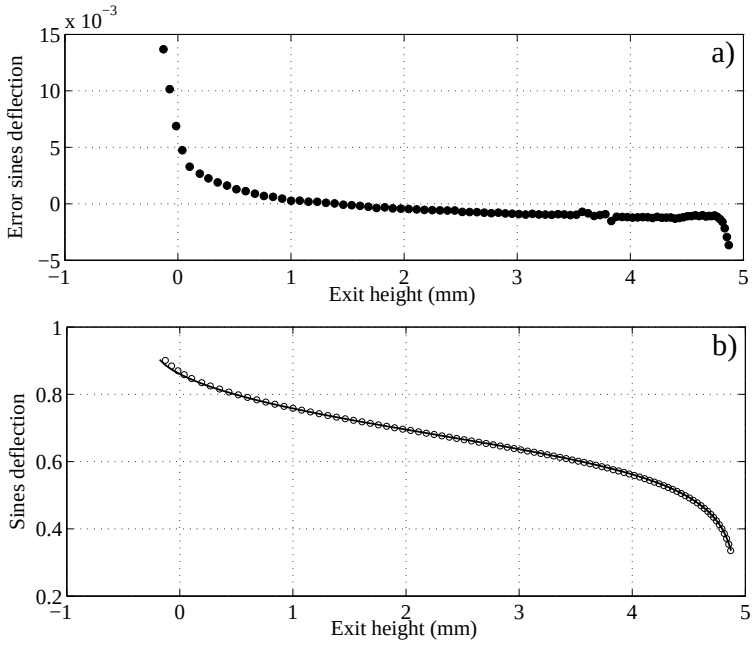

Figure 6.19: Distribution of the theoretical (solid line) and experimental sines of deflection (circles) at the exit of the lens (b), as well as the difference between both (a) for the case of θ_3.

7 Experimental results

In this last chapter we will show the results obtained with the experimental implementation of the tomographic method of reconstruction of the gradient index. A first section will be focused on the teleost fish lenses, which, as it was mentioned before (see section 5.2), are approximated as spherical symmetric gradient index lenses. Next, we will study the most general case of the rotational symmetry through the gradients retrieved for pig lenses. For each case, fish and pigs, we will analyze the accuracy with which the retrieved gradients reproduce the optical behaviour of the lenses, as well as the approximation of spherical and rotational symmetry, respectively.

7.1 Teleost fish lenses (spherical symmetry)

Besides its availability, the spherical symmetry makes the teleost fish lenses a perfect lens to carry out an initial check of the tomographic method. By assuming accurate this symmetry, any of the meridional planes of the lens shows a radially symmetrical gradient index $n(r)$ with a functional form that can be written as a particular case of the equation 4.11:

$$n(r) = n_0 + n_1 r^2 + n_2 r^4 + \ldots = \sum_{i=0}^{M} n_i r^{2i}, \tag{7.1}$$

where $r = \sqrt{x^2 + z^2}$ is the radial coordinate. Consequently, the tomographic inversion of the algorithm is simplified because of reducing the number of the modal coefficients of the gradient, what, on the other hand, should make this inversion more robust against the experimental errors. In addition, no more than one projection is needed to perform the inversion, what simplifies not just the experimental procedure but the mounting needed to implement it. For these reasons, the first experimental works we carried out were aimed at retrieving the gradient index of this kind of eye lenses [Vaz03, Aco05]. We did not start the experimentation on lenses with a more general rotational symmetry, final objective of this work, until we did not show the good performance of the method for the particular case of the spherical symmetric lens.

In table 7.1 it can be seen the data corresponding to five fish lenses, representatives

of those used throughout our experiments. The three species to which they belong are included in three different taxonomic families (*centrolophidae* (1-3), *polyprionidae* (4) and *berycidae* (5)) and two different taxonomic orders (*perciformes* (1-4) and *beryciformes* (5)). This should make the sample more representative as for the possible evolutive solutions of the gradient index. For each one of the lenses, we tomographed 90% of their equatorial plane (that orthogonal to the optical axis) with 80 equally spaced laser beams ($\lambda = 594$ nm), being the lenses immersed in a phosphate-buffered saline solution ($n_{ext} = 1.3345$, measured for $\lambda = 589$ nm at 22 ^{o}C). In all cases we see the best fitting of the equatorial plane is a circumference ($SD_{ajuste} \simeq 30$ μm). Thus, it is reasonable to assume that, at least at this plane, such lenses show a gradient with a functional form that follows that of the expression 7.1. Therefore, in the tomographic inversion (see Eq. 4.16), instead of a more general form 4.11, we consider directly the expression 7.1, calculating its coefficients n_i by least squares fitting.

Lens	**Species**	$\boldsymbol{R}$ **(mm)**	$\overline{\boldsymbol{dc_p}}$ **(R=1)**
1	*Hyperoglyphe antarctica*	12.225 ± 0.002	1.35 ± 0.03
2	*Hyperoglyphe antarctica*	12.140 ± 0.002	1.36 ± 0.04
3	*Hyperoglyphe antarctica*	13.368 ± 0.002	1.35 ± 0.03
4	*Polyprion Oxygeneios*	8.304 ± 0.002	1.38 ± 0.03
5	*Beryx Decadactylus*	8.631 ± 0.003	1.33 ± 0.03

Table 7.1: Features of five representative crystalline lenses, where R is its radius and $\overline{dc_p}$ the distance between the point where the rays intersect the optic axis and the posterior vertex of the equatorial plane of the lens (*Hyperoglyphe antarctica*: Bluenose; *Polyprion Oxygeneios*: Hapuka; *Beryx Decadactylus*: Alfonsino).

By applying the tomographic algorithm to the experimental data of each one of the lenses we obtained their respective coefficients n_i, with around 5 iterations (10 interpolated points) (see section 4.3). In table 7.2 the resulting orders M are given for each case, as well as the standard deviation of the tomographic fitting, SD_{tomo}. Besides, with the obtained geometries and gradients, we propagated the experimental entry beams and we compared the resulting optical behaviour with that experimentally recorded through the following optic parameters:

- $rms_{\Delta S}$, the *rms* error of the distribution of the optical path in the straight line

tangent to the exit lens vertex ($z = t$), where the piston retrieved by the algorithm is included.

- $PV_{\Delta S}$, the peak-valley error of that same distribution of optical paths.
- $rms_{\Delta sin}$, the *rms* error in the distribution of the sines of deflection of the exit rays at $z = t$.
- $PV_{\Delta sin}$, the peak-valley error of that distribution of sines.
- Δdc_p, the relative average error in the posterior vertex distance, i.e. the distance between the posterior vertex[1] of the equatorial plane of the lens and the point where the rays intersects the optic axis.

	Lens 1	**Lens 2**	**Lens 3**	**Lens 4**	**Lens 5**
$\boldsymbol{M}$	2	2	2	2	3
$\boldsymbol{SD_{tomo}}$ $\boldsymbol{(\lambda)}$	11.5	14.1	7.6	4.8	1.1
$\boldsymbol{rms_{\Delta S}}$ $\boldsymbol{(\lambda)}$	11.1	12.8	7.4	4.4	1.1
$\boldsymbol{PV_{\Delta S}}$ $\boldsymbol{(\lambda)}$	23.2	25.9	16.5	11.0	4.1
$\boldsymbol{rms_{\Delta sin}}$	5.5×10^{-3}	5.7×10^{-3}	6.5×10^{-3}	4.2×10^{-3}	2.2×10^{-3}
$\boldsymbol{PV_{\Delta sin}}$	3.3×10^{-2}	2.6×10^{-2}	3.2×10^{-2}	3.2×10^{-2}	1.7×10^{-2}
$\boldsymbol{\Delta dc_p}$ **(%)**	2 ± 2	2 ± 2	3 ± 2	1 ± 1	1 ± 1

Table 7.2: List of the parameters indicative of how accurately the retrieved gradient indices reproduce the optical behaviour of the eye lenses.

(In Appendices A and B it can be seen all data and graphs resulting from the tomographic retrieval and optical propagation for the crystalline lenses that give rise to the worst and best tomographic retrieval, lens 3 and 5, respectively).

From the analysis of the results of table 7.2 we deduce that:

1. Both in the final order of the retrieved gradient and the accuracy of the reproduction of the optical behaviour, lenses 1-4 are different to 5. This can be due to:

[1] In this section, the term posterior is referred to the surface of the lens through which the rays leave the lens.

a) Experimental errors: as it was explained, the experiments with fish lenses correspond to the first stages of this research. Because of this, the experimental setup used with these lenses do not correspond exactly with that described in chapter 6. As a result, the magnitude of the experimental errors is higher in the first analyzed lenses (1-4) that in the last ones (5), where the setup was more similar to that used with pig lenses.

b) Differences among species: when studying the distribution of sines of deflection at $z = t$ (see Appendices A and B) it stands out the existence of an important change in the deflection of the rays that takes place in a radial position quite constant among species, $x\,(z = t) \simeq 0.4\ (R = 1)$ [Vaz03]. This behaviour may be related with the multifocality proposed in reference [Kro99] in order to offset the chromatic aberration. It might also be due to degenerative processes inside the lens, although in the shown cases we have always tried to work with lenses as fresh as possible. Anyway, this "bump" in the deflection angles seems to be different among species and in the case of lenses 3 and 5 it is clear it is sharper and more irregular in the first than in the second of cases, where it changes more monotonically (see distributions of posterior vertex distances in Appendices A and B). Such changes in the distribution of sines can be difficult to follow by a relatively smooth model of gradient, as that proposed in 7.1, what affects negatively to the accuracy of the retrieval. The alternative would be to use a model like that of 7.1 but ring-wise, assuming a continuity of at least class 0 between rings.

2. In the expression 5.8 the average error in the sines of deflection was related with the average error in the calculation of the gradient index. From the application of this relationship to the error of the sines in table 7.2 we deduce that the error in the calculation of $n\,(r)$ is of the order of the high third decimal digit in lenses 1-4 and in the low third in lens 5. This conclusion is supported by the calculation of the average gradient of the five retrieved cases and their standard deviation (see Figs. 7.1 and 7.2), where such a deviation is of that order of magnitude. The fact that the error is higher at the surface (see table 7.3) could be explained according to what was explained in section 4.3.1 about the influence of the piston on the retrieval of the gradient index. Indeed, figure 7.2 shown a similar behaviour to that shown in chapter 5 (see Fig. 5.1), where it was shown that the accuracy of the retrieval was lower at the surface. A variability among species can not be ruled out either, but that would require a very detail study of much more cases.

Anyway, it is outstanding the high resemblance of the gradient index obtained for three different species, what would confirm the idea of a "unique solution" shared by all of them with slight variations, as it might be the mentioned multifocality. From a physiological point of view this is not so odd if we consider that, once set the geometry, the only thing that could affect the distribution of the refractive index is the metabolic rate of generation of the different crystallin proteins in the process of cellular differentiation, the proportion among them and the final resulting concentration. If theses three parameters are not too different among species, great changes in the gradient index should not be expected.

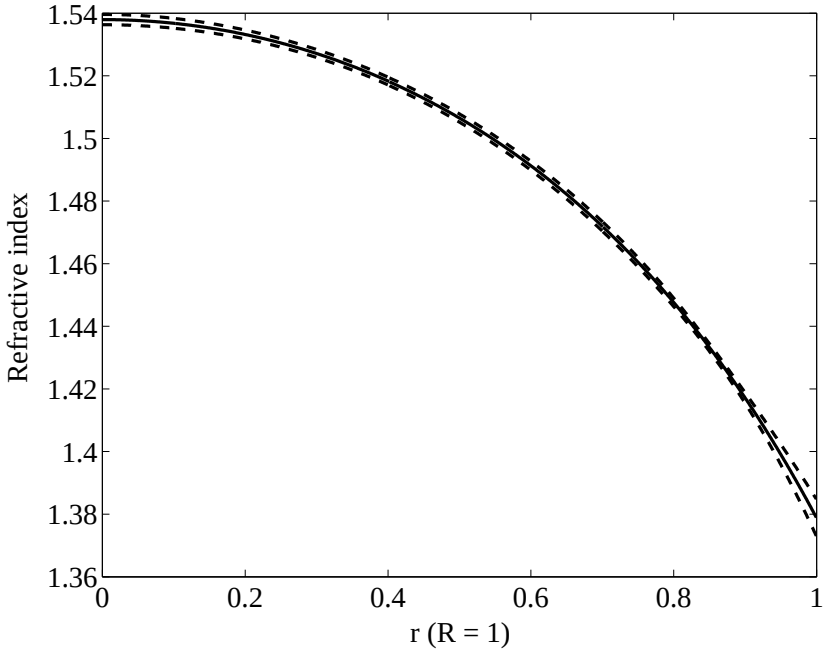

Figure 7.1: Average gradient obtained from those of lenses 1-5, with confidence intervals that represent the standard deviation of the index value at each point.

n_0	n_1	n_2	n_3	$\overline{n}_c$	$\overline{n}_s$
1.5380	-0.1183	-0.0264	-0.0143	1.538 ± 0.002	1.379 ± 0.006

Table 7.3: Coefficients n_i of the average gradient index fitted to the expression 7.1 ($SD_{fit} = 2.8 \times 10^{-8}$), as well as the average values of the central, $\overline{n}_c$, and surface index, $\overline{n}_s$.

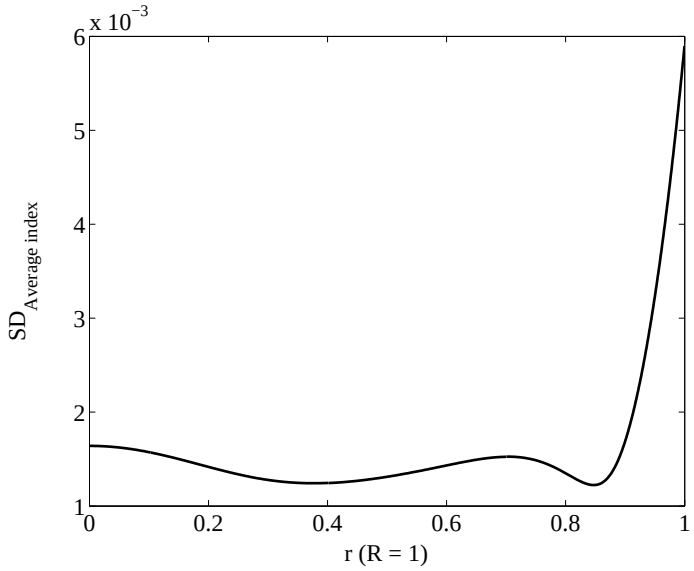

Figure 7.2: Standard deviation of the values of the average refractive index at each point of r.

7.1.1 Analysis of the spherical symmetry in teleost fish lenses

So far we have just shown results obtained for the equatorial plane of the lens. This is not by chance. Throughout our experiments we could realize that, if we did not take into account the orientation of the lens, the distribution of the sines at its exit was not always symmetrical about the optic axis, even once corrected the misalignments and the entry angle of the laser beams. When checking how that symmetry changed with the shape of the profile of the lens, we noticed that its origin was in the lack of spherical symmetry of the fish lenses. This made us to think about how accurate was the approximation of spherical symmetry and the error this approximation involved in the optical behaviour of the lens. Next, we show three evidences with which we assess the degree of non sphericity of the teleost fish lenses and with which we analyze this lack of symmetry from the different but complementary perspectives: the determination of the profile of the sagittal plane (the plane that contains the optic axis), the study of the distribution of the sines of deflection at the equatorial and sagittal planes and the analysis of the interferograms at the exit of the lens.

7.1.1.1 Profile of the sagittal plane

For each one of lenses 1 to 5 we also recorded an image of their sagittal plane, that which contains the optic axis and, therefore, has a great importance in the optical behaviour of

the lens. After fitting their anterior and posterior profiles according to what was explained in section 6.2.2 we found out that the best fit for each one of them was a semiellipse with the parameters shown in table7.4. These results shown clearly that the sagittal profile is not spherical, with asphericities significantly different from zero. Indeed, whereas in the case of lens 4 the sagittal plane could be approximated as a unique ellipse, in the other two lenses the plane is bielliptical with a posterior asphericity lower than the anterior one. This fact agrees with what is notices in pig lenses, as it will be shown later, as well as in many other animal species. These data are representatives of those calculated for the sagittal planes of other teleost fish lenses.

	Lens 2	**Lens 3**	**Lens 4**
$\boldsymbol{R_{eq}}$ **(mm)**	12.140±0.002	13.368±0.002	8.304 ± 0.002
$\boldsymbol{R_{sag\ ant}}$ **(mm)**	12.934±0.001	14.279±0.001	8.727 ± 0.001
$\boldsymbol{Q_{sag\ ant}}$	0.156 ± 0.008	0.17 ± 0.01	0.12 ± 0.01
$\boldsymbol{R_{sag\ post}}$ **(mm)**	12.638±0.001	14.096±0.001	8.786 ± 0.001
$\boldsymbol{Q_{sag\ post}}$	0.100 ± 0.009	0.128 ± 0.007	0.13 ± 0.02

Table 7.4: Anterior and posterior sagittal asphericities and radii of crystalline lenses 2-4, as well as their equatorial radius.

7.1.1.2 Distribution of the sines of deflection at the exit of the lens

As we mentioned before, in our experiments we could notice the distribution of sines at the exit of the lens varied with its orientation. This can be seen in figure 7.3, where it is shown that the difference in the sines of deflection at the exit of the lens between the equatorial and sagittal plane can come to be of the order of the second decimal digit. Therefore, any model of the gradient of fish lenses that intends to reproduce its optical behaviour with a higher accuracy can not keep on assuming a spherical symmetry, at least not for any fish. Taking into account the expression 5.8 and the results obtained in the numerical simulations of section 5.2, not to take into account the lack of spherical symmetry could lead to errors of up to the second decimal digit of the index in the retrieved gradient index.

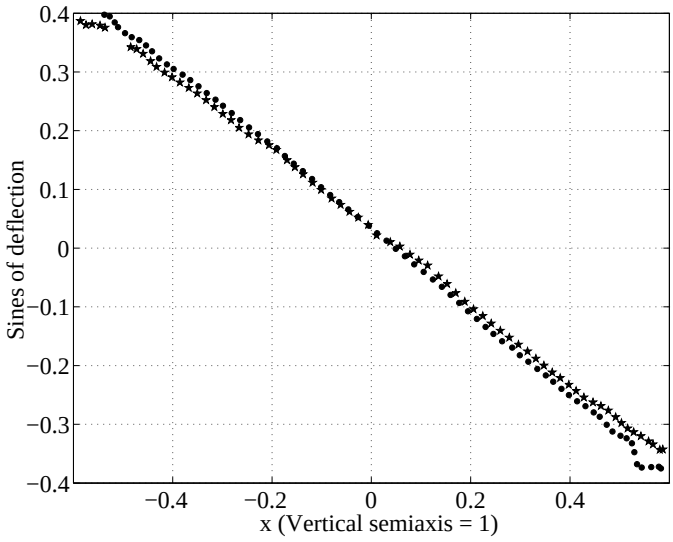

Figure 7.3: Comparison of the distributions of the sines of deflection at the exit of lens 4 at its equatorial (circles) and sagittal plane (stars). Because of being obtained both distributions for laser beams with the same entry angle and being this angle slightly different from zero, none of them is centered at (0,0).

7.1.1.3 Study of the phase at the exit of the lens by means of the interferometry

In the former points we have studied the lens at just one of its planes, working always with bidimensional incident wavefronts. However, by using a modified point diffraction interferometer [Aco06] it is possible to study and to characterize the whole phase at the exit of a lens for tridimensional incident wavefronts. This way is much easier and more immediate to study a lack of symmetry in the optical behaviour of the lens. The procedure is similar to that used in reference [Aco06]. The difference is that in this case the crystalline lens is the lens used to focalize a plane wavefront on a semitransparent plate with a diffraction hole (or on a point nearby such a hole). The recorded interferogram is the result of the interference of the wavefront that leaves the lens with a spherical wavefront centered at the proximities of the focus of the eye lens. In our case, we illuminated with a plane wavefront the crystalline lenses of two species, *Trachurus trachurus* (Horse mackerel, Fam. *Carangidae*, Order *Perciformes*) and *Pagellus Bogaraveo* (Sea bream, Fam. *Sparidae*, Order *Perciformes*), with radii comprised withing the range of 4 and 5 mm. In both species, when the sagittal plane contained the optic axis of the interferometer it was always noticed that the resulting interferogram was very radially symmetrical (see Fig. 7.4). However, when the equatorial plane contained such an optic axis, the fringes of the interferogram became elliptical, with axes that followed the

rotation produced on the eye lens..

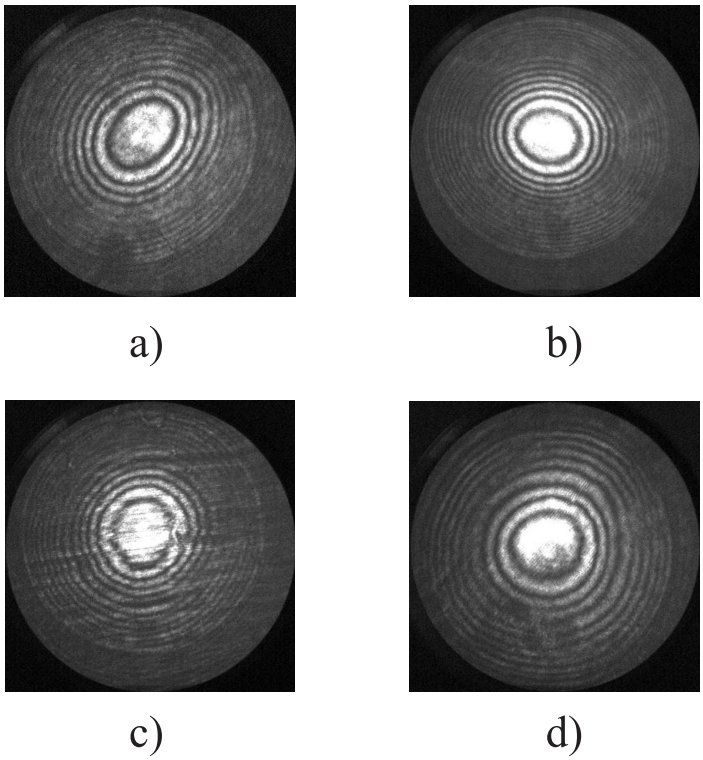

Figure 7.4: Interferograms at the exit of a lens of *Pagellus Bogaraveo* as this lens is rotated from a position where the optic axis of the interferometer is contained by its equatorial plane up to other where it is contained by the sagittal one. From the analysis of the most internal fringes of the interferograms we have calculated the *rms* deviation of the wavefront regarding a radially symmetric interferogram: $\varepsilon = 2.2\,\lambda$ (a), $\varepsilon = 0.99\,\lambda$ (b), $\varepsilon = 0.66\,\lambda$ (c) and $\varepsilon = 0.3\,\lambda$ (d).

Other feature that can be seen in the interferograms of figure 7.4, and that *a priori* has nothing to do with the lack of symmetry of the lens, is the existence of different focal zones.

Taking into account all what has been previously show it is obvious that in the future it will be necessary to consider and to study more general models than those spherically symmetrical to describe the teleost fish lenses. A rotationally symmetrical model about its optic axis is a good first option.

Once checked the good performance of the tomographic method in a radially symmetric distribution of the refractive index we go on the last part and final aim of this work: to apply the method in a crystalline lens similar to the human one and to study the obtained

results, as well as their accuracy.

7.2 Pig lenses (rotational symmetry)

The pig lens, like that of many other mammals, is asymmetrical about its equatorial plane, with clearly different anterior and posterior surfaces [2]. Besides, the fact the pig hardly accommodates is related to a more rigid crystalline lens that is easier to handle than that of animals with a larger accommodation, like the human beings [Vil01]. For these reasons and its availability, we have chosen the pig lens to experimentally check the accuracy of our tomographic method in the retrieval of rotationally symmetrical gradient indices.

The eye lenses used in our experiments were extracted from the eye ball in a time no longer than 8 hours after the death of the animal in the local abattoir. Before the extraction, the experimental setup (see chapter 6) was calibrated as it is explained in section 6.3, by using deionized water as immersion medium of the homogeneous lens. Once finished the calibration, the water was replaced by BSS Plus® ($n_{ext} = 1.3338$, measured for $\lambda = 633$ nm at 20 ^{o}C), a biocompatible medium that minimizes the degradation of the lens and that keeps its properties for six hours after its preparation. Since each projection means about 25-30 minutes including the alignment and the data collection, in order to tomograph at least three eye lenses the number of projections was limited to three (θ_1 $\sim 0^{o}$, θ_2 $\sim 20^{o}$, θ_3 $\sim 40^{o}$) and the number of rays per projection to about seventy (see table 7.5). This decision is justified in the numerical simulations of section 5.3, where we showed that in these conditions it is possible to obtain gradient indices with an average accuracy that in the worst of cases would be of the order of the second decimal digit of the index. Regarding the aperture of each one of the projections, in table 7.5 it can be seen that this aperture[3] diminish for larger incidence angles, due to the vignetting produced by the lens itself and the remains of the ciliary body. On the other hand, as it was explained in section 6.1.1, the most curved surface of the lens, the posterior one, was oriented always towards the base of the glass cell to prevent as much as possible the supporting plate from affecting the characterization of the lens profile (see Fig. 7.5). As a result, the propagation of the laser beams is the opposite to the natural direction of light in the ocular system, since they enter the lens by its posterior surface

[2] In this section we label as anterior surface of the lens that which is oriented towards the cornea and posterior surface that which is oriented towards the retina.

[3] We define aperture as the portion of the entrance pupil illuminated by the laser beams, regardless of the position of this portion in relation with the axis of the lens. Thus, as θ increases the aperture decreases and it becomes more eccentric.

and they leave the lens by its anterior surface, something that does not affect at all the tomographic retrievals.

	1st projection	**2nd projection**	**3rd projection**
$\boldsymbol{\theta}$ (°)	3 ± 3	21 ± 3	39 ± 3
Aperture (%)	93 ± 2	82 ± 7	60 ± 6
Number of rays	73 ± 4	71 ± 7	70 ± 7

Table 7.5: Average parameters of the projections, where the angle θ is referred to the optic axis of the lens and the aperture to its equatorial diameter.

In the beginning of the first projection and at the end of all an image of the lens profile was recorded (see Fig. 7.5 in page 131). Whereas the whole of the images allows to determine how much the profile has changed between projections, it is the image recorded for the second projection the one we use to mathematically characterize it. Thus, according to what was explained in section 6.2.2 we fitted the anterior and posterior surfaces. Since in the pig lenses we checked that the best fitting always involved a $Q > 0$ for both surfaces, we modified the equations 6.2-6.5 to directly fit an ellipse plus polynomial terms, yielding a lower standard deviation. In table 7.6 it can be seen the average and extreme values of the obtained geometrical and optical values for the 14 pig lenses used to retrieve their gradient indices:

- $\emptyset_{eq}$, the equatorial diameter.
- t, the thickness.
- R_{ant}, Q_{ant} and $SD_{fit\,ant}$, the radius and the asphericity of the anterior surface, as well as the standard deviation of its fitting.
- R_{post}, Q_{post} and $SD_{fit\,post}$, the radius and the asphericity of the posterior surface, as well as the standard deviation of its fitting.
- the detected swelling between one projection and the other in relation with the total thickness of the lens.
- dc_a, the anterior vertex distance[4].

	Average value	Minimum	Maximum
$\emptyset_{eq}$(mm)	9.6 ± 0.2	9.3 ± 0.1	10.2 ± 0.1
t (mm)	7.5 ± 0.2	7.10 ± 0.09	7.8 ± 0.1
R_{ant} (mm)	7.5 ± 0.2	7.00 ± 0.05	7.98 ± 0.05
Q_{ant}	1.4 ± 0.2	1.11 ± 0.02	1.81 ± 0.02
$SD_{fit\,ant}$ (μm)	6.5 ± 0.5	6	7.4
R_{post} (mm)	5.2 ± 0.2	4.86 ± 0.02	5.40 ± 0.05
Q_{post}	0.10 ± 0.05	0.02 ± 0.02	0.163 ± 0.006
$SD_{fit\,post}$ (μm)	40 ± 20	14.8	69.3
Swelling (%)	0.2 ± 0.1	0.14	0.76
dc_a (t = 1)	3.0 ± 0.1	2.9	3.3

Table 7.6: Geometrical and optical parameters of the used pig lenses.

In the following sections we will study the results obtained in the retrieval of the 14 gradient indices, as well as the accuracy with which they reproduce the experimental optical behaviour of the crystalline lenses. Finally, we will analyze the validity of the approximation of rotational symmetry according to different experimental evidences.

7.2.1 Reconstruction of the gradient index

From the tomographic data obtained for each one of the 14 lenses, we apply the tomographic algorithm to retrieve in each case the coefficients n_{ij} of the expression

$$n(x,z) = n_0(z) + n_1(z)\,x^2 + n_2(z)\,x^4 + \ldots = \sum_{i=0}^{M} \sum_{j=0}^{2(M-i)} n_{ij} x^{2i} z^j, \qquad (7.2)$$

both in its monopolynomial and in its bipolynomial expression (see section 4.2). In twelve of the lenses the best obtained gradient (in terms of the significance of the tomographic

[4] This parameter is shown in table 7.6 for the projection with the lower angle of incidence.

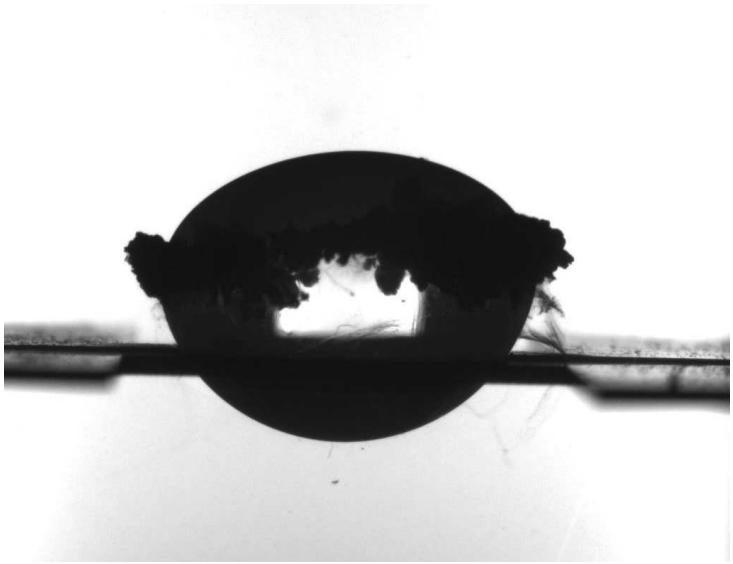

Figure 7.5: Image of the lens profile obtained from the measurement camera with background diffuse light. The anterior surface of the lens is oriented upwards and the posterior one downwards.

fitting and the accuracy in the reproduction of the experimental optical behaviour) was a monopolynomial gradient of order $M = 2$, whereas in other two it was a monopolynomial gradient of order $M = 1$.

The fact some gradient were retrieved with order $M = 1$ seems to be mainly related with a lower degree of rotational symmetry of such a gradient and, in a lower degree, a larger swelling of the crystalline lens. It is also interesting to question why it was not retrieved any bipolynomial gradient. The answer lies in the fact the asymmetry between both segments of the lens is perfectly fittable by an expression of order $M = 2$. Indeed, in those case where we obtained a plausible bipolynomial gradient of order $M = 1$, we also obtained a monopolynomial gradient of order $M = 2$ with a better optical better optical behaviour.

Other important aspect of the retrieval is the number of necessary interpolated points to the algorithm to converge. In the retrieved gradients this number varied depending on the case, being higher in those of order $M = 2$ than in those of order $M = 1$, with an average value of 14 ± 8. Regarding the convergence, in all cases such a convergence occurred when the *rms* variation of the retrieved index at an iteration in relation with the former one was lower than 10^{-4}.

With all the retrieved gradients is possible to calculate an average distribution of refractive index, as well as the standard deviation at each point (see Figs. 7.6, 7.7 and

7.8) and the coefficients n_{ij} that better fit this average distribution (see table 7.7). To obtain this average gradient the coefficients n_{ij} of each one of the retrieved gradients were normalized for $t = 1$ and, with the average geometrical values of table 7.6, the values of the refractive index calculated from these normalized coefficients were averaged at each point of the lens. In the Appendix E the optical properties on axis of this average gradient are studied for the actual sense of propagation of light inside the eye, i.e. from the anterior towards the posterior surface of the crystalline lens.

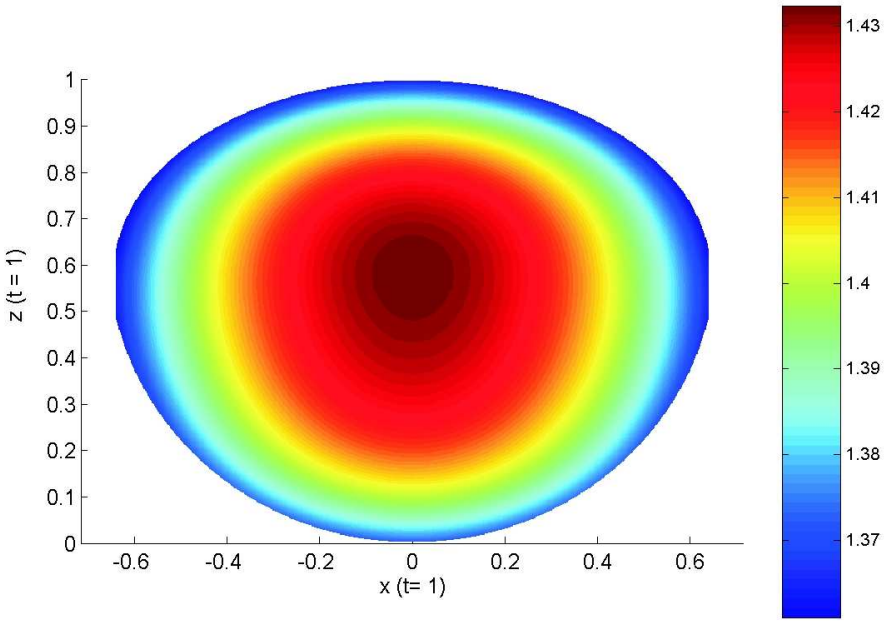

Figure 7.6: Average gradient index (the posterior vertex is placed in (0,0) and the anterior in (0,1)).

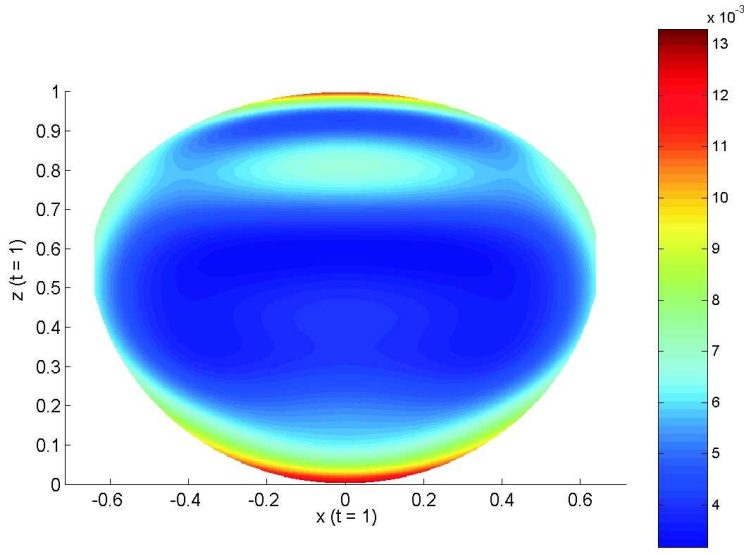

Figure 7.7: Standard deviation of the refractive index at each point of the crystalline lens.

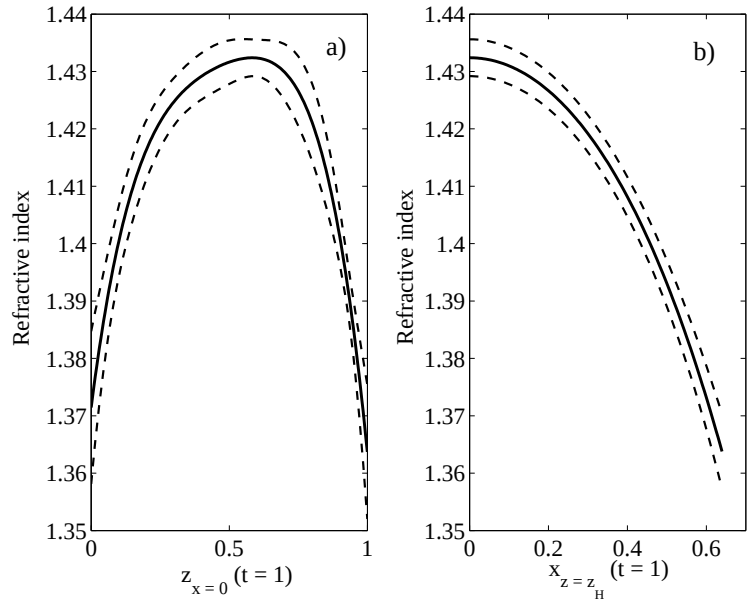

Figure 7.8: Profiles of the average gradient index at the optic axis (a) and at $z = z_H$ (b) with confidence intervals that represent the standard deviation of the value of the index at each point.

Average gradient index			
n_{00}	1.3716	n_{12}	-0.4202
n_{01}	0.3736	n_{20}	-0.0670
n_{02}	-0.9807	z_H $(t=1)$	0.58
n_{03}	1.2951	$\overline{n}_n$	1.434 ± 0.003
n_{04}	-0.6954	$\overline{n}_p$	1.37 ± 0.01
n_{10}	-0.2444	$\overline{n}_a$	1.36 ± 0.01
n_{11}	0.4237	$\overline{n}_{eq}$	1.361 ± 0.006

Table 7.7: Normalized coefficients n_{ij} $(t = 1)$ of the average gradient fitted to the expression 7.2 ($SD_{fit} = 7.7 \times 10^5$), as well as the position of the plane z_H (maximum of the gradient at the optic axis). The average values of the nucleus ($\overline{n}_n = n\,(0, z_H)$), posterior index ($\overline{n}_p$), anterior vertex ($\overline{n}_a$) and equatorial ($\overline{n}_{eq} = \overline{n}\,(\emptyset/2, z_H)$) indices are also shown.

7.2.1.1 Analysis of the retrieved gradient indices

From the analysis of the retrieved results, both at individual and at average level, we deduce that:

1. In figure 7.7 it is shown the standard deviation of the refractive indices found at each point of the lens, with an average value of 5×10^{-3}. Within this magnitude the error in the retrieval of the gradient and the variability among cases are included. Therefore, we can assume that the average accuracy in the tomographic retrieval is of the order of the third decimal digit of the gradient. On the other hand, both in the anterior and in the posterior poles of the eye lens it can be noticed an increase of the deviation up to values about 1×10^{-2}. Although it might be due to variations of each one of the lenses in their processes of cellular differentiation, this increases resembles that observed in fish in figure 7.2, i.e. to the effect the pistons K_p have in the retrieval of the gradient (see section 4.3.1). It would be, hence, reasonable to assume that in the case of the pig lenses the residual error in the calculation of K_p involved an increase of the error in the calculation of the gradient in the poles of the lens.

2. The total variation of the index in the average gradient of figure 7.6 is very similar to that proposed for the strong gradient in the chapter of Numerical simulations (see Fig. 5.9). Thus, the variation between the index at the surface and at the nucleus[5] of the lens is around 0.07, a bit less than half of what was detected for fish lenses (see Fig 7.1). The main difference with the strong gradient of chapter 5 is the thickness, that in the case of pig lenses is a bit more than double. This means that the maximum local values of the derivative of the index should be lower in the case of the pig and, thus, the trajectories of the rays less curved. As a result, a more accurate tomographic retrieval is expected or, at least, less interpolated points will be needed to have a good approximation of the ray trajectories inside the lens.

3. Except for the most immediate zone to the anterior and posterior poles, the isoindicial surfaces have a different geometry to that of the surfaces of the lens, getting more curved as they are closer to the nucleus (see Fig. 7.6). This is due to a histological fact, since the crystalline fibers are also more curved in that region [Kus96]. It is also important to point out the asymmetry of the isoindicial surfaces between the anterior and posterior segments of the lens, flatter in the former than in the latter, as it occurs with the respective surfaces of the lens. As it was explained in section 1.3, this difference might have its origin in the bigger thickness of the fibers of the posterior segment.

4. When examining the profile of the average distribution of the index along the optic axis (see Fig. 7.8) we distinguish two regions at its extremes where the index steeply falls towards the poles. This fall is a bit smoother in the posterior segment, what might be also related with the bigger thickness of the fibers in the posterior segment. It can be also noticed a central region where the index varies more slowly, reaching its maximum at a position ($z = z_H$) decentered towards the anterior vertex. This flatter central zone would correspond with those fibers that have completed their stage of cellular differentiation, the secondary mature fibers (see section 1.2.3). The detection of this region requires a polynomial of order $M = 2$, since one of order $M = 1$ just obtains a parabolic profile, generally centered at the geometrical center of the lens. Finally, it should be also noticed that, since the process of cellular differentiation is completed at a fixed number of layers from the surface (see section 1.2.3), it is expected that that flat region of the gradient takes up a

[5]Even if it is not a bipolynomial gradient, we use the variable z_H to label the position of the nucleus of the lens, i.e. the position $z \in (0, t)$ for which $n(0, z)$ reaches a global maximum.

larger proportion of the lens as it ages.

5. Like in fish lenses, the nucleus index shows a lower standard deviation than the index at the surface (see table 7.7). As it was previously mentioned, in addition to individual variations, this behaviour would be related with the influence of the pistons in the retrieval. However, it is interesting the similarity of the surface indices in pigs (1.36-1.37) and fish lenses (1.379), what might have its origin in very similar cellular metabolisms in the younger fibers of both groups of animals. Nevertheless, the central index in fish lenses is much higher, what is necessary to achieve larger dioptric powers (see section 1.5). Finally, it is worth commenting that the results seem to point to a posterior vertex index slightly higher than the anterior one.

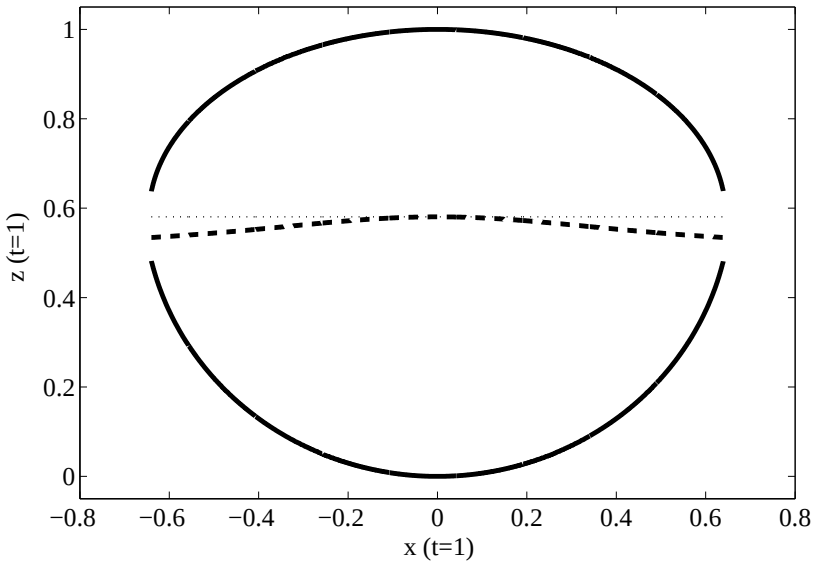

Figure 7.9: Line formed by the points where $(\partial n(x,z)/\partial z) = 0$ (thick dashed line), in relation with $z = z_H$ (thin dotted line) and the surfaces (thick solid lines).

6. Both at the average gradient and at the retrieved gradients of order $M = 2$ the line formed by the points where $(\partial n(x,z)/\partial z) = 0$ does not follow a straight line (a plane in 3-D), but the mathematical expression obtained from such a derivative and that crosses the optic axis at $z = z_H$. In the particular case of the average gradient the result is shown in figure 7.9. We guess, thus, that is not very likely the existence of a supposed equatorial plane where such a derivative is always zero so that any ray that enters it do not leave that plane [Cha88, Pie89]. On the other hand, both in figure 7.9 and in figures 7.8 and 7.6 it is noticed that the nucleus of

the lens ($z = z_H$) it is not at the geometrical center of the lens but at $0.58t$. By taking into account the lens is made up by a continuous deposit of fibers formed at the equator and that such a equator is displaced towards the anterior surface, it seems reasonable to expect the nucleus also to be displaced towards the anterior surface.

7.2.2 Optical behaviour of the retrieved gradient indices

With the retrieved gradients and by using a numerical ray tracing [Sha82] we can determine the accuracy with which these gradients reproduce the experimental optical behaviour of the crystalline lenses. To perform the study of this accuracy we analyze four different magnitudes:

1. *rms* difference between the experimental and propagated distributions of optical path at $z = t$ ($rms_{\Delta S}$): as it can be noticed in table 7.8 this error is of the order of λ, like the average error in the tomographic fitting ($SD_{tomo} = 4 \pm 2\ \lambda$). In table 7.8 it can be noticed that the best result is obtained for the second projection. This could be due to the effect of the lens swelling in the retrieval of the gradient, since the geometry used to characterize its surfaces is that of the second projection. Taking into account that such a swelling is around $15 - 20\ \mu$m $\simeq 24 - 32\ \lambda$ and that the difference in $rms_{\Delta S}$ between the third and first projections and the second one is about $1\ \lambda$, we can assume that most of the swelling is homogeneous enough in terms of optical path as to be "absorbed" by the pistons K_p. An explanation would be that the swelling, instead of changing the shape of the gradient index, generated a region of more or less constant index at the periphery of the lens with a very similar thickness along each one of the surfaces.

	Average value
$\boldsymbol{rms_{\Delta S_1}}$ **(**$\boldsymbol{\lambda}$**)**	5 ± 3
$\boldsymbol{rms_{\Delta S_2}}$ **(**$\boldsymbol{\lambda}$**)**	2 ± 1
$\boldsymbol{rms_{\Delta S_3}}$ **(**$\boldsymbol{\lambda}$**)**	3 ± 2

Table 7.8: Average of the *rms* differences between the experimental and propagated distributions of optical paths at $z = t$ for the 14 retrieved gradients. The results are shown for each one of the three projections.

2. *rms* difference between the experimental and propagated distributions of sines of deflection at $z = t$ ($rms_{\Delta sin}$): in table 7.9 it can be noticed that the error in the sines is in the third decimal digit. The fact this error decreases as the projections are more out of axis can be mainly due to a lower aperture of such projections.

	Average value
$\boldsymbol{rms_{\Delta sin_1}}$ $\mathbf{(10^{-3})}$	2.7 ± 0.9
$\boldsymbol{rms_{\Delta sin_2}}$ $\mathbf{(10^{-3})}$	2.2 ± 0.6
$\boldsymbol{rms_{\Delta sin_3}}$ $\mathbf{(10^{-3})}$	2.0 ± 0.5

Table 7.9: Average of the *rms* differences between the experimental and propagated distributions of sines of deflection at $z = t$ for the 14 retrieved gradients. The results are shown for each one of the three projections.

This error in the third decimal digit of the sines and of λ in the optical paths confirms what was already mentioned when explained the standard deviation of the average gradient: the average accuracy in the tomographic retrieval of the distributions of the refractive indices is also in the third decimal digit (see equations 5.6-5.8 in section 5.1). This accuracy, on the other hand, fits with that predicted by the numerical simulations (see chapter 5.3) for an error in the experimental data of the third decimal digit in the sines of deflection, which is the one we have estimated (see section 6.3).

3. Average relative error in the anterior vertex distance (Δdc_a): in table 7.10 the values corresponding to this magnitude for each one of the projections are provided. Like in the optical paths and in the sines, it is seen that the error is larger for the projection close to axis as a result of working with larger apertures as θ decreases (see table 7.5) .

	Average value
$\boldsymbol{\Delta dc_{a1}}$ (%)	2 ± 2
$\boldsymbol{\Delta dc_{a2}}$ (%)	2 ± 1
$\boldsymbol{\Delta dc_{a3}}$ (%)	2 ± 1

Table 7.10: Average relative errors in the anterior vertex distance of the retrieved gradients for each one of the projections.

To perform the calculation of the anterior vertex distance for each one of the projections we previously calculated the position of an optic axis of reference. To do so, we fitted the distribution of the sines of deflection at $z = t$ and we searched for the position at which the angle of deflection is equal to the entry angle of the incoming laser beams. This position and the entry angle define the optic axis of reference for each projection. To carry out the comparison between the experimental case and that of the retrieved gradient index, in both cases we used the reference axis obtained for the experimental case.

To study with more detail the optical behaviour of the retrieved gradients, in Appendices C and D we show the results obtained for the two cases with the worst and the best reproduction of such a behaviour in terms of their optical paths and sines of deflection. Likewise, in Appendix E we provide the optical properties on axis of the average retrieved gradient, by considering the actual sense of propagation of light inside the eye, i.e. from the anterior surface towards the posterior surface of the crystalline lens. Finally, in Appendix F an effective homogeneous index is retrieved by tomography for one of the eye lenses and its experimental optical behaviour is compared with that it would have in case of having a homogeneous index and not a gradient.

7.2.3 Analysis of the rotational symmetry in pig lenses

Like in the case of the fish lenses, throughout the experiments carried out with pig lenses we have found out several evidences that question the initial symmetric model, in this case the rotational one. This fact, rather than to doubt about the results obtained, should be useful to set an upper bound to how accurately a rotationally symmetrical model of the lens can reproduce the optical behaviour of an actual crystalline lens. For reasons of time and minimization of the metabolic damage, we were not able to characterize the gradient

of the same lens for more than one plane. However, as we have mentioned, we have obtained different evidences that have allowed us to shown in which degree the pig lenses are not rotationally symmetrical. These evidences are referred to both the geometry of the eye lens (best fitting of its surfaces at the same and at different meridional planes) and the characterization of its optical behaviour (for just one meridional plane and for all the aperture of the lens by means of point diffraction interferometry).

7.2.3.1 Symmetry of the surfaces of the lens

As it was explained in section 6.2.2, the first fitted surface is the anterior and afterwards, centered with anterior surface and its same angle of rotation, the posterior surface is fitted. If the crystalline lens were a rotationally symmetrical object this procedure should provide the best fit of both surfaces. Nevertheless, in the performed fittings we have noticed that whereas the fitting of the anterior surface shows a constant and low standard deviation, that of the posterior surface is higher and, above all, more variable (see table 7.6 on page 130). This is due to the lack of symmetry between both surface and such a lack of symmetry seems to vary depending on the plane of the lens to be characterized. Thus, out of the 14 analyzed lenses, in 13 the best fitting of the posterior surface requires non rotationally symmetrical terms, of which the statistical significance is checked for each one of the cases with an F-test. With these terms it is possible to reduce and make more constant the average standard deviation of the posterior fitting , going from 40 ± 20 μm in the rotationally symmetrical fitting to 13 ± 2 μm in the non rotationally symmetrical one.

7.2.3.2 Profile of the eye lens in two different meridional planes

We have analyzed in two eye lenses their profiles in two different meridional planes, assuming once again rotational symmetry in the fitting of the anterior and posterior surfaces. To obtain the images of these two different meridional planes, one of the lenses was rotated about 45^{o} (Lens 1) and the other about 90^{o} (Lens 2). The results of the fittings are shown in table 7.11, where it can be noticed that the standard deviation of the posterior surface changes in the same lens from one plane to the other. This fact would explain why in the lenses used for the tomographic retrievals such a deviation varies so much from one case to the other, since it depends on the chosen meridional plane. Regarding the curvature radii and the asphericities, the variation of these parameters in the posterior surface is low and within the range of the error of measurement. However, the variation is stronger in the anterior surface, mainly in Lens 2, where the angle of

rotation is higher. It seems, thus, that the anterior surface is the main cause of the lack of rotational symmetry of the geometry of the pig lens.

		Position 1	Position 2
LENS 1	R_{ant} (mm)	7.40 ± 0.04	7.50 ± 0.03
	Q_{ant}	1.35 ± 0.02	1.50 ± 0.01
	$SD_{fit\ ant}$ (μm)	7.1	5.9
	R_{post} (mm)	5.16 ± 0.05	5.19 ± 0.04
	Q_{post}	0.09 ± 0.02	0.14 ± 0.01
	$SD_{fit\ post}$ (μm)	64.1	37.5
	t (mm)	7.4 ± 0.1	7.41 ± 0.07
LENS 2	R_{ant} (mm)	7.43 ± 0.03	7.07 ± 0.03
	Q_{ant}	1.44 ± 0.02	1.22 ± 0.02
	$SD_{fit\ ant}$ (μm)	6.4	6.3
	R_{post} (mm)	5.17 ± 0.02	5.16 ± 0.02
	Q_{post}	0.136 ± 0.007	0.140 ± 0.006
	$SD_{fit\ post}$ (μm)	29.2	14.8
	t (mm)	7.45 ± 0.03	7.46 ± 0.03

Table 7.11: Geometrical parameters of the profile of lenses 1 and 2 for two different angular positions (with a difference of about 45° in Lens 1 and about 90° in Lens 2).

7.2.3.3 Distribution of the sines at the exit of two different meridional planes

In addition to study the profile, in each one of the former cases we analyzed the optical behaviour of the meridional planes for incoming rays at $\theta \simeq 0^{o}$. To make significative the comparison between planes of the same lens, we tried to prevent θ from varying from one plane to the other as a result of an unwanted inclination of the lens. The inclination

we could not correct manually was corrected by rotating the distribution of sines at the exit of the lens to match the entry angles of the rays in both planes. Once rotated, we compared the distributions of the two different planes of the same lens. Both in Lens 1 and in Lens 2 the difference between these two distributions of sines is of the order of the third decimal digit of the index (and of λ in optical paths), without noticing any trend due to the noise. We deduce hence that the difference that there may be in the optical behaviour between one plane of the lens and the other is masked by the experimental error in the measurement of the sines of deflection but also that such a difference is not larger than the third decimal digit in sines and of the order of λ in the optical paths.

7.2.3.4 Deflection of the rays in the meridional plane

In a rotationally symmetrical optical system the rays contained in one of its meridional planes propagate themselves along such a plane along its whole trajectory (see section 3.1.1). Therefore, if the crystalline lens were rotationally symmetrical we would expect the alignment camera to record at the exit of the lens a deflection of the laser beams no larger than that recorded in the calibration with the homogeneous spherical lens (see section 6.3). As it is shown in table 7.12, the difference is not very big, but even so in the case of the crystalline lenses the average deflection is slightly the double of that recorded in the homogeneous lens. It has been noticed too, in both cases, that this error increases with the angle of projection. As this angle increases, the trajectory of rays inside the lens also increases. Therefore, it is reasonable to expect that any deviation of the rotational symmetry becomes more evident with larger angles of projection. Anyway, this evidence is not totally conclusive. The homogeneous lens, because of its spherical symmetry, does not have the problems of alignment of the crystalline lens, which we have to align as well as possible with a laser beam and within a reasonable time to minimize any possible degradation.

	$\boldsymbol{\theta_1}$	$\boldsymbol{\theta_2}$	$\boldsymbol{\theta_3}$
$\mathbf{Slope_{homo}(10^{-4})}$	4 ± 2	6 ± 4	8 ± 4
$\mathbf{Slope_{cryst}(10^{-3})}$	1.0 ± 0.6	1.4 ± 0.6	2 ± 1

Table 7.12: Average slope of the rays at the exit of the crystalline lens and the homogeneous lens for each one of the projections, measured from the alignment camera.

7.2.3.5 Optical characterization of the crystalline lenses by interferometry

As in the case of the fish lenses, the use of a modified point diffraction interferometer allows to widen the study of the optical behaviour of the crystalline lenses from two to three dimensions, making more clear the lack of symmetries. Thus, once illuminated the lens with a plane wavefront inciding on its posterior surface, like in the tomographic setup, we recorded the obtained interferograms (see Fig. 7.10). Later, and from the analysis of their fringes, we calculated the Zernike modes that fit the best the phase of the studied wavefront. Assuming that all inclination of this wavefront is due to a misalignment of the lens in the interferometer, the contribution of the remaining non radially symmetrical modes will be indicative of the lack of the rotational symmetry of the lens. In a representative case, like that of figure 7.10, that contribution is of 3.8 λ. This value is of the order of error in optical paths of the retrieved gradients (see table 7.8), from what we deduce that such gradients (and the fitted surfaces) are able to reproduce the optical behaviour of the rotationally symmetrical component of the crystalline lens.

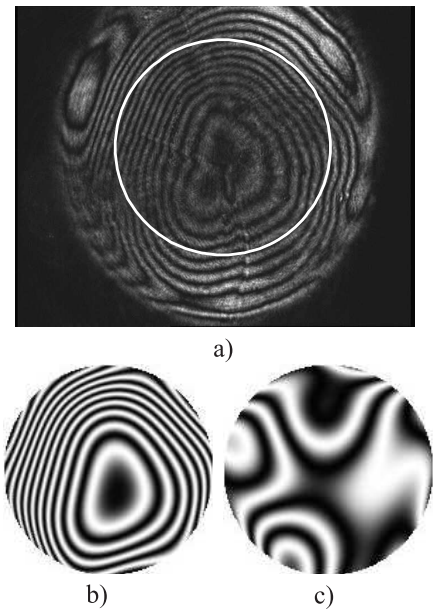

Figure 7.10: In the image (a) it is shown the interferogram obtained for a pig lens illuminated on axis with a plane wavefront, as well as the circumference that limits the area of the phase we will characterize. The result of its fitting to Zernike modes ($SD = 0.1\ \lambda$) is shown in the reconstruction of the image (b). Finally in (c) the non rotationally symmetrical components of the interferogram are also shown, mainly astigmatism, coma and trefoil (we assume all inclination of the wavefront due to a misalignment of the crystalline lens).

In addition to by transmission, the point diffraction interferometer can be used by reflection, by interfering a spherical wavefront with that reflected by the surface we intend to optically characterize. When we used this technique to study the surfaces of the lenses we obtained again a very similar result to that commented in point 7.2.3.2. Once again it is noticed a high degree of radial symmetry in the posterior surface, whereas the anterior one shows a clear astigmatism and coma (see Fig. 7.11). Although these results correspond to lenses of just one species, it is reasonable to assume that this lack of symmetry can be generalized to many other species. An evidence of this is given in reference [Man04], where a corneal topographer was used to characterize the surfaces of the human lens. In this work it was also shown that the surfaces of the human lens are not rotationally symmetrical, although in this case a higher asymmetry was obtained in the posterior surface.

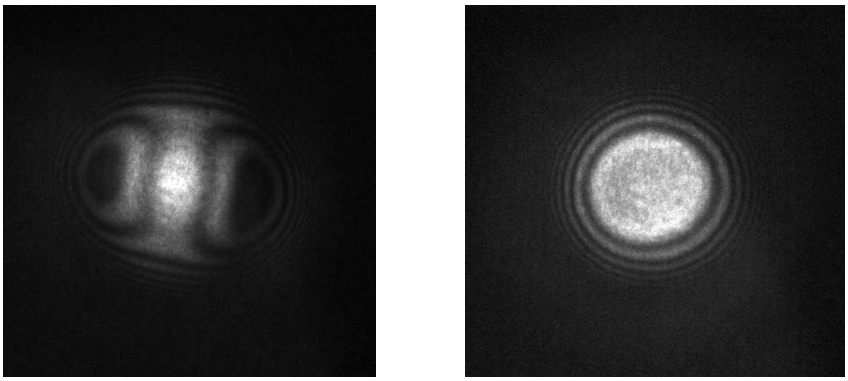

Figure 7.11: Interferograms by reflection obtained for the anterior (a) and posterior surfaces (b) of a pig lens.

According to what was exposed in the four former points we have shown the lens is not a rotationally symmetrical element. It is not both in its geometry and in its gradient index, something reasonable given the implications the geometry of the lens has in the arrangement of the crystalline fibers. However, it is also deduced that if our aim is to reproduce the optical behaviour of the lenses with an accuracy of up to the third decimal digit in the sines of deflection or of the order of λ in optical paths, the approximation of rotational symmetry is still good enough. Related to this, we have shown that the gradients we have retrieved, with an accuracy of the third decimal digit of the index, are able to reproduce all the optical behaviour due to the rotationally symmetrical component

of the lens, both in axis and out of axis. It is just if we wish higher accuracies than those mentioned that is necessary to consider a non rotationally symmetrical model of the lens.

7.3 Discussion of the results. Comparison with other methods.

The obtained results, both for fish and pigs lenses, allow us to assure the tomographic method we have developed and applied is able to obtain average accuracies of the third decimal digit in the refractive index for sines of deflection with an experimental error in the third decimal digit (or, equivalently, optical paths with an error of the order of λ). Likewise, these gradients can reproduce the optical behaviour of the crystalline lenses with an accuracy of the third decimal digit in the sines of deflection (or, equivalently, optical paths with an error of the order of λ). We have also seen that this is the limit allowed by the assumption of rotational symmetry of the gradient index. Therefore, any improvement would imply not just a reduction of the experimental error but necessarily a non rotationally symmetrical model without which such a reduction would be pointless..

At this point it is worth questioning if the accuracy of the tomographic method is similar or better than that of the other non destructive or hybrid methods developed and applied in the reconstruction of the gradient index of crystalline lenses (see sections 2.2 and 2.3):

- Ray deflectometry and Abel integral inversion [Chu77, Cam84, Cha88, Pie89, Kro94, Kro96, Kro01]: both this method and the rest do not shown a thorough study of the influence of the experimental errors in the accuracy of the obtained gradients. Besides, a clear and detailed comparison of the optical behaviour of the retrieved gradient and that of the experimental one is not done either, what makes difficult to determine the accuracy of the reconstructions. For instance, in references [Kro94, Kro01, Kro96] the comparisons are done with averaged results or the lens of one eye is used to retrieve the gradient and that of the contra lateral eye is used to characterize the experimental optical behaviour. Even so, from the data of one of those references [Kro96], it is deduced that its error in the prediction of the posterior vertex distance for a fish, Δdc_p, is around 4-5 %, a bit higher than what has been obtained by us (see table 7.2 on page 121). In any case, as it was explained in section 2.2, this method is limited by the need of working with external indices very similar or identical to the surface index and the fact that just spherical gradients, or slightly elliptical, concentric with the surface can be retrieved. Therefore, their use would

be limited to fish lenses, as long as its lack of symmetry were not higher than that tolerated by the method and the isoindicial surfaces were concentric. Regarding the possibility of using this method to characterize the gradient at the equatorial plane of a mammalian lens and then to extrapolate the result to the rest of the lens by assuming isoindicial surfaces concentric with the surface of the lens [Cha88], we have already shown in points 3 and 6 of section 7.2 that the result would not be realistic.

- Ray deflectometry and optimization algorithms [Gar01]: in the specific case of this reference, the merit function used in the optimization should provide a good idea of how accurately the retrieved gradient reproduces the experimental optical behaviour. However, in the mentioned reference these data are not provided, what makes difficult to estimate the accuracy of this method in the reconstruction of the gradient index. Besides, no result has been published for models of gradient with a more complex symmetry than the spherical one.

- Interferometry [Nil83, Nil05]: this method has been just applied in small invertebrates lenses and from its results it is deduced that its error increases towards the nucleus, being of the order of the second decimal digit.

- Fitting of ocular and visual parameters [Pom84]: this method, as it was applied, does not guarantee the unicity of the solution. Besides, it can not be determined the accuracy of the retrieved gradient since its optical behaviour can not be compared with the experimental one.

- MRI (Magnetic Resonance Imaging) [Mof02a, Mof02b, Jon05, Jon04]: in section 2.3 we explained several reasons according to which we expect errors of about the second decimal digit in the measurement of the index, both in the periphery and in the nucleus of the lens. When studying how accurately the gradients retrieved by this method reproduce the optical behaviour of the lens [Jon05] we see that this accuracy is one order of magnitude lower than ours, what would confirm that the gradient retrieved with MRI has an average accuracy of the second decimal digit. In fact, the gradient retrieved for a pig lens in reference [Jon04] agrees with ours within that range of error. A result of this error would be also the fact that fitting the sagittal profile of a pig lens gradient to a polynomial of sixth grade they do not obtain a similar profile to that we have always obtained with gradients of order $M = 2$ (fourth grade in z), i.e. maximum displaced towards the anterior vertex and a flatter zone in the center.

In short, we can state that our method has currently enough objective merits to be considered as the most accurate of those applied so far for the reconstruction of the gradient index in crystalline lenses. Likewise, it is the only method that has made a qualitative estimation of the accuracy of its retrievals by means of a complete collection of numerical simulations. Thanks to these simulations, we can *a priori* estimate the accuracy of the results of the retrievals for a wide set of factors: angular distribution of projections, number of rays, strength and symmetry of the gradient or order of magnitude of the experimental error. Besides, from the obtained experimental results we have shown that the method is able to retrieve all the rotationally symmetrical component of the eye lens, of which we have studied its contribution in the optical behaviour of the lens. Finally, but not least important, it must be pointed out that ours is the only work where the optical behaviour of the lens out of axis has been characterized and reproduced.

Conclusions

The main conclusions that can be drawn from the work presented in this thesis are the following:

1. A new algorithm has been developed for the reconstruction of the gradient index in crystalline lenses, by using concepts from tomography and geometrical optics. The algorithm has been designed to retrieve gradient indices with two features: rotational symmetry, according to the histological features of the lens, and analiticity. No other constraints have been considered, neither a particular layout of the isoindicial surfaces nor a given index for the surface of the gradient.

2. The unicity of the obtained solution by the tomographic algorithm has been guaranteed. By using a least squares fitting, the method retrieves the gradient that fits the best the experimental data according to the trajectories simulated by the iterative procedure of the tomographic algorithm. Neither it is necessary to start from some initial values nor it exists the risk of falling in local minima, as it might be the case if having used minimization algorithms.

3. It has been shown in the numerical simulations that the theoretical accuracy of the tomographic method is much higher than the third decimal digit of the index. Besides, both in these simulations and in the experimental results, it has been also shown that in real experimental conditions the method retrieves gradient indices with an average error in the third decimal digit. As it has been proved in the experimental results, this accuracy is the maximum one admitted by a rotationally symmetrical gradient index model, at least in the lenses that have been studied. It is inferred, thus, that this tomographic method can retrieve all or most of the rotationally symmetrical component of the gradient index of the crystalline lens.

4. For all retrieved gradients it has been checked how accurately they reproduce the experimental optics of the lens, both in axis and out of axis. In all cases this accuracy is of the order of 10^{-3} in sines of the angles of deflection and of the order of λ in optical paths (reaching orders of 10λ in the larger fish lenses). In the

experimental results it has been shown that this accuracy is the maximum admitted by a rotationally symmetrical model of the lens. To obtain higher accuracies it would be necessary to consider non rotationally symmetrical models of the lens.

5. A low computational cost has been achieved. Once obtained the data of the surfaces and the entry and exit rays, the algorithm, programmed in Matlab, takes no longer than a few seconds to obtain a solution in a current computer (Pentium 4, 1 GB RAM).

6. It has been shown, by achieving the former objectives, that this method implies an objective improvement in relation with all developed so far.

7. Gradient indices of fish and pig lenses have been retrieved. For each one of the cases it has been provided an average gradient. Likewise, we have studied their main features. Finally, we have also analyzed in which degree are applicable to the gradients of each one of the cases the symmetries generally assumed: spherical for fish and rotational for mammals.

A Worst tomographic reconstruction of a fish gradient index

As it was shown in table 7.2 (page 121), the gradients retrieved for fish lenses 1, 2 and 3 reproduce the optics of their corresponding crystalline lenses worst than lenses 4 and 5. Among those three lenses, we show the data of lens 3 as a representative case of a not very accurate retrieval of a gradient index with the tomographic method.

The comments and explanations of the results are shown in the caption of each one of the tables and figures.

***Hyperoglyphe Antarctica* (Lens 3)**				
n_0	n_1	n_2	n_s	R (mm)
1.5376	-0.1128	-0.0434	1.381	13.368 ± 0.002

Table A.1: Coefficients n_i of the gradient index retrieved for lens 3, as well as the index of the surface and its radius.

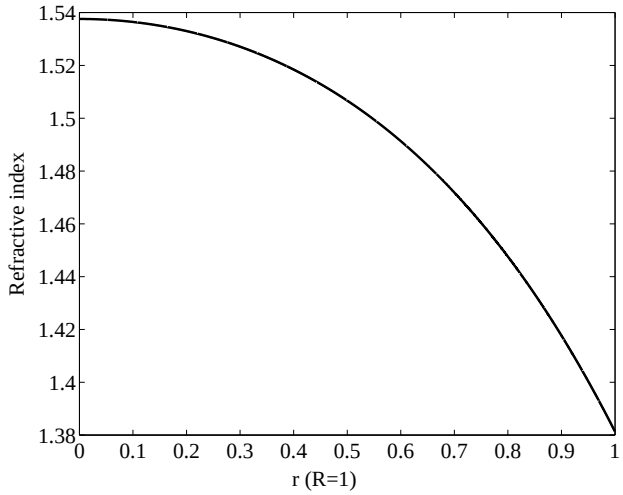

Figure A.1: Retrieved gradient index.

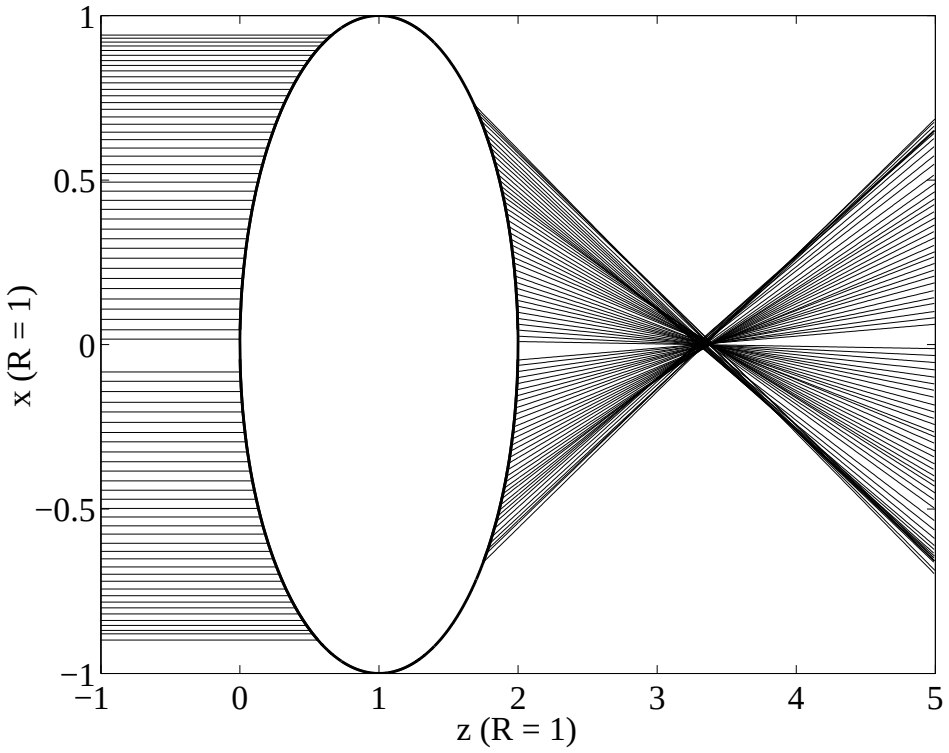

Figure A.2: Graphic illustration of the equatorial plane of the crystalline lens and of the exit and entry rays fitted to straight lines. At the center a zone without rays can be noticed. This zone is due to the diffraction generated at this point by the suture (in fish lenses the suture line is approximately formed along the optical axis, orthogonal to the plane here depicted). Some caustics inside the set of exit rays can also be noticed, being such caustics indicative of a strong variation of the deflection of the rays.

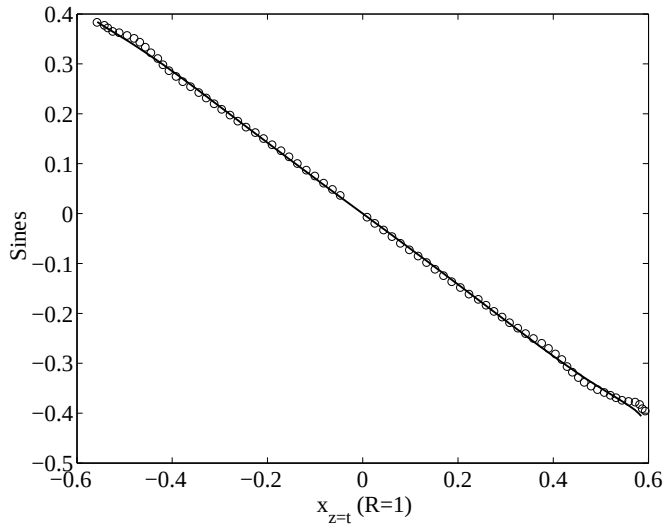

Figure A.3: Experimental distribution of the sines of deflection at the exit of the crystalline lens (circles) and that obtained by propagation of the entry rays in the retrieved gradient index (solid line). An important change of the evolution of the deflection occurs at $x\,(z=t) \simeq 0.4$ (R=1) , being this change related with the caustics pointed out in figure A.2. It is interesting to see how the propagated distribution averages the variation of sines at the periphery of the lens.

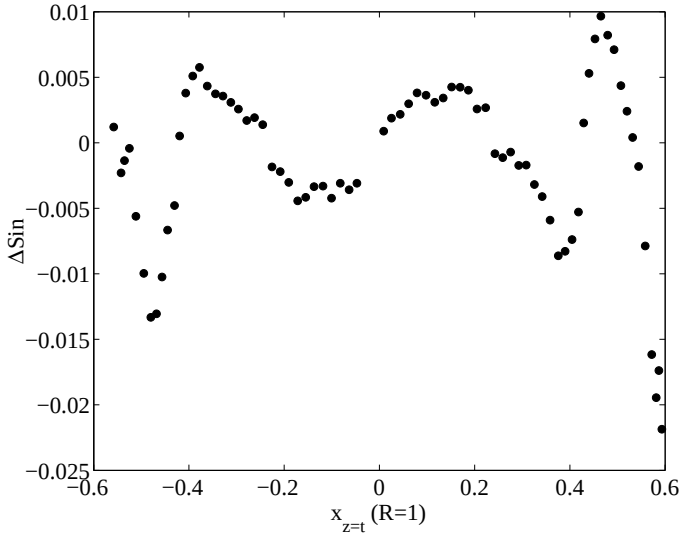

Figure A.4: Difference between the experimental and propagated distributions of the sines of deflection at the exit of the lens, Δsin ($rms_{\Delta sin} = 6.5 \times 10^{-3}$ and $PV_{\Delta sin} = 3.2 \times 10^{-2}$).

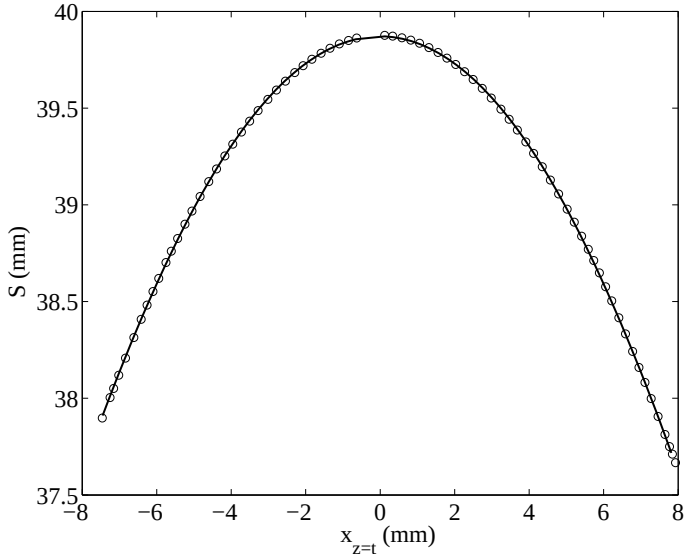

Figure A.5: Experimental distribution of the optical path at the exit of the crystalline lens (circles) and that obtained by propagation of the entry rays in the retrieved gradient (solid line).

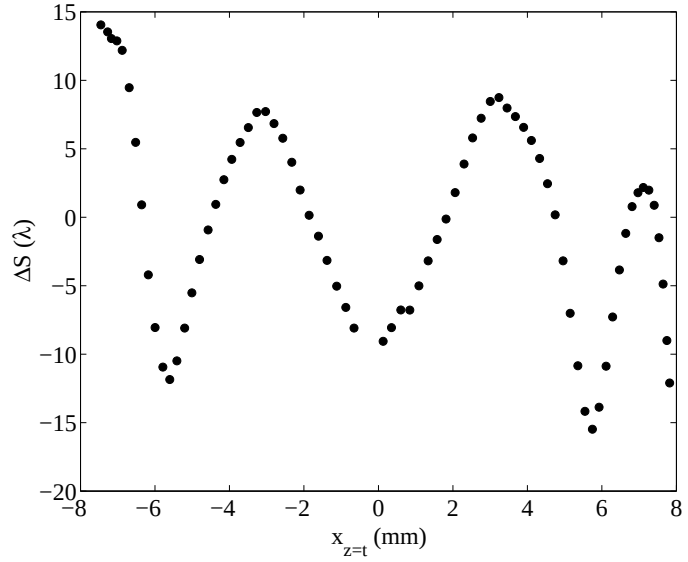

Figure A.6: Difference between the experimental and the propagated distributions of the optical path at the exit of the lens, ΔS ($rms_{\Delta S} = 7.4\ \lambda$ and $PV_{\Delta S} = 16.5\ \lambda$). By studying such a difference, it seems to be essentially due to a small tilt of the wavefront that the retrieved gradient is not able to reproduce and spherical aberrations as those that produce the formerly mentioned caustics.

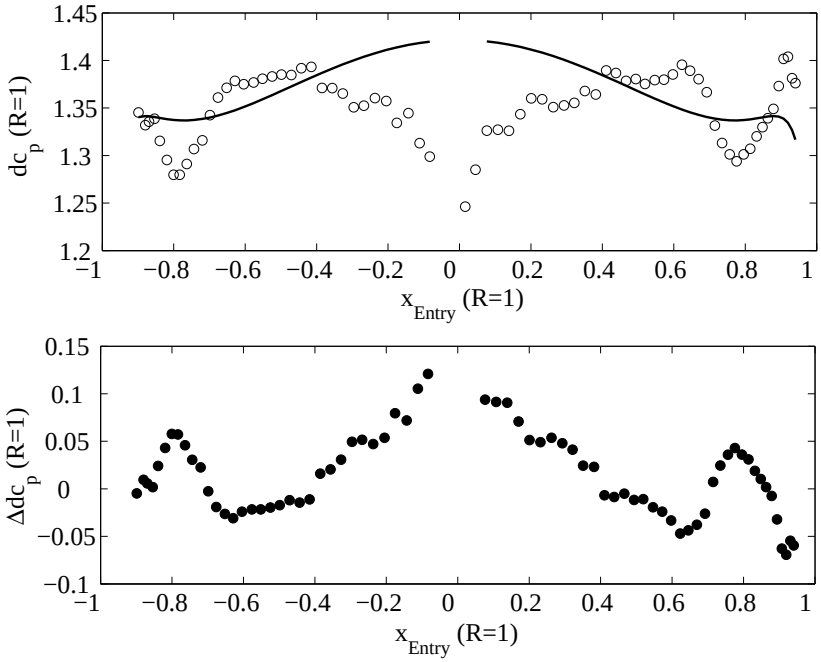

Figure A.7: Experimental variation of the posterior vertex distance dc_p with the height of entry of the rays in the lens (circles) and that obtained in the retrieved gradient (solid line), as well as the difference between both Δdc_p ($rms_{\Delta dc_p} = 4.4\times10^{-2}$ and $PV_{\Delta dc_p} = 1.9\times10^{-1}$ (R=1)). The calculation of this difference is done for all ray such $|x_{Entry}| > 0.05$, since in the paraxial region the error in the calculation of dc_p tends to infinity. It is noticed again that the retrieved gradient can not reproduce the strong variations of the posterior vertex distance at the periphery.

B Better tomographic reconstruction of a fish gradient index

In this appendix we show different data and graphs resulting from the tomographic retrieval of the gradient index of the lens 5, as well as those of its optical behaviour (see section 7.1). Because of its accuracy at reproducing the experimental optics (see table 7.2, page 121) we have chosen this case as representative of a good tomographic reconstruction of the gradient index of a fish lens.

The comments and explanations of the results are done in the caption of each one of the tables and figures.

***Beryx Decadactylus* (Lens 5)**					
n_0	n_1	n_2	n_3	n_s	R (mm)
1.5406	-0.1374	0.0356	-0.0716	1.367	8.631 ± 0.003

Table B.1: Coefficients n_i of the gradient index retrieved for lens 5, as well as the index of the surface and its radius.

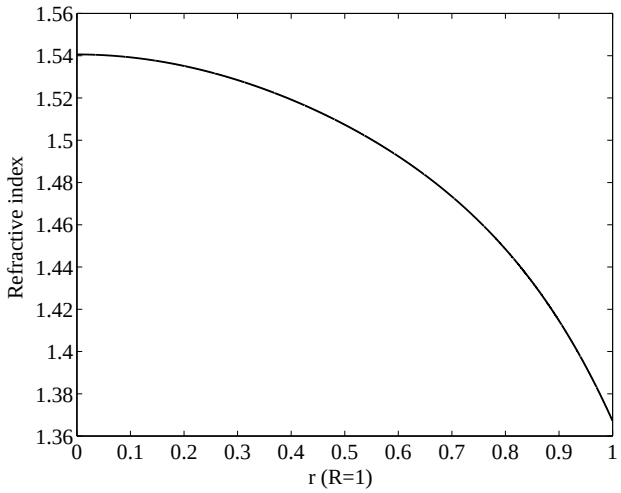

Figure B.1: Retrieved gradient index.

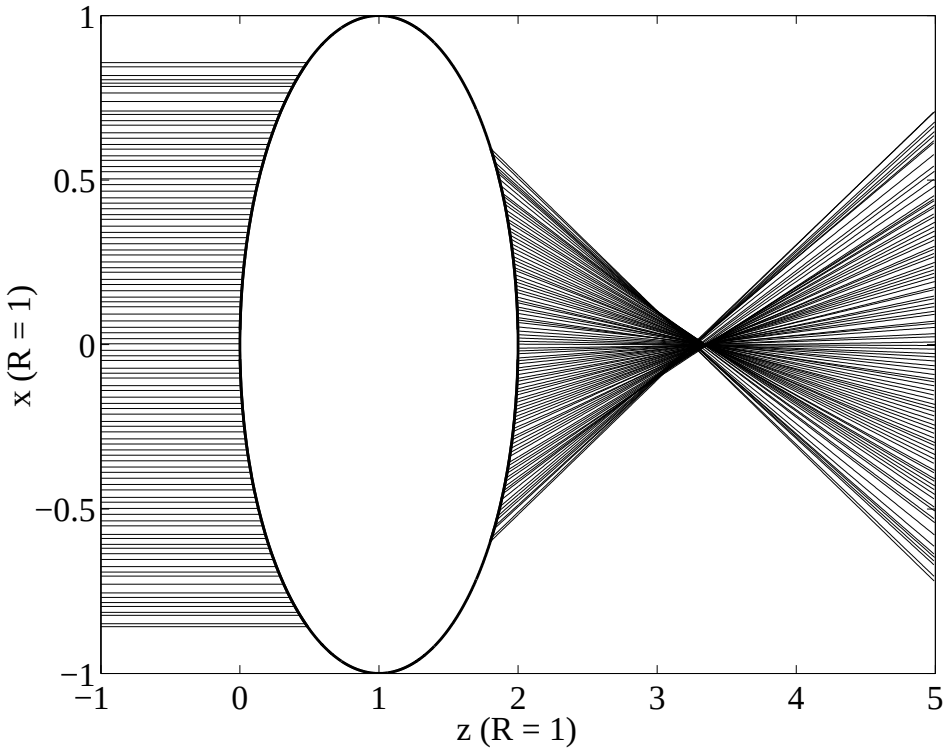

Figure B.2: Graphic illustration of the equatorial plane of the crystalline lens and of the exit and entry rays fitted to straight lines. Besides not noticing diffraction at the center of the lens, other important difference regarding figure A.2 is how the deflection of the rays changes at the periphery. In this case such a variation has the same sign, giving rise to a clear positive spherical aberration

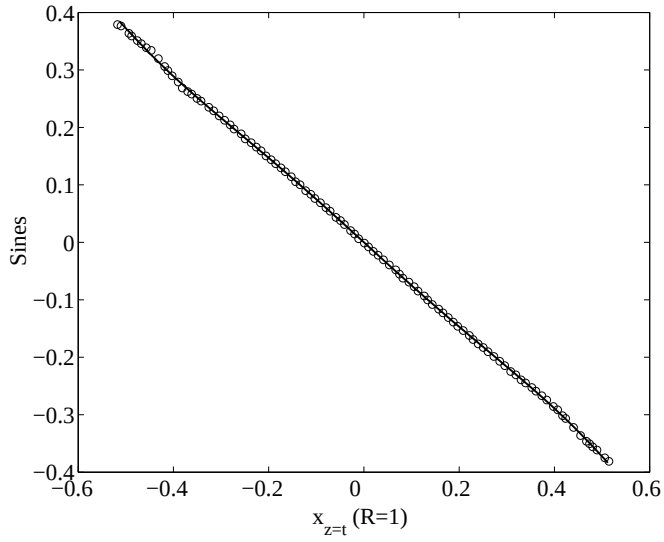

Figure B.3: Experimental distribution of the sines of deflection at the exit of the crystalline lens (circles) and that obtained by propagation of the entry rays in the retrieved gradient index (solid line). In relation with figure A.3, in this case the propagated distribution follows better the variation of the sines at the periphery, although such a variation occurs at a similar radial position, $x\,(z=t) \simeq 0.4$ (R=1).

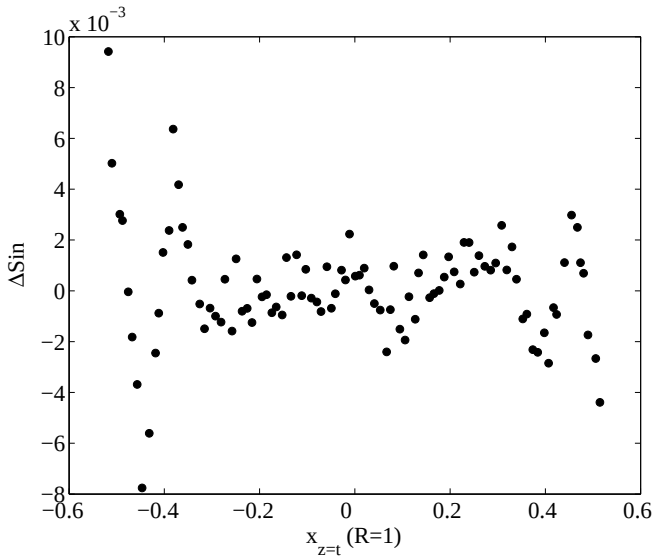

Figure B.4: Difference between the experimental and propagated distributions of the sines of deflection at the exit of the lens, Δsin ($rms_{\Delta sin} = 2.2 \times 10^{-3}$ and $PV_{\Delta sin} = 1.7 \times 10^{-2}$).

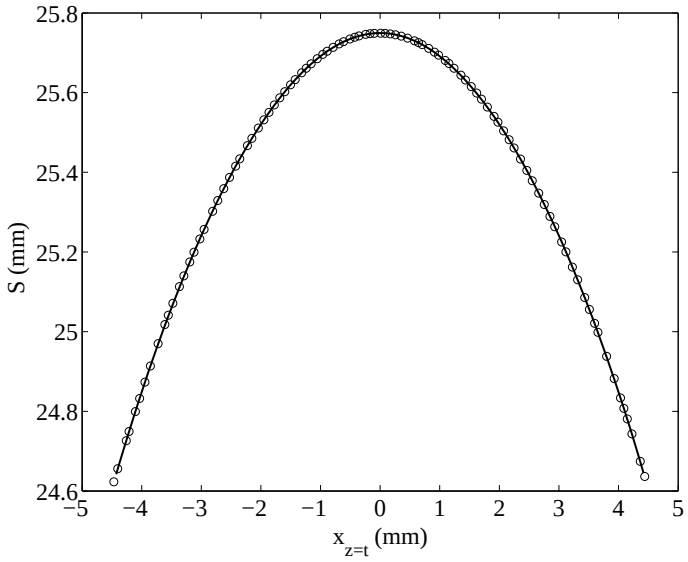

Figure B.5: Experimental distribution of the optical path at the exit of the crystalline lens (circles) and that obtained by propagation of the entry rays in the retrieved gradient (solid line).

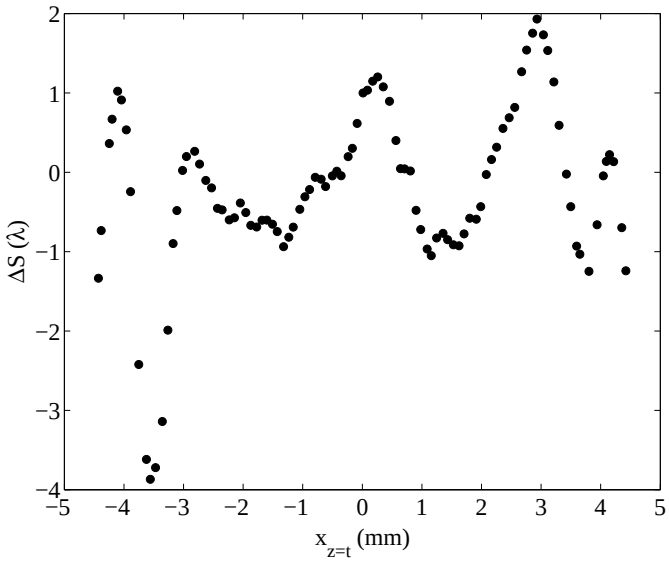

Figure B.6: Difference between the experimental and the propagated distributions of the optical path at the exit of the lens, ΔS ($rms_{\Delta S} = 1.1\ \lambda$ and $PV_{\Delta S} = 4.1\ \lambda$). By studying such a difference, it seems to be essentially due to high order spherical aberrations and experimental noise.

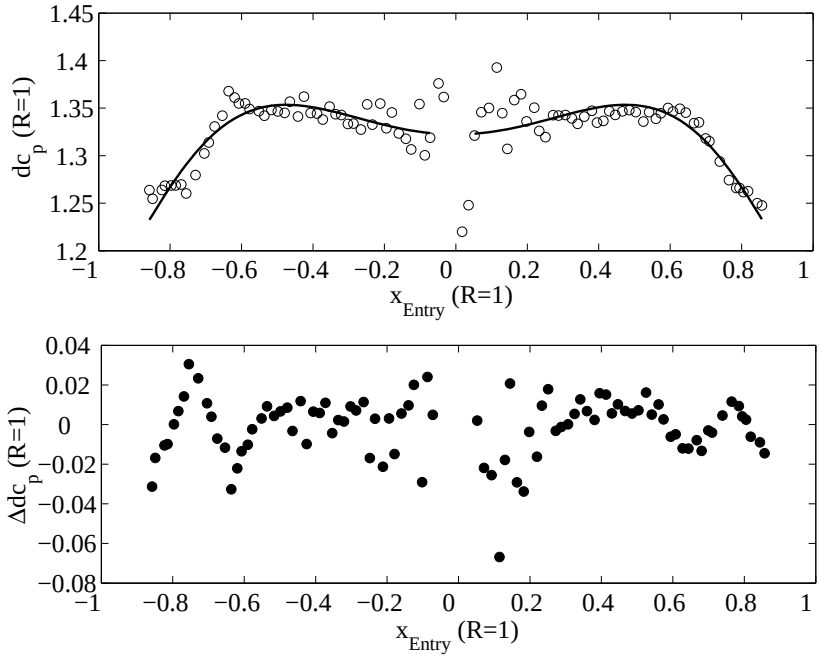

Figure B.7: Experimental variation of the posterior vertex distance dc_p with the height of entry of the rays in the lens (circles) and that obtained in the retrieved gradient (solid line), as well as the difference between both Δdc_p ($rms_{\Delta dc_p} = 1.5\times10^{-2}$ and $PV_{\Delta dc_p} = 9.7\times10^{-2}$ (R=1)). The calculation of this difference is done for all ray such $|x_{Entry}| > 0.05$, since in the paraxial region the error in the calculation of dc_p tends to infinity. Unlike figure A.7, in this case the monotonic variation of dc_p can be reproduced by the retrieved gradient index.

C Worst tomographic reconstruction of a pig gradient index

In this appendix we show the data and graphs that correspond to the case for which the worst tomographic reconstruction of section 7.2 is obtained, as well as the worst optical behaviour of the resulting gradient index. We name the worst tomographic reconstruction that which reproduces the worst the experimental optics of the crystalline lens according to the following magnitudes:

- $rms_{\Delta S}$: the *rms* error in the distribution of the optical path in the straight line tangent to the exit vertex of the lens ($z = t$), where it is included the piston retrieved by the algorithm.
- $PV_{\Delta S}$: the peak-valley error of that same distribution of optical paths.
- $rms_{\Delta sin}$: the *rms* error in the distribution of sines of deflection of the exit rays at $z = t$.
- $PV_{\Delta sin}$: the peak-valley error of that distribution of sines.
- Δdc_a: the average relative error in the anterior vertex distance[1] (the calculation of this parameter is explained in section 7.2.2, point 3).

The comments and explanation of the results are done in the captions of each one of the tables and figures.

[1] Like in section 7.2, in this appendix we name anterior vertex of the crystalline lens that one that is placed closer to the cornea in the eye ball and at the exit of the rays in the experimental setup.

$\emptyset_{eq}$**(mm)**	9.7 ± 0.1
t **(mm)**	7.67 ± 0.02
R_{ant} **(mm)**	7.69 ± 0.05
Q_{ant}	1.43 ± 0.02
$SD_{fit\,ant}$ **(μm)**	6
R_{post} **(mm)**	5.24 ± 0.02
Q_{post}	0.094 ± 0.006
$SD_{fit\,post}$ **(μm)**	18.1
Swelling (%)	0.16

Table C.1: Geometric parameters of the crystalline lens: $\emptyset_{eq}$, equatorial diameter; t, thickness; R_{ant}, Q_{ant} and $SD_{fit\,ant}$, the radius and asphericity of the anterior surface, as well as the standard deviation of its fitting; R_{post}, Q_{post} and $SD_{fit\,post}$, the radius and asphericity of the posterior surface, besides the standard deviation of the fitting; the swelling detected between one projection and another in relation with the total thickness of the eye lens.

	1st projection	**2nd projection**	**3rd projection**
θ (°)	-1.23 ± 0.02	19.25 ± 0.05	36.88 ± 0.05
Aperture (%)	97.3	90.0	64.1
Number of rays	75	75	73

Table C.2: Parameters of the projections.

$\boldsymbol{n_{00}}$	1.3855
$\boldsymbol{n_{01}}$	0.2004
$\boldsymbol{n_{02}}$	-0.2052
$\boldsymbol{n_{10}}$	-0.1636
$\boldsymbol{n_n}$	1.434
$\boldsymbol{n_p}$	1.386
$\boldsymbol{n_a}$	1.381
$\boldsymbol{n_{eq}}$	1.369
$\boldsymbol{z_H}$ $\boldsymbol{(t=1)}$	0.49

Table C.3: Coefficients n_{ij} of the gradient normalized to $t = 1$, as well as the index of the nucleus ($n_n = n\,(0, z_H)$), of the posterior vertex (n_p), of the anterior vertex (n_a) and equatorial ($n_{eq} = n\,(\emptyset/2, z_H)$). It is also provided the position of the plane z_H (maximum of the gradient in the optic axis) in relation with the posterior vertex of the crystalline lens.

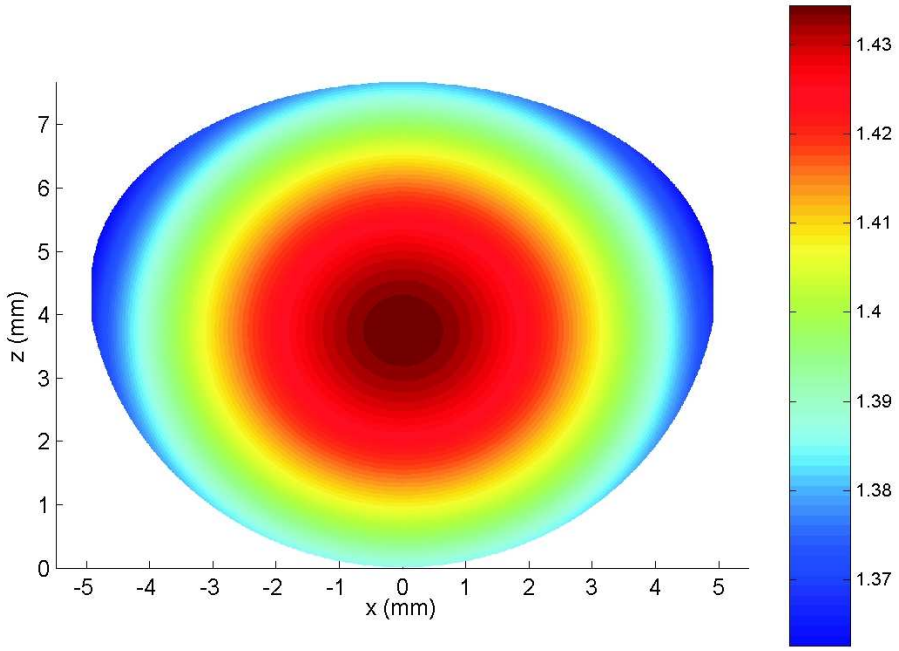

Figure C.1: Retrieved gradient index.

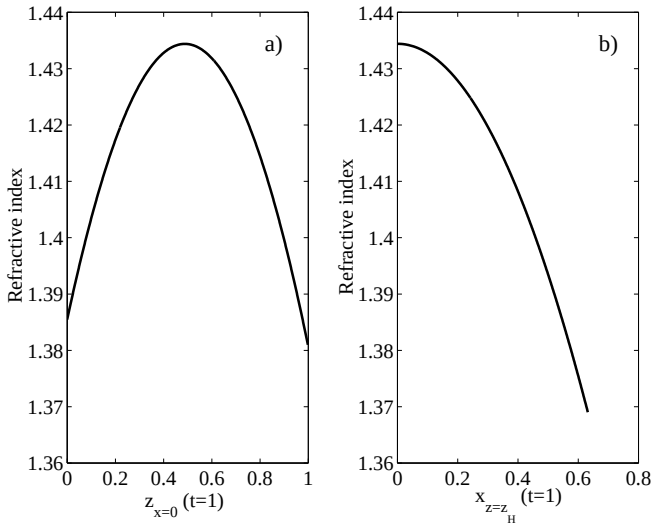

Figure C.2: Profiles of the retrieved gradient index along the optic axis (a) and at $z = z_H$ (b).

C.1 First projection

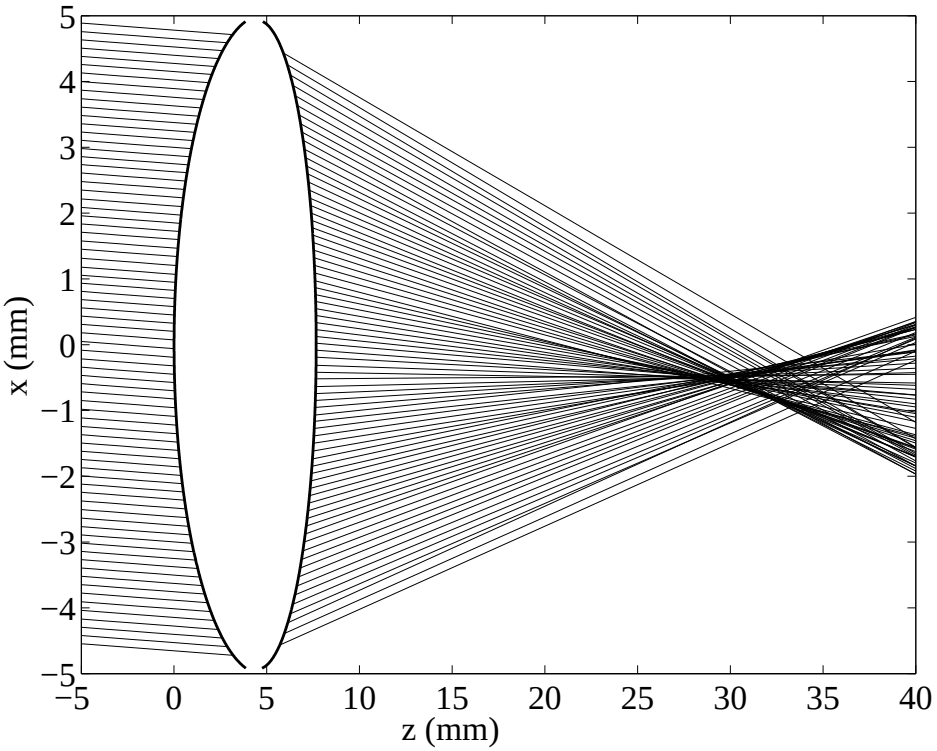

Figure C.3: Graphic illustration of a meridional plane of the eye lens and of the exit and entry rays fitted to straight lines ($\theta_1 = -1.23^{\circ} \pm 0.02^{\circ}$). It can be clearly noticed the existence of a strong negative spherical aberration.

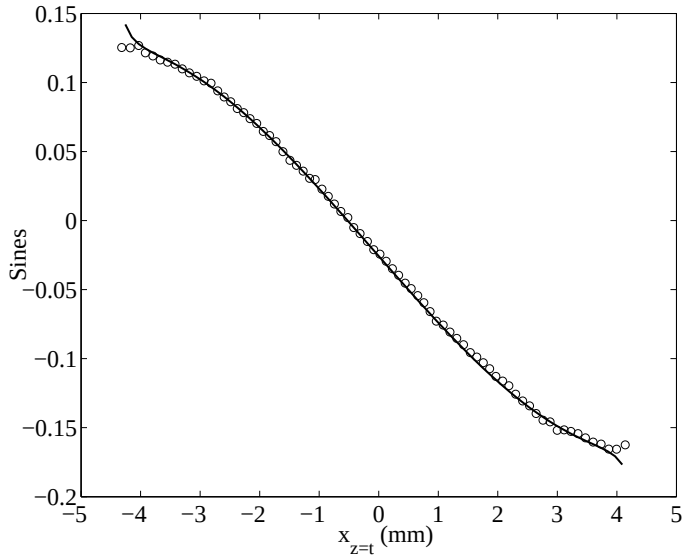

Figure C.4: Experimental distribution of the sines of deflection at the exit of the eye lens (circles) and that obtained by propagation of the entry rays in the retrieved gradient (solid line) [First projection].

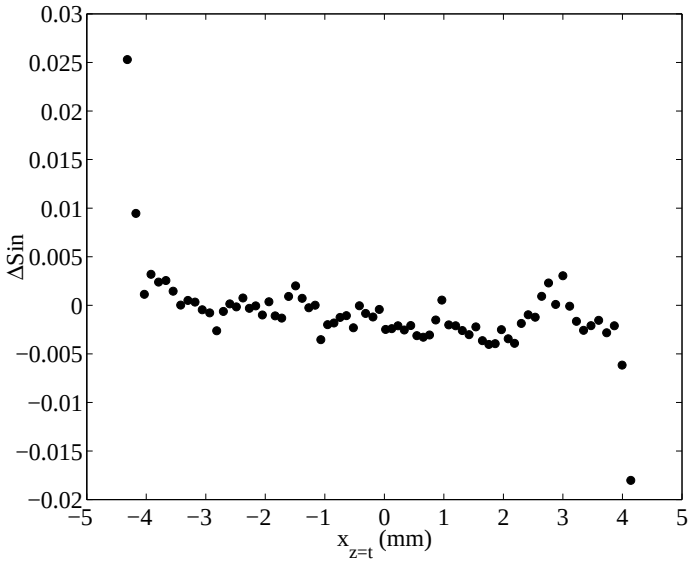

Figure C.5: Difference between the experimental and the propagated distributions of sines of deflection at the exit of the eye lens, Δsin ($rms_{\Delta sin} = 4.3 \times 10^{-3}$ and $PV_{\Delta sin} = 4.3 \times 10^{-2}$). It can be noticed how the error rises at the extremes of the lens as a result of the remaining misalignments of the experimental setup. [First projection].

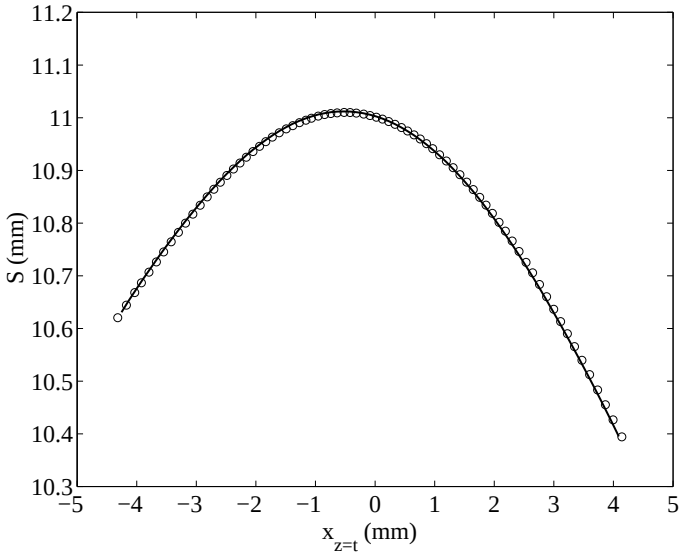

Figure C.6: Experimental distribution of the optical path at the exit of the eye lens (circles) and that obtained by propagation of the entry rays in the retrieved gradient index (solid line) [First projection].

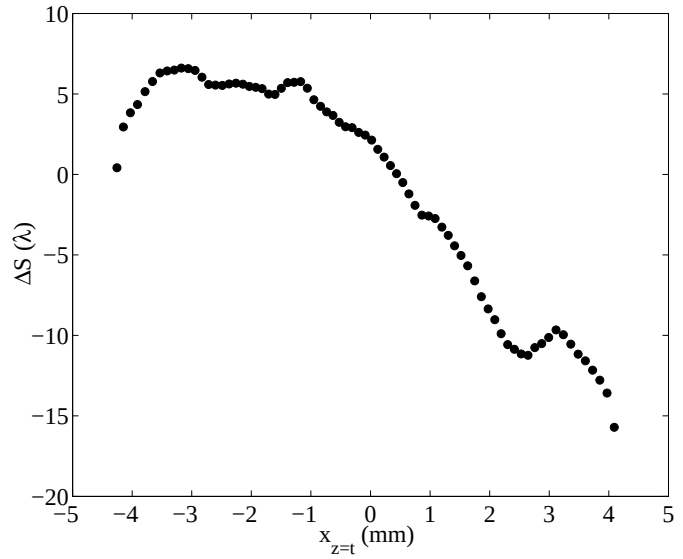

Figure C.7: Difference between the experimental and the propagated distributions of the optical path at the exit of the eye lens, ΔS ($rms_{\Delta S} = 6.9\ \lambda$ and $PV_{\Delta S} = 22.3\ \lambda$), standing out in this difference the presence of a tilt of the wavefront not properly reproduced by the retrieved gradient index [First projection].

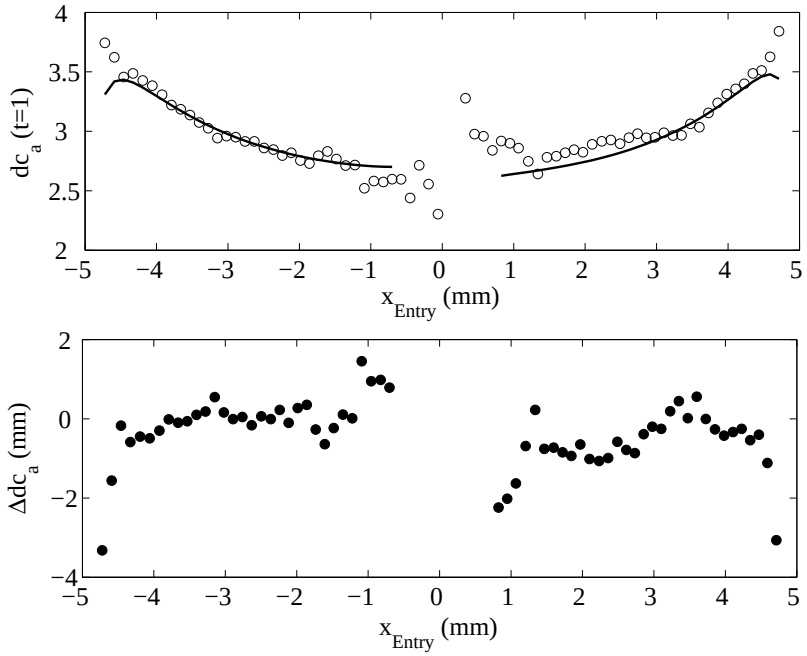

Figure C.8: Experimental variation of the anterior vertex distance dc_a with the height of entry of the rays in the lens (circles) and that obtained with the retrieved gradient index (solid line), as well as the difference between both Δdc_a ($rms_{\Delta dc_a} = 0.91$ mm and $PV_{\Delta dc_a} = 4.78$ mm). The calculation of this difference is done for all rays but the ten rays closest to the optic axis of reference (see section 7.2.2, point 3), since in this paraxial region the error in the calculation of dc_a tends to infinity [First projection].

C.2 Second projection

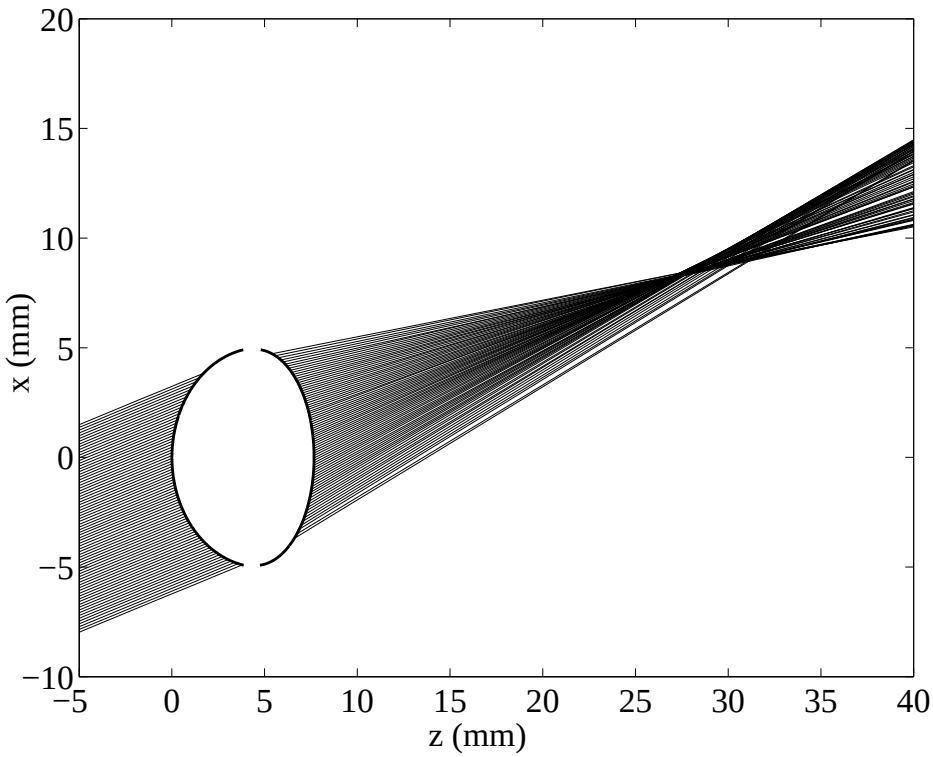

Figure C.9: Graphic illustration of a meridional plane of the eye lens and of the exit and entry rays fitted to straight lines ($\theta_2 = 19.25^{\circ} \pm 0.05^{\circ}$).

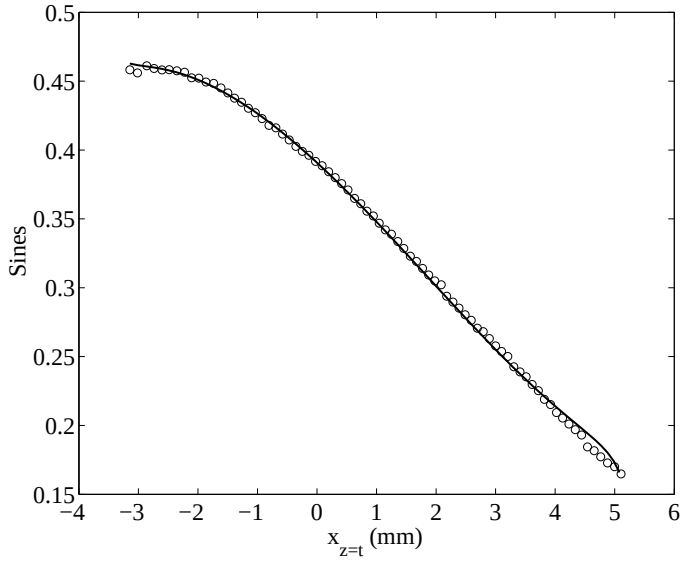

Figure C.10: Experimental distribution of the sines of deflection at the exit of the eye lens (circles) and that obtained by propagation of the entry rays in the retrieved gradient (solid line) [Second projection].

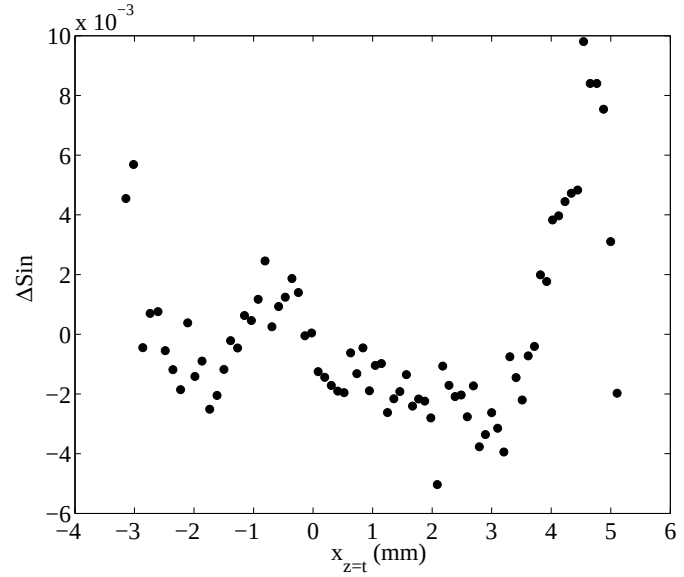

Figure C.11: Difference between the experimental and the propagated distributions of sines of deflection at the exit of the eye lens, Δsin ($rms_{\Delta sin} = 3.0 \times 10^{-3}$ and $PV_{\Delta sin} = 1.5 \times 10^{-2}$) [Second projection].

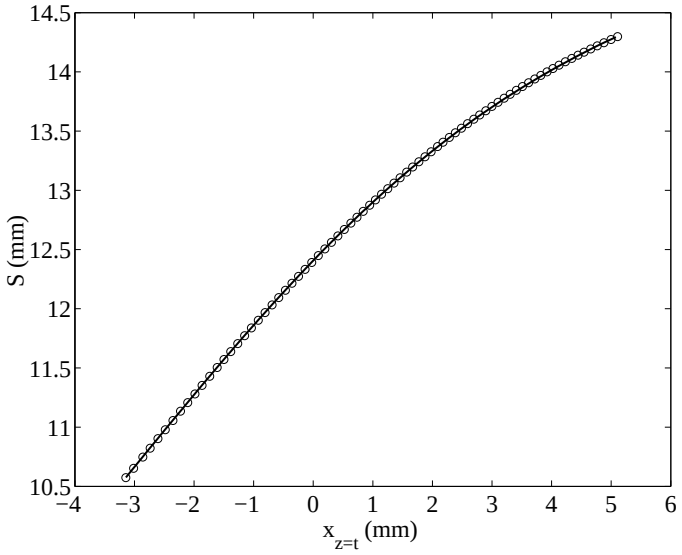

Figure C.12: Experimental distribution of the optical path at the exit of the eye lens (circles) and that obtained by propagation of the entry rays in the retrieved gradient index (solid line) [Second projection].

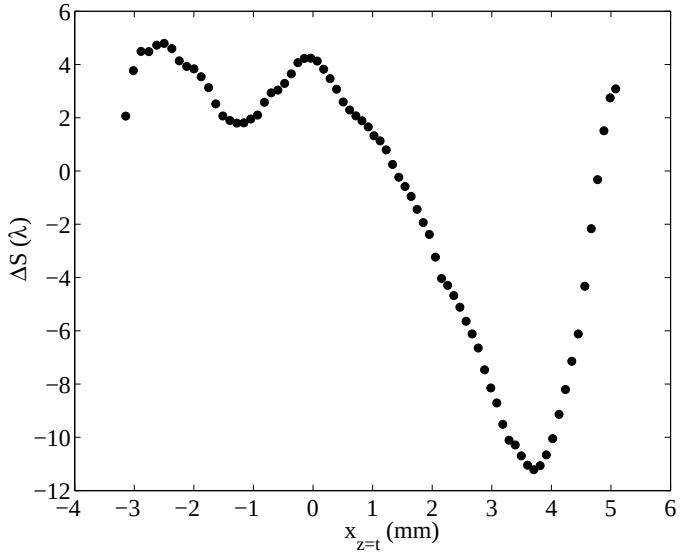

Figure C.13: Difference between the experimental and the propagated distributions of the optical path at the exit of the eye lens, ΔS ($rms_{\Delta S} = 5.3\ \lambda$ and $PV_{\Delta S} = 16.0\ \lambda$) [Second projection].

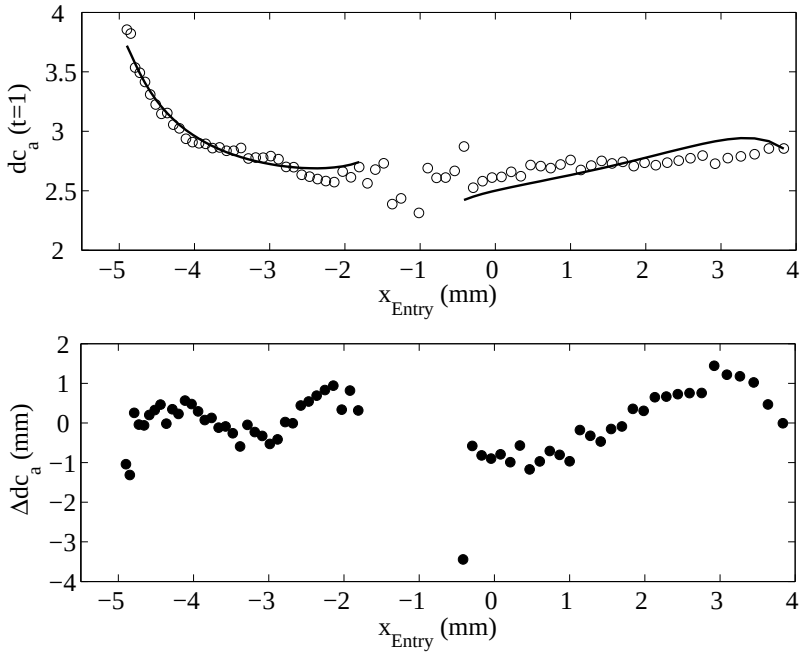

Figure C.14: Experimental variation of the anterior vertex distance dc_a with the height of entry of the rays in the lens (circles) and that obtained with the retrieved gradient index (solid line), as well as the difference between both Δdc_a ($rms_{\Delta dc_a} = 0.76$ mm and $PV_{\Delta dc_a} = 4.89$ mm). The calculation of this difference is done for all rays but the ten rays closest to the optic axis of reference (see section 7.2.2, point 3), since in this paraxial region the error in the calculation of dc_a tends to infinity [Second projection].

C.3 Third projection

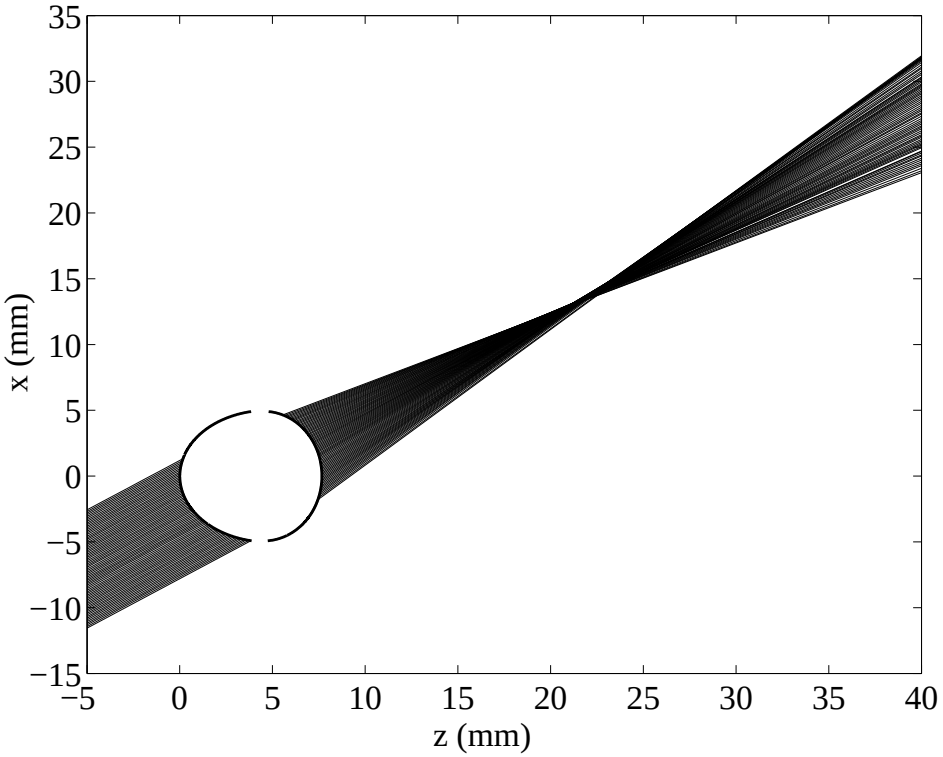

Figure C.15: Graphic illustration of a meridional plane of the eye lens and of the exit and entry rays fitted to straight lines ($\theta_3 = 36.88^{\circ} \pm 0.05^{\circ}$).

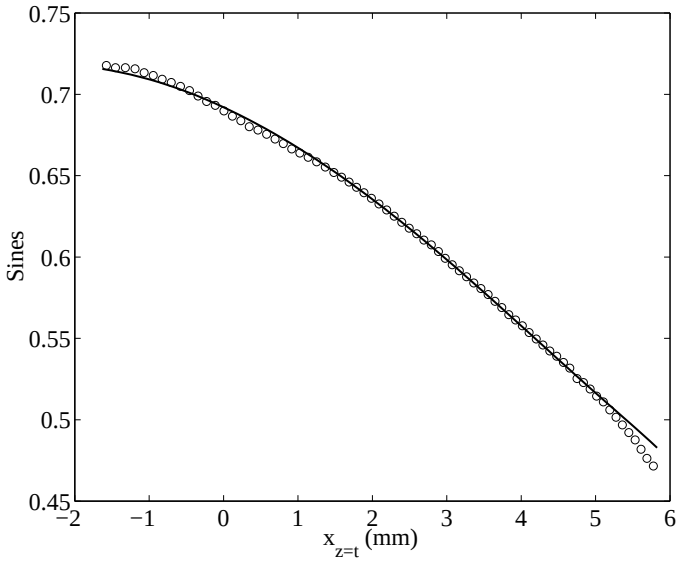

Figure C.16: Experimental distribution of the sines of deflection at the exit of the eye lens (circles) and that obtained by propagation of the entry rays in the retrieved gradient (solid line) [Third projection].

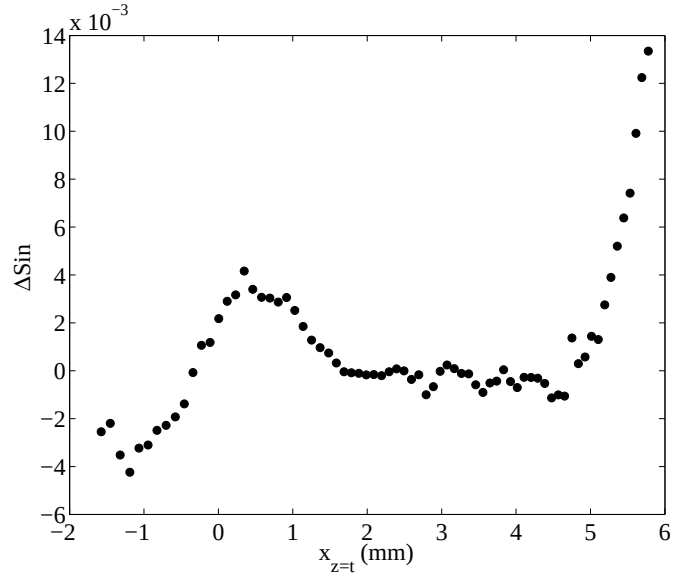

Figure C.17: Difference between the experimental and the propagated distributions of sines of deflection at the exit of the eye lens, Δsin ($rms_{\Delta sin} = 3.2 \times 10^{-3}$ and $PV_{\Delta sin} = 1.8 \times 10^{-2}$) [Third projection].

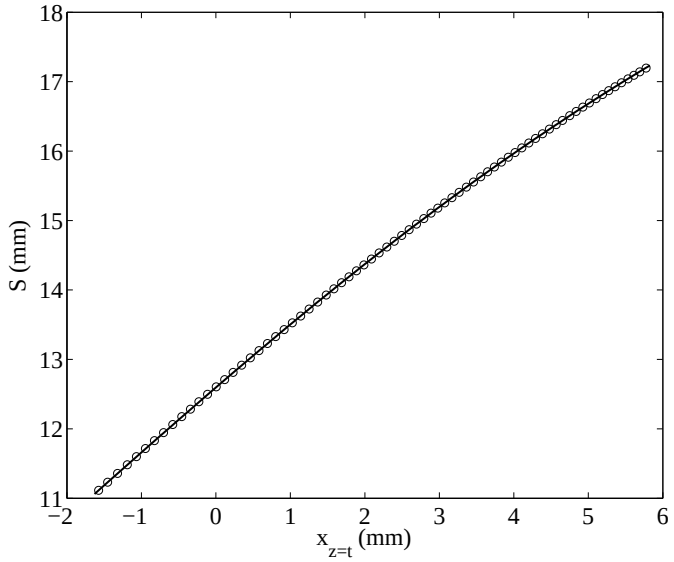

Figure C.18: Experimental distribution of the optical path at the exit of the eye lens (circles) and that obtained by propagation of the entry rays in the retrieved gradient index (solid line) [Third projection].

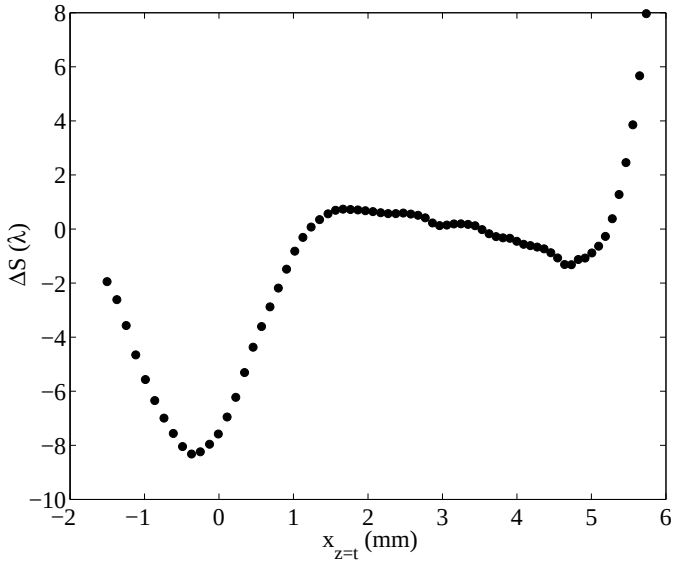

Figure C.19: Difference between the experimental and the propagated distributions of the optical path at the exit of the eye lens, ΔS ($rms_{\Delta S} = 3.4\ \lambda$ and $PV_{\Delta S} = 16.3\ \lambda$) [Third projection].

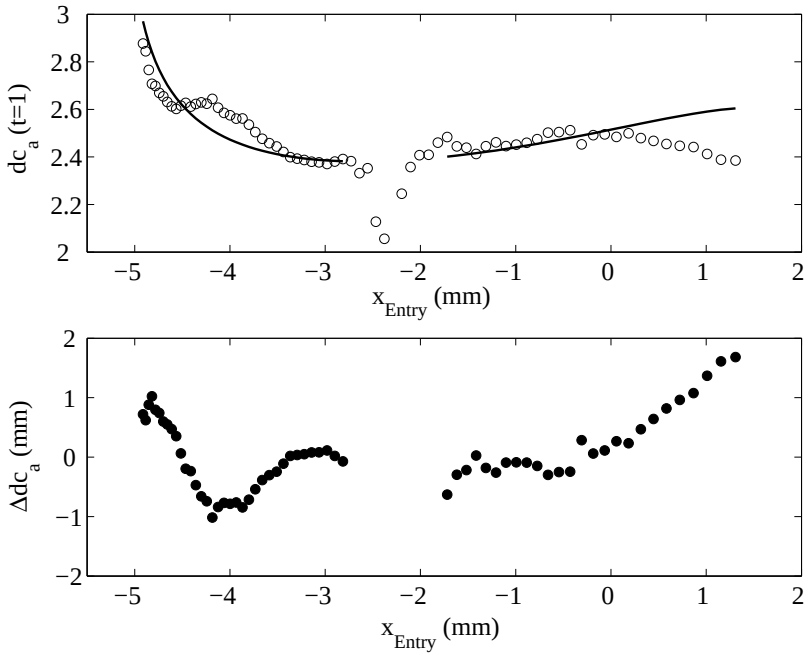

Figure C.20: Experimental variation of the anterior vertex distance dc_a with the height of entry of the rays in the lens (circles) and that obtained with the retrieved gradient index (solid line), as well as the difference between both Δdc_a ($rms_{\Delta dc_a} = 0.61$ mm and $PV_{\Delta dc_a} = 2.70$ mm). The calculation of this difference is done for all rays but the ten rays closest to the optic axis of reference (see section 7.2.2, point 3), since in this paraxial region the error in the calculation of dc_a tends to infinity [Third projection].

D Best tomographic reconstruction of a pig gradient index

In this appendix we show the data and graphs that correspond to the case for which the best tomographic reconstruction of section 7.2 is obtained, as well as the best optical behaviour of the resulting gradient index. We name the best tomographic reconstruction that which reproduces the best the experimental optics of the crystalline lens according to the following magnitudes:

- $rms_{\Delta S}$: the *rms* error in the distribution of the optical path in the straight line tangent to the exit vertex of the lens ($z = t$), where it is included the piston retrieved by the algorithm.
- $PV_{\Delta S}$: the peak-valley error of that same distribution of optical paths.
- $rms_{\Delta sin}$: the *rms* error in the distribution of sines of deflection of the exit rays at $z = t$.
- $PV_{\Delta sin}$: the peak-valley error of that distribution of sines.
- Δdc_a: the average relative error in the anterior vertex distance[1] (the calculation of this parameter is explained in section 7.2.2, point 3).

The comments and explanation of the results are done in the captions of each one of the tables and figures.

[1] Like in section 7.2, in this appendix we name anterior vertex of the crystalline lens that one that is placed closer to the cornea in the eye ball and at the exit of the rays in the experimental setup.

$\emptyset_{eq}$**(mm)**	10.2 ± 0.1
t **(mm)**	7.8 ± 0.1
R_{ant} **(mm)**	7.98 ± 0.05
Q_{ant}	1.46 ± 0.02
$SD_{fit\,ant}$ **(μm)**	6.6
R_{post} **(mm)**	5.32 ± 0.06
Q_{post}	0.03 ± 0.02
$SD_{fit\,post}$ **(μm)**	69.3
Swelling (%)	0.14

Table D.1: Geometric parameters of the crystalline lens: $\emptyset_{eq}$, equatorial diameter; t, thickness; R_{ant}, Q_{ant} and $SD_{fit\,ant}$, the radius and asphericity of the anterior surface, as well as the standard deviation of its fitting; R_{post}, Q_{post} and $SD_{fit\,post}$, the radius and asphericity of the posterior surface, besides the standard deviation of the fitting; the swelling detected between one projection and another in relation with the total thickness of the eye lens.

	1st projection	**2nd projection**	**3rd projection**
θ (°)	0.44 ± 0.01	20.96 ± 0.06	38.64 ± 0.06
Aperture (%)	95.2	86.3	67.5
Number of rays	76	76	77

Table D.2: Parameters of the projections.

$\boldsymbol{n_{00}}$	1.3669	$\boldsymbol{n_{12}}$	-0.4405
$\boldsymbol{n_{01}}$	0.4077	$\boldsymbol{n_{20}}$	-0.0766
$\boldsymbol{n_{02}}$	-1.0172	$\boldsymbol{n_n}$	1.434
$\boldsymbol{n_{03}}$	1.2613	$\boldsymbol{n_p}$	1.367
$\boldsymbol{n_{04}}$	-0.6483	$\boldsymbol{n_a}$	1.370
$\boldsymbol{n_{10}}$	-0.2535	$\boldsymbol{n_{eq}}$	1.365
$\boldsymbol{n_{11}}$	0.4657	$\boldsymbol{z_H\ (t=1)}$	0.56

Table D.3: Coefficients n_{ij} of the gradient normalized to $t = 1$, as well as the index of the nucleus ($n_n = n\,(0, z_H)$), of the posterior vertex (n_p), of the anterior vertex (n_a) and equatorial ($n_{eq} = n\,(\emptyset/2, z_H)$). It is also provided the position of the plane z_H (maximum of the gradient in the optic axis) in relation with the posterior vertex of the crystalline lens.

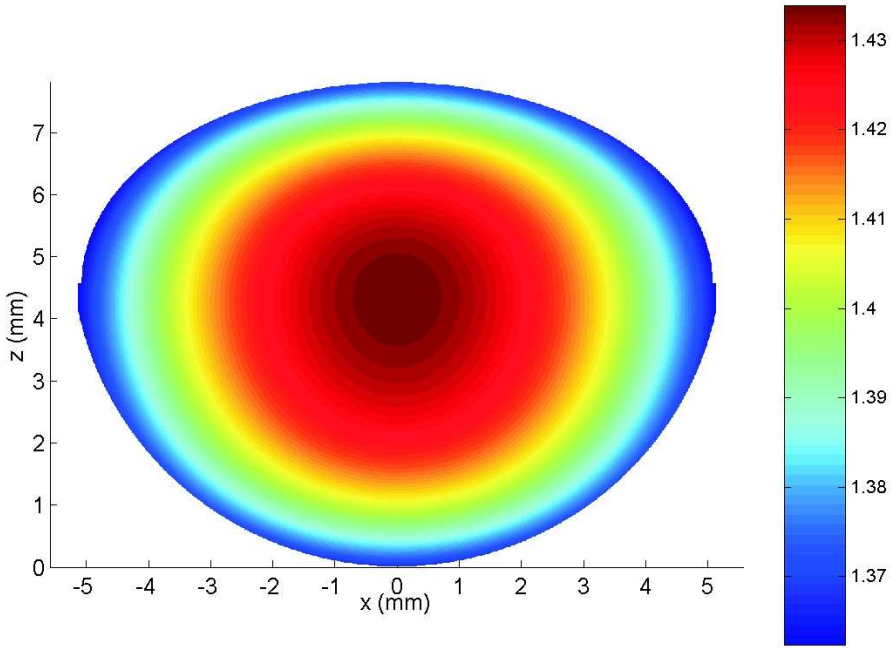

Figure D.1: Retrieved gradient index.

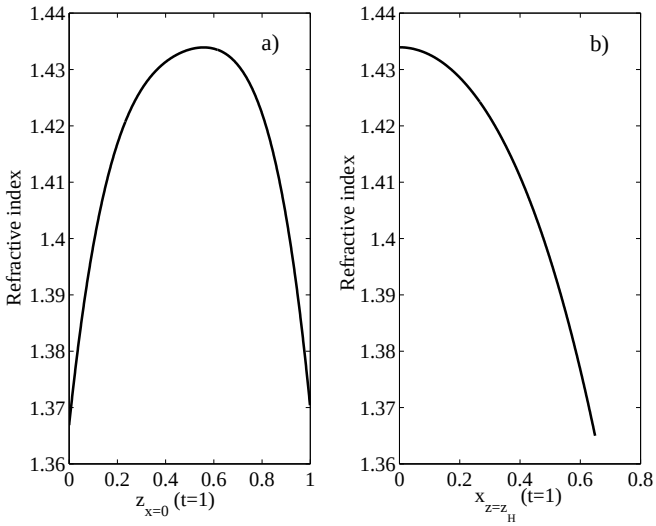

Figure D.2: Profiles of the retrieved gradient index along the optic axis (a) and at $z = z_H$ (b).

D.1 First projection

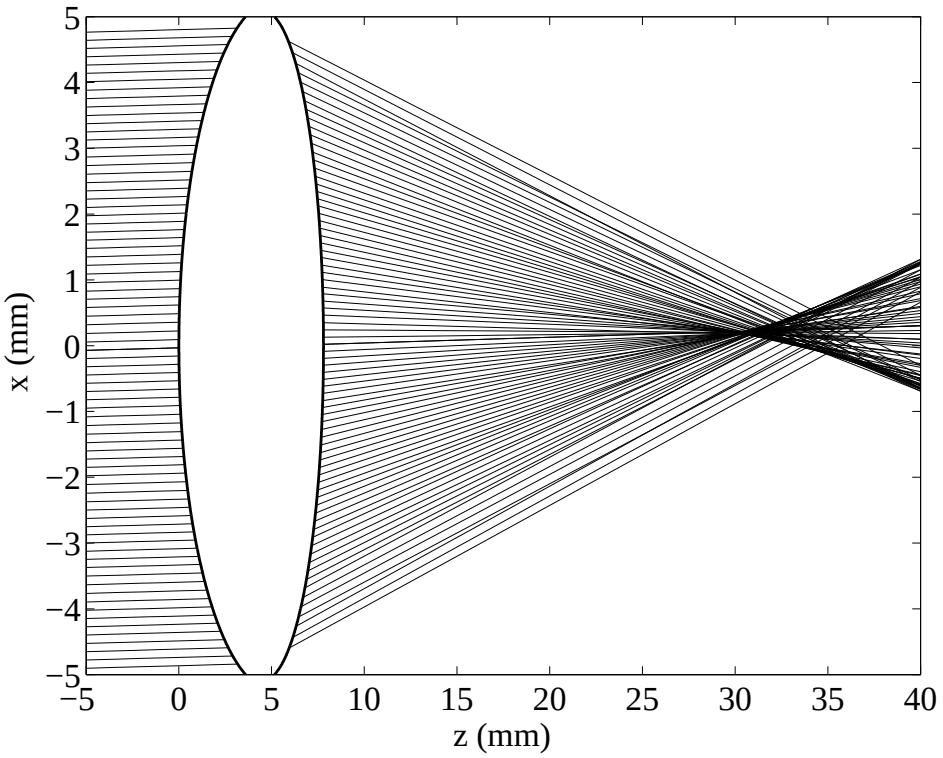

Figure D.3: Graphic illustration of a meridional plane of the eye lens and of the exit and entry rays fitted to straight lines ($\theta_1 = 0.44^{\circ} \pm 0.01^{\circ}$). It can be clearly noticed the existence of a strong negative spherical aberration.

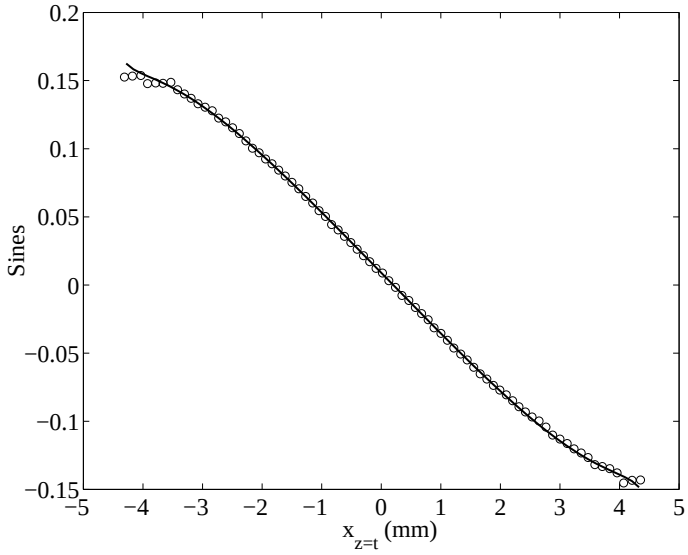

Figure D.4: Experimental distribution of the sines of deflection at the exit of the eye lens (circles) and that obtained by propagation of the entry rays in the retrieved gradient (solid line) [First projection].

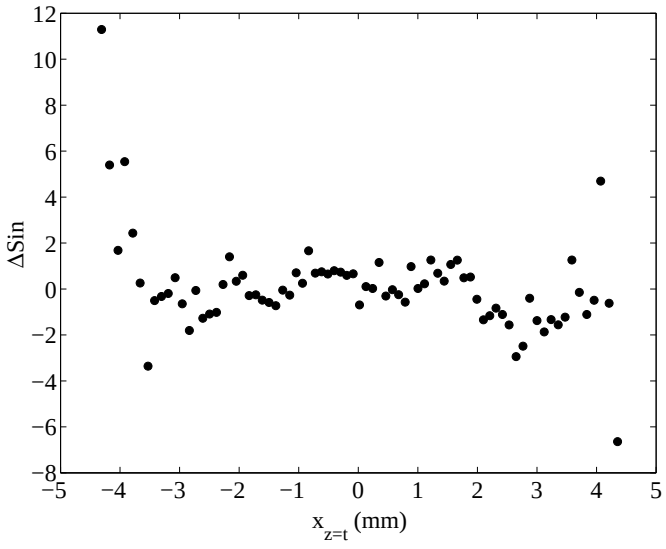

Figure D.5: Difference between the experimental and the propagated distributions of sines of deflection at the exit of the eye lens, Δsin ($rms_{\Delta sin} = 2.1 \times 10^{-3}$ and $PV_{\Delta sin} = 1.8 \times 10^{-2}$) [First projection].

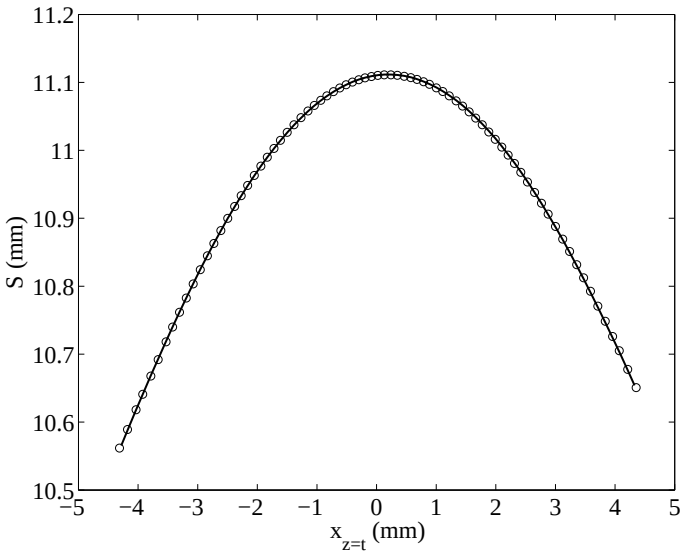

Figure D.6: Experimental distribution of the optical path at the exit of the eye lens (circles) and that obtained by propagation of the entry rays in the retrieved gradient index (solid line) [First projection].

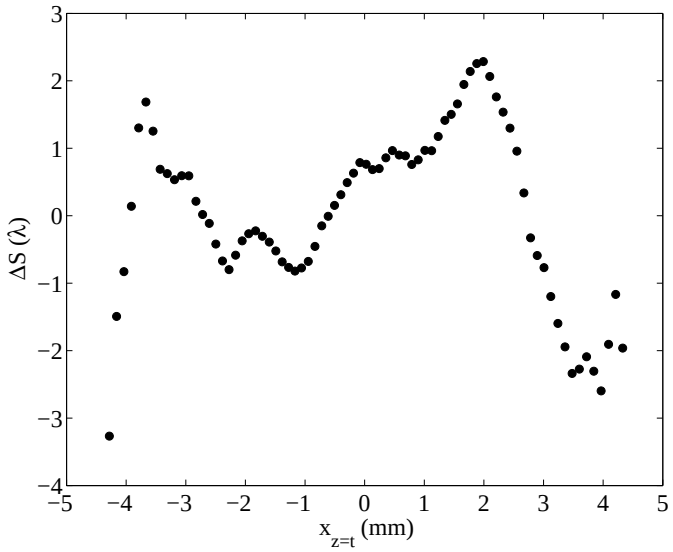

Figure D.7: Difference between the experimental and the propagated distributions of the optical path at the exit of the eye lens, ΔS ($rms_{\Delta S} = 1.2\ \lambda$ and $PV_{\Delta S} = 5.6\ \lambda$) [First projection].

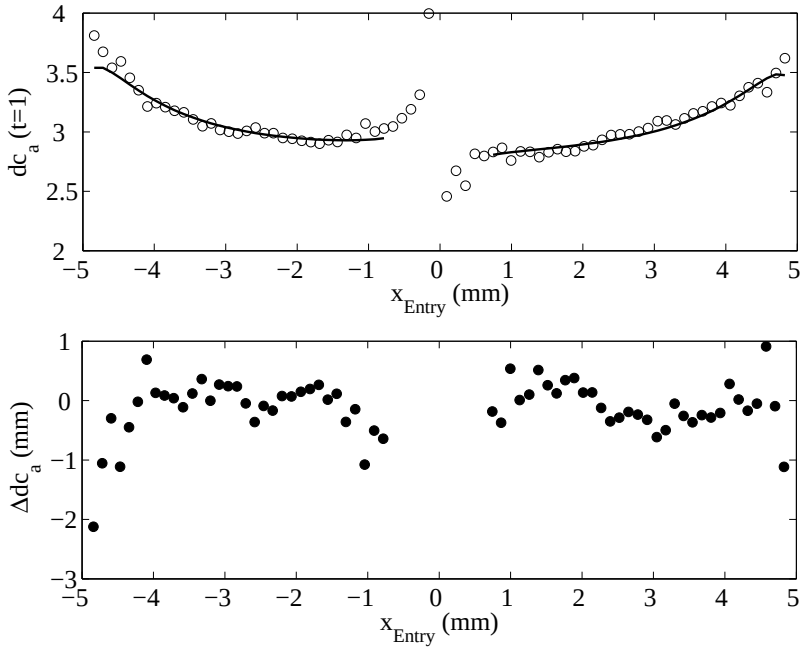

Figure D.8: Experimental variation of the anterior vertex distance dc_a with the height of entry of the rays in the lens (circles) and that obtained with the retrieved gradient index (solid line), as well as the difference between both Δdc_a ($rms_{\Delta dc_a} = 0.48$ mm and $PV_{\Delta dc_a} = 3.04$ mm). The calculation of this difference is done for all rays but the ten rays closest to the optic axis of reference (see section 7.2.2, point 3), since in this paraxial region the error in the calculation of dc_a tends to infinity [First projection].

D.2 Second projection

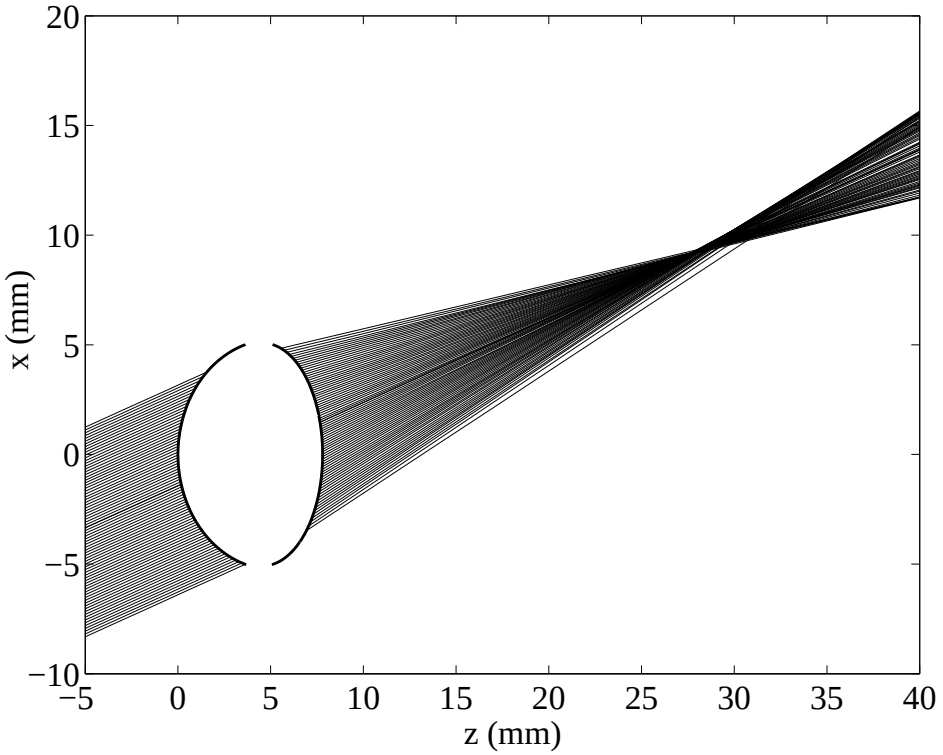

Figure D.9: Graphic illustration of a meridional plane of the eye lens and of the exit and entry rays fitted to straight lines ($\theta_2 = 20.96^{\circ} \pm 0.06^{\circ}$).

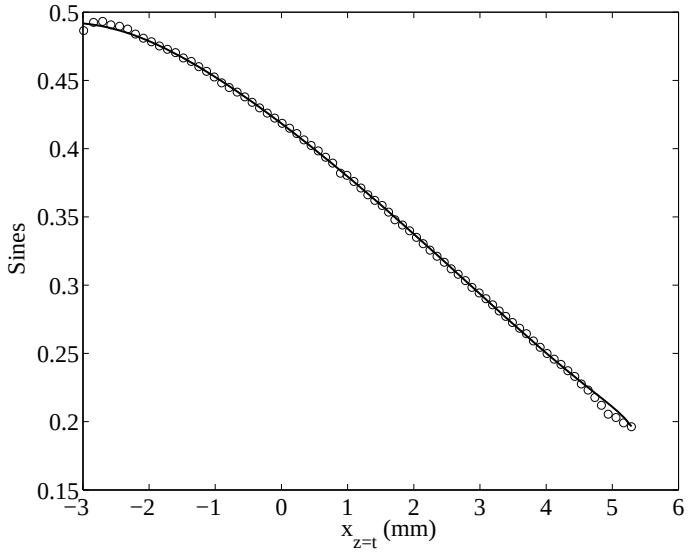

Figure D.10: Experimental distribution of the sines of deflection at the exit of the eye lens (circles) and that obtained by propagation of the entry rays in the retrieved gradient (solid line) [Second projection].

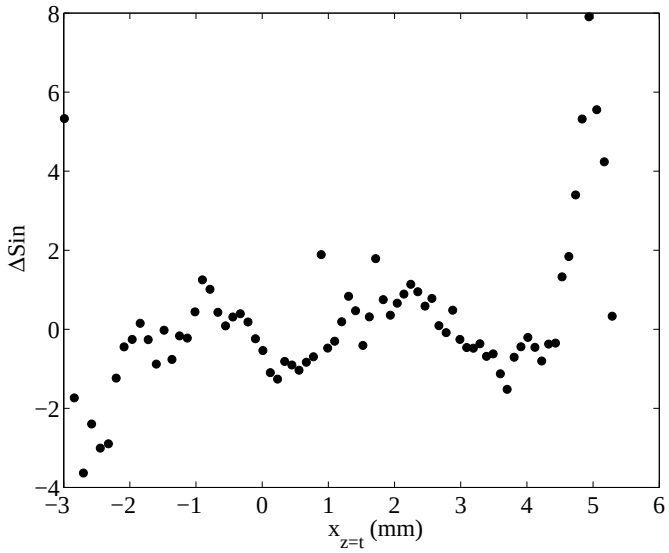

Figure D.11: Difference between the experimental and the propagated distributions of sines of deflection at the exit of the eye lens, Δsin ($rms_{\Delta sin} = 1.8 \times 10^{-3}$ and $PV_{\Delta sin} = 1.2 \times 10^{-2}$) [Second projection].

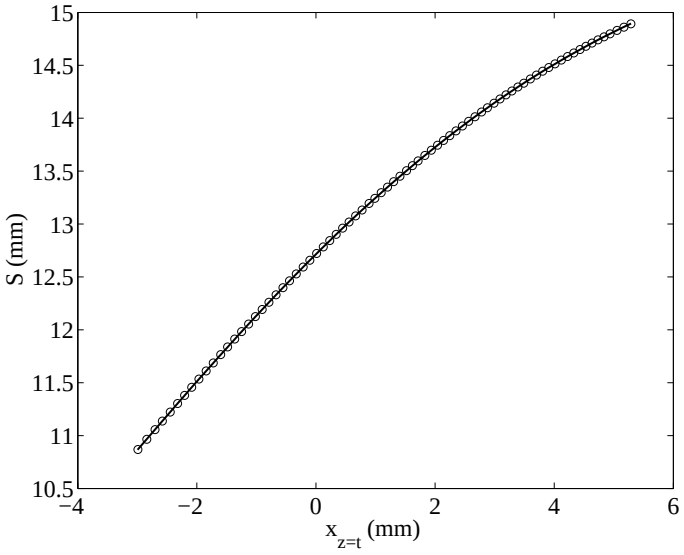

Figure D.12: Experimental distribution of the optical path at the exit of the eye lens (circles) and that obtained by propagation of the entry rays in the retrieved gradient index (solid line) [Second projection].

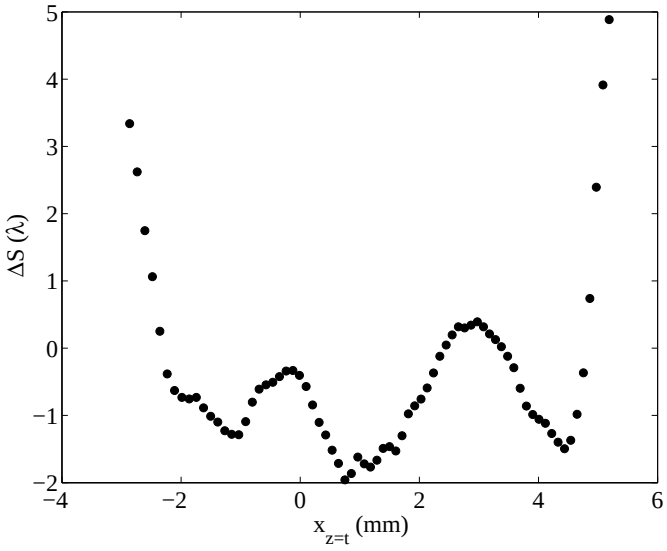

Figure D.13: Difference between the experimental and the propagated distributions of the optical path at the exit of the eye lens, ΔS ($rms_{\Delta S} = 1.4\ \lambda$ and $PV_{\Delta S} = 6.8\ \lambda$) [Second projection].

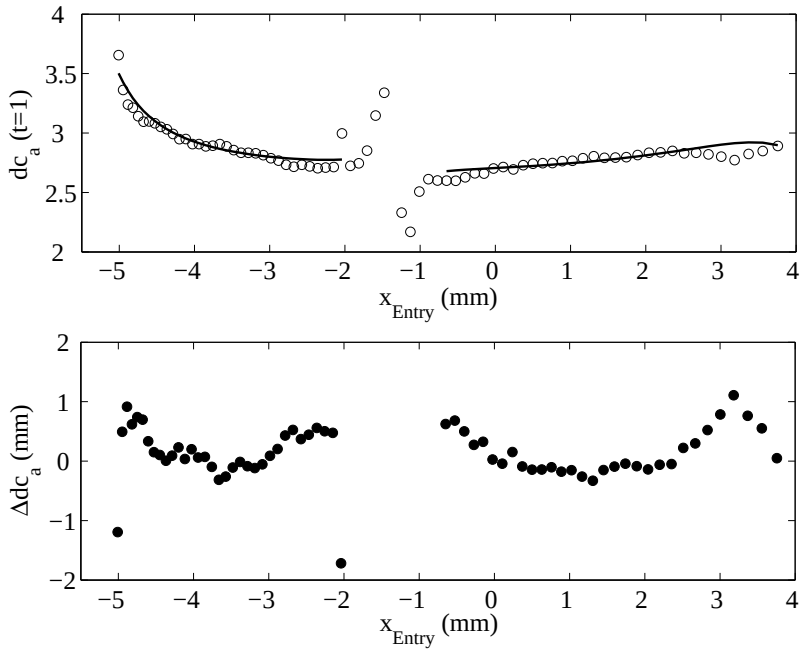

Figure D.14: Experimental variation of the anterior vertex distance dc_a with the height of entry of the rays in the lens (circles) and that obtained with the retrieved gradient index (solid line), as well as the difference between both Δdc_a ($rms_{\Delta dc_a}$ = 0.46 mm and $PV_{\Delta dc_a}$ = 2.83 mm). The calculation of this difference is done for all rays but the ten rays closest to the optic axis of reference (see section 7.2.2, point 3), since in this paraxial region the error in the calculation of dc_a tends to infinity [Second projection].

D.3 Third projection

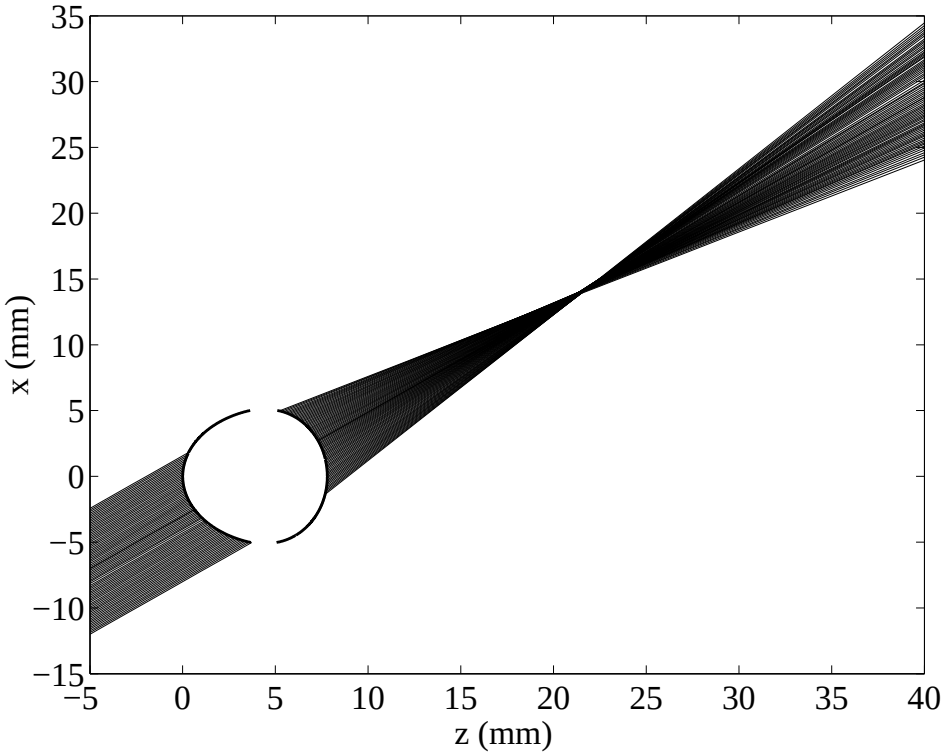

Figure D.15: Graphic illustration of a meridional plane of the eye lens and of the exit and entry rays fitted to straight lines ($\theta_3 = 38.64^{\circ} \pm 0.06^{\circ}$).

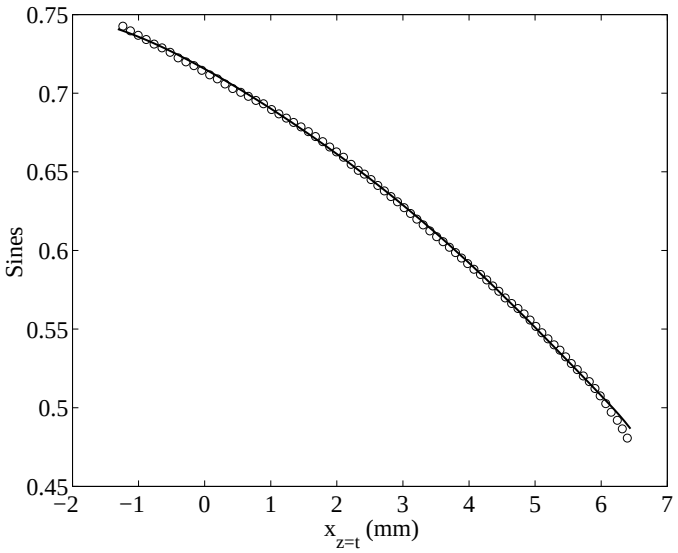

Figure D.16: Experimental distribution of the sines of deflection at the exit of the eye lens (circles) and that obtained by propagation of the entry rays in the retrieved gradient (solid line) [Third projection].

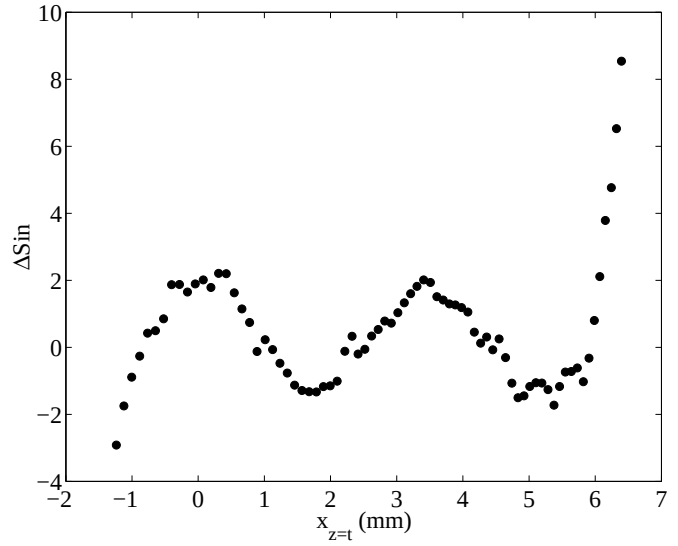

Figure D.17: Difference between the experimental and the propagated distributions of sines of deflection at the exit of the eye lens, Δsin ($rms_{\Delta sin} = 1.9 \times 10^{-3}$ and $PV_{\Delta sin} = 1.1 \times 10^{-2}$) [Third projection].

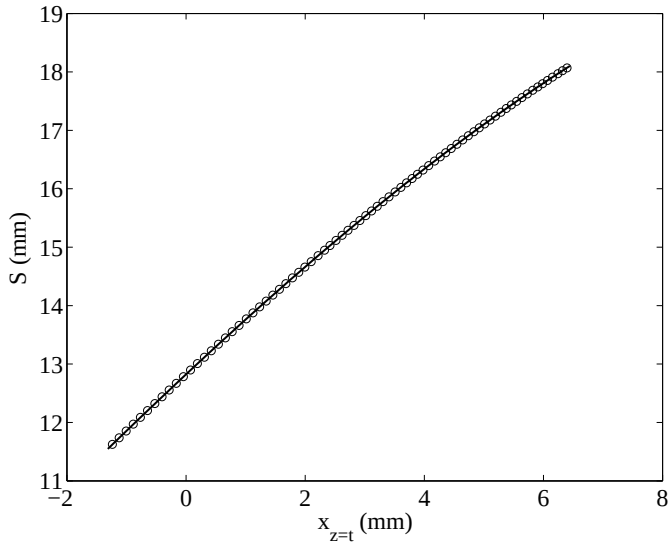

Figure D.18: Experimental distribution of the optical path at the exit of the eye lens (circles) and that obtained by propagation of the entry rays in the retrieved gradient index (solid line) [First projection].

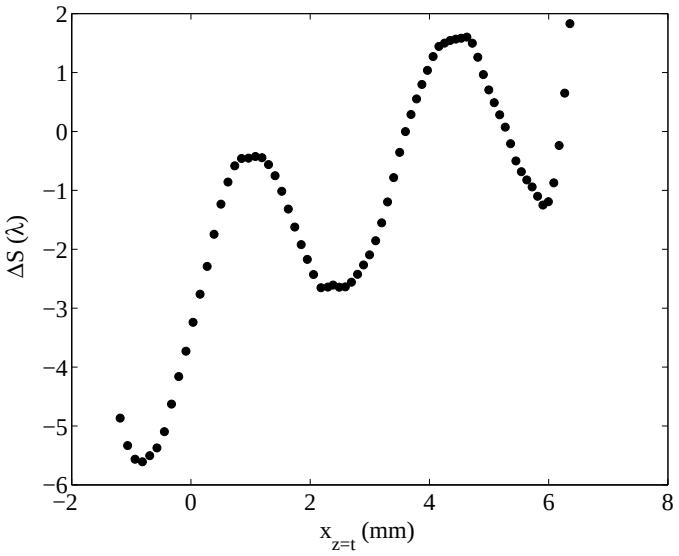

Figure D.19: Difference between the experimental and the propagated distributions of the optical path at the exit of the eye lens, ΔS ($rms_{\Delta S} = 2.3\ \lambda$ and $PV_{\Delta S} = 7.4\ \lambda$) [Third projection].

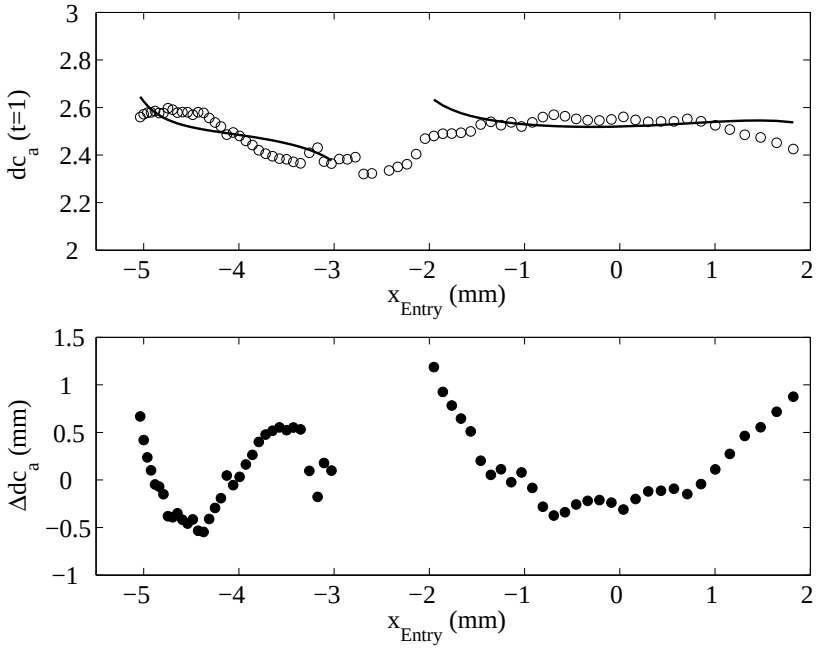

Figure D.20: Experimental variation of the anterior vertex distance dc_a with the height of entry of the rays in the lens (circles) and that obtained with the retrieved gradient index (solid line), as well as the difference between both Δdc_a ($rms_{\Delta dc_a} = 0.41$ mm and $PV_{\Delta dc_a} = 1.73$ mm). The calculation of this difference is done for all rays but the ten rays closest to the optic axis of reference (see section 7.2.2, point 3), since in this paraxial region the error in the calculation of dc_a tends to infinity [Third projection].

E On axis optics of the average pig lens

In section 7.2.1 the average gradient index of the 14 analyzed pig lenses is shown (see Figs. 7.6 and 7.8), as well as the coefficients n_{ij} that fit the best that gradient (see table 7.7). By using these coefficients and the average geometric parameters of table 7.6, we have numerically propagated a plane wavefront that enters the lens through its anterior surface with $\theta = 0^o$. From the study of the wavefront at its exit we have obtained a paraxial posterior vertex focus $f_{post} = 21.172$ mm $= 2.823$ $(t = 1)$, that corresponds to a posterior vertex power $F_{post} = 62.96$ D (for an vitreous humour index of 1.333 at $\lambda = 633$ nm [Siv82]).

Next, we show several graphs of the on axis optical behaviour of this average pig lens.

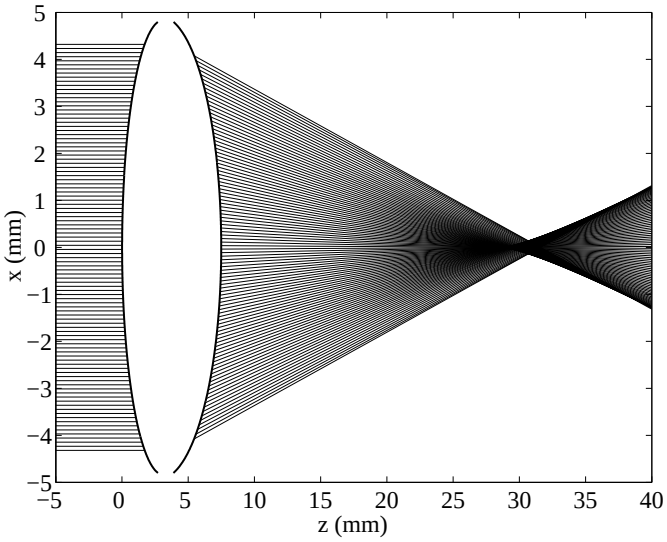

Figure E.1: Graphic illustration of the deflection of the rays at the exit of the average crystalline lens for an on axis projection ($\theta = 0^o$), where entry rays illuminate the anterior surface of the lens.

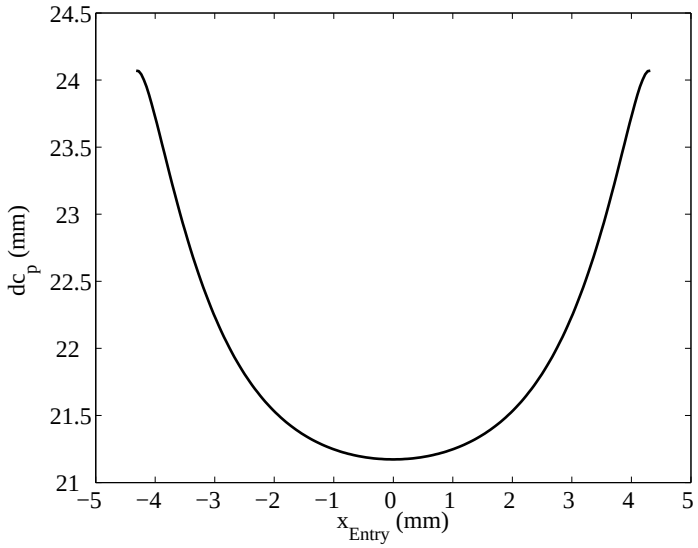

Figure E.2: Variation of the posterior vertex distance, dc_p, with the height of entry of the rays in the average lens. Like in the previous figure, it stands out a strong negative spherical aberration. The study of the geometry of the cornea in pigs would be very useful to determine if this strong aberration has any compensating role of that produced by the cornea.

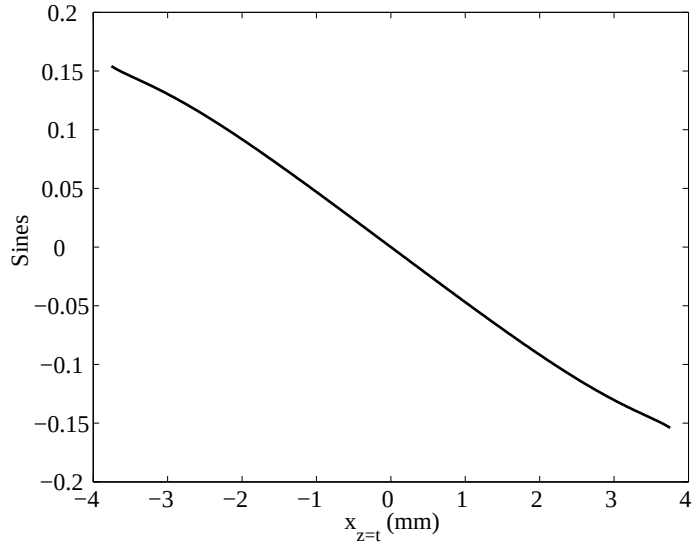

Figure E.3: Distribution of the sines of deflection at the exit of the average lens for the on axis projection.

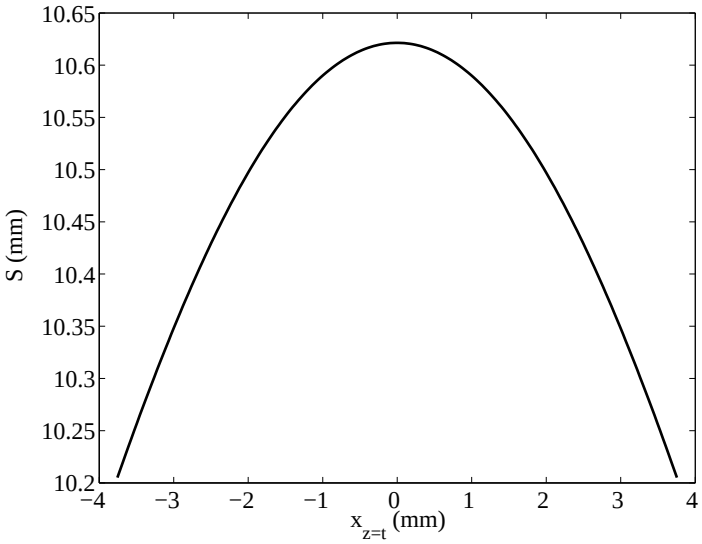

Figure E.4: Distribution of the optical paths at the exit of the average lens for the on axis projection (By fitting the phase at this position to Zernike modes we obtain a defocus of $Z_2^0(\rho,\theta) = 11.9\ \lambda$ and a spherical aberration of $Z_4^0(\rho,\theta) = 3.7\ \lambda$ (Standard notation [Thi02]), being all remaining terms not significative).

F Optics of a crystalline lens with a homogeneous refractive index

A very important topic in the study of the crystalline lens is the analysis of the role played by the gradient index in its optical behaviour. To carry out this analysis in this appendix we will compare the experimental optical behaviour of an eye lens with that it would have if it had a homogeneous refractive index. We perform the calculation of this effective homogeneous index by applying the tomographic algorithm to the same input data we have used to retrieve the gradient index. In table F.1 it can be seen the indices obtained for the lens studied in Appendix D by considering different options for the input data: by using all projections, just one of them or different selections of the first projection. If just the most central rays of the first projection are taken into account the standard deviation of the tomographic fitting is of the order of that obtained for the calculation of the gradient ($SD_{tomo} = 1.4\ \lambda$). We infer, thus, that this central region could be approximated as a lens with a homogeneous index $n \simeq 1.5$, higher than the maximum index retrieved in the gradient ($n_n = 1.434$) and close to that of the glass ($n = 1.51509$ at $\lambda = 633$ nm for BK7 glass). On the other hand, when just using the data from the most peripheral rays of the first projection, the effective index falls up to $n = 1.4331$ and the fitting deviation rises considerably since the inhomogeneous nature of the refractive index becomes more noticeable in this region. The order of this standard deviation does not change when we calculate the effective index of each one of the three projections and for all of them together. The calculated effective homogeneous index for this last case, $n = 1.4575$, is the one we use to compare the experimental optics of the lens with that it would have if it were a homogeneous index lens. Next, we show the graphs that result form this comparison for the three projections carried out in the laboratory, as well as a list of the main optical properties that can be ascribed to the existence of a gradient index (as we have mentioned before, the experimental data correspond to those of the crystalline lens in the Appendix D).

Input data	$\boldsymbol{SD_{tomo}}$ **(λ)**	$\boldsymbol{n_{homo}}$
central 25% θ_1	0.6	1.4995
central 50% θ_1	1.7	1.4944
peripheral 50% θ_1	24.9	1.4331
θ_1	36.7	1.4515
θ_2	31.3	1.4600
θ_3	32.0	1.4691
θ_1, θ_2 and θ_3	35.5	1.4575

Table F.1: Homogeneous indices indices, n_{homo}, and standard deviations of the tomographic fit, SD_{tomo}, obtained for different sets of input data: data from the three projections, from each one of them and from particular cases of the first projection (the most central 25% and the 50% of the rays of that projection and the most peripheral 50%).

F.1 First projection

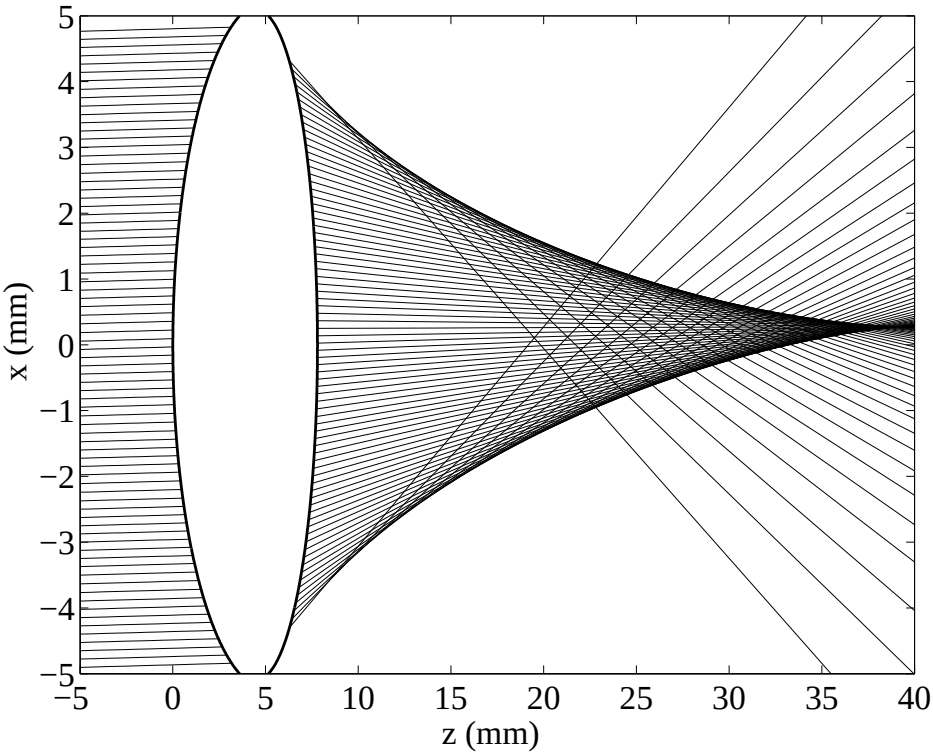

Figure F.1: Graphic illustration of the deflection of the rays at the exit of the homogeneous eye lens for the first projection ($\theta_1 = 0.44^{\circ} \pm 0.01^{\circ}$). It can be clearly noticed the existence of a strong spherical aberration, of different sign and stronger than the experimental case (see Fig. D.3).

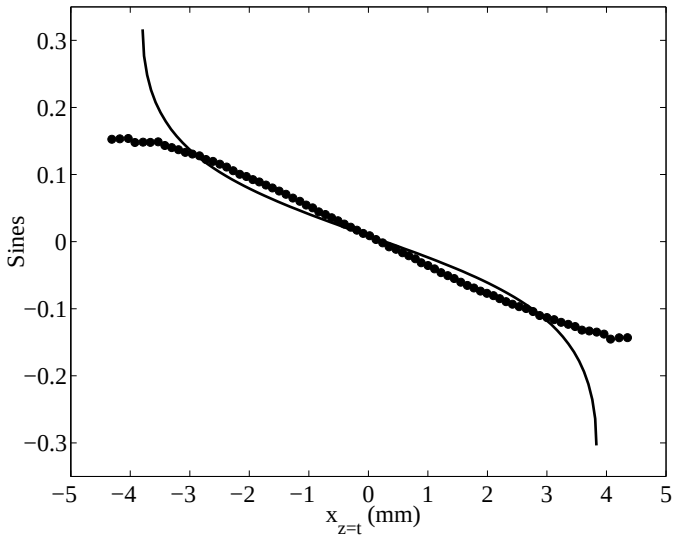

Figure F.2: Experimental distribution of the sines of deflection at the exit of the eye lens (circles) and that obtained by propagation of the entry rays through the homogeneous index (solid line). Here it is also noticeable how the homogeneous index changes the sign of the spherical aberration at the exit of the lens and becomes stronger [First projection].

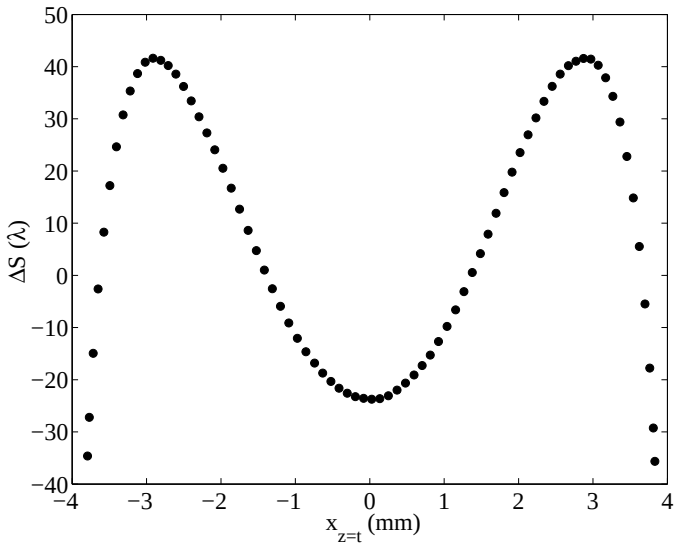

Figure F.3: Difference between the experimental distribution of the optical path at the exit of the lens and that obtained by propagation in the homogeneous index, ΔS. At first glance, important differences in defocus and spherical aberration can be seen [First projection].

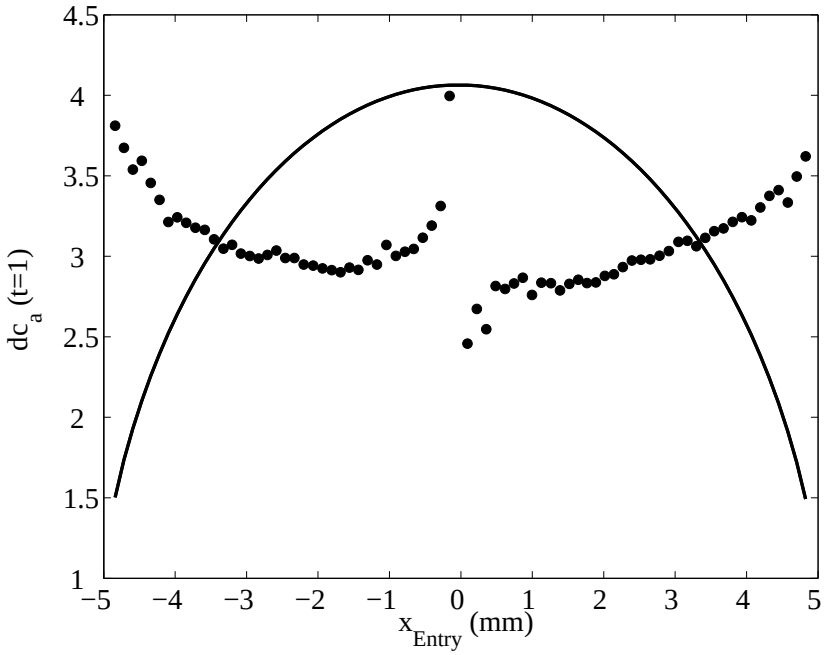

Figure F.4: Experimental variation of the anterior vertex distance dc_a with the entry of height of the rays in the crystalline lens (circles) and that obtained with the homogeneous index (solid line). In this graph it can be also noticed the worst behaviour of the homogeneous index, as well as the opposite sign of the spherical aberration (Because of the difference between the optic axes of reference of the experimental and homogeneous case, dc_a has been calculated by using the optic axis obtained for each one of the cases) [First projection].

F.2 Second projection

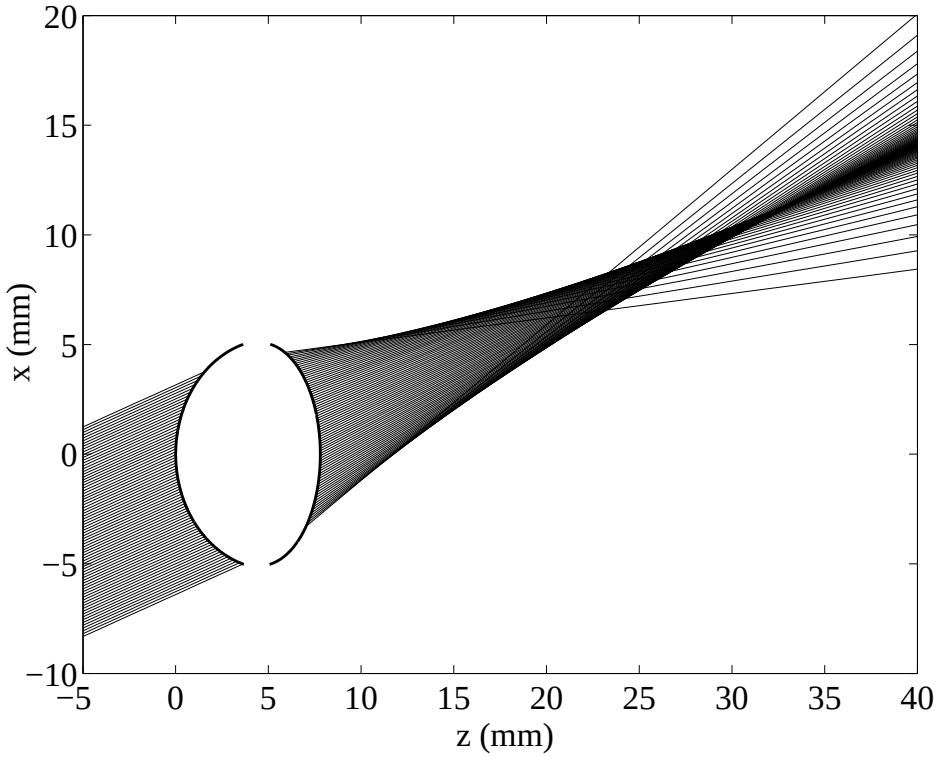

Figure F.5: Graphic illustration of the deflection of the rays at the exit of the homogeneous eye lens for the second projection ($\theta_2 = 20.96^{o} \pm 0.06^{o}$). In relation with the experimental case, the optics are clearly worst with a homogeneous index, as it can be seen in its larger circle of minimum confusion (see Fig. D.9).

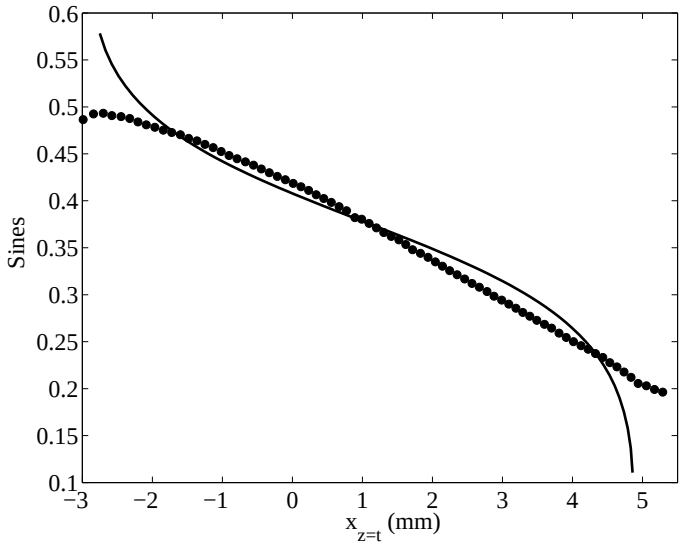

Figure F.6: Experimental distribution of the sines of deflection at the exit of the eye lens (circles) and that obtained by propagation of the entry rays through the homogeneous index (solid line). Like in the former projection, also in this case the homogeneous index causes a change of sign and a larger spherical aberration at the exit of the lens [Second projection].

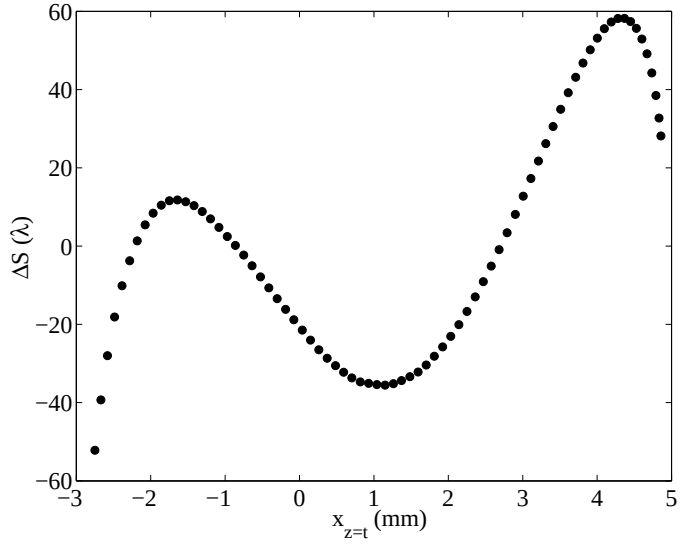

Figure F.7: Difference between the experimental distribution of the optical path at the exit of the lens and that obtained by propagation in the homogeneous index, ΔS. As in the former projection, there are also important differences in defocus and spherical aberration [Second projection].

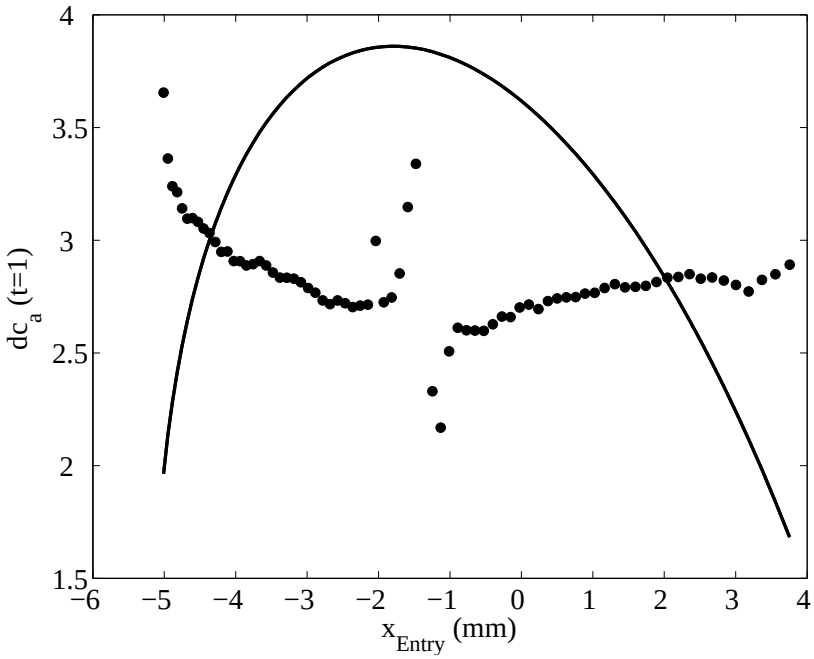

Figure F.8: Experimental variation of the anterior vertex distance dc_a with the entry of height of the rays in the crystalline lens (circles) and that obtained with the homogeneous index (solid line). In this graph it can be also noticed the worst behaviour of the homogeneous index, as well as the opposite sign of the spherical aberration (Because of the difference between the optic axes of reference of the experimental and homogeneous case, dc_a has been calculated by using the optic axis obtained for each one of the cases) [Second projection].

F.3 Third projection

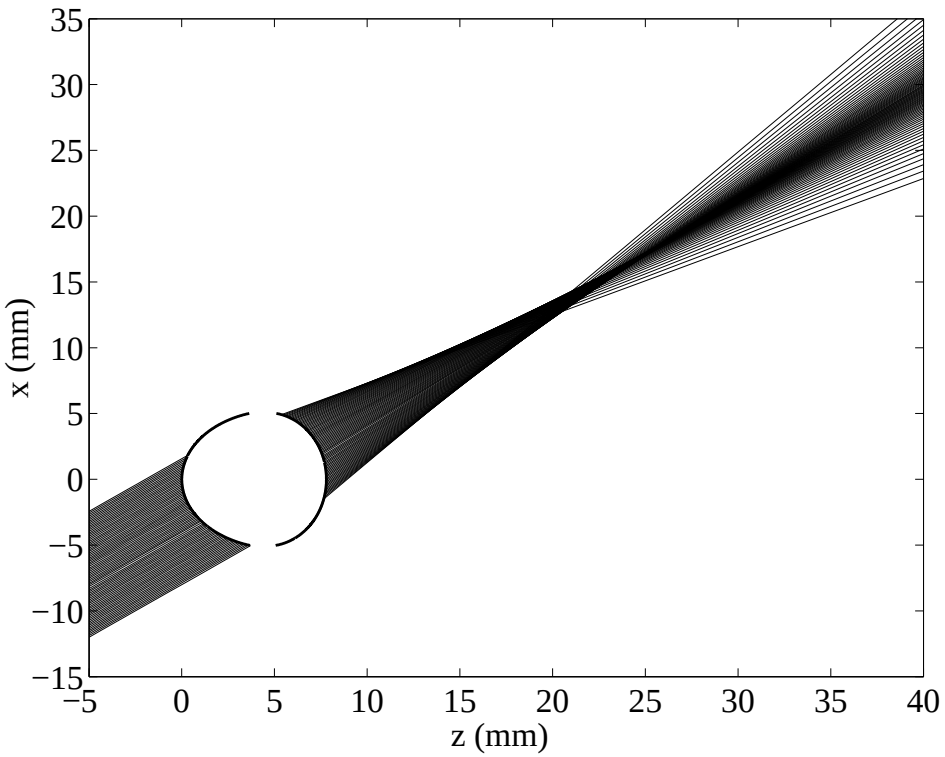

Figure F.9: Graphic illustration of the deflection of the rays at the exit of the homogeneous eye lens for the third projection ($\theta_3 = 38.64^{\circ} \pm 0.06^{\circ}$). The circle of minimum confusion is clearly larger than in the experimental case (see Fig. D.15).

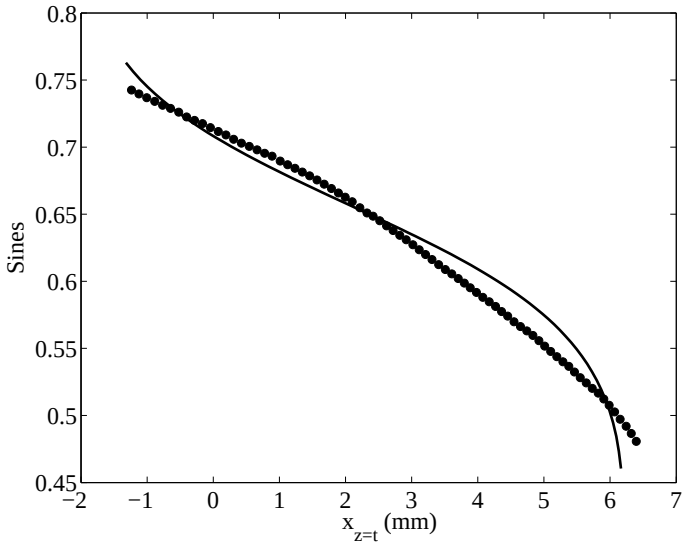

Figure F.10: Experimental distribution of the sines of deflection at the exit of the eye lens (circles) and that obtained by propagation of the entry rays through the homogeneous index (solid line) [Third projection].

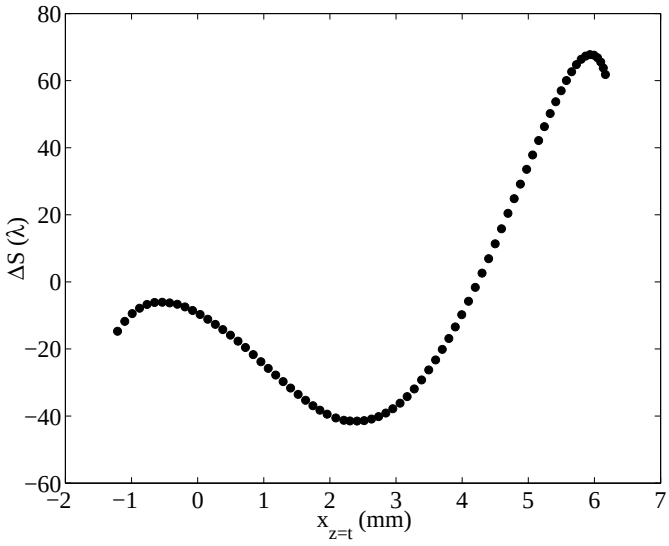

Figure F.11: Difference between the experimental distribution of the optical path at the exit of the lens and that obtained by propagation in the homogeneous index, ΔS [Third projection].

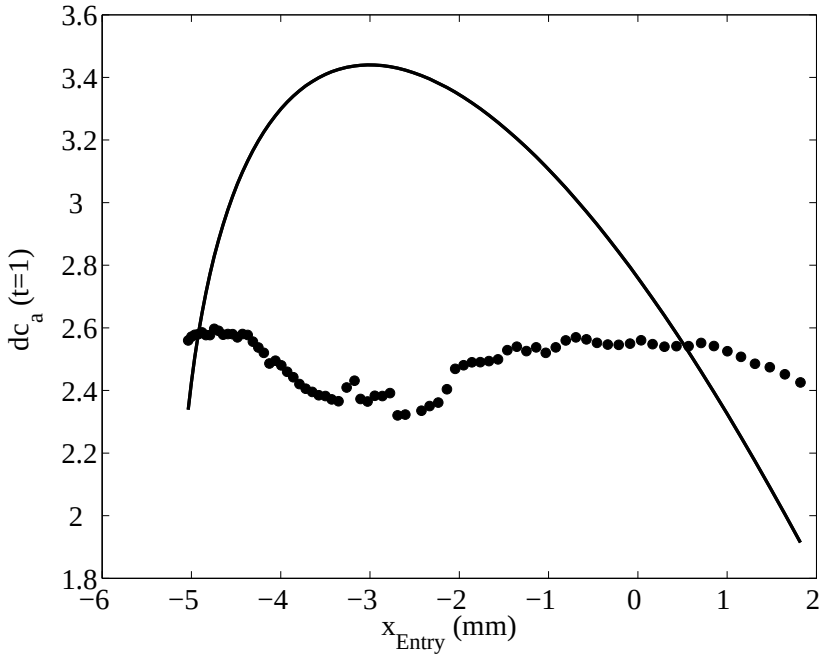

Figure F.12: Experimental variation of the anterior vertex distance dc_a with the entry of height of the rays in the crystalline lens (circles) and that obtained with the homogeneous index (solid line). In this graph it can be also noticed the worst behaviour of the homogeneous index, as well as the opposite sign of the spherical aberration (Because of the difference between the optic axes of reference of the experimental and homogeneous case, dc_a has been calculated by using the optic axis obtained for each one of the cases) [Third projection].

From the analysis of the previous figures we can deduce the following optical properties stemmed from the existence of the gradient index in the crystalline lens:

1. Minimization of the optical aberrations, more noticeable as we go further from the optic axis, as well as a change of sign of the aberration in relation with a homogeneous index. This second feature might have something to do with a possible compensation of the aberrations of the cornea.

2. Higher paraxial dioptric power, with an equivalent index higher than the maximum value of the gradient index.

3. Better optical behaviour for objects out of axis, with circles of minimum confusion much smaller than those that would correspond to the case of a homogeneous lens.

4. Differences of the order of 10^{-2} in sines and 10λ in optical paths at the exit of the crystalline lens regarding the homogeneous lens.

Bibliography

[Aco02] E. Acosta, R. Flores, D. Vazquez, S. Rios, L. Garner and G. Smith, "Tomographic method for measurement of the refractive index profile of optical fibre preforms and rod GRIN lenses", Japanese Journal of Applied Physics 41, 4821-4824 (2002)

[Aco05] E. Acosta, D. Vazquez, L. Garner and G. Smith, "Tomographic method for measurement of the gradient refractive index of the crystalline lens. I. The spherical fish lens", J. Opt. Soc. Am. A 22 , 424-433 (2005)

[Aco06] E. Acosta, S. Chamadoira and R. Blendowske, "Modified point diffraction interferometer for inspection and evaluation of ophthalmic components", J. Opt. Soc. Am. A 23, 632-637 (2006)

[Alh95] I.H. Al-Ahdali and M.A. El-Messiery, "Examination of the effect of the fibrous structure of a lens on the optical characteristics of the human eye: a computer-simulated model", Applied Optics 34, 5738-5745 (1995)

[Are04] J. Ares and J. Arines, "Influence of thresholding on centroid statistic: full analytical description", Applied Optics 43, 5796-5805 (2004)

[Axe88] D. Axelrod, D. Lerner and P.J. Sands, "Refractive index within the lens of a goldfish eye determined from the paths of thin laser beams", Vision Res. 28, 57-65 (1988)

[Bas04] S. Bassnett and D. Beebe, "Lens Fiber Differentiation", en *Development of the ocular lens*, F.J. Lovicu and M.L. Robinson, eds. (Cambridge University Press, UK, 2004)

[Bar57] R. Barer, "Refractometry and interferometry of living cells", J. Opt. Soc. Am. 47, 545-557 (1957)

[Bel98] G. Beliakov and D.Y.C. Chan, "Analysis of inhomogeneous optical systems by the use of ray tracing. II. Three-dimensional systems with symmetry", Applied Optics 37, 5106-5111 (1998)

[Bev92] P.R. Bevington and D.K. Robinson, *Data reduction and error analysis for the physical sciences*, (McGraw-Hill, 1992)

[Bla80] J.W. Blaker, "Toward an adaptive model of the human eye", J. Opt. Soc. Am. 70, 220-223 (1980)

[Bor59] M. Born and E. Wolf, *Principles of optics*, (Cambridge University Press, 6th edition, UK, 1993), p. 122

[Brl78] K.F. Barrell and C. Pask, "Nondestructive index profile measurement of non-circular optical fibre preforms", Opt. Commun. 27, 230-234 (1978)

[Bro04] S. Barbero, A. Glasser, C. Clark and S. Marcos, "Accuracy and possibilities for evaluating the lens gradient-index using a ray tracing tomography global optimization strategy", Invest. Ophthalmol. Vis. Sci. 45, E-Abstract 1723 (2004)

[Bru65] J. Bruce Brackenridge and W. Paul Gilbert, "Schlieren Interferometry. An optical method for determining temperature and velocity distributions in liquids", Applied Optics 4, 819-821 (1965)

[Bss] http://www.bssplus.com/

[Cam84] M.C.W. Campbell, "Measurement of refractive index in an intact crystalline lens", Vision Res. 24, 409-415 (1984)

[Cha88] D.Y.C. Chan, J.P. Ennis, B.K. Pierscionek and G. Smith, "Determination and modeling of the 3-D gradient refractive indices in crystalline lenses", Applied Optics 27, 926-931 (1988)

[Chr91] W.N. Charman, "The Vertebrate Dioptric Apparatus", in *Evolution of the Eye and Visual System (Vision and Visual Dysfunction, vol. 2)*, J.R. Cronly-Dillon and R.L. Gregory, eds. (MacMillan Press, UK, 1991), p. 96

[Chu77] P.L. Chu, "Nondestructive measurement of index profile of an optical-fibre preform", Electron. Lett. 13, 736-738 (1977)

[Chu79] P.L. Chu and T. Whitbread, "Nondestructive determination of refractive index profile of an optical fiber: fast Fourier transform method", Appl. Opt. 18, 1117-1122 (1979)

[Coo75] R.J. Cook, "Beam wander in a turbulent medium: An application of the Ehrenfest's theorem", J. Opt. Soc. Am 65, 942-948 (1975)

[Cor64] A.M. Cormack, "Representation of a function by its line integrals, with some radiological applications. II" J. Appl. Phys 35, 2908-2912 (1964)

[Dub05] M. Dubbelman, G.L. Van der Heijde and H.A. Weeber, "Change in shape of the aging human crystalline lens with accommodation", Vision Res. 45, 117-132 (2005)

[Edm] http://www.edmundoptics.com/TechSupport/DisplayArticle.cfm?articleid=239

[Fag81] P.P. Fagerholm, B.T. Philipson and B. Lindstrom, "Normal human lens - distribution of protein", Exp. Eye Res. 33, 615-620 (1981)

[Fer90] R.D. Fernald, "The optical system of fishes", in *The Visual System of Fish*, R.H. Douglas and M.B.A. Djamgoz, eds. (Chapman & Hall, Cambridge, UK, 1990)

[Gar01] L.F. Garner, G. Smith, S. Yao and R.C. Augusteyn, "Gradient refractive index of the crystalline lens of the Black Oreo Dory (Allocytus Niger): comparison of magnetic resonance imaging (MRI) and laser ray-trace methods", Vision Res. 41, 973-979 (2001)

[Gon93] R. C. González and R. E. Woods, *Digital image processing*, (Addison-Wesley, USA, 1993), chap.7

[Gul09] A. Gullstrand, Apéndice II en *Handbuch der Physiologischen Optik* (H.v. Helmholtz), Vol. 1, 3rd edition, 1909 (English translation edited by J.P. Southall, Optical Society of America, Dover, 1924), pp. 351-352

[Hal98] R. Halír and J. Flusser, "Numerically stable direct least squares fitting of ellipses", in *Proceedings of the Sixth International Conference in Central Europe on Computer Graphics and Visualization (WSCG'98)*, V. Skala, ed. (Vydavatelstvi Zapadoceske University, 1998), Vol. 1, pp. 125-132

[Hem95] R.P. Hemenger, L.F. Garner and C.S. Ooi, "Change with age of the refractive index gradient of the human ocular lens", Invest. Ophthalmol. Vis. Sci. 36, 703-707 (1995)

[Her80] G.T. Herman, *Image reconstructions from projections (The fundamentals of computerized tomography)*, (Academic Press, London, 1980), chap. 6

[Hil89] B.P. Hills, S.F. Takacs and P.S. Belton, "The effects of proteins on the proton NMR transverse relaxation times of water", Mol. Phy. 67, 903-918 (1989)

[Hol02] J.A. Holgado Terriza, *Medida de magnitudes dinámicas por análisis de interfases curvas* (Tesis doctoral, Universidad de Granada, 2002), cap. 4

[Hug48] A. Huggert, "On the form of the iso-indicial surfaces of the human crystalline lens", Acta Ophthalmol. (Suppl) (Kbh) 30, 1-126 (1948)

[Iga78] K. Iga and Y. Kokubun, "Formulas for calculating the refractive index profile of optical fibres from their transverse interference patterns", Appl. Opt. 17, 1972-1974 (1978)

[Iga84] K. Iga, Y. Kokubun and M. Oikawa, "Fundamentals of microoptics. Distributed index, microlens and stacked planar optics" (Academic Press, Tokyo, 1984)

[Jag90] W.S. Jagger, "The refractive structure and optical properties of the isolated crystalline lens of the cat", Vision Res. 30, 723-738 (1990)

[Jag92] W.S. Jagger, "The optics of the spherical fish lens", Vision Res. 32, 1271-1284 (1992)

[Jon04] C.E. Jones and J.M. Pope, "Measuring optical properties of an eye lens using magnetic resonance imaging", Magnetic Resonance Imaging 22, 211-220 (2004)

[Jon05] C.E. Jones, D.A. Atchison, R. Meder and J.M. Pope, "Refractive index distribution and optical properties of the isolated human lens measured using magnetic resonance imaging (MRI)", Vision Res. 45, 2352-2366 (2005)

[Kau94] P.L. Kaufman, "Acomodación y presbiopía: aspectos neuromusculares y biofísicos", en *Adler. Fisiología del ojo. Aplicación clínica*, William M. Hart, ed. (Mosby/Doyma Libros, Madrid, 1994)

[Kor02] J.F. Koretz, C.A. Cook and P.L. Kaufman, "Aging of the human lens: changes in lens shape upon accommodation and with accommodative loss", J. Opt. Soc. Am. A 19, 144-151 (2002)

[Kro94] R.H.H. Kröger, M.C.W. Campbell, R. Munger and R.D. Fernald, "Refractive index distribution and spherical aberration in the crystalline lens of the african cichlid fish Haplochromis burtoni", Vision Res 34, 1815-1822 (1994)

[Kro96] R.H.H. Kröger and M.C.W. Campbell, "Dispersion and longitudinal chromatic aberration of the crystalline lens of the African cichlid fish *Haplochromis burtoni*", J. Opt. Soc. Am. A 13, 2341-2347 (1996)

[Kro99] R.H.H. Kröger, M.C.W. Campbell, R.D. Fernald and H.J. Wagner, "Multifocal lenses compensate for chromatic defocus in vertebrate eyes", J. Comp. Physiol. A 184, 361-369 (1999)

[Kro01] R.H.H. Kröger, M.C.W. Campbell and R.D. Fernald, "The development of the crystalline lens is sensitive to visual input in the African cichlid fish, Haplochromis burtoni", Vision Res 41, 549-559 (2001)

[Kus96] J.R. Kuszak, K.L. Peterson and H.G. Brown, "Electron Microscopic Obervations of the Crystalline Lens", Microscopy Research and Technique 33, 441-479 (1996)

[Kus04a] J.R. Kuszak and M.J. Costello, "The Structure of the Vertebrate Lens", in *Development of the ocular lens*, F.J. Lovicu and M.L. Robinson, eds. (Cambridge University Press, UK, 2004)

[Kus04b] J.R. Kuszak, R.K. Zoltoski and C. Sivertson, "Fibre cell organization in crystalline lenses", Experimental Eye Research 78, 673-687 (2004)

[Kus04c] J.R. Kuszak, R.K. Zoltoski and C.E. Tiedemann, "Development of lens sutures", Int. J. Dev. Biol. 48, 889-902 (2004)

[Lop02] A. López González, *Análise da precisión do método Ray Tracer optimizado computacionalmente para a determinación de características focalizadoras de cristalinos oculares,* (Memoria de licenciatura, Universidad de Santiago de Compostela, 2002)

[Man04] F. Manns, V. Fernandez, S. Zipper, S. Sandadi, M. Hamaoui, A. Ho and J-M. Parel, "Radius of curvature and asphericity of the anterior and posterior surface of human cadaver crystalline lenses", Experimental Eye Research 78, 39-51 (2004)

[Mar78] E.W. Marchand, "Gradient index optics", (Academic Press, Nueva York, 1978)

[Mat82] L. Matthiessen, "Über die Beziehungen, Welche Zwischen dem Brechungsindex des Kernzentrums der Kristallinse und den Dimensionen des Auges Bestehen", Pflügers Arch. ges. Physiol. 27, 510-523 (1882)

[Mej99] P. Mejías Arias and R. Martínez Herrero, *Óptica geométrica*, (Editorial Síntesis, Madrid, 1999), cap. 2

[Mof02a] B.A. Moffat and J.M. Pope, "The interpretation of multi-exponential water proton transverse relaxation in the human and porcine eye lens", Magnetic Resonance Imaging 20, 83-93 (2002)

[Mof02b] B.A. Moffat, D.A. Atchison and J.M. Pope, "Age-related changes in refractive index distribution and power of the human lens as measured by magnetic resonance microimaging in vitro", Vision Res. 42, 1683-1693 (2002)

[Moo71] D.T. Moore, "Design of singlets with continuously varying indices of refraction", J. Opt. Soc. Am. 61, 886-894 (1971)

[Mtl] www.mathworks.com/access/helpdesk/help/toolbox/stats/robustfit.html

[Nak68] S. Nakao, S. Fujimoto, R. Nagata and K. Iwata, "Model of refractive-index distribution in the rabbit crystalline lens", J. Opt. Soc. Am. 58, 1125-1130 (1968)

[Nak69] S. Nakao, T. Ono, R. Nagata and K. Iwata, "Model of refractive indices in the human crystalline lens", Jpn. J. Clin. Ophthalmol. 23, 903-906 (1969)

[Nil83] D.E. Nilsson, M. Andersson, E. Hallberg and P. McIntyre, "A microinterferometric method for analysis of rotation-symmetric refractive-index gradients in intact objects", Journal of Microscopy 132, 21-29 (1983)

[Nil05] D.E. Nilsson, L. Gislen, M.M. Coates, C. Skogh and A. Garm, "Advanced optics in a jellyfish eye", Nature 435, 201-205 (2005)

[Pap81] A. Papoulis, *Systems and Transforms with Applications in Optics*, (Robert E. Krieger Publishing Company, Florida, 1981), pp. 40-41

[Pat94] C.A. Paterson and N.A. Delamere, "El cristalino", en *Adler. Fisiología del ojo. Aplicación clínica*, William M. Hart, ed. (Mosby/Doyma Libros, Madrid, 1994)

[Phi68] B. Philipson, "Distribution of protein within the normal rat lens", Invest. Ophthalmol. 8, 258-270 (1968)

[Pie87] B.K. Pierscionek, G. Smith and R.C. Augusteyn, "The refractive increments of bovine $\alpha-$, $\beta-$ and $\gamma-$crystallins", Vision Res. 27, 1539-1541 (1987)

[Pie89] B.K. Pierscionek and D.Y.C. Chan, "Refractive index gradient of human lenses", Optometry and Vision Science 66, 822-829 (1989)

[Pie93] B.K. Pierscionek, "Surface refractive index of the eye lens determined with an optic fiber sensor", J. Opt. Soc. Am A 10, 1867-1871 (1993)

[Pie95] B.K. Pierscionek and R.C. Augusteyn, "The refractive index and protein distribution in the blue eye trevally lens", Journal of the American Optometric Association 66, 739-743 (1995)

[Pie97] B.K. Pierscionek, "Refractive index contours in the human lens", Exp. Eye Res. 64, 887-893 (1997)

[Pom84] O. Pomerantzeff, M. Pankratov, G. Wang and P. Dufault, "Wide-Angle Optical Model of the Eye", American Journal of Optometry And Physiological Optics 61, 166-176 (1984)

[Pop98] A. Popiolek Masajada, "Numerical study of the influence of the shell structure of the crystalline lens on the refractive properties of the human eye", Ophthal. Physiol. Opt. 19, 41-49 (1998)

[Pre99] W.H. Press, S.A. Teutolsky, W.T. Vetterling and B.P. Flannery, *Numerical recipes in C. The art of scientific computing*, (Cambridge University Press, USA, 1999)

[Pri99] S. Priolo, J.G Sivak and J.R. Kuszak, "Effect of age on the morphology and optical quality of the avian crystalline lens", Exp. Eye. Res. 69, 629-640 (1999)

[Qua95] X. Quan and E.S. Fry, "Empirical equation for the index of refraction of seawater", Applied Optics 34, 3477-3480 (1995)

[Ram96] A.G. Ramm and A.I. Katsevich, *The Radon transform and local tomography*, (CRC Press, USA, 1996)

[Rob04] M.L. Robinson and F.J. Lovicu, "The Lens: Historical and Comparative Perspectives", in *Development of the ocular lens*, F.J. Lovicu and M.L. Robinson, eds. (Cambridge University Press, UK, 2004)

[Sgm] http://www.sigmaaldrich.com/catalog/search/ProductDetail/SIGMA/P4417

[Sha82] A. Sharma, D.V. Kumar and A.K. Ghatak, "Tracing rays through graded-index media: a new method", Appl. Opt. 21, 984-987 (1982)

[Siv82] J.G. Sivak and T. Mandelman, "Chromatic dispersion of the ocular media", Vision Res. 22, 997-1003 (1982)

[Siv90] J.G. Sivak, "Optical variability of the fish lens", in *The Visual System of Fish*, R.H. Douglas and M.B.A. Djamgoz, eds. (Chapman & Hall, Cambridge, UK, 1990)

[Smi91] G. Smith, B.K. Pierscionek and D.A. Atchison, "The optical modelling of the human lens", Ophthalmic Physiol. Opt. 11, 359-369 (1991)

[Thi02] L.N. Thibos, R.A. Applegate, J.T. Schwiegerling, R. Webb and VSIA Standards Taskforce Members, "Standards for reporting the optical aberrations of eyes", Journal of Refractive Surgery 18, S652-S660 (2002)

[Tom05] P.H. Tomlins and R.K. Wang, "Theory, developments and applications of optical coherence tomography", J. Phys. D: Appl. Phys. 38, 2519-2535 (2005)

[Vaz03] D. Vázquez, *Reconstrucción tomográfica de gradientes de índice con simetría esférica: aplicación a cristalinos de peixes*, (Memoria de licenciatura, Universidad de Santiago de Compostela, 2003)

[Vaz06] D. Vazquez, E. Acosta, G. Smith and L. Garner, "Tomographic method for measurement of the gradient refractive index of the crystalline lens. I. The rotationally symmetrical lens", J. Opt. Soc. Am. A 23, 2551-2565 (2006)

[Vil01] A.S. Vilupuru and A. Glasser, "Optical and biometric relationships of the isolated pig crystalline lens", Ophthal. Physiol. Opt. 21, 296-311 (2001)

[Wea63] R.A. Weale, "The ageing eye", en *The Lens*, H.K. Lewis, ed. (London, 1963)

[Wik] http://es.wikipedia.org/wiki/Tele%C3%B3steos

[You01] T. Young, "On the mechanism of the eye", Philos. Trans. Royal Soc. 92, 23-88 (1801)

Papers published during this research

- E. Acosta, R. Flores, D. Vazquez, S. Rios, L. Garner and G. Smith, "Tomographic method for measurement of the refractive index profile of optical fibre preforms and rod GRIN lenses", Japanese Journal of Applied Physics 41, 4821-4824 (2002)
- E. Acosta, D. Vazquez, L. Garner and G. Smith, "Tomographic method for the measurement of the gradient refractive index of the crystalline lens. I. The spherical fish lens", J. Opt. Soc. Am. A 22, 424-433 (2005)
- D. Vazquez, E. Acosta, G. Smith and L. Garner, "Tomographic method for the measurement of the gradient refractive index of the crystalline lens. II. The rotationally symmetrical lens", J. Opt. Soc. Am. A 23, 2551-2565 (2006)